

High-Speed Rapid-Single-Flux-Quantum Multiplexer and Demultiplexer Design and Testing

Lizhen Zheng



Electrical Engineering and Computer Sciences
University of California at Berkeley

Technical Report No. UCB/EECS-2007-106
<http://www.eecs.berkeley.edu/Pubs/TechRpts/2007/EECS-2007-106.html>

August 22, 2007

Report Documentation Page		<i>Form Approved OMB No. 0704-0188</i>
<p>Public reporting burden for the collection of information is estimated to average 1 hour per response, including the time for reviewing instructions, searching existing data sources, gathering and maintaining the data needed, and completing and reviewing the collection of information. Send comments regarding this burden estimate or any other aspect of this collection of information, including suggestions for reducing this burden, to Washington Headquarters Services, Directorate for Information Operations and Reports, 1215 Jefferson Davis Highway, Suite 1204, Arlington VA 22202-4302. Respondents should be aware that notwithstanding any other provision of law, no person shall be subject to a penalty for failing to comply with a collection of information if it does not display a currently valid OMB control number.</p>		
1. REPORT DATE 22 AUG 2007	2. REPORT TYPE	3. DATES COVERED 00-00-2007 to 00-00-2007
4. TITLE AND SUBTITLE High-Speed Rapid-Single-Flux-Quantum Multiplexer and Demultiplexer Design and Testing		5a. CONTRACT NUMBER
		5b. GRANT NUMBER
		5c. PROGRAM ELEMENT NUMBER
6. AUTHOR(S)		5d. PROJECT NUMBER
		5e. TASK NUMBER
		5f. WORK UNIT NUMBER
7. PERFORMING ORGANIZATION NAME(S) AND ADDRESS(ES) University of California at Berkeley, Department of Electrical Engineering and Computer Sciences, Berkeley, CA, 94720		8. PERFORMING ORGANIZATION REPORT NUMBER
9. SPONSORING/MONITORING AGENCY NAME(S) AND ADDRESS(ES)		10. SPONSOR/MONITOR'S ACRONYM(S)
		11. SPONSOR/MONITOR'S REPORT NUMBER(S)
12. DISTRIBUTION/AVAILABILITY STATEMENT Approved for public release; distribution unlimited		
13. SUPPLEMENTARY NOTES		

14. ABSTRACT

Superconductor electronics excel for high operation speed and low power consumption (several orders of magnitude lower than the equivalent semiconductor circuits). Rapid-Single-Flux- Quantum (RSFQ) circuits, in which information is stored in superconductor loops as tiny magnetic flux quanta and transferred as several picosecond-wide voltage pulses with quantized area (), are demonstrated to work at a few tens of gigahertz with the current niobium process and has the potential to work up to a few hundred gigahertz with technology scaling. A large superconductor RSFQ system or a hybrid system combined with the low-power highdensity cryogenic CMOS memory can be realized with a multi-chip module (MCM) packaging technique. The goal of this thesis project is to design and to experimentally demonstrate 20-50 GHz operation of a 1:8 demultiplexer (DEMUX) and an 8:1 multiplexer (MUX). DEMUX and MUX are important interface circuits that are required to take advantage of the ultra-high speed of the RSFQ logic. They are required to interface the superconductor and the lower-speed semiconductor circuits in a hybrid system. In a superconducting MCM system, the DEMUX and MUX can be used to convert the data rate between chips. The speed of RSFQ circuits scales with the process technology. An analysis is done to show that the maximum speed of RSFQ circuits is proportional to the shunted Josephson junction's critical current times its shunt resistance (I_cR) value. Furthermore, I_cR is proportional to the square root of the junction's critical current density (J_c 1/2) in the low-T_c niobium process. Superconductor integrated circuits using a 1 kA/cm², 3.5 μm niobium fabrication technology can operate up to 30- 40 GHz. Simulations reveal that simple RSFQ elements and gates based on a 6.5 kA/cm² technology can operate up to 70-100 GHz. With typical circuit parameters, the minimum features are around 1.35 μm. Combining the possible larger process variations caused by the reduced feature size and thinner junction barrier layer, operation of DEMUX and MUX circuits at 50 GHz is taken as a reasonable and challenging design goal. 20 GHz multiplexers (8:1, 4:1 and 2:1) and 20 GHz demultiplexers (1:8, 1:4 and 1:2) were designed and fabricated using the 1 kA/cm² process. With the external test equipment, the correct functioning of a 1:4 DEMUX was observed up to 9.2 GHz. 3.5 GHz testing result has been achieved for a 2:1 MUX. When the designs were migrated to 50 GHz using a 6.5 kA/cm² process all the circuit components were re-optimized for the new process and higher operation speed. A few specialized optimization tools were used to maximize the circuit parameter margins and yields. It was found that it is necessary to do post-layout re-optimization including

15. SUBJECT TERMS

16. SECURITY CLASSIFICATION OF:			17. LIMITATION OF ABSTRACT	18. NUMBER OF PAGES	19a. NAME OF RESPONSIBLE PERSON
a. REPORT unclassified	b. ABSTRACT unclassified	c. THIS PAGE unclassified	Same as Report (SAR)	183	

Copyright © 2007, by the author(s).
All rights reserved.

Permission to make digital or hard copies of all or part of this work for personal or classroom use is granted without fee provided that copies are not made or distributed for profit or commercial advantage and that copies bear this notice and the full citation on the first page. To copy otherwise, to republish, to post on servers or to redistribute to lists, requires prior specific permission.

High-Speed Rapid-Single-Flux-Quantum Multiplexer and Demultiplexer
Design and Testing

by

Lizhen Zheng

B.S. (Tsinghua University, China) 1992
M.S. (Academy of Sciences, China) 1995

A dissertation submitted in partial satisfaction of the

requirements for the degree of

Doctor of Philosophy

in

Engineering-Electrical Engineering and Computer Sciences

in the

GRADUATE DIVISION

of the

UNIVERSITY of CALIFORNIA, BERKELEY

Committee in charge:

Professor Theodore Van Duzer, Chair

Professor Jan M. Rabaey

Professor Adrian T. Lee

Fall 2007

The dissertation of Lizhen Zheng is approved:

Chair

Date

Date

Date

University of California, Berkeley

Fall 2007

High-Speed Rapid-Single-Flux-Quantum Multiplexer and Demultiplexer
Design and Testing

Copyright 2007

by

Lizhen Zheng

Abstract

High-Speed Rapid-Single-Flux-Quantum Multiplexer and Demultiplexer Design and Testing

by

Lizhen Zheng

Doctor of Philosophy in Engineering-Electrical Engineering and Computer Sciences

University of California, Berkeley

Professor Theodore Van Duzer, Chair

Superconductor electronics excel for high operation speed and low power consumption (several orders of magnitude lower than the equivalent semiconductor circuits). Rapid-Single-Flux-Quantum (RSFQ) circuits, in which information is stored in superconductor loops as tiny magnetic flux quanta and transferred as several picosecond-wide voltage pulses with quantized area ($\int V(t)dt = \frac{h}{2e} = 2.07mV \cdot ps$), are demonstrated to work at a few tens of gigahertz with the current niobium process and has the potential to work up to a few hundred gigahertz with technology scaling. A large superconductor RSFQ system or a hybrid system combined with the low-power high-density cryogenic CMOS memory can be realized with a multi-chip module (MCM) packaging technique.

The goal of this thesis project is to design and to experimentally demonstrate 20-50 GHz operation of a 1:8 demultiplexer (DEMUX) and an 8:1 multiplexer (MUX). DEMUX and MUX are important interface circuits that are required to take advantage of the ultra-high speed of the RSFQ logic. They are required to interface the superconductor and the lower-speed semiconductor circuits in a hybrid system. In a superconducting MCM system, the DEMUX and MUX can be used to convert the data rate between chips.

The speed of RSFQ circuits scales with the process technology. An analysis is done to show that the maximum speed of RSFQ circuits is proportional to the shunted Josephson junction's critical current times its shunt resistance (I_cR) value. Furthermore, I_cR is proportional to the square root of the junction's critical current density ($J_c^{1/2}$) in the low- T_c niobium process. Superconductor integrated circuits using a 1 kA/cm^2 , $3.5 \mu\text{m}$ niobium fabrication technology can operate up to 30-40 GHz. Simulations reveal that simple RSFQ elements and gates based on a 6.5 kA/cm^2 technol-

ogy can operate up to 70-100 GHz. With typical circuit parameters, the minimum features are around 1.35 μ m. Combining the possible larger process variations caused by the reduced feature size and thinner junction barrier layer, operation of DEMUX and MUX circuits at 50 GHz is taken as a reasonable and challenging design goal.

20 GHz multiplexers (8:1, 4:1 and 2:1) and 20 GHz demultiplexers (1:8, 1:4 and 1:2) were designed and fabricated using the 1 kA/cm² process. With the external test equipment, the correct functioning of a 1:4 DEMUX was observed up to 9.2 GHz. 3.5 GHz testing result has been achieved for a 2:1 MUX. When the designs were migrated to 50 GHz using a 6.5 kA/cm² process, all the circuit components were re-optimized for the new process and higher operation speed. A few specialized optimization tools were used to maximize the circuit parameter margins and yields. It was found that it is necessary to do post-layout re-optimization including parasitic inductances. Monte Carlo analyses based on process variations were performed to predict the circuit yield and timing variations.

When the clock speed is above 20 GHz, RSFQ circuit verifications using the external test equipment are not feasible due to the unavailability of room temperature test equipment and heavy dispersion along the cables. A data-driven-self-timed (DDST) on-chip test system was re-designed and optimized at 50 GHz assuming a 6.5 kA/cm² process.

The 50 GHz 2-bit DEMUX, basic cells of the MUX and the high-speed test system layouts were fabricated in the UCB 6.5 kA/cm² process. But due to an irreparable failure of the fabrication process, the chips could not be verified by testing.

To

Elizabeth, Andrew and my parents

Table of Contents

List of Figures	iv
Chapter 1. An Overview of Rapid-Single-Flux-Quantum Logic and Circuits	1
1.1. Introduction	1
1.2. Device and Physics	3
1.2.1. Josephson Junction.....	3
1.2.2. Static I-V Characteristics of Shunted Josephson Junctions	7
1.2.3. Driven-Pendulum Analog	9
1.2.4. Single Flux Quantum	11
1.3. Basic RSFQ Gates and Logic Presentation	13
1.3.1. Asynchronous RSFQ Circuit Components	14
1.3.2. Synchronous RSFQ Circuit Components.....	18
1.3.3. Interconnect	20
1.3.4. The Interface Circuits.....	20
1.3.5. The RSFQ Information Presentation and Logic Gates	23
Chapter 2. Technology Scaling and UCB High-J_c Niobium Process.....	25
2.1. Technology Scaling	25
2.1.1. RSFQ Circuit Speed vs. I_cR Product	26
2.1.2. Dependence of I_cR on J_c in Low- T_c Niobium Process	39
2.1.3. Junction Size Limitation	44
2.2. UCB High- J_c Niobium Process	46
Chapter 3. Design and Optimization of a Demultiplexer and a Multiplexer	53
3.1. Introduction	53
3.2. Architecture Choice	54
3.2.1. DEMUX	54
3.2.2. MUX	56
3.3. Circuit Factors of Merit.....	58
3.4. The Design Procedure	60
3.4.1. Schematic Capture	62
3.4.2. Circuit Simulation	63
3.4.2.1 Functional Check.....	63
3.4.2.2 Margin Analysis	63
3.4.2.3 Monte Carlo Analysis	64
3.4.3. Comparison of Optimization CAD tools	66
3.4.4. Layout and Inductance Extraction	68
3.4.4.1 Junction Layout.....	69
3.4.4.2 Inductance Estimation and Extraction	71

3.5. 1:8 DEMUX Design and Optimization	71
3.5.1. 20 GHz DEMUX Design, Layout and Optimization	72
3.5.2. 50 GHz DEMUX Design, Layout, and Optimization	83
3.6. MUX Simulation and Optimization Result	90
3.6.1. 20 GHz Ripple Logic MUX Design, Layout and Optimization	90
3.6.2. 50 GHz MUX Design, Layout and Optimization	95
Chapter 4. 50 GHz On-Chip Testing System	101
4.1. Introduction	101
4.2. 50 GHz Pulse Generator	103
4.3. Data-Driven Self-Timed (DDST) Shift Registers	108
4.3.1. Front Stage	110
4.3.2. SR Stage	113
4.3.3. D Flip-Flop	118
4.3.4. 4-bit DDST Shift Register	121
4.4. Whole System	124
Chapter 5. Test Results	129
5.1. Testing Setup	129
5.1.1. Special Considerations	129
5.1.2. Low-Speed Testing Setup	131
5.1.3. Medium-Speed and High-Speed Testing Setup	131
5.2. Testing Results	133
5.2.1. MUX Testing Results	133
5.2.1.1 Low-Speed Testing Results of a 2:1 MUX	133
5.2.1.2 Medium-Speed and High-Speed Testing Results of a 2:1 MUX	134
5.2.2. DEMUX Testing Results	135
5.2.2.1 Low-Speed Testing Results of a 1:2 DEMUX	135
5.2.2.2 Medium-Speed Testing Results of a 1:2 DEMUX	137
5.2.2.3 Medium-Speed Testing Results of a 1:4 DEMUX	138
5.2.2.4 High-Speed Testing Results of a 1:4 DEMUX	140
5.3. Unmeasured Test Chips	141
5.4. Conclusion	149
Appendix High-T_c Superconductor RSFQ Circuits; Monte-Carlo Analysis	151
A.1. Introduction	151
A.2. Monte-Carlo Calculation on T Flip-Flops	156
A.2.1. TRW T Flip-Flop	156
A.2.2. Conductus T Flip-Flop	159
A.3. 3-Stage Counter	162
A.4. Conclusion and Future Work	164

References	167
-------------------------	-----

List of Figures

Figure 1.1 SIS Josephson junction.....	3
Figure 1.2 The RSJ circuit model of a Josephson tunnel junction	5
Figure 1.3 Specific capacitance of Nb/AlOx/Nb Josephson junctions.....	6
Figure 1.4 SIS Josephson junction.....	6
Figure 1.5 Normalized I–V characteristics for a Josephson junction	8
Figure 1.6 Driven-pendulum analog for the Josephson junction.....	9
Figure 1.7 Contour of integration within a superconductive ring.....	11
Figure 1.8 A few stages of the Josephson Transmission Lines (JTLs).....	14
Figure 1.9 A compact two-stage JTL.....	15
Figure 1.10 Some asynchronous RSFQ circuit components.	16
Figure 1.11 A T flip-flop.	17
Figure 1.12 A RS flip-flop.....	18
Figure 1.13 A D flip-flop.....	19
Figure 1.14 A DC/SFQ	21
Figure 1.15 An SFQ/DC converter.....	22
Figure 1.16 A general RSFQ gate.....	23
Figure 2.1 The RCL equivalent circuit for the shunted junction	27
Figure 2.2 50-stage Josephson ring oscillator.....	29
Figure 2.3 Simulation of the 50-stage Josephson ring oscillator.....	30
Figure 2.4 Simulation of the 50-stage Josephson ring oscillator.....	33
Figure 2.5 Simulation on a 50-stage Josephson ring oscillator	34
Figure 2.6 200-stage JTL.	35

Figure 2.7 Pulse interval during the propagation in a JTL array	36
Figure 2.8 Normalized saturation time t_s/τ_0 , pulse FWHM/ τ_0	37
Figure 2.9 Normalized saturation time t_s/τ_0 , pulse FWHM/ τ_0	38
Figure 2.10 A pendulum analog for a 3-stage JTLs.	38
Figure 2.11 DC bias margins vs. frequency for the T flip-flop	41
Figure 2.12 Simulation of the T flip-flop	42
Figure 2.13 Cross section of UCB Nb integrated circuit process	47
Figure 2.14 SEM photos of a $0.3 \mu\text{m}^2$ high J_c junction.	49
Figure 2.15 I-V characteristics of high- J_c junctions.....	50
Figure 3.1 Block diagrams of two synchronous DEMUX architectures.	54
Figure 3.2 Block diagram of an asynchronous 1:8 DEMUX binary tree architecture.	55
Figure 3.3 Block diagrams of two 8:1 MUX architectures.....	57
Figure 3.4 Design flow chart.	61
Figure 3.5 Junction library layout.....	70
Figure 3.6 An asynchronous 1:2 DEMUX circuit.	72
Figure 3.7 Simulation waveforms of a correct function of the 2-bit DEMUX.....	74
Figure 3.8 Layout of the 2-bit DEMUX.	77
Figure 3.9 2-bit DEMUX schematic with parasitic inductances.	78
Figure 3.10 2-bit DEMUX dc bias margins vs. frequency.	82
Figure 3.11 Micrograph of a 1:4 DEMUX.	82
Figure 3.12 Micrograph of a 1:8 DEMUX	83
Figure 3.13 Dc bias margin comparison.....	84
Figure 3.14 1:2 DEMUX simulation waveforms at 50 GHz.	85

Figure 3.15 1:2 DEMUX layout in the 6.5 kA/cm ² process.....	85
Figure 3.16 50 GHz 1:2 DEMUX schematic with parasitic inductances.....	87
Figure 3.17 WinS margin report of the 50 GHz 1:2 DEMUX	88
Figure 3.18 1:2 DEMUX dc bias margins vs. frequency.....	89
Figure 3.19 A 2:1 MUX block diagram.....	90
Figure 3.20 A circuit diagram of confluence buffer with optimized parameters.....	91
Figure 3.21 A circuit diagram of RSff with optimized parameters	91
Figure 3.22 A circuit diagram of Dff with optimized parameters	92
Figure 3.23 Waveforms of the 20 GHz 8:1 MUX data path delay simulation.	93
Figure 3.24 Histogram of the delay variation for one data path	94
Figure 3.25 Waveforms of the 20 GHz 8:1 MUX simulation.	94
Figure 3.26 Layout of a 20 GHz 8:1 MUX in 1 kA/cm ² UCB Nb process.....	95
Figure 3.27 Histogram of the 50 GHz 8:1 MUX data path delay variation	96
Figure 3.28 50 GHz 8:1 MUX simulation waveforms.	97
Figure 3.29 The 6.5 kA/cm ² Tff layout.	98
Figure 3.30 Simulation waveforms of the 6.5 kA/cm ² Tff.	99
Figure 3.31 Layout of the 6.5 kA/cm ² Dff.	100
Figure 4.1 Block diagram of a DDST on-chip high-speed testing system.	102
Figure 4.2 A 4-bit ladder pulse generator.	103
Figure 4.3 The circuit schematic of one stage PS–CB combination	104
Figure 4.4 WinS margin report on the pulse generator.....	105
Figure 4.5 Post-layout circuit schematic of one stage PS–CB combination	106
Figure 4.6 Pulse frequency vs. dc bias voltage,.....	107

Figure 4.7 Micrograph of a 16-bit pulse generator.....	108
Figure 4.8 Block diagram of a 4-bit DDST shift register.	109
Figure 4.9 Block diagrams of the front stage in the DDST shift register.	110
Figure 4.10 Post-layout circuit schematics of the components in the front stage.	111
Figure 4.11 Post-layout circuit schematics of one stage SR.....	113
Figure 4.12 Two-dimensional operation range of a one-stage SR at 50 GHz.	114
Figure 4.13 Timing at the input of the first SR in the DDST shift register at 50 GHz..	115
Figure 4.14 Timing at the input of the 2nd and 3rd SR in the DDST shift register	116
Figure 4.15 Two-dimensional operation range of 3-stage cascaded SRs at 50 GHz....	117
Figure 4.16 Post-layout schematics	118
Figure 4.17 Two-dimensional operation range of the D flip-flop at 50 GHz.....	120
Figure 4.18 Timing at the input of the D flip-flop in the DDST shift register	121
Figure 4.19 Simulation waveforms of the 4-bit DDST shift register	122
Figure 4.20 Simulation waveforms of two cascaded 4-bit shift registers.....	123
Figure 4.21 A block diagram of the DDST on-chip high-speed testing system.....	124
Figure 4.22 Simulation waveforms of the high-speed testing system	125
Figure 4.23 A micrograph of a 50 GHz testing system in 6.5 kA/cm^2 process.....	127
Figure 5.1 The equipment setup for the low-speed testing experiment.....	131
Figure 5.2 The equipment setup for medium-speed testing.....	132
Figure 5.3 The equipment setup for high-speed testing.....	133
Figure 5.4 Testing results of a 2:1 MUX at 250 kHz.	134
Figure 5.5 Testing results of a 2:1 MUX at 5 MHz.	135
Figure 5.6 Testing results of a 2:1 MUX at 3.5 GHz.....	136

Figure 5.7 Testing results of a 1:2 DEMUX at 1 kHz.	137
Figure 5.8 Testing results of a 1:2 DEMUX at 10 MHz.....	138
Figure 5.9 Testing results of a 1:2 DEMUX at 1 GHz.	138
Figure 5.10 Testing results of a 1:4 DEMUX at 100 MHz.....	139
Figure 5.11 Testing results of a 1:4 DEMUX at 1 GHz.	140
Figure 5.12 Testing results of a 1:4 DEMUX at 9.2 GHz.	141
Figure 5.13 Mask set No. 1 for UCB 1 kA/cm ² Nb process.....	142
Figure 5.14 Mask set number two for UCB 1 kA/cm ² Nb process.	143
Figure 5.15 Mask set number three for UCB 1 kA/cm ² Nb process.	145
Figure 5.16 Mask set number one for UCB 6.5 kA/cm ² Nb process.	146
Figure 5.17 A 6.5 kA/cm ² Tff micrograph.	146
Figure 5.18 A 6.5 kA/cm ² 1:2 DEMUX micrograph.	147
Figure 5.19 Micrograph of two versions of 6.5 kA/cm ² Dffs.....	148
Figure A.1 TRW T flip-flop schematic.	156
Figure A.2 Simulation waveform of TRW Tff at 50 GHz.....	157
Figure A.3 TRW Tff theoretical yield with $I_cR_n = 500$ mV.....	160
Figure A.4 Conductus T flip-flop.	160
Figure A.5 Conductus idealized Tff theoretical yield with $I_cR_n = 500$ mV.	161
Figure A.6 TRW 3b-counter.	162
Figure A.7 TRW 3b-counter theoretical yield with $I_cR_n = 500$ mV.....	163

Acknowledgment

First and foremost, I would like to express my deepest gratitude to my advisor Professor Theodore Van Duzer, for his support and invaluable guidance throughout my graduate study in UC Berkeley. I'm grateful for the excellent research facilities he provided and his vast knowledge on cryo-electronics and the talented people in the cryo group. The research experience and knowledge on the integrated circuit design, fabrication and testing I gained in UC Berkeley proved to be a solid foundation when I started my current job on high-speed CMOS circuit design and testing. I'm greatly indebted to Professor Van Duzer for his enormous encouragement, his careful editing and patience during the long course of my thesis writing. The completion of this thesis would not be possible without his support. He also sets a good example for being dedicated to work and being kind to people.

I'm thankful to Professor Jan M. Rabaey, Professor Andrew R. Neureuther and Professor Paul Richards for serving on my qualifying examination committee. I also thank Professor Jan M. Rabaey and Professor Adrian T. Lee for reading my thesis and giving prompt feedbacks.

Special thanks go to Dr. Stephen R. Whiteley for the numerous discussions and the advice on all aspects of and beyond my research work. His knowledge on the superconductor circuit design, CAD tools, and high-speed testing has been a great resource. He also read most of my papers and gave useful feedback. Professor Nobuyuki Yoshikawa of Yokohama National University, Japan also shared his knowledge on RSFQ circuit design and laboratory testing during his stay in the cryo- group. I thank Xiaofan Meng for fabricating the high- J_c circuits in this work, providing the micro-lab training and helping with testing. I would also like to thank other cryo-group members, Dr. Anupama Bhat Kaul, Dr. Yiqun Xie, Dr. John Deng, Dr. Hui Zhang, Alex Flores, Jonathan Du, Zuoqin Wang, Dr. Andre Wong, Dr. Zhenglei Bao, Dr. Jiaoqin Ling, Dr. Mark Jeffrey, Dr. Huaming Jiang, Dr. Qingguo Liu for their help on various occasions.

Dr. V. K. Kaplunenko provided the WinS tool for circuit optimization in this work. HYPRES, Inc. fabricated all the working chips reported in this thesis.

This research work was supported by the University Research Initiative (ONR).

Last but not least, I'm grateful for the unconditional love from my parents Wenju Zhang and Chongmao Zheng. I thank them for nurturing my interest in sciences and technologies and encour-

aging me to be independent. And I promise to make up some playing time which is sacrificed during this writing to my son Andrew and my daughter Elizabeth.

CHAPTER 1

An Overview of Rapid-Single- Flux-Quantum Logic and Circuits

1.1 Introduction

Superconductor devices and electronics have their unique high performances and find their niche applications where traditional semiconductor electronics can not provide the needed performance [1][2].

The main advantages of superconductor circuits include:

1. High operation speed combined with low power consumption. Rapid-Single-Flux-Quantum (RSFQ) circuits in the current technology can work at a few tens of gigahertz with the potential to operate above 100 GHz with scaled device size [3][4]. A basic T flip-flop was demonstrated at 750 GHz with 0.5 μ m feature size. And the power consumption of superconductor circuits is a few orders lower than that of the semiconductor circuits. The switching energy of a typical 200 μ A junction is 4×10^{-19} J. A rich library of basic cells such as flip-flops, buffers, adders, multipliers, clock generator circuits, and phase-locking circuits have been developed. Superconductor technology finds applications in ultra-fast digital signal processing (DSP) circuits, network switching and supercomputing. A 20 GHz microprocessor based on the 4 kA/cm², 1.75 μ m low-T_c niobium pro-

cess, including 25,000 Josephson junctions on a 5 mm x 5 mm chip was designed as part of the Hybrid-Technology-Multi-Threaded (HTMT) project aiming at 10^{15} floating point operations per second [5]. A multi-gigabit network switch was demonstrated in a hybrid system including photo detectors [6]. Recent switch circuit components are demonstrated at a few tens of gigahertz [7].

2. Low noise and low pulse dispersion. Lossless ultra-high Q passive superconductor microwave filters offer unmatched sharpness, low noise figure, and interference rejection in cellular base station RF receivers [8].

3. The superconducting quantum interference device (SQUID) based sensor can detect a single flux quantum ($\Phi_0 = 2.07 \times 10^{-15}$ Wb). This high sensitivity is applied in the superconductor magnetoencephalography (MEG) systems for imaging the human brain. It also provides high sensitivity and linearity to the superconductor analog-to-digital converter (ADC). And recently, the RSFQ superconductor ADC technology has been envisioned as an enabling technology for software defined radio (SDR). In SDR receivers, ADCs digitize RF signals directly from the antenna with sufficient resolution. All the following signal processing can be implemented in the digital domain. The tens of gigahertz operation of RSFQ DSP circuits enable high speed digital down-conversion. With such a prospect, a set of ADCs could cover the spectrum from dc to a few gigahertz, each providing more than 100 dB of SFDR in its own band [9][10].

However, superconductor integrated circuits need to operate under special conditions. First, low- T_c superconductor (LTS) circuits operate at a few degrees Kelvin with a cryocooler or immersed in liquid helium. High- T_c superconductor (HTS) circuits operate at a few tens of degrees Kelvin with a cryocooler or immersed in liquid nitrogen. Another difficulty in using superconductor ICs is flux trapping. The earth's field is about 500 mG. Magnetic shielding to reduce the ambi-

ent field to less than $10 \mu\text{G}$ is desired. Even with that and special layout precaution, the power supply currents and the signal noise in the circuit may still trigger flux trapping.

1.2 Device and Physics

1.2.1 Josephson Junction

The active device in superconductor electronics is the Josephson junction, a two-terminal device which is an electrically weak contact between two superconductor electrodes. In 1962, B.D. Josephson predicted that it should be possible for electron pairs to tunnel between closely spaced superconductors even without a potential difference [11]. Anderson and Rowell made an observation of the Josephson effect in 1964 [12].

There are numerous ways to form Josephson junctions. At present, the most common practice in low-temperature superconductor (LTS) electronics is using a niobium-trilayer ($\text{Nb}/\text{AlO}_x/\text{Nb}$) structure as shown in Fig. 1.1a. The top and bottom layers are niobium, which is a superconductor below 9.2 K. In the middle is a thin layer insulator of AlO_x , which is about 1 nm thick. The barrier is thin enough for the electron pair wave functions of the two superconductors to couple with each other, so that the electron pairs can tunnel from one superconductor electrode to the other super-

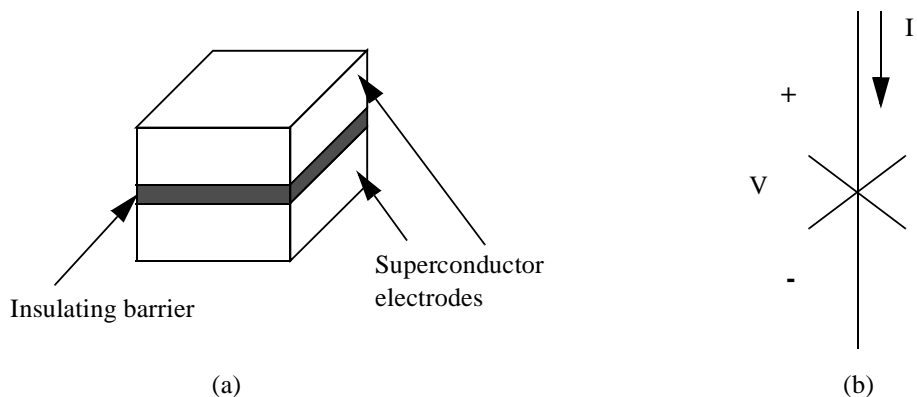


Figure 1.1 SIS Josephson junction. (a) The physical structure. (b) The circuit symbol.

conductor electrode even with zero voltage applied on the junction. Such a Josephson junction is also called an SIS tunnel junction. Fig. 1.1b shows the circuit symbol of a Josephson junction.

A simple quantum-mechanical derivation [13] gives the Josephson relations, which can be expressed in two equations:

$$I = I_c \sin \phi \quad (1.1)$$

where the constant I_c is the critical current of the Josephson junction and ϕ is the phase difference of the pair wave functions in the two superconductors. I is the pair current tunneling through the junction.

$$\frac{\partial \phi}{\partial t} = \frac{2e}{\hbar} V = \frac{2\pi}{\Phi_0} V \quad (1.2)$$

where t is time, e is electron charge, \hbar is the Plank's constant, and V is the voltage across the junction. $\Phi_0 = h/2e = 2.0679 \times 10^{-15}$ Wb is a flux quantum.

As we can see from the above two equations, with zero applied voltage, the phase difference ϕ remains constant. And a pair current less than I_c can tunnel through the junction. This is called the dc Josephson effect.

It can be inferred from Eq. (1.1) and (1.2) that the coupling of the wave functions reduces the system energy by an amount (for small junctions)

$$E_c = (\hbar I_c / 2e) \cos \phi \quad (1.3)$$

When $\phi = 0$, the current is zero and the coupling energy has its maximum value. When ϕ approaches $\pi/2$, the tunneling current reaches its maximum I_c , and the coupling energy is reduced

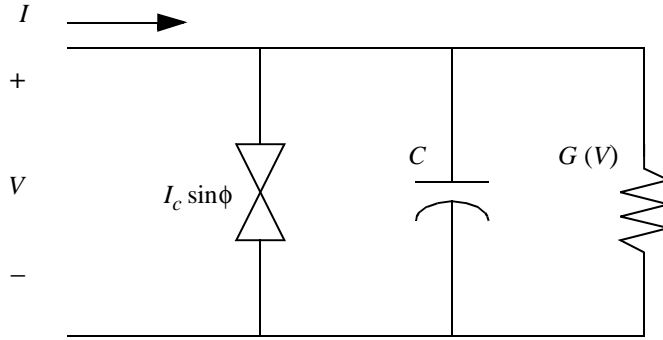


Figure 1.2 The RSJ circuit model of a Josephson tunnel junction after Fig. 4.09a in [1].

to zero. For higher currents, the wavefunctions will be uncoupled; voltage appears across the junction and varies according to Eq. (1.2).

The Josephson relations above describe only pair current in the Josephson junction. There also exists single-particle tunneling in the junction when a potential difference is applied. A well-accepted so-called RSJ (Resistor Shunted Junction) or CRSJ (Capacitor Resistor Shunted Junction) equivalent circuit model can be used to analyze the Josephson junction as shown in Fig. 1.2. Pair current is the leftmost branch labeled as $I_c \sin \phi$. Capacitance C is used to model the displacement current flowing between the two superconductor electrodes, which can be estimated from the parallel-plane capacitance formula; $C = (\epsilon_0 \epsilon_r A)/d$, where A is the junction area, d is the barrier thickness, ϵ_r is the relative permittivity of the barrier material. For the actual modeling, the capacitance is obtained experimentally. One published result [14] is shown in Fig. 1.3. The conductance element $G(V)$ on the right represents the quasiparticle current and the barrier leakage current. Fig. 1.4a shows a typical I - V curve for a tunnel junction. The current for the voltage state part can be approximated as a piece-wise linear function of the voltage. The conductance $G(V)$ is defined as the ratio of the current over the voltage for a point on the curve as shown in Fig. 1.4a. For voltage above the gap voltage, the junction has a conductance $G_n = R_n^{-1}$. For the sub-gap voltage, the con-

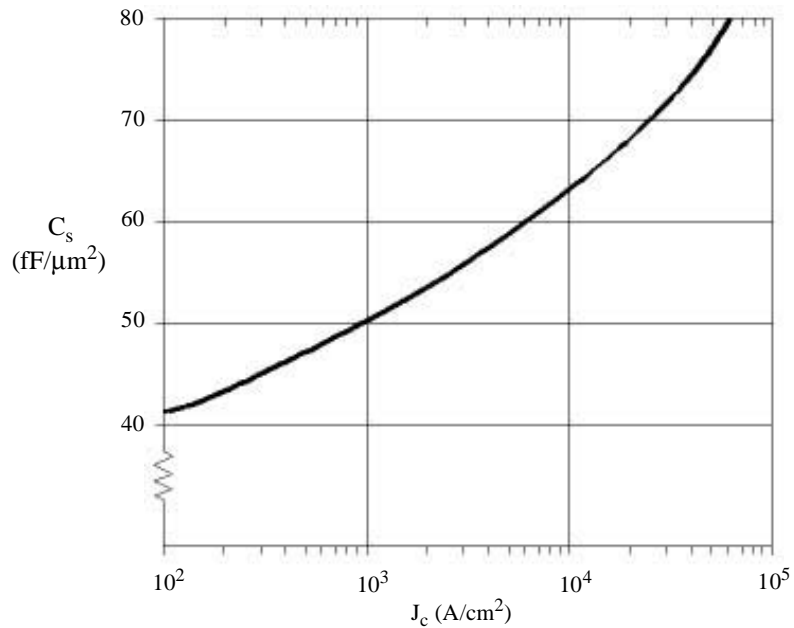


Figure 1.3 Specific capacitance of Nb/AlO_x/Nb Josephson junctions [14].

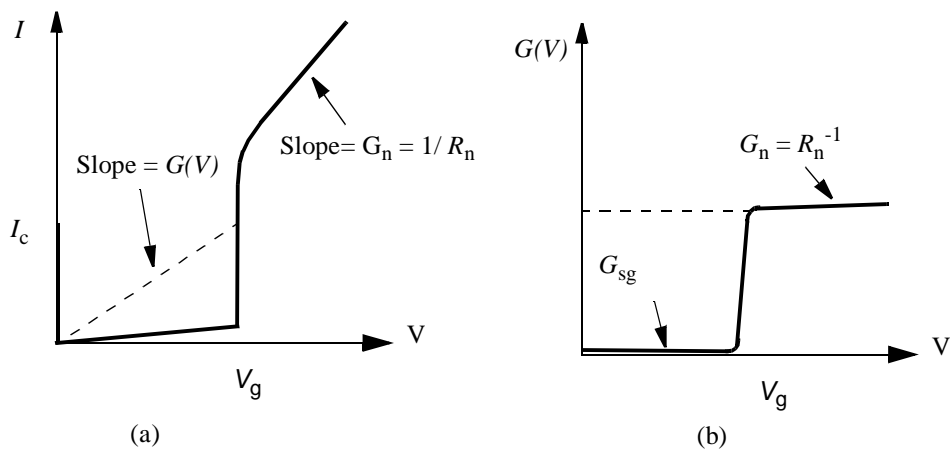


Figure 1.4 SIS Josephson junction (a) The static I - V characteristic and (b) conductance $G(V)$.

ductance G_{sg} is very small. Usually we use a quantity $V_m = I_c/G(2\text{mV})$ to measure the quality of a tunnel junction. $V_m > 40 \text{ mV}$ is considered good for the critical current density of 1 kA/cm^2 . Equivalently, $G(2\text{mV})$ is about 15–25 times lower than G_n .

1.2.2 Static I-V Characteristics of Shunted Josephson Junctions

In this section we'll study the I – V characteristics of a Josephson junction with a constant conductance G and driven by a dc current source. Through the analysis below, we can see with different shunt condition, the I – V curve can be changed between hysteretic and non-hysteretic ones. The latter is used for RSFQ circuits.

We can write a differential equation for the junction equivalent circuit shown in Fig. 1.2, with a dc current source I and a constant conductance G .

$$I = I_c \sin \phi + GV + C \frac{dV}{dt} \quad (1.4)$$

If we use the Josephson relation Eq. (1.2), and define a new time variable

$$\theta \equiv \omega_c t \equiv (2e/\hbar)(I_c/G)t \quad (1.5)$$

we obtain

$$\frac{I}{I_c} = \beta_c \frac{d^2 \phi}{d\theta^2} + \frac{d\phi}{d\theta} + \sin \phi \quad (1.6)$$

where

$$\beta_c \equiv \frac{\omega_c C}{G} = \left(\frac{2e}{\hbar}\right) \left(\frac{I_c}{G}\right) \left(\frac{C}{G}\right) \quad (1.7)$$

is the McCumber constant.

Now we are going to find the average voltage $V = \langle (\hbar/(2e))(d\phi/dt) \rangle$ with a given applied dc current. We take a look at two simplest cases. First, when $C = 0$, $\beta_c = 0$, Eq. (1.6) can be integrated directly, and we obtain

$$\begin{aligned} V &= 0 && \text{for } I < I_c \\ V &= (I_c/G)[(I/I_c)^2 - 1]^{1/2} && \text{for } I > I_c \end{aligned} \quad (1.8)$$

This is shown in Fig. 1.5a. For $I > I_c$. It shows a parabolic dependence of V on I . And notice that for each value of I , there is an unique value of V on the I - V curve. For the other extreme case, $\beta_c = \infty$, the I - V curve shows a linear dependence determined by the conductance G . For each value of $I < I_c$, there are two values of V on the I - V curve. It shows a hysteretic I - V curve. For a more general case, $\beta_c \neq 0$, numerical calculation needs to be carried out to find the I - V relation. Fig. 1.5b shows a normalized I - V characteristic for a junction with $\beta_c = 4$. Study shows there is no hysteresis for case $\beta_c < 1$. When $\beta_c > 1$, the hysteresis starts and increases with the increasing β_c . In RSFQ cir-

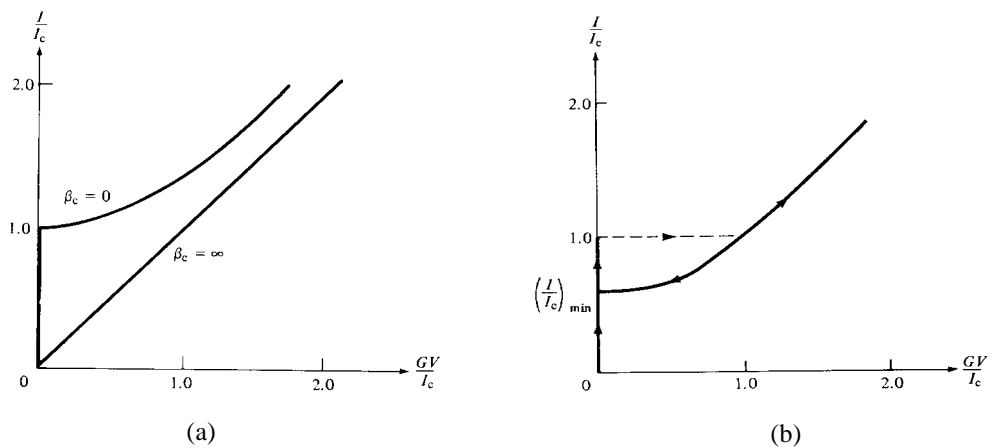


Figure 1.5 Normalized I - V characteristics for a Josephson junction (a) negligible ($\beta_c = 0$) and dominating ($\beta_c = \infty$) capacitance, and (b) $\beta_c = 4$.

cuits, the non-hysteretic I – V characteristic is necessary for the circuit operations. So junctions with β_c around 1 are used in RSFQ circuits. Larger damping $\beta_c \ll 1$ would slow the circuit.

1.2.3 Driven-Pendulum Analog

A driven-pendulum analog as shown in Fig. 1.6 can help to visualize the dynamics of the Josephson junction. Assuming the pendulum arm is weightless with length l and the pendulum bob has a mass m , the moment of inertia of the pendulum will be $M = ml^2$. The motion equation governing the angular acceleration of the pendulum is:

$$T = M d^2\phi/dt^2 \quad (1.9)$$

where ϕ is the angle between the pendulum arm and the vertical direction. T is the total torque, which consists of three parts: 1) the applied torque T_a , 2) the torque produced by the gravitation of the pendulum bulb, $-mgl\sin\phi$, where g is the gravitational acceleration; 3) the damping torque, $-D d\phi/dt$, where D is a damping constant. So

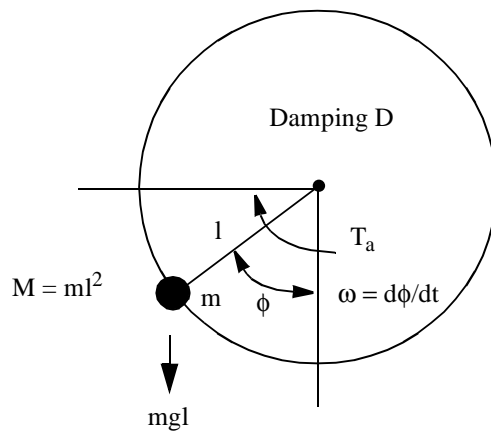


Figure 1.6 Driven-pendulum analog for the Josephson junction.

$$M \frac{d^2\phi}{dt^2} + D \frac{d\phi}{dt} + mgl \sin\phi = T_a \quad (1.10)$$

If we compare this with Eq. (1.6)

$$\frac{\hbar C}{2e} \frac{d^2\phi}{dt^2} + \frac{\hbar G}{2e} \frac{d\phi}{dt} + I_c \sin\phi = I \quad (1.11)$$

we can see that,

- 1) the angle ϕ is the analog of the phase difference ϕ ;
- 2) the angular velocity $d\phi/dt$ is the analog of the voltage V ;
- 3) the moment of inertia M is the analog of the capacitance C ;
- 4) the damping constant D is the analog of the conductance G ;
- 5) the maximum of the gravitational torque mgl is the analog of the critical current I_c ;
- 6) the applied torque T_a is the analog of the source current I .

So for a resistively shunted junction with $\beta_c = 1$ used in the RSFQ circuit, we can see how the analog helps us to imagine the junction switching dynamics. The junction is biased to $0.7I_c$, with phase close to 45 degrees. This is equivalent to the analog with a torque applied to the pendulum and the pendulum bob moved away from the vertical to angle ϕ of 45 degrees. Now if a kick is applied to the pendulum, moving the pendulum bob beyond $\phi = 90$ degrees, the gravitational torque decreases and the pendulum bob will continue over the top and come back to the original position after several small swings near the angle ϕ of 45 degrees. During the whole process, the pendulum experienced a 2π angle change; the angular velocity reaches a maximum at a point near $\phi = 0$ and then is reduced to zero with a few oscillations around the final equilibrium position. For the junction, when a proper current pulse is applied, the junction will be switched to its voltage

state (phase ϕ above $\pi/2$) and reset to its original phase plus a 2π increase. A voltage pulse is developed across the junction with a sharp peak and some ringing when it resets.

1.2.4 Single Flux Quantum

Now we are going to introduce the concept of the magnetic flux quantization in the superconductor loop. It is another unique macroscopic quantum mechanical property of a superconductor. The Cooper pairs in the superconductor can be described by a boson wave function

$$\psi(\vec{r}) = |\psi(\vec{r})| e^{i\theta(\vec{r})} \quad (1.12)$$

where the phase has to obey the equation

$$\hbar \nabla \theta = e^* \Lambda \vec{J}_S + e^* \vec{A} \quad (1.13)$$

with

$$\Lambda = m^*/n^* e^* \quad (1.14)$$

In a superconductive ring shown in Fig. 1.7, if we integrate Eq. (1.13) along a closed path C marked as the dashed line lying inside the superconductor surrounding the non-superconductive hole, we'll have:

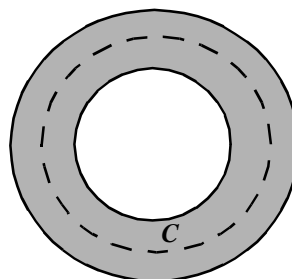


Figure 1.7 Contour of integration within a superconductive ring.

$$\hbar \oint \nabla \theta \cdot d\vec{l} = e^* \oint (\Lambda \vec{J}_s + \vec{A}) \cdot d\vec{l} \quad (1.15)$$

The phase θ of the wave function is unique or differs by a multiple of 2π at each point. So the left-hand side of Eq. (1.15) becomes $\hbar \cdot 2n\pi = nh$, where n is an integer. The integral on the right-hand side is London's *fluxoid*. If the path is deep inside the superconductor (away from the surface more than a few penetration depths), $J_s \approx 0$, so the right hand side of Eq.(1.15) becomes,

$$e^* \oint_C \vec{A} \cdot d\vec{l} = e^* \int_S (\nabla \times \vec{A}) \cdot d\vec{S} = e^* \int_S \vec{B} \cdot d\vec{S} = e^* \Phi_s \quad (1.16)$$

where Stokes' theorem is used for the first equality and Φ_s is the magnetic flux enclosed by the contour C . So

$$\Phi_s = nh/e^* , \quad \text{where } n = 0, \pm 1, \pm 2, \pm 3, \dots \quad (1.17)$$

The magnetic flux here is quantized in the unit of $h/|e^*|$, which is called a magnetic flux quantum expressed by a constant

$$\Phi_0 = h/2e = 2.0679 \times 10^{-15} \text{ Wb} \quad (1.18)$$

This result is well established experimentally.

A properly shunted junction can generate a single flux quantum pulse when it switches. As we discussed in Sec. 1.2.3, if a tunnel junction is biased near its critical current value, the junction will switch with a proper input pulse, and the phase of the junction changes by 2π ; a voltage pulse is generated across the junction during the switching. The integral of the voltage pulse over time $\int V(t)dt$ is equal to a flux quantum Φ_0 . Such a pulse is called a single-flux-quantum (SFQ) pulse.

1.3 Basic RSFQ Gates and Logic Presentation

The RSFQ circuits are composed of junctions, inductors and bias resistors. Also, each junction is shunted with an external resistor. The value of β_c is usually chosen equal to be about 1.0 so that the shunted junction has a non-hysteretic static I - V characteristic. The researchers at Northrop Gramman chose to use $\beta_c \sim 2$, which gives a higher I_cR product. RSFQ pulses can be generated, transferred and stored in the circuits based on how the junctions are biased and the inductor values are chosen.

All the basic RSFQ circuit components can be divided into two categories, asynchronous components and synchronous components.

Asynchronous components are not clocked and include simple elements such as active Josephson transmission lines (JTLs), splitters, buffers, and confluence buffers. They are used as the connections, the forks and the mergers in the logic. The more complicated toggle flip-flop (*T flip-flop*) with an internal memory is also an asynchronous circuit. The asynchronous circuits are transparent to the input signals; the signals ripple through them. The outputs are generated shortly after the inputs arrive. They are used for connections and in sequential logic.

Synchronous components are clocked. All the synchronous components contain internal memory. The incoming data set the logic states of the internal memories. The information is stored there until the arrival of a clock pulse releases it to the output. The basic synchronous components are the latches. Two widely used latches are discussed below, *RS flip-flop* and *D₂ flip-flop*. There are other latches not discussed here. Most synchronous RSFQ gates are formed as combinational logic followed by a latch.

An RSFQ circuit represents the bit information in its own unique way. The convention for the RSFQ logic presentation will be discussed in this chapter.

1.3.1 Asynchronous RSFQ Circuit Components

The simplest component is the Josephson transmission line (JTL), which is used as an interconnection in RSFQ circuits. Figure 1.8 shows a few stages of JTLs. The circuit parameters are

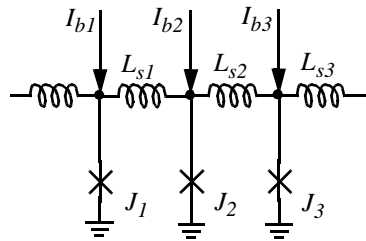


Figure 1.8 A few stages of the Josephson Transmission Lines (JTLs). I_b s are the dc biases to the junctions, L_s s are the JTL inductances connecting to the next stage.

chosen so that $I_c L_s = \Phi_0/2$, where I_c is the critical current of the junction. The dc current supply is set to about $0.7 I_c$, which is equivalent to a $\pi/4$ phase drop across the junction. When an SFQ voltage pulse comes across the junctions, it will be switched and the SFQ pulse will be reproduced and propagate along the JTLs. Both the inductance L_s and the dc bias level can be adjusted to achieve different propagation delays. Besides interconnection, JTLs can reshape the SFQ pulses and even amplify the voltage of the SFQ pulses if progressively larger I_c values or higher dc bias levels are chosen in the JTLs. For a compact layout, usually two stages of JTLs share a common dc bias current supply as shown in Fig. 1.9. The dc bias is inserted in the middle of the connection inductor between the two stages. This arrangement doesn't affect the circuit dc bias margins or the circuit dynamics. JTLs are bidirectional. Pulses can propagate from either end to the other end.

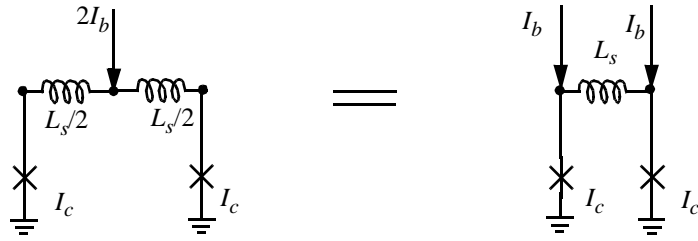


Figure 1.9 A compact two-stage JTL by sharing one dc bias input line between two neighboring stages of JTLs.

Shown in Fig. 1.10a is an SFQ pulse splitter. It provides the function of a fork. The junctions J_1 , J_2 and J_3 are biased close to their critical currents. An SFQ pulse from the input A will switch J_1 and the produced pulse current is divided between L_2 and L_3 to switch J_2 and J_3 . A pulse will be produced at each of the outputs B and C . Like the JTL, the pulse splitter doesn't protect its input from signals at its outputs. But the two circuit components discussed below only allow one directional transfer of SFQ pulses from input to output.

A simple buffer stage is shown in Fig. 1.10b. I_{c1} is larger than I_{c2} . So J_1 is biased closer to its critical current than J_2 by I_b . When an SFQ pulse arrives at the input A , the incoming pulse current adds to the bias current to switch J_1 . But for J_2 , the direction of the incoming pulse current is opposite to that of the bias current, the two currents tend to cancel each other and J_2 stays in the zero voltage state. So the SFQ voltage pulse produced at the top of J_1 will appear on the top of J_2 and propagate to the output B . On the other hand, if an SFQ pulse arrives at the output B , the incoming current will add to the bias current of both J_1 and J_2 . But since J_2 has smaller I_c , it will be switched first and set to the high impedance state. So the bias current for J_1 will be temporarily shut off, and J_1 will stay unswitched during the period of the incoming pulse. So pulses from the output B will be absorbed by J_2 , not being able to reach the input A .

Shown in Fig. 1.10c is a confluence buffer which merges the pulses from the two inputs A and B into one single output C . As we can see, each incoming branch is like a buffer stage. If a pulse comes from input A , J_1 is switched, while J_3 stays unswitched. An SFQ pulse produced at the top of J_1 then propagates through J_3 , L_3 to switch J_5 . So the pulse is reproduced at the output C . Meanwhile, the input B is protected from the pulse propagating from the input A to the output since J_4 absorbs the current caused by the pulse. Likewise, an SFQ pulse coming from input B will be reproduced and propagate to the output C . For the correct function of this confluence buffer, pulses coming from A have to keep a certain delay from the pulses coming from B . If a pulse from A is too close to a pulse from B , only one pulse with larger amplitude will be generated at the output C instead of two as it is supposed to be.

Now we are going to introduce a more complicated asynchronous component in RSFQ circuits, the *T flip-flop*. It contains a storage loop which is absent in the previous asynchronous com-

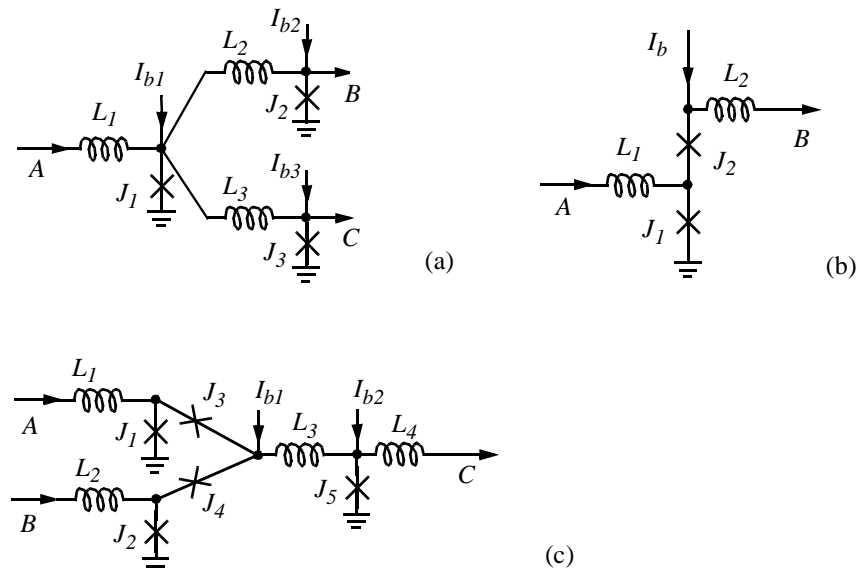


Figure 1.10 Some asynchronous RSFQ circuit components. (a) SFQ pulse splitter. $I_{c2} = I_{c3} = I_c$, $I_{c1} = 1.4I_c$, $I_{b1} = 0.75I_{c1}$, $L_2 = L_3 = 0.6\Phi_0/I_c$. (b) Simple buffer stage. $I_{c1} = 1.4I_{c2}$, $I_b = 0.7I_{c2}$. (c) Confluence buffer. $I_{c3} = I_{c4} = I_{c5} = I_c$, $I_{c1} = I_{c2} = 1.4I_c$, $I_{b1} = 1.4I_c$, $I_{b2} = 0.7I_c$, $L_3 = 0.5\Phi_0/I_c$.

ponents we've discussed. As shown in Fig. 1.11, a *T flip-flop* has one input and two outputs. The input pulses going to the *T flip-flop* are alternately diverted to the two outputs. So a *T flip-flop* can function as a 2-bit counter. In the circuit schematic diagram, J_1 , J_3 and L_1-L_2 form a storage loop. The storage loop has two states according to the direction of the circulating current flowing in it. If the current is circulating clockwise, it is state "1"; if counter-clockwise, it is state "0". The storage loop flips its state for each input pulse. Quiescently, I_b is unevenly divided between J_1 and J_3 . We can view the dc bias currents I_{J1} and I_{J3} in J_1 and J_3 as a superposition of the $I_{b1}/2$ and a counter-clockwise circulating current I_{cir} . If the storage loop is in state "0" and a pulse arrives at the input A, the current passing through J_2 adding to I_{J1} will exceed I_{c1} and switch J_1 into its voltage state, an RSFQ pulse is produced at F_0 . While at the same time, the current passing through J_4 will switch J_4 , J_3 remains in the zero-voltage state and no output pulse is generated at F_1 . For the storage loop, after J_1 is switched to its high impedance state, the bias current I_{b1} is redirected to L_1-L_2 and J_3 . The loop contains a clockwise circulating current now and is switched to state "1". Now J_3 is biased close to I_{c3} and J_1 is biased to a low phase. Similarly, now if an input pulse arrives at the input, the input current will switch J_2 and J_3 , an output pulse will be produced at F_1 , and the storage loop resets to the state "0".

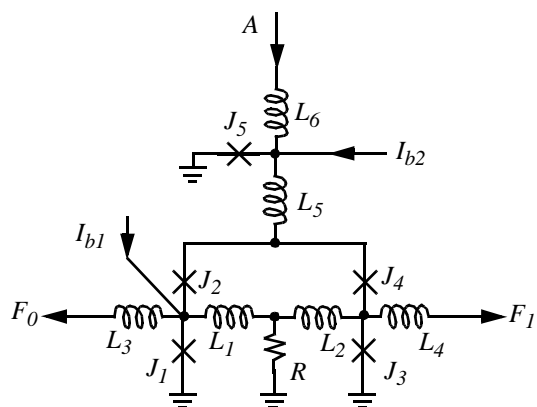


Figure 1.11 A *T flip-flop*. Example values: $I_{c1} = 279 \mu\text{A}$, $I_{c2} = 251 \mu\text{A}$, $I_{c3} = 356 \mu\text{A}$, $I_{c4} = 224 \mu\text{A}$, $I_{c5} = 264 \mu\text{A}$, $L_1 = 2.95 \text{ pH}$, $L_2 = 2.38 \text{ pH}$, $L_3 = 4.04 \text{ pH}$, $L_4 = 3.87 \text{ pH}$, $L_5 = 1.11 \text{ pH}$, $R = 1.15 \Omega$, $I_{b1} = 297 \mu\text{A}$, $I_{b2} = 311 \mu\text{A}$.

1.3.2 Synchronous RSFQ Circuit Components

Figure 1.12 shows a key component, the simplest latch in RSFQ circuits, *RS flip-flop*. The core of the circuit is a two-junction interferometer J_3-L-J_4 , with $I_c L = 1.25\Phi_0$, so that it can store a flux quantum. The interferometer has two states, “0” and “1”, corresponding to a circulating current $I_p = \Phi_0/2L$ flowing counter-clockwise or clockwise in the loop. The current in the loop can be expressed as the sum of one half of the dc bias current and the circulating current, $I_{J3} = (I_b/2) + I_p$, $I_{J4} = (I_b/2) - I_p$. Initially, the circuit is biased to state “0”, with the sample circuit parameter values, $I_{J3} = 0.8I_c$, $I_{J4} = 0$, and $I_{J1} = 0$, $I_{J2} = 0$. Pulses applied to the S and R inputs will set the circuit to the state “1” and reset the circuit to the state “0”. When a pulse arrives on the S (set) input, the current will transfer through J_2 , adding to the initial bias current on I_{J3} and switching J_3 to its high impedance voltage state. So the dc bias current is redirected to $L-J_4$, $I_{J4} = (I_b/2) - I_p = 0.8I_c$. J_3 resets to the superconductive state, $I_{J3} = 0$. The circulating current is clockwise, and the circuit is set to state “1”. When a pulse arrives at the R (reset) input at the circuit state “1”, it will pass through L_1 , J_1 and switch J_4 to its high impedance state, so I_b returns to J_3 , resetting the circuit to the “0” state. At the same time an RSFQ pulse is released to the output F .

J_1 and J_2 have lower critical current value than J_3 , J_4 and this prevents the circuit from erroneous function in the cases of unwanted pulses. When the circuit is in state “1”, if there is a pulse

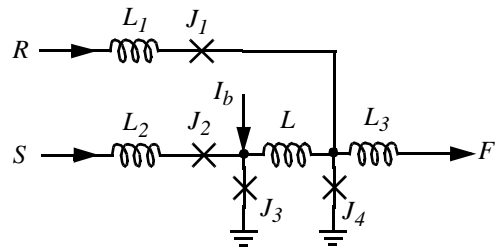


Figure 1.12 A RS flip-flop. Example values: $I_{c1} = I_{c2} = I_c$, $I_{c3} = I_{c4} = 1.41I_c$, $I_b = 0.8I_c$, $L = 1.25\Phi_0/I_c$.

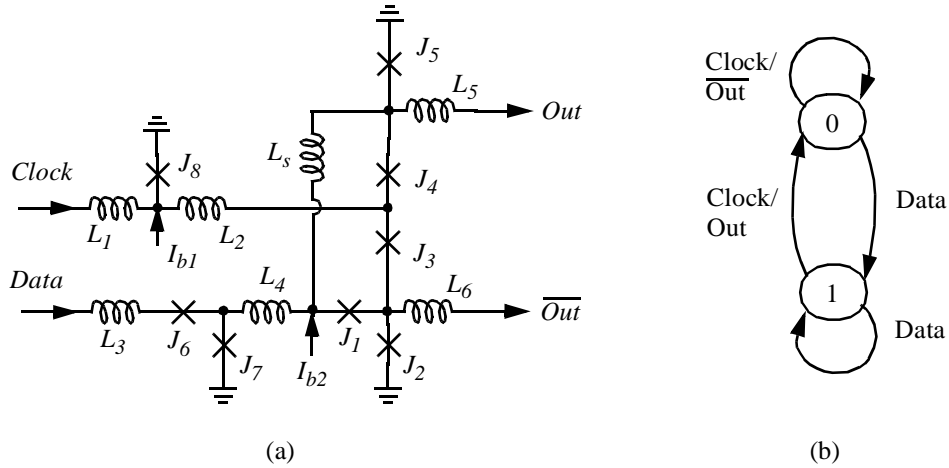


Figure 1.13 A D flip-flop (a) circuit diagram and (b) the Moore diagram for its operation.

coming from the S input, J_2 will be switched instead of J_3 , the incoming pulse voltage is absorbed by J_2 and the storage loop state remain unattacked. And if there is a pulse coming from R input when the circuit is in state “0”, J_1 is switched instead of J_4 , no output pulse is produced at F . And the storage loop stays at the original state. When the clock is fed to R , and data fed to S , the *RS flip-flop* functions as a single rail latch.

In RSFQ circuits, sometimes there is advantage to use dual-rail signals. The *D flip-flop* is a latch which can accept a single-rail input and reproduce dual-rail outputs. As we can see in Fig.1.13a, the *D flip-flop* is much more complicated than the *RS flip-flop* since it has to recover the \overline{output} from input signal. The main storage loop is $J_7-L_4-L_s-J_5$. It has two states. Initially, the current circulates counter-clockwise, J_7 is biased close to its critical state, while J_5 has phase close to zero. A pulse arriving at the input Data will switch J_7 , set the loop to state “1”, switching the circulating current in the loop to clockwise, making J_5 biased close to its critical state. Now a pulse arriving at the input Clock will switch J_5 , J_3 sequentially, generating an output pulse at Out. The circuit state is reset to “0”. If a clock pulse arrives during the state “0”, J_4 , J_2 and J_1 will be

switched sequentially and an output pulse is generated at \overline{Out} instead of Out . The operation described above can be understood more clearly in a Moore diagram, as shown in Fig. 1.13b.

1.3.3 Interconnect

JTLs are broadly used for on-chip interconnect for blocks with short separation. It has advantage to regenerate and reshape the SFQ pulse. But for chip-to-chip, on-chip long-distance interconnection, and in recent years even on-chip short distance interconnection, passive transmission lines (PTL) (a microstrip line or a stripline) are used. A JTL has a few-picosecond delay for each stage. For long interconnections, the delay is large and hard to control because of process variation and thermal jitter. And routing is difficult. However, the signal transmission in the PTL is ballistic, with very short delay (a few ps/mm). Routing is much easier. Special driver and receiver circuits [5][15][16] are needed at the two ends of a PTL to launch and accept the SFQ pulses. Connected to the transceiver circuits are usually JTL stages to shape the SFQ pulses. Efforts are made to integrate the transceiver circuits into the basic RSFQ gate library to facilitate broad PTL interconnection [5]. Another application note on using PTL interconnection is proper shielding to avoid crosstalk. The SFQ pulse energy is very small, less than 10 crossovers can make the SFQ pulse totally disappear due to the capacitive coupling [5].

1.3.4 The Interface Circuits

In RSFQ circuits, data are carried by the SFQ pulses. But in many other types of circuits, voltage levels "high" and "low" are used to represent "1" and "0". So when RSFQ circuits are used with such other circuits, interface circuits are needed to convert the signals between the two forms. There are many ways to construct a DC/SFQ converter and an SFQ/DC converter. In this section, we are going to introduce two examples.

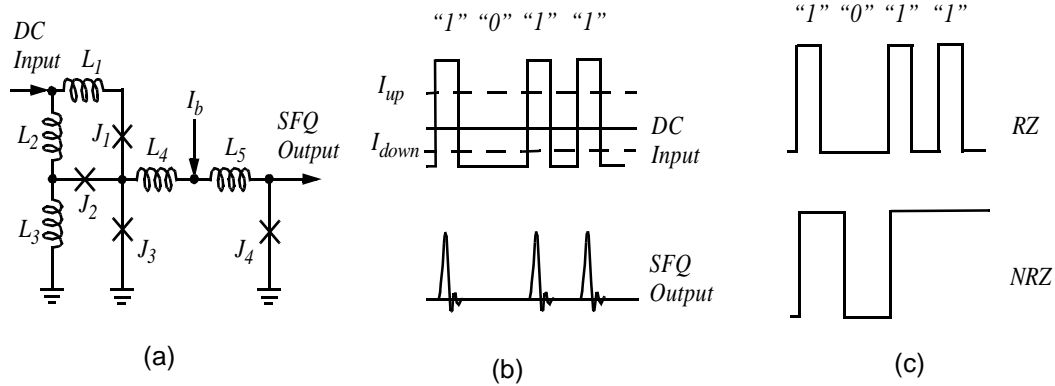


Figure 1.14 A DC/SFQ (a) circuit diagram (b) waveforms (c) illustrations of return-to-zero (RZ) and non-return-to-zero (NRZ) data.

A DC/SFQ converter transforms the voltage waveforms into a series of SFQ output pulses.

Fig. 1.14a shows the circuit diagram for a DC/SFQ converter. And Fig. 1.14b shows the input and output waveforms for the DC/SFQ converter. For this circuit, the dc input has a return-to-zero (RZ) waveform, which means that for each "1", the waveform goes to high first but must fall back to low level again before the next digit. A comparison of the waveforms for the RZ data and the non-return-to-zero data (NRZ) is shown in Fig. 1.14c. For each rise in the input wave form, which is a "1", an SFQ pulse is generated at the output. Let's take a close look at how the circuit actually realizes this conversion. When its input is raised above a certain level I_{up} , the critical state of J_3 is reached, and an SFQ pulse is generated across it. At the same time, the internal interferometer is switched to another flux state. In order to reset it to the initial state, the input current has to be reduced below a certain level I_{down} . Both J_1 and J_2 will be triggered through a 2π phase leap and J_3 is biased to its initial state. This happens during the input return-to-zero path. And actually I_{down} is less than zero. This design was originally done by Polonsky *et al.* [17]. Simulation and experi-

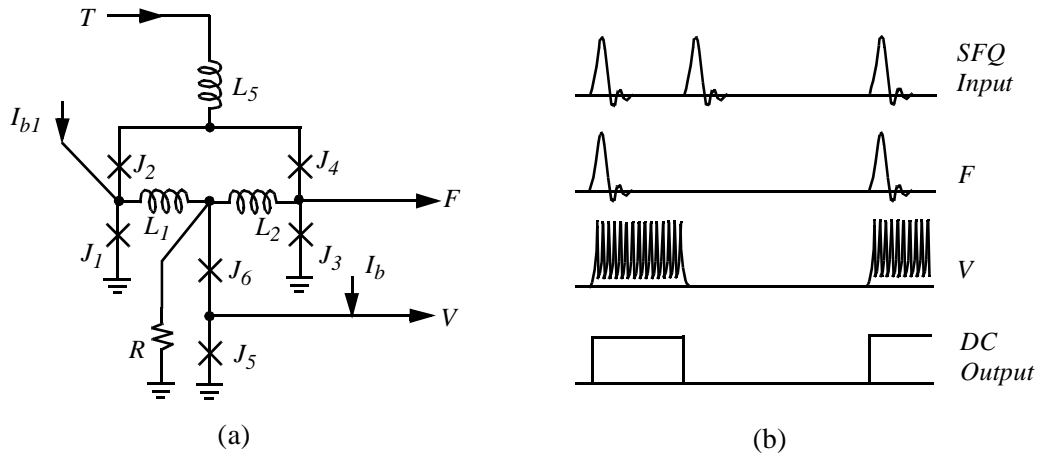


Figure 1.15 An SFQ/DC converter (a) the circuit diagram and (b) the waveforms of its input and outputs.

ments shows that this converter has larger margins (up to $\pm 60\%$ in simulation) than other variations.

An SFQ/DC converter will do the reverse of a DC/SFQ converter. SFQ input pulses will be converted to a voltage waveform at the output. Fig. 1.15 shows a *T flip-flop*-based SFQ/DC converter and its input and output waveforms. The output waveform needs some explanation since it is neither a standard RZ nor a standard NRZ waveform. Each transition in the output waveform represents a "1", corresponding to an input SFQ pulse. As we can see from the circuit diagram, this converter is based on a *T flip-flop*. Junctions J_5 and J_6 are inserted in the middle of the *T flip-flop* storage loop to read the *T flip-flop* state. If the basic interferometer is in state "0", there will be a small current flowing through J_6 and J_5 , so the voltage reading across J_5 is zero. When the storage loop switches to state "1", there is larger current from I_{b1} flowing through the J_6 , J_5 branch, adding to the bias current from I_b . This leads J_5 to its voltage state, and an average voltage is developed across it. So for an input SFQ pulse, the *T flip-flop* will reverse its storage state, the voltage across

J_5 will switch between “zero” and “high”, producing a transition in the output waveform. The typical amplitude of the output waveform is about 100 μ V for the 1 kA/cm² Nb process, which usually takes some pre-amplification either on-chip or off-chip when it is fed to the oscilloscope. Such SFQ/DC converters have been tested experimentally with large margins (+/-30%), which agrees with the simulation results - see e.g., Kaplunenko *et al.* and Polonsky *et al.* [17][18].

1.3.5 The RSFQ Information Presentation and Logic Gates

An RSFQ gate such as an AND gate, OR gate, inverter etc. can be constructed from a combination of asynchronous circuits and a latch at the end. Since data are represented by picosecond pulses instead of voltage levels, RSFQ logic uses its own convention for clocking and the decision of logic gates. Shown in Fig. 1.16a. is a block diagram of a general RSFQ clocked gate. S_1, S_2, \dots, S_n are the inputs to the gate, T is the clock, and S_{out} are the outputs. Fig. 1.16b shows the timing diagram of the signals for an OR gate with two inputs S_1, S_2 , and one output S_{out} . The time interval between the two clock pulses is one clock period τ . If a pulse arrives on the input S_n at any time during the clock period, it is considered a “1”. The absence of an input pulse at S_n in the clock

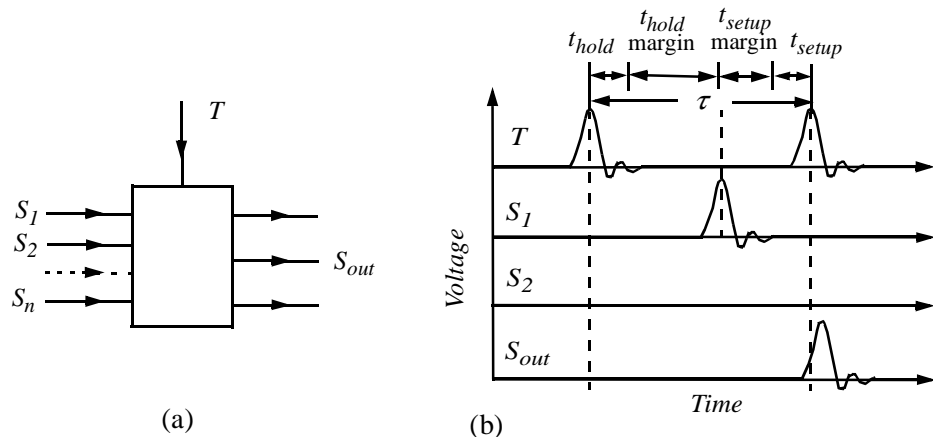


Figure 1.16 A general RSFQ gate (a) the block diagram and (b) the timing diagram of the input pulses on S_1 and S_2 arriving between two clock pulses and the output pulse at S_{out} produced at the end of the clock period for an OR gate.

period represents a “0”. The order of the arrival of the inputs doesn’t matter. Usually the gate has several internal logic states. The inputs together will set the gate to a certain logic state during the period. The gate will hold the evaluation until the arrival of the clock pulse ending the period. A pulse or no pulse will appear at the output S_{out} accordingly. And the internal state of the gate will reset to its original state. For the OR gate, a pulse arrives at S_1 and no pulse at S_2 between the two clock pulses, i.e., “1” for S_1 and “0” for S_2 . So after the arrival of the second clock pulse at the beginning of the next clock period, a pulse is produced at S_{out} , representing “1”, which is the correct function of an OR gate. For the proper function of the gate, inputs pulses should arrive after the first clock pulse with a delay t_{hold} for the gate to reset its logic state and before the second clock pulse by a time t_{setup} for the gate to fully set up its internal logic state corresponding to the inputs.

The delay (D) gate implemented by the *RS flip-flop* shown in Fig. 1.12 is the simplest clocked gate in RSFQ circuits. If we feed data to the *S* terminal, and clock to the *R* terminal, the *RS flip-flop* behaves like a latch. Any data arriving at the input in one clock period will set the internal logic state of the *RS flip-flop* and be released to the output at the beginning of the next clock period. JTLs can be combined with the *RS flip-flop* to change the delay of the gate. The *D₂ flip-flop* is another D gate with the dual-rail outputs.

CHAPTER 2

Technology Scaling and UCB High- J_c Niobium Process

2.1 Technology Scaling

The speed of RSFQ circuits scales up with the increase of I_cR product of the Josephson junction. I_c is the critical current for the Josephson junction. R is the shunt resistance on the Josephson junction. For low T_c Nb-AlO_x-Nb tunnel junctions, an external shunt resistance is connected parallel with the junction to make β_c equal to 1. When $\beta_c = 1$, I_cR is proportional to $(J_c)^{1/2}$ independent of I_c of the junction. So the higher J_c , the higher I_cR of the junctions, the faster RSFQ circuits we can achieve. At the same time, if we keep the same I_c for the circuits, junction size will be smaller. Assuming we can scale down the size of the inductors and the shunt resistors, the density of the circuits on a chip will be increased. The power consumption for each circuit is determined by I_c and dc supply voltage instead of J_c . So the circuit power dissipation stays the same with the scaling of J_c , but the power density will scale with the circuit density on the chip. For this thesis project, we had designs for both 1 kA/cm² and 6.5 kA/cm² Nb processes. We focused on the junction scaling to achieve higher circuit speed, while leaving the size of inductors and resistors unchanged. Shrinking the size of inductors and resistors is difficult due to process variation control. Layouts of some 1 kA/cm² designs can be modified simply with the sizes of the junctions changed for the 6.5

kA/cm² implementation if some margin loss is allowed. Many groups are striving to make high J_c junctions with small spreads [19][20][21][22][23].

Besides the low-T_c Nb process, SNS junctions and high-T_c YBCO junctions are two alternative technologies where RSFQ circuits can be implemented. Both of them have intrinsic non-hysteretic I-V curves. The state of the art of I_cR in these technologies is comparable with the one used in Nb process. And β_c could be much less than 1 depending on the process. The penta-layer Nb/NbTiN/TaN/NbTiN/Nb SNS junction has a similar sandwich structure [24][25]. The barrier layer TaN is a conductor, which offers a constant internal shunt resistance for a junction by itself. The advantage of absence of external shunt resistance is saving area and reducing parasitic inductances. YBCO junctions can operate at a higher temperature than Nb junctions, which is valuable for some applications. Since YBCO junctions are formed with different geometric structures, even with the absence of the external shunt resistance, the parasitic inductance values are large enough to affect the circuit performance. Thermal noise and the process variation are the other two factors to limit the complexity of the circuit built with YBCO junctions.

2.1.1 RSFQ Circuit Speed vs. I_cR Product

We can relate the junction switching speed with I_cR qualitatively through the following analysis. Let's recall the junction CRSJ equivalent circuit model shown in Fig. 1.2. The leftmost branch is the junction supercurrent $I = I_c \sin\phi$, which can be viewed as a nonlinear inductance. The voltage V across the junction can be related to the total equivalent inductance L_{Jt} by the equation, $V = d[L_{Jt}(I)I]/dt$, where I is the instantaneous pair current. Using Eq. (1.1) and (1.2), V can be expressed as

$$V = \frac{d}{dt} \left[\frac{\Phi_0}{2\pi} \sin^{-1} \frac{I}{I_c} \right] \quad (2.1)$$

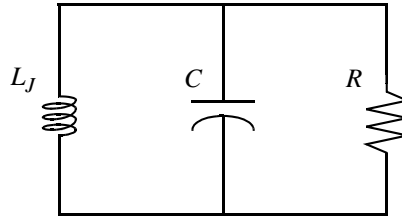


Figure 2.1 The RCL equivalent circuit for the shunted junction in RSFQ circuits when the junction supercurrent is viewed as a nonlinear inductance. Here the constant inductance L_J is used as an approximation.

so that

$$L_{Jt} = L_J \frac{\sin^{-1}(I/I_c)}{I/I_c} \quad (2.2)$$

where

$$L_J = \Phi_0 / (2\pi I_c) \quad (2.3)$$

L_{Jt} varies from L_J to $(\pi/2)L_J$ when I changes from 0 to I_c . So we can use L_J as a measure of the junction equivalent inductance. For $I_c = 125 \mu\text{A}$, $L_J = 2.64 \text{ pH}$. Now the junction equivalent circuit can be viewed as an RCL parallel combination as shown in Fig. 2.1. There are two time constants for this combination. $L_J/R = \Phi_0/(2\pi I_c R)$, and RC . The junction switching speed is determined by the larger one of these two time constants. When these two time constants are equal, $\beta_c = RC/(L_J/R) = 2\pi I_c R^2 C / \Phi_0 = 1$, the junction is critically damped in the case without any loading and has optimal switching speed for fixed I_c and C . With β_c around 1, when $\beta_c < 1$, the pulse main lobe would be wider than that in the case $\beta_c = 1$; but when $\beta_c > 1$, the envelope of the ringing tail in the SFQ pulse will decay slower. So $\beta_c = 1$ is the optimal case. Of course the actual switching

dynamics are much more complicated since it is a nonlinear process. And in the circuits, each junction has different loading, which requires an individual optimal shunt condition slightly different from $\beta_c = 1$. Normally in low- T_c Nb RSFQ circuits, people chose the same β_c around 1 for all junctions since it is difficult to define the loading and find the individual optimal β_c for each junction. $\beta_c \leq 1$ is required for the junction to have a non-hysteretic I - V characteristic to guarantee the reset of the junction after the generation of an SFQ pulse. In this case, the junction switching speed is determined by the time constant L/J . We define a time unit $\tau_0 = L/J = \Phi_0/(2\pi I_c R)$. τ_0 is inversely proportional to $I_c R$. So the higher $I_c R$, the smaller τ_0 is, the faster the junction switches and the narrower the SFQ pulse full-width-half-maximum (FWHM). In typical RSFQ circuits, the SFQ pulse FWHM is about $4\tau_0$. And the maximum speed of the circuits ranges from $1/(40\tau_0)$ to $1/(25\tau_0)$ since enough time has to be left between the consecutive data pulses or between the data pulse and the clock pulse in a clocked gate to avoid pulse interferences.

Simulations in this section will show how the SFQ pulse FWHM and speed of the circuits scale with $I_c R$ of the junctions as predicted above. Effects of other parameters such as dc bias level, junction shunt condition β_c , and inductance values in the circuits are also investigated. We will further find out that not only the pulse width but also the interactions between the pulses determine the speed of the circuits.

First we will examine the SFQ pulse FWHM and the one-stage JTL delay in a 50-stage Josephson ring oscillator as shown in Fig. 2.2. Each stage is one-JTL. All the 50 stages are identical in terms of the junction I_c , junction shunt resistance R and capacitance C , dc bias level I_b and the circuit inductance L_s connecting to the next stage. In the simulation, we feed one artificial SFQ pulse to the ring oscillator. This single pulse will be reshaped, propagates and circulates in the ring

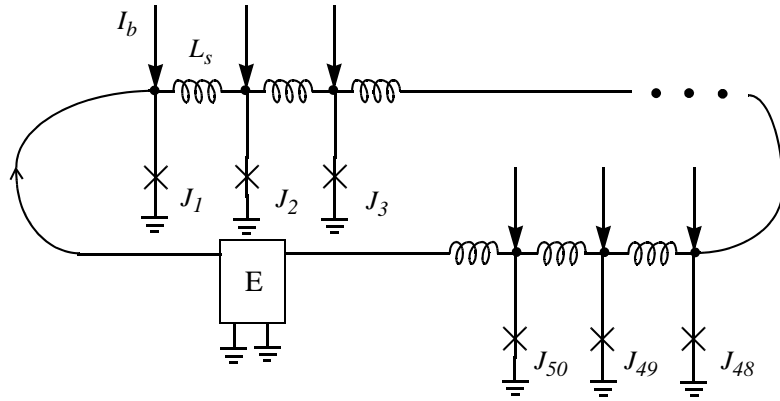


Figure 2.2 50-stage Josephson ring oscillator. All the fifty stages are identical JTL stages, including I_c of the junctions, L_s , and the dc bias level I_b .

oscillator. The ring is closed by inserting a voltage-controlled-voltage-source between stage 50 and stage 1. So the SFQ pulse circulates in the ring in one direction.

Fig. 2.3 shows the simulation results for fixed dc bias level $I_b/I_c = 0.7$ and $\beta_L/(2\pi) = I_c L_s / \Phi_0 = 0.5$, which are typical design values for a JTL, while varying $I_c R$ and β_c . Shown in Fig. 2.3a is the relation of the SFQ pulse FWHM and τ_0 vs. the junction $I_c R$ for β_c ranging from 0 to 2. We can see the RSFQ pulse FWHM is inversely proportional to the value of $I_c R$ as the τ_0 . However, β_c affects the pulse width in a weak manner. When β_c varies from 0 to 2, the pulse width only increases about 1.4 times. Don't get confused here with the statement that the $\beta_c = 1$ is the optimal shunt condition. There I_c (so as L_J) and C are fixed, we are trying to find the optimal R to make the larger one of the two time constants L_J/R and RC to have a minimum value. Here I_c and R are fixed, so one time constant L_J/R is fixed. Now by increasing C (so as β_c), the other time constant RC is increased, which puts some weak slowing effect on the junction since L_J/R is the dominant time constant when $\beta_c < 1$, and when $\beta_c > 1$, the main effect of the increasing C (so β_c) is slower decay of the ringing in the SFQ pulse. So the junction FWHM is increased weakly with increasing β_c . Shown in Fig. 2.3b, the RSFQ pulse peak voltage is proportional to the $I_c R$, which is expected

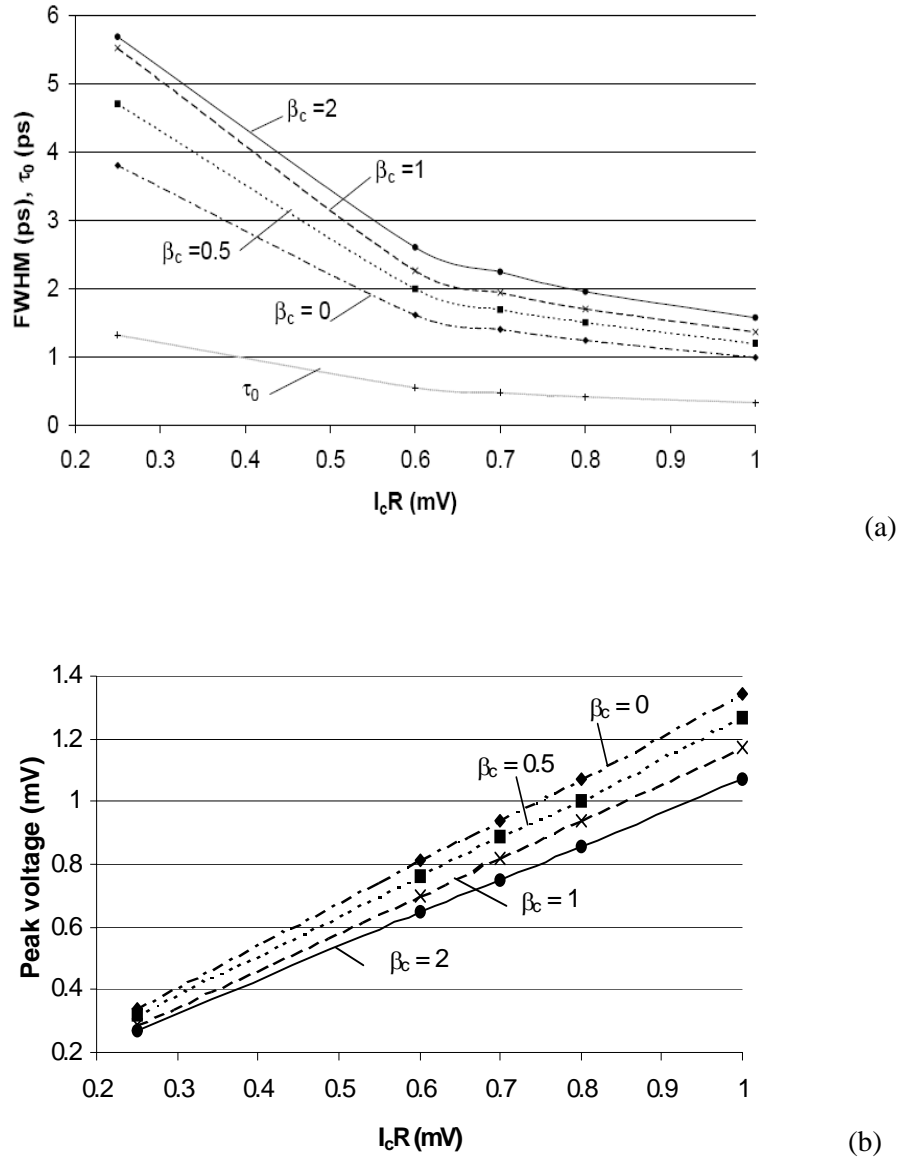
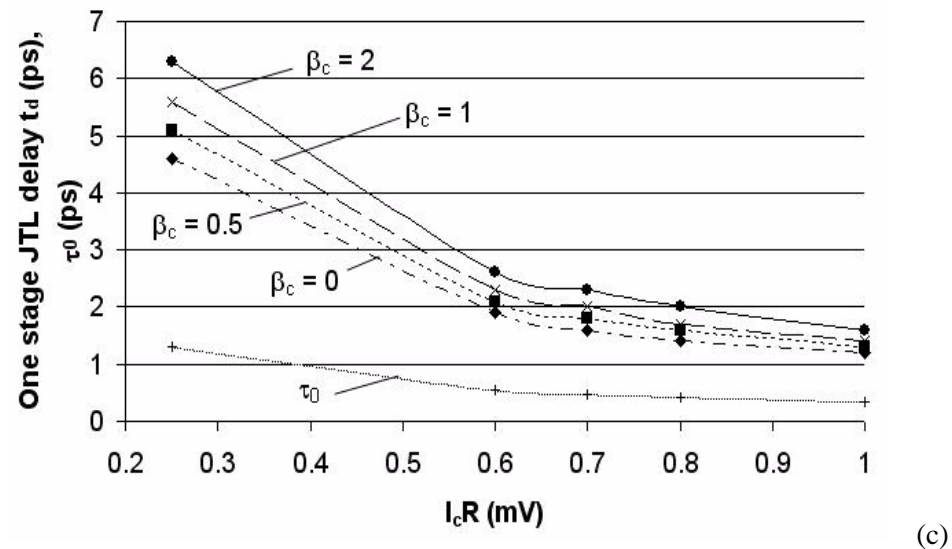
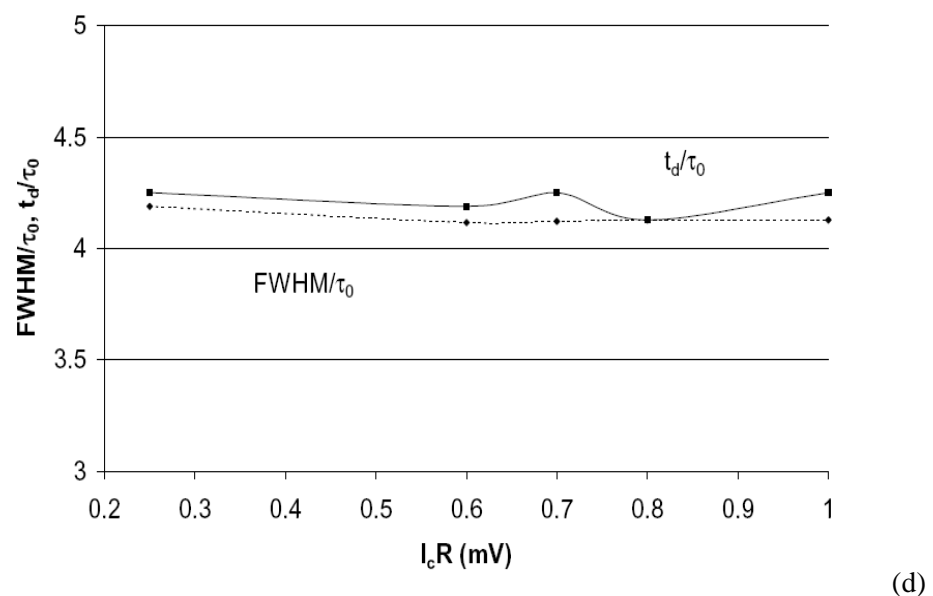


Figure 2.3 Simulation of the 50-stage Josephson ring oscillator in Fig. 2.2. $I_c = 0.2$ mA, $I_b/I_c = 0.7$, $L_s = 5.2$ pH, $\beta_L/(2\pi) = 0.5$. (a) The RSFQ pulse FWHM, τ_0 vs. $I_c R$. (b) The RSFQ pulse peak voltage vs. $I_c R$. (c) The delay of one stage JTL, τ_0 vs. $I_c R$. (d) Normalized FWHM and one-stage JTL delay for $\beta_c = 1$.



(c)



(d)

since the area under the pulse is a constant, one flux quantum. With β_c increasing from 0 to 2, the pulse peak voltage decreases weakly. The delay of a one-stage JTL t_d in the ring oscillator and τ_0 vs. I_cR are plotted in Fig. 2.3c. The delay is inversely proportional to I_cR . And β_c affects the delay weakly. If we normalize the pulse width and the one-stage JTL delay by τ_0 as plotted in Fig. 2.3d, they are almost constant for the entire I_cR range. At the typical JTL design values, 70% dc bias level, $\beta_L/(2\pi) = 1$, and $\beta_c = 1$, the SFQ pulse FWHM and one-stage JTL delay t_d in the ring oscillator are slightly larger than $4\tau_0$.

Fig. 2.4 shows the effect of the dc bias level I_b/I_c on the SFQ pulse FWHM and the one stage JTL delay t_d . Here we have a fixed $I_cR = 0.6$ mV, $\beta_c = 1$, and $\beta_L/(2\pi) = 0.5$, so $\tau_0 = 0.55$ ps. From Fig. 2.4a, we can see both the pulse FWHM and the delay t_d decrease with the increasing dc bias level I_b/I_c . When $I_b/I_c < 75\%$, the delay t_d is larger than the pulse FWHM. With $I_b/I_c > 75\%$, t_d is smaller than the pulse FWHM. While I_b/I_c varies from 0.5 to 0.9, the FWHM changes from $4.8\tau_0$ to $3.3\tau_0$ and t_d changes from $6.3\tau_0$ to $3\tau_0$ as plotted in Fig. 2.4b. By increasing the dc bias level, the circuit is faster, but there is loss of the upper dc bias margin by doing so. So usually we design and optimize the circuit starting with a 70% dc bias level to have enough dc bias margin at the design frequency. But we can expect to push the circuit to run at higher speed by increasing the dc bias level with reduced dc bias margin if needed.

The JTL inductance L_s affects the SFQ pulse FWHM and the one stage JTL delay t_d differently as shown in Fig. 2.5. In this simulation, we have fixed $I_cR = 0.6$ mV, so $\tau_0 = 0.55$ ps; $I_b/I_c = 0.7$, $\beta_c = 1$ and vary L_s . The FWHM changes very little when L_s varies, but t_d increases almost linearly with the increasing L_s . When L_s varies from 1.3 pH to 15.6 pH, i.e., $\beta_L/(2\pi)$ varies from 0.125 to 1.5, the one-stage JTL delay t_d changes from 0.99 ps to 6.26 ps, i.e., from $1.8\tau_0$ to $11.4\tau_0$. The pulse FWHM first increases from 2.12 ps to 2.26 ps, i.e., $3.9\tau_0$ to $4.1\tau_0$ with L_s increasing from

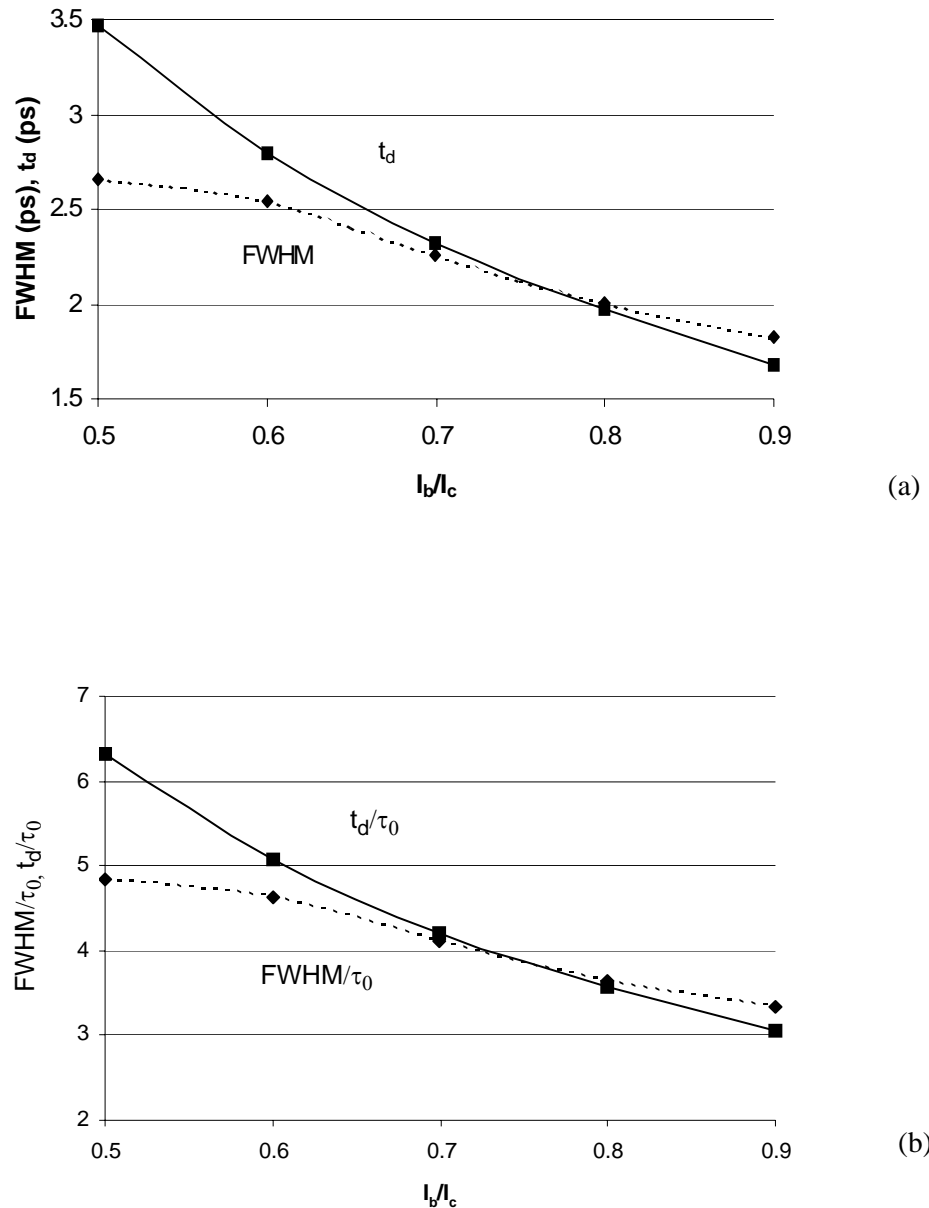


Figure 2.4 Simulation of the 50-stage Josephson ring oscillator in Fig. 2.2. $I_c = 0.2 \text{ mA}$; $I_c R = 0.6 \text{ mV}$; $\tau_0 = 0.55 \text{ ps}$; $\beta_c = 1$; $L_s = 5.2 \text{ pH}$, $\beta_L/(2\pi) = 0.5$. (a) The SFQ pulse FWHM and the one stage JTL delay t_d vs. the dc bias level I_b/I_c . (b) FWHM/τ_0 and t_d/τ_0 vs. I_b/I_c .

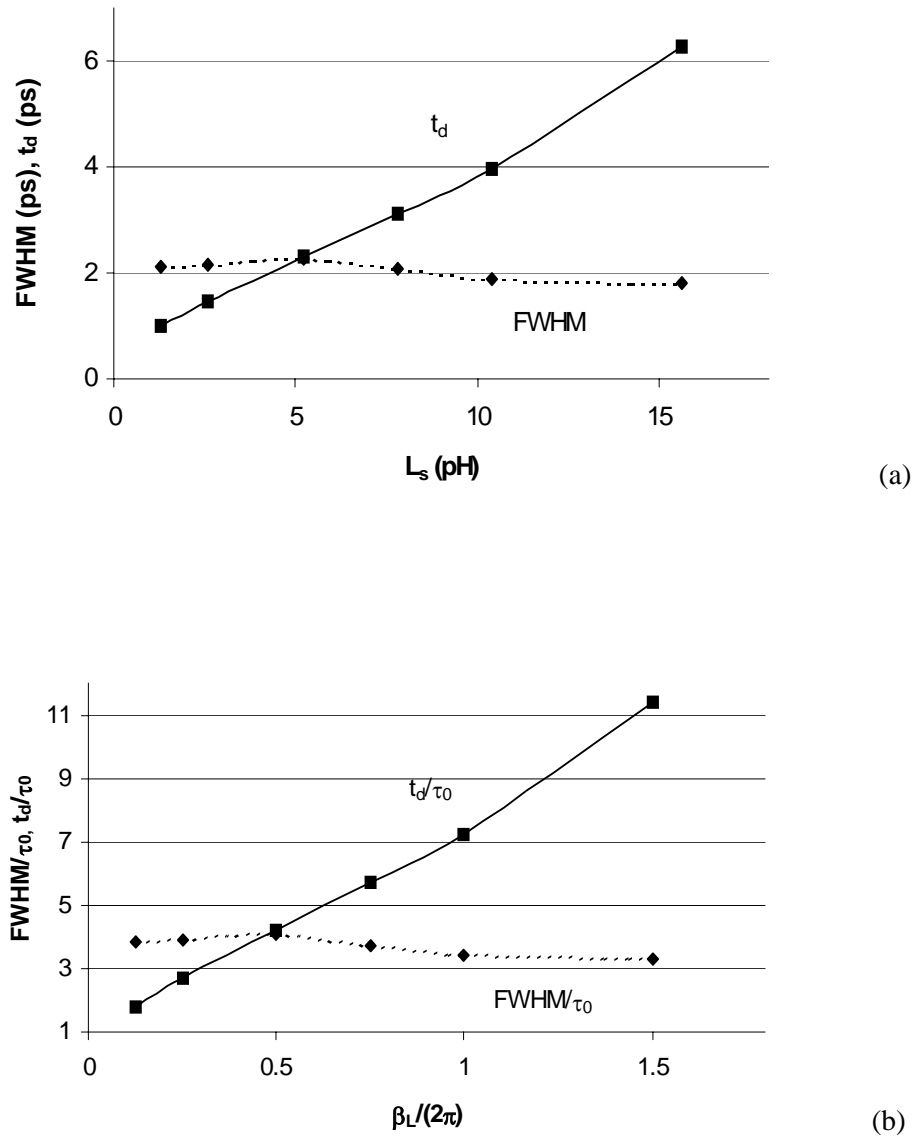


Figure 2.5 Simulation on a 50-stage Josephson ring oscillator in Fig. 2.2. $I_c = 0.2 \text{ mA}$, $I_b = 0.14 \text{ mA}$; $I_c R = 0.6 \text{ mV}$, $\tau_0 = 0.55 \text{ ps}$; $\beta_c = 1$. (a) The SFQ pulse FWHM and one stage JTL delay t_d vs. L_s . (b) FWHM/τ_0 and t_d/τ_0 vs. $\beta_L/(2\pi)$.

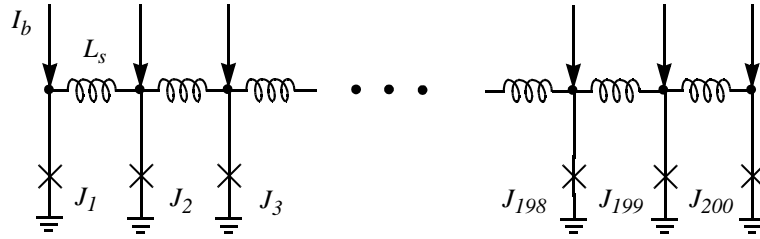


Figure 2.6 200-stage JTL. All the stages are identical, including I_c , dc bias I_b , inductance L_s and shunt condition β_c .

1.3 pH to 5.2 pH, i.e., $\beta_L/(2\pi)$ changing from 0.125 to 0.5. Then it starts to decrease from 2.26 ps to 1.81 ps, i.e., $4.1 \tau_0$ to $3.3 \tau_0$ when L_s continues to increase from 5.2 pH to 15.6 pH, i.e., $\beta_L/(2\pi)$ from 0.5 to 1.5. Although for a JTL itself, L_s is usually chosen with $\beta_L/(2\pi)$ around 0.5, in some other circuits the inductance values could be larger, such as the storage inductor in the RS flip-flop, which has a value of $\beta_L/(2\pi)$ about 1.5, so we'll expect it causes a larger delay. We'll find out in the next simulation that the delay is governed by L_s in the same way as the minimum time interval for two consecutive incoming pulses not to interfere with each other. It is the pulse width combined with the interaction between the pulses that determines the circuit speed. We'll quote some simulation results on JTLs [29] reported by V. K. Kaplunenko to verify this point.

Shown in Fig. 2.6 is a 200-stage JTL in which all stages are identical, including the junction critical current I_c , bias current I_b , inductance L_s and the shunt condition β_c . Study shows that if the interval between two incoming SFQ pulses is less than a certain value t_s , the two pulses will expel each other while they propagate through the JTLs until the saturation interval value t_s is reached. So the JTLs can only operate correctly at a speed up to $1/t_s$, otherwise the timing information carried by the pulses won't be retained. The curves in Fig. 2.7 shows the time separation between the two pulses vs. the junction number as they propagate along the array for various initial delays

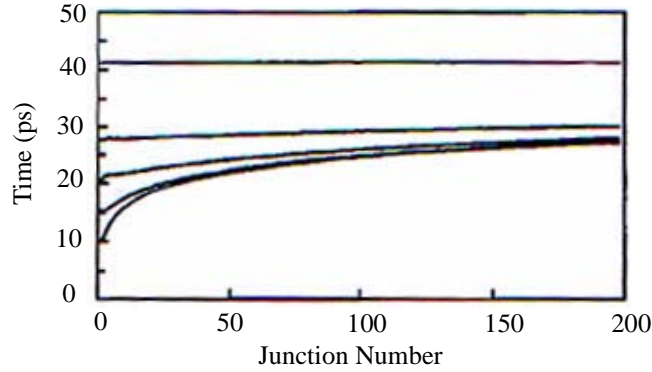


Figure 2.7 Pulse interval during the propagation in a JTL array of 200 junctions with different initial delay between the two pulses. $L_s = 7.8 \text{ pH}$, $I_b = 0.1 \text{ mA}$, $I_c = 0.125 \text{ mA}$, $R = 2 \Omega$, $\beta_c = 0$. After Fig. 3 in [29].

between them. As we can see, as long as the delay between the two pulses is less than 27.1 ps, the two pulses will keep expelling each other until the delay reaches 27.1 ps. For curves with initial delay larger than 27.1 ps, the delay between the two pulses will remain stable during the pulse propagation. So for this example, the value of the saturation time t_s is 27.1 ps. Here, the bias level is $I_b/I_c = 80\%$, $\beta_c = 0$, $\beta_L/(2\pi) = 0.5$, $I_cR = 0.25 \text{ mV}$, $\tau_0 = \Phi_0/(2\pi I_c R) = 1.32 \text{ ps}$, so $1/t_s$ is about $0.3(I_cR/\Phi_0)$, or $1/(20\tau_0)$. JTLs are used for interconnections broadly in RSFQ circuits; its speed will set an upper limit of the speed of the RSFQ circuits. Considering a more general case of 70% dc bias level and $\beta_c = 1$, $1/(25\tau_0)$ is a better estimate of the speed limit of RSFQ circuits.

Simulations are also done to check how the saturation time t_s changes with the parameters β_c , L_s and dc bias level I_b/I_c . It was found variation of β_c has a very small affect on t_s , causing less than 10% change of t_s with β_c varying from 0 to 1, which is consistent with the small effect of β_c on the pulse width and one-stage JTL delay as we discussed previously. The trend of t_s vs. I_b/I_c and L_s also agrees with what we found earlier on the pulse width and the one-stage JTL delay. We have extracted the data of t_s from Fig. 4 and Fig. 5 of Kaplunenko's paper and plot the normalized t_s/τ_0 for $\beta_c = 0$ together with the normalized pulse FWHM/ τ_0 and one-stage JTL delay t_d/τ_0 we calcu-

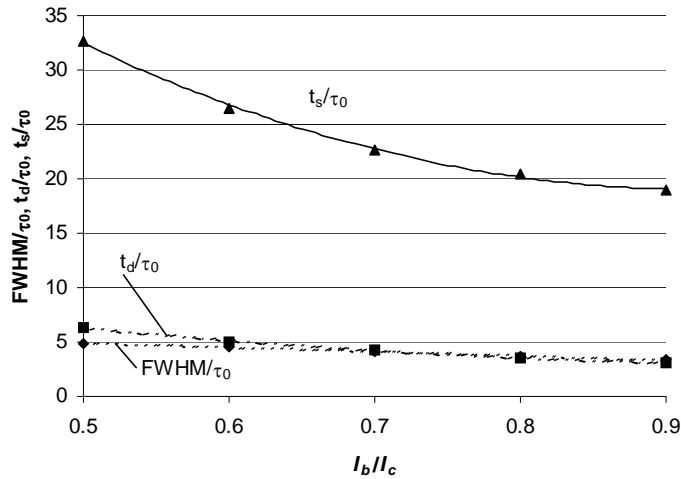


Figure 2.8 Normalized saturation time t_s/τ_0 , pulse FWHM/ τ_0 and one-stage JTL delay t_d/τ_0 vs. I_b/I_c . $\beta_c = 0$ for the calculation of t_s/τ_0 and $\beta_c = 1$ for the calculation of FWHM/ τ_0 and t_d/τ_0 . $\beta_L/(2\pi) = 0.5$ for all three cases.

lated earlier vs. I_b/I_c in Fig 2.8. And we plot the normalized t_s/τ_0 with $\beta_c = 0$, $I_b/I_c = 0.8$ together with FWHM/ τ_0 and t_d/τ_0 with $\beta_c = 1$, $I_b/I_c = 0.7$ vs. $\beta_L/(2\pi)$ in Fig. 2.9. We can see from Fig. 2.8, t_s reduces from $33\tau_0$ to $19\tau_0$ when I_b/I_c increases from 0.5 to 0.9. At 70% dc bias level, t_s is about $23\tau_0$. With the 10% increase when β_c changes to 1, t_s is about $25\tau_0$. This is because both t_d and pulse FWHM reduce with I_b/I_c . From Fig. 2.9, we can see t_s is increasing almost linearly with the increase of β_L , or L_s , following the trend of t_d while the FWHM almost remains constant. Not only the SFQ pulse width but also the interaction between the pulses determines the speed of the circuit. It would be easier to understand the dynamics with the aid of the pendulum analog. Picture the JTLs as the pendulums connected by the torsion springs as shown in Fig. 2.10. The pendulums are the analogs of the junctions and the torsion springs are the analogs of the inductors connecting the junctions in the JTLs. The larger inductance value in the JTL is equivalent with the looser springs connecting the pendulums. The time it takes for a pendulum to flip once is an analog to the SFQ

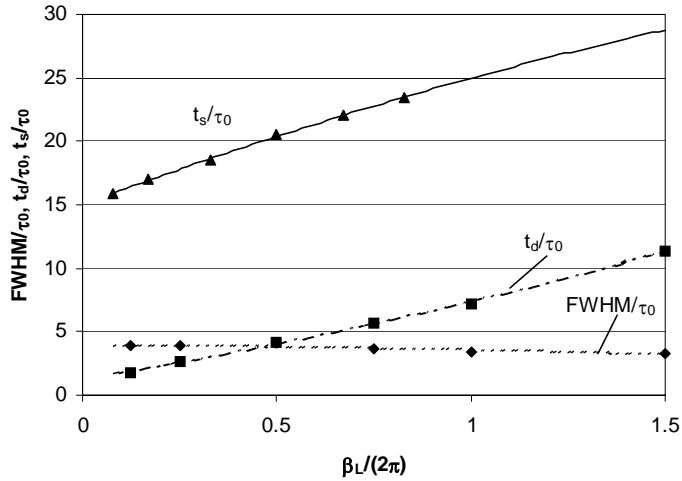


Figure 2.9 Normalized saturation time t_s/τ_0 , pulse FWHM/ τ_0 and one-stage JTL delay t_d/τ_0 vs. $\beta_L/(2\pi)$. $\beta_c = 0$, $I_b/I_c = 0.8$ for the calculation of t_s/τ_0 and $\beta_c = 1$, $I_b/I_c = 0.7$ for the calculation of FWHM/ τ_0 .

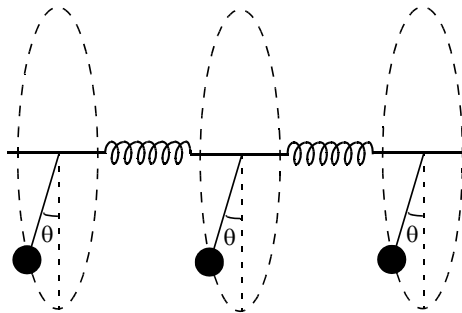


Figure 2.10 A pendulum analog for a 3-stage JTLs. Each pendulum is the analog of a junction. And the torsion springs connecting the pendulums are the analogs of the inductors connecting the junctions in the JTLs.

pulse FWHM in the JTLs. All three pendulums are initially lifted to an angle θ away from the vertical line in a surface represented by the dotted circle perpendicular to the axis along which the springs lie. With an appropriate kick applied to the first pendulum, it will rotate around the axis by 360 degrees and reset to its initial position. Then the torsion in the first spring will fire the rotation

of the second pendulum, so inducing a torsion in the second spring to fire the third pendulum. So the disturbance is propagated along the stages. The torsion in the first spring will die down after a few stages of pendulums reset. If we want to pass two kicks along the stages without interfering with each other, we would apply the second kick after a few stage delays until the motion in the first spring dies down. The stiffer the springs are, the faster the disturbance is propagated. The faster the pendulum flips, the larger torque is applied to the spring, so the faster the next pendulum is fired. Back in the JTLs, the smaller the inductance L_s is and the higher $I_c R$ is, the shorter is the one-stage delay and the smaller the minimum interval t_s between two incoming pulses.

2.1.2 Dependence of $I_c R$ on J_c in Low-T_c Niobium Process

The low-T_c Nb/AlO_x/Nb tunnel junction has a very hysteretic I – V characteristics as shown in Fig. 1.4. To be used in RSFQ circuits, a tunnel junction is shunted with an external resistance to make $\beta_c = 1$ in order to have a nonhysteretic I – V characteristics. Recalling the expression for β_c in Eq.(1.7), we can rearrange it as

$$I_c R = \sqrt{\frac{\beta_c \Phi_0}{2\pi} \cdot \frac{J_c}{C_s}} \quad (2.4)$$

where J_c is critical current density and C_s is specific capacitance of the junction and R is the total resistance of the external shunt resistance R_{ex} in parallel with the junction subgap resistance R_{sub} . J_c increases exponentially with the reduction of the barrier thickness while C_s increases linearly. As seen in Fig. 1.3, when J_c increases 10 times from 1 kA/cm² to 10 kA/cm², C_s increases only by 1.26 times from 50 fF/μm² to 63 fF/μm². So we can almost treat C_s as a constant value when J_c is varied. With $\beta_c = 1$, a constant, we can make the approximation

$$I_c R \propto \sqrt{J_c} \quad (2.5)$$

So for the niobium tunnel junctions we use in RSFQ circuits, the higher J_c , the higher I_cR , and the faster the circuits.

In the actual calculation, the C_s value from Fig. 1.3 is used in the junction model, so the dependence of C_s on I_cR is also counted. From Eq. (2.4), with $\beta_c = 1$, we have

$$I_cR = 1.815 \sqrt{\frac{J_c}{C_s}} \text{ (mV)} \quad (2.6)$$

where J_c is in unit of kA/cm^2 and C_s is in unit of $\text{fF}/\mu\text{m}^2$. For the two process we used for our designs, the J_c values are 1 kA/cm^2 and 6.5 kA/cm^2 , with C_s equal to $50 \text{ fF}/\mu\text{m}^2$ and $61 \text{ fF}/\mu\text{m}^2$, respectively, so the values of I_cR are 0.257 mV and 0.592 mV . The junction models used in the *WRspice* simulation are listed below.

```
.model jjmod1k jj(rtype=1, cct=1, icon=10m, vg=2.8m, delv=0.3m,
+ icrit=0.1m, r0=300, rn=26, cap=0.5p)
.model jjx1k jj(rtype=1, cct=1, icon=10m, vg=2.8m, delv=0.3m,
+ icrit=0.1m, r0=2.57, rn=2.36, cap=0.5p)
* Nb 1 kA/cm2, area=10 square microns

.model jjmod6k5 jj(rtype=1, cct=1, icon=10m, vg=2.8m, delv=0.3m,
+ icrit=0.1m, r0=300, rn=26, cap=0.094p)
.model jjx6k5 jj(rtype=1, cct=1, icon=10m, vg=2.8m, delv=0.3m,
+ icrit=0.1m, r0=5.92, rn=4.9, cap=0.094p)
* Nb 6.5 kA/cm2, area=1.538 square microns
```

jjmod1k is the model for a tunnel junction with J_c of 1 kA/cm^2 . For $I_c = 0.1 \text{ mA}$, the junction has an area equal to $10 \mu\text{m}^2$, subgap resistance $R_{\text{sub}} = 300 \Omega$, and the normal resistance $R_n = 26 \Omega$, capacitance $C = 0.5 \text{ pF}$. *jjx1k* is the model for the shunted junction. An external shunt resistance $R_{\text{ex}} = 2.59 \Omega$ paralleled with junction internal resistance will give the new $R_{\text{sub}} = 2.57 \Omega$, $R_n = 2.36 \Omega$. The switching of the shunted junction is happening in the subgap region. So, $I_cR = 0.257 \text{ mV}$.

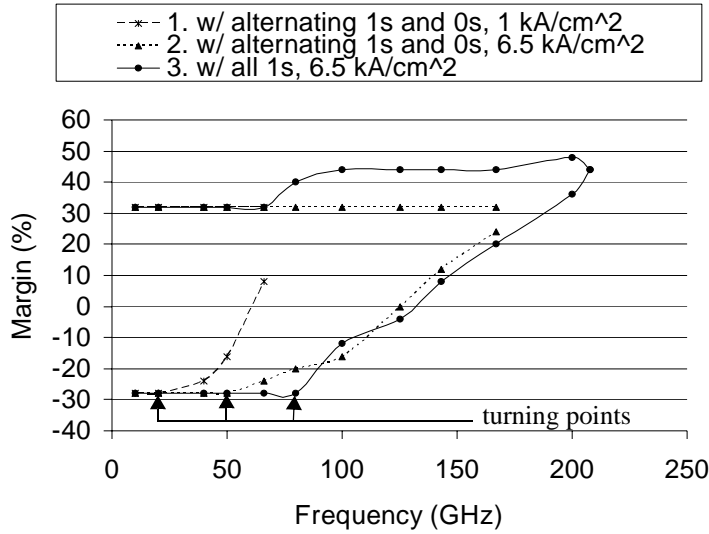


Figure 2.11 DC bias margins vs. frequency for the T flip-flop shown in Fig. 1.11 with J_c of 1 kA/cm^2 and 6.5 kA/cm^2 and different input data patterns.

jjmod6k5 is the model for a tunnel junction with J_c of 6.5 kA/cm^2 . For $I_c = 0.1 \text{ mA}$, the junction has an area equal to $1.538 \mu\text{m}^2$, subgap resistance $R_{\text{sub}} = 300 \Omega$, and the normal resistance $R_n = 26 \Omega$, capacitance $C = 0.094 \text{ pF}$. *jix6k5* is the model for the shunted junction. An external shunt resistance $R_{\text{ex}} = 6.04 \Omega$ will give the new $R_{\text{sub}} = 5.92 \Omega$, $R_n = 4.9 \Omega$. So, $I_c R = 0.592 \text{ mV}$.

Using the estimation $1/(25\tau_0) = 2\pi I_c R / (25\Phi_0) = 121.4 I_c R \text{ GHz}$, where $I_c R$ is in the unit of mV, we estimate the maximum circuit speed in the 1 kA/cm^2 and 6.5 kA/cm^2 niobium process is 31 GHz and 72 GHz, respectively. For more complicated circuits the maximum speed will be lower than these numbers. Shown in Fig. 2.11 is the dc bias margins vs. frequency for the T flip-flop shown in Fig. 1.11. For all three conditions, the circuit dc bias margins keep constant up to a certain frequency; then the lower margin starts to reduce with the frequency. The turning point (see Fig. 2.11) corresponds to the frequency when the pulses in the circuits start to interfere with each

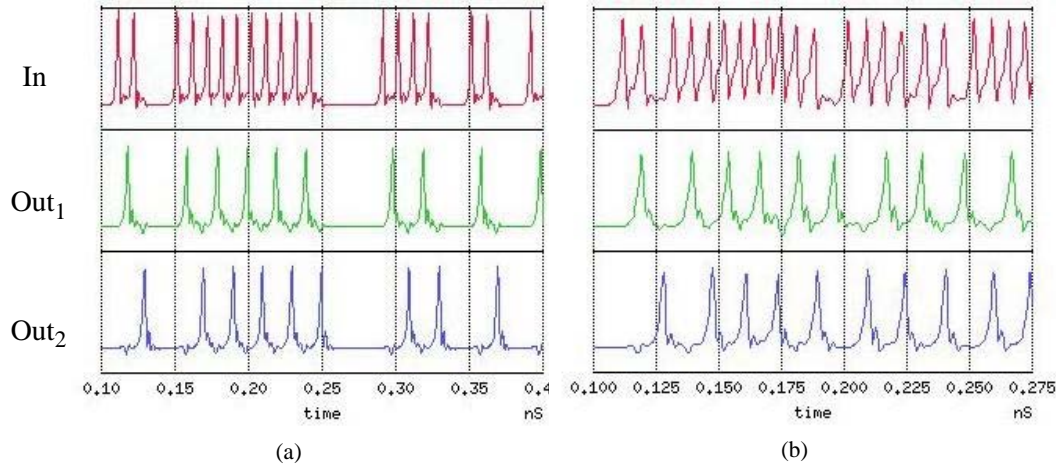


Figure 2.12 Simulation of the T flip-flop shown in Fig. 1.11 with $J_c = 6.5 \text{ kA/cm}^2$. (a) correct operation at 100 GHz. (b) erroneous operation at 200 GHz.

other. Higher dc bias makes the pulse width narrower. At frequencies above the turning point, the optimum dc bias increases to accommodate the shorter period.

Fig. 2.12 shows a comparison of correct operation at 100 GHz and erroneous operation at 200 GHz of the T flip-flop with J_c of 6.5 kA/cm^2 . At 200 GHz, for both input and outputs, the pulses repel each other, the interval between the consecutive pulses is expanded, and the position of 0s are occupied by pulses now. We can easily see it is the interference between the pulses that causes the failure of the circuit. With the input data pattern shown in Fig. 2.12, the dc margins of the T flip-flop start to decrease above 20 GHz. The circuit works up to a frequency above 66 GHz with J_c of 1 kA/cm^2 as shown in Fig. 2.11. As a comparison, the dc margins of the T flip-flop made with J_c of 6.5 kA/cm^2 start to decrease above 50 GHz but continues to work up to a frequency of 167 GHz. With an input data pattern of all 1s, the circuit dc bias margins start to decrease at a higher frequency of 80 GHz, and continues to work up to 208 GHz with J_c of 6.5 kA/cm^2 . This is because in this specific data pattern, a pulse gets repelled from both sides, so the effect of the pulse interfer-

ence on timing is reduced. The case with an input pattern of all 1s corresponds to the much reported direct high-speed testing results on T flip-flops; where an input junction is overbiased to generate continuous 1s as input, and average dc voltages across an input junction and an output junction are measured to compare the input frequency and the output frequency since the average voltage across a junction is proportional to the pulse frequency, $\bar{V} = \Phi_0 f$. Table 2-1 lists the

TABLE 2-1 Reported T flip-flop speed vs. J_c , and the minimum junction size a_{min} .

Process	J_c (kA/cm ²)	a_{min} (μm)	Speed (GHz)
Hypres	1	3.0	120
Hypres	5	1.75	220
SUNY	6	1.5	240
SUNY	50	0.25	770

reported T flip-flop speed vs. J_c of the process in which the circuit is implemented [20][21]. We can see the circuit speed is roughly proportional to $J_c^{1/2}$. Notice for the SUNY 6 kA/cm² process, chemical mechanical polishing is used to help the lithography to define small junction area better. For the SUNY 50 kA/cm² process, E-beam writing; which is not suitable for larger circuits, is used to define the junctions instead of photolithography due the small size of the junction,. The minimum size of the junctions is discussed in the section below. As we discussed earlier, the speed tested in this way is overly optimistic compared to the case where more complicated data patterns are fed to the circuit. Also, for a realistic circuit operation speed, we want the circuit to operate at a frequency below the turning point, so that the circuit has large dc bias margins. Compared to our simulated speed of 208 GHz at 6.5 kA/cm², the reported speed 240 GHz at 6 kA/cm² is slightly higher possibly because of the difference between the actual and design parameters.

2.1.3 Junction Size Limitation

When we decide on the junction I_c level, there are limitations and trade-offs. First, since the power consumption is proportional to the I_c of the junctions, we want to keep the I_c level as low as possible. The power consumption of RSFQ circuits includes two parts, static power dissipated in the bias resistors and dynamic power dissipated in the junctions during the junction switching. The voltage across the junction is zero except during its switching, so for static power, the voltage drop across the resistor is the full bias voltage V_b . For each junction, the static power is

$$P_{\text{static}} = I_b V_b = (I_b/I_c) I_c V_b \quad (2.7)$$

where, I_b/I_c is the dc bias level. For each switching, the junction consumes energy $E = \int I_c V(t) dt = I_c \Phi_0$, where $V(t)$ is the SFQ pulse voltage across the junction. So for each junction, the dynamic power is

$$P_{\text{dynamic}} = I_c \Phi_0 f \quad (2.8)$$

Here f is the clock frequency of the circuit, and P_{dynamic} increases with the clock frequency f . If we insert some typical parameters from our designs, $I_c = 250 \mu\text{A}$, $I_b/I_c = 0.7$, $V_b = 5.75 \text{ mV}$, and $f = 50 \text{ GHz}$, we get $P_{\text{static}} = 1 \mu\text{W}$ and $P_{\text{dynamic}} = 26 \text{ nW}$, about 40 times smaller. The static power is the dominating one. But both P_{static} and P_{dynamic} are proportional to I_c . So lower I_c is favored for reducing circuit power consumption.

On the other hand, it requires that I_c stays above a certain level to overcome thermal noise. The junction coupling energy is $E_c = (\hbar I_c / 2e) \cos \phi$, and the thermal noise energy is proportional to $k_B T$. Detailed analyses [30] show that to achieve bit error rate less than Γ , I_c should satisfy

$$I_c \geq \frac{6\pi k_B T}{\Phi_0} \ln \frac{1}{2\pi\Gamma\tau_0} \quad (2.9)$$

For a reasonably low bit error rate, $\Gamma\tau_0 \leq 10^{-30}$, temperature $T = 4.2$ K, I_c should not be less than 50 μ A. During switching, the effect of fluctuations is even more severe, so the minimum I_c is usually taken above 100 μ A [3]. We use 120 μ A as the minimum I_c in our designs. So the minimum junction size $a_{min} = \sqrt{120\mu\text{A}/J_c}$ assuming a square junction. For $J_c = 1$ kA/cm², $a_{min} = 3.5$ μ m. For $J_c = 6.5$ kA/cm², $a_{min} = 1.4$ μ m.

When junction size is larger than a few times of Josephson penetration depth λ_J , I_c of the junction will stop increasing with the junction area. So we use λ_J as the maximum allowed junction size.

$$\lambda_J = \sqrt{\frac{\Phi_0}{2\pi\mu_0(2\lambda + d)J_c}} \quad (2.10)$$

where λ is the magnetic penetration depth, d is the barrier thickness, $\mu_0 = 1.26$ $\mu\text{H/m}$ is the permeability of free space (and can be used for nonmagnetic materials with good accuracy). Taking typical values $\lambda = 90$ nm, $d = 1$ nm, $a_{max} = \lambda_J \approx \sqrt{(1500 \mu\text{A})/J_c}$. So $a_{max}/a_{min} \approx 3.5$ and $I_{cmax}/I_{cmin} \approx 12$. The ratio is large enough for the typical I_c values in RSFQ circuits.

For the designs in this thesis, we used two different processes, the commercially available HYPRES 1 kA/cm² and UCB high-J_c 6.5 kA/cm² Nb process. Using the discussion above, we can summarize the main parameters for the circuits in Table 2-2.

TABLE 2-2 Key parameters for RSFQ circuits in the 1 kA/cm² and 6.5 kA/cm² Nb process.

Key parameters	Hypres Present	UCB High J _c
J_c (kA/cm ²)	1	6.5
a_{min} (μ m)	3.5	1.35
I_cR (mV)	0.257	0.592
f_{max} (GHz)	30-40	70-100

Considering the process variations, we chose to design 20 GHz circuits in the 1 kA/cm² process and 50 GHz in the 6.5 kA/cm² process. The $1.35 \times 1.35 \mu\text{m}^2$ junction is achievable yet challenging. It was chosen as the smallest for which we had reliable spread data.

2.2 UCB High-J_c Niobium Process

In this section, we will briefly introduce the UCB high-J_c niobium process [22][26][27] from a designer's point of view. The success of the comeback of the superconductor digital IC after the closedown of the IBM superconductor supercomputer project is largely credited to the establishment of the Nb-based junction process to replace the Pb-based junction used in the project. Unlike the lead-based junction, which suffers from aging effects, the Nb-based junction is very stable over the time.

The UCB Nb process has 10 masks and 12 layers. Fig 2.13 shows a schematics of the cross section of the process. As we can see in Fig. 2.13, a tunnel junction can be formed by a sandwich structure Nb(CE)/AlO_x/Nb(BE). The bottom Nb is called base electrode (BE) and the top Nb is called counter electrode (CE). The junction area is determined by the size of the CE. Notice the barrier thickness listed above is actually the thickness of the Al. Only a very thin layer on the top of the Al is oxidized to form the barrier thickness. Then barrier thickness can be adjusted through oxidation to give different J_c values. A typical thickness of the AlO_x is 1 nm. The highest J_c achieved for the UCB Nb process is 26 kA/cm².

Table 2-3 lists the materials, thickness and the process methods for each layer and the order of the layers is from bottom to top according to the process flow. Insulator I and insulator II share one mask and etching step. Junction counter electrode and anodization share one mask.

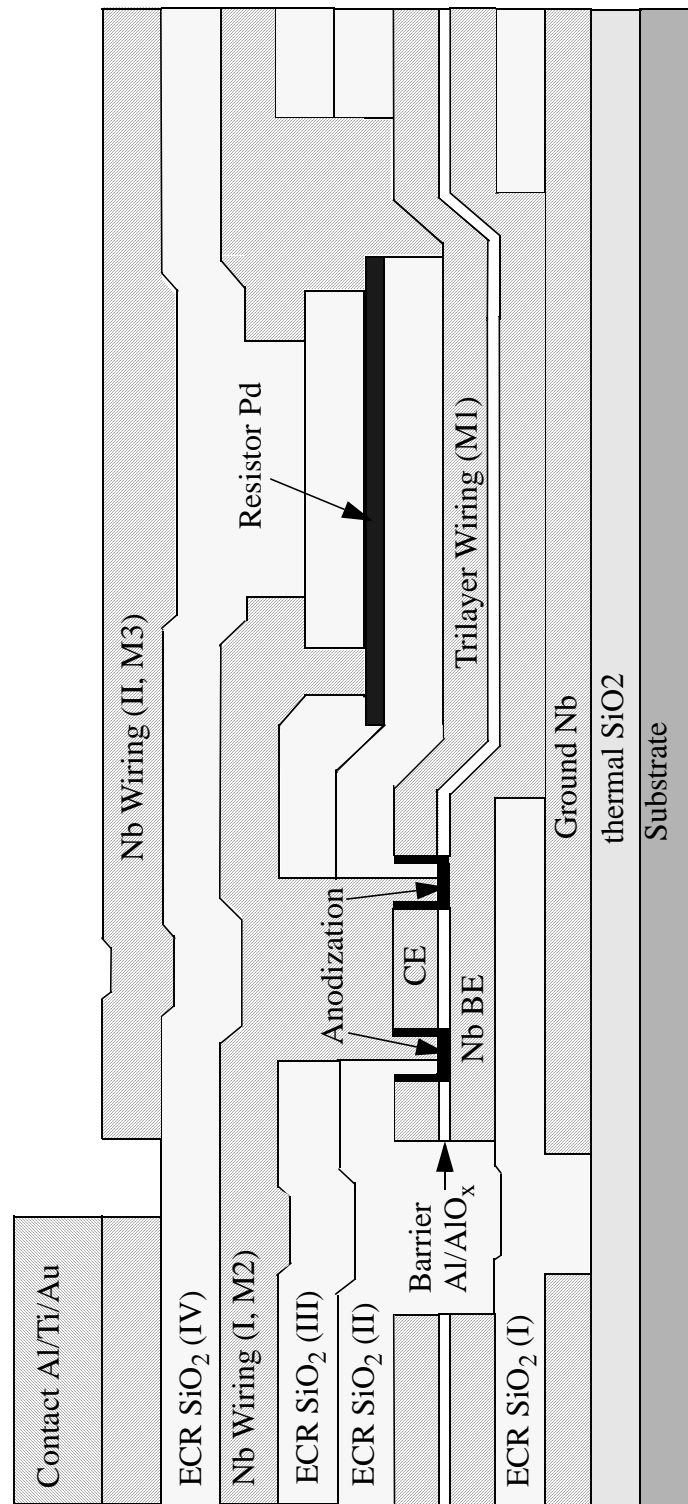


Figure 2.13 Cross section of UCB Nb integrated circuit process (not to scale).

TABLE 2-3 UCB Nb IC process flow

Layer	Material	Thickness (Å)	Process Method
Ground plane	Nb	1000	dc sputtering and RIE
Insulator (I)	SiO ₂	1500	ECR PECVD and RIE
Base electrode	Nb	2000	dc sputtering and RIE
Barrier	Al/AlO _x	90(Al)	dc sputtering and thermal oxidation
Counterelect.	Nb	600	dc sputtering and RIE
Insulator (II)	SiO ₂	1000	ECR PECVD and RIE
Resistor	Pd	400-800	E-beam evaporation
Insulator (III)	SiO ₂	1000	ECR PECVD and RIE
Wire (I)	Nb	3000	dc sputtering and RIE
Insulator (IV)	SiO ₂	5000	ECR PECVD and RIE
Wire (II)	Nb	6000	dc sputtering and RIE
Contact pads	Al/Ti/Au	100/100/2000	E-beam evaporation and lift-off

A few characteristics enable the UCB Nb process to produce high quality small junctions with small critical current spreads. First, a 10:1 wafer stepper is used for lithography. Second, high precision E-beam mask is used for the junction-definition layer [28]. On the mask, maximum variation is controlled below 0.05 μm. With the 10:1 reduction, the variation caused by mask only would be 0.005 μm on-chip, which is 1% area error for a 1 μm² junction. Third, light anodization is done in a ring area surrounding junctions as shown in Fig. 2.13. Our understanding is that this serves three functions. The Nb CE and the thin barrier experience some degradation during the RIE etching, causing the critical current density on the edge to be reduced. This reduction can't be well controlled, producing a large I_c variation among junctions. Anodization oxidizes this degraded thin layer along the edge of junctions, greatly reducing the spreads of the junction I_c . At the same time, the anodized layer is a good insulating layer to prevent leakage current from the CE to BE which might exist through the pinholes in the SiO₂ layer at the edge of the junction or

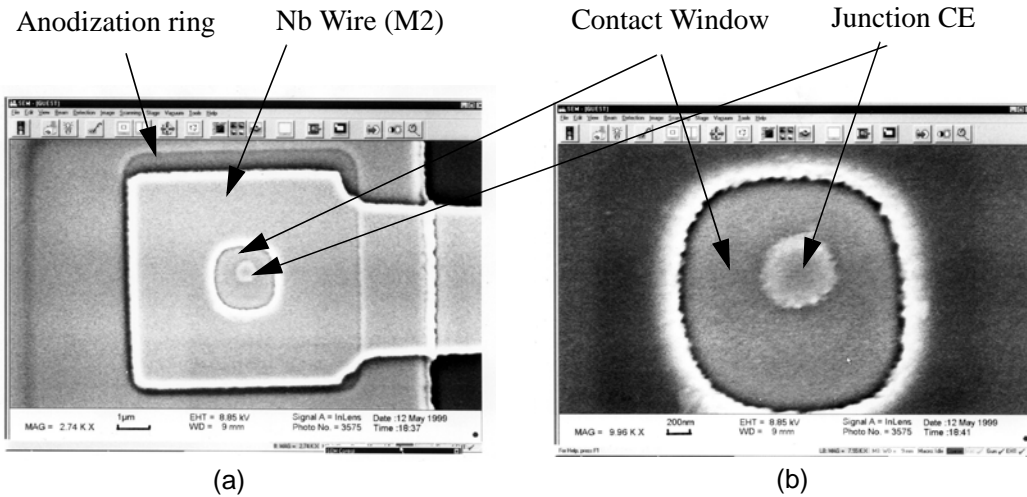


Figure 2.14 SEM photos of a $0.3 \mu\text{m}^2$ high J_c junction. (a) The junction with wiring. (b) Enlarged image of the junction CE and the contact window.

through the degraded AlO_x , thus producing high quality tunnel junctions. For the small junctions in the high J_c process, the junction size is typically less than $2 \times 2 \mu\text{m}^2$. We may want to use a contact hole for the CE with size equal or larger than $2 \times 2 \mu\text{m}^2$. So the size of the contact hole is actually larger than the size of the CE itself, which is only possible with the insulation of the anodization layer. Fig.2.14 shows SEM photos of a $0.3 \mu\text{m}^2$ junction. Notice the contact window to the CE is actually larger than the CE and the entire contact window outside the CE is sitting in the anodization ring area. So the upper wiring can only contact the CE, insulated from the BE.

Fig. 2.15a shows the I - V characteristics of the $0.3 \mu\text{m}^2$ junction with $J_c = 12 \text{ kA/cm}^2$. We can see that even with such a small size, the junction still retains a good tunnel junction I - V characteristics. $V_m = 12 \text{ mV}$, which gives large enough subgap resistance to be ignored when the junction is shunted by a small external resistance of a few ohms. That is why the exact value of the subgap resistance r_0 is not important in the junction models which we presented in Sec.2.1.2.

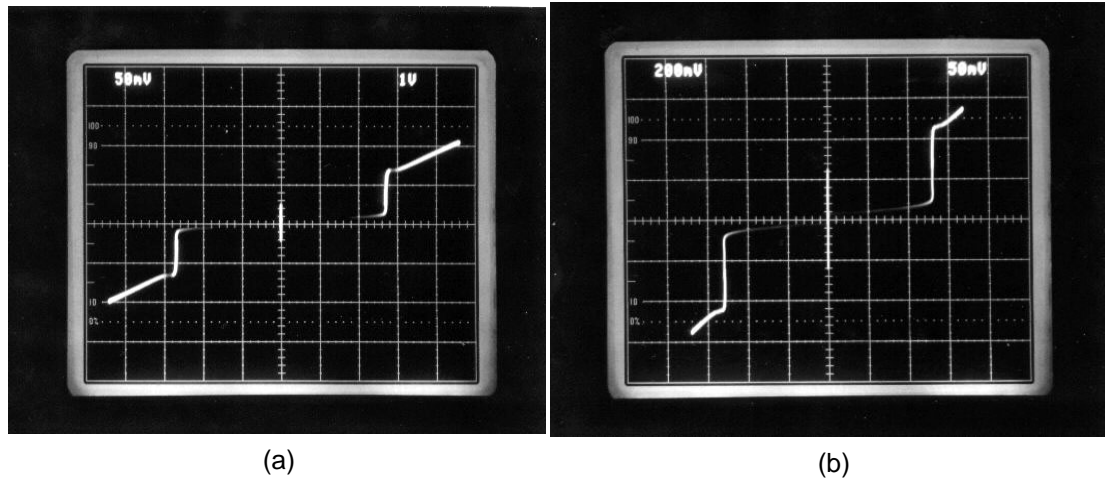


Figure 2.15 I - V characteristics of high- J_c junctions. (a) the $0.3 \mu\text{m}^2$ junction shown above, $J_c = 12 \text{ kA/cm}^2$, $V_m = 12 \text{ mV}$. (x-axis: 1 mV/div, y-axis: 50 $\mu\text{A}/\text{div}$) (b) 50 series junctions, the junction size is $1.5 \times 1.5 \mu\text{m}^2$, $J_c = 12 \text{ kA/cm}^2$, J_c spread is 1%. (x-axis: 50 mV/div, y-axis: 200 $\mu\text{A}/\text{div}$).

Fig. 2.15b shows the I - V characteristics for a 50-junction series array. The junction size is $1.5 \times 1.5 \mu\text{m}^2$, $J_c = 12 \text{ kA/cm}^2$. The critical current spread (minimum to maximum) is only 1%. This spread doesn't consider the run-to-run and chip-to-chip variations. A more realistic state of art J_c spread is 2% (1σ) on junctions with size down to $1.5 \times 1.5 \mu\text{m}^2$ reported by TRW [23] after they adopted the anodization approach in their process.

Another uniqueness of the UCB Nb process is the low-temperature, low-stress ECR PECVD SiO₂ process for junction insulation. Since the ECR microwave plasma has a much higher density and a very low ion energy compared to the traditional RF plasma, the ECR PECVD system can deposit SiO₂ at a high deposition rate and a low substrate temperature with very small damage to surfaces. As a result, the insulation quality of the SiO₂ layer is better. Uniformity of the layer is also improved. And junctions experience much less damage because of the low stress and the low substrate temperature.

The knowledge of the process flow and the thickness of layers are used for inductance calculation. And we usually connect the wire II (M_3) layer with the ground plane through vias to form double ground planes to reduce the inductance value per unit length for inductors implemented by M_1 or M_2 . The trilayer Nb/AlO_x/Nb can be used as wire beyond the junction area. We call it M_1 in that case.

Sheet resistance of the resistor layer can be adjusted through the layer thickness. It is 1 ohm per square for the 1 kA/cm² process and 2.3 ohms per square for the 6.5 kA/cm² process.

CHAPTER 3

Design and Optimization of a Demultiplexer and a Multiplexer

3.1 Introduction

Demultiplexers (DEMUX) and multiplexers (MUX) are useful circuits to change the data rate and to implement conversion between serial data and parallel data. Large RSFQ systems are usually composed of chips mounted on a multi-chip module (MCM). The connecting solder bumps limit the data rate from chip to chip [31][32]. On-chip RSFQ circuits can operate up to several tens of gigahertz in the current technologies and have potential to run above 100 GHz. DEMUX and MUX circuits can be used to change the data rate when the signals go between chips and back onto chips. Due to the maturity of the semiconductor circuits in digital signal processing and memory, hybrid systems such as an RSFQ analog-to-digital converter followed by VLSI CMOS digital signal processing circuits, or an RSFQ microprocessor combined with hybrid Josephson-CMOS memory circuits, are proposed and researched [33][34][35][36]. In such a system, DEMUX and MUX are needed as interface circuits between the high-speed RSFQ circuits and the lower-speed CMOS circuits. The serial-to-parallel converter also has applications in arithmetic logic units (ALU) and special purpose hardware such as fast Fourier transform circuits and network switches.

3.2 Architecture Choice

3.2.1 DEMUX

Based on applications, the DEMUX circuit can be either a synchronous or an asynchronous design. There are mainly two types of architecture adopted in the synchronous designs, shift-and-dump structure and binary tree structure. In a shift-and-dump structure [37], shown in Fig. 3.1a, an N-bit DEMUX can be constructed from N-stage modified non-destructive-read-out (NDRO) shift registers. All N-bit data are shifted along the shift registers at the clock rate; then a read signal is

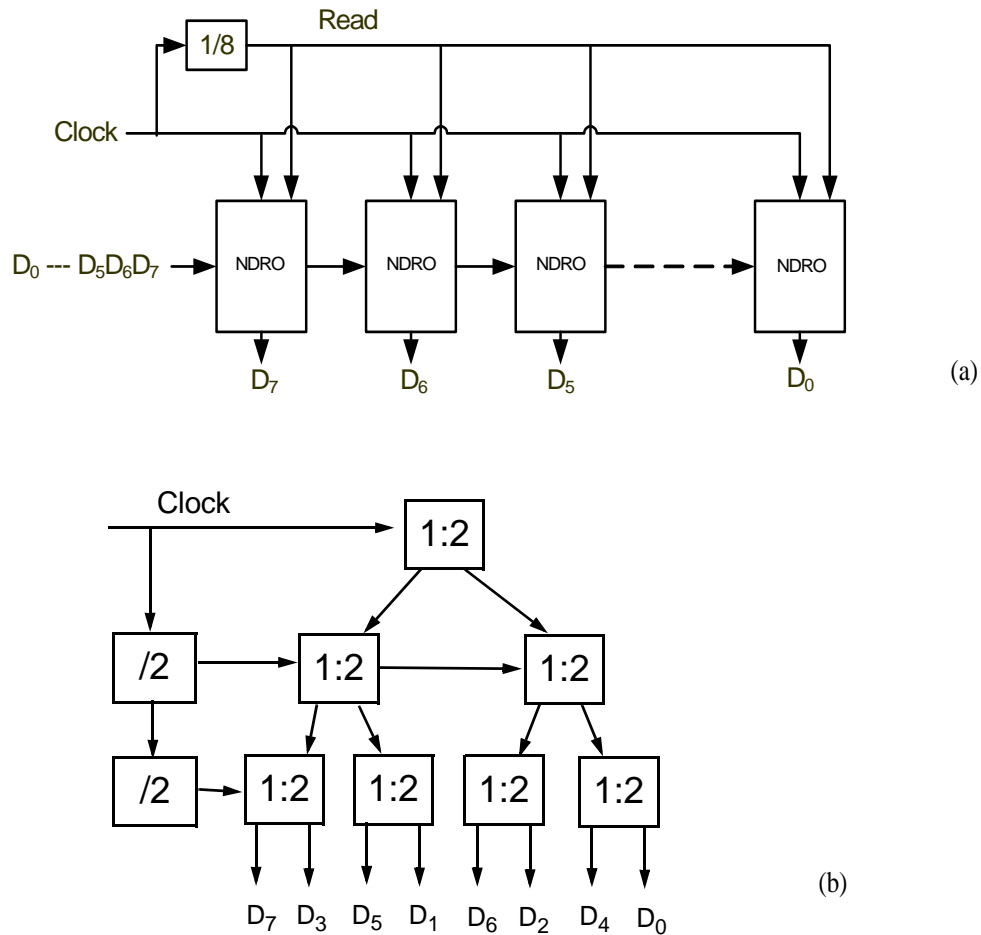


Figure 3.1 Block diagrams of two synchronous DEMUX architectures. (a) an 8-bit shift-and-dump DEMUX (b) an 8-bit binary tree DEMUX.

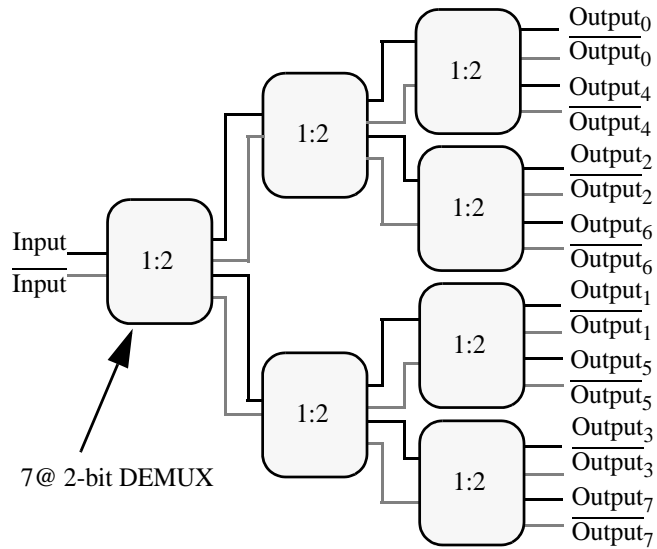


Figure 3.2 Block diagram of an asynchronous 1:8 DEMUX binary tree architecture.

released to read out the N bits of data simultaneously. The advantage is that an arbitrary N -bit DEMUX can be constructed in this way. The layout configuration is straight forward. The drawback is that every unit has to operate at the speed of the input signal during the data shifting. The timing between the clock, data, and read signals is intricate since the delay variations of the clock and read signals along the path can accumulate. The higher the speed and larger the number of bits, the more challenging it is in terms of timing control. In the binary tree structure [38] shown in Fig. 3.1b, an 8-bit DEMUX is constructed from seven 2-bit DEMUX modules. In general, a 2^n -bit DEMUX can be built from $2^n - 1$ 2-bit DEMUX modules. Only the module on the top of the tree is operating at the speed of the input data. The modules at each step down operate at a two-fold reduced speed. At the bottom of the tree, the modules operate at $1/2^{n-1}$ of the input speed.

We design a 1:8 DEMUX based on the asynchronous binary tree architecture [39][40] shown in Fig. 3.2. Compared to the two synchronous architectures above, it eliminates the complex tasks

of clock generation and distribution. And it retains the advantage of the binary tree structure of lowering operation speed after the first stage.

3.2.2 MUX

Several architectures for MUX circuits are compared. Shown in Fig. 3.3a is a load-and-shift 8:1 MUX architecture. It consists of eight stages of identical shift registers (SR). Each basic cell is a one-stage shift register. With a Load pulse, external parallel data D_0, D_1, \dots, D_N are selected by the SRs to shift to their outputs, otherwise the output from the previous stage is selected. So every eight high-speed clock cycles, the external data are loaded once. Then the high-speed clock shifts all the remaining seven bits of data from left to right serially. The high-speed clock rate and the output data rate are eight times the input data rate. Similar to the shift-and-dump DEMUX, a load-and-shift MUX has the advantage that an arbitrary N-bit MUX can be built and the layout configuration is straightforward. But every basic cell in this architecture needs to operate at the output speed, the highest data rate in this circuit. Besides the timing between input data D_0, D_1, \dots, D_N and Clock, the timing between the data output from the previous stage and Clock, and the timing between Load and Clock all have to be controlled at the highest data rate. The design of the basic cell is also very challenging. The possible multi-loops needed in the basic cell due to the complexity of its function could limit the dc bias margin to a very small value at high-speed.

As a comparison, shown in Fig. 3.3b is a ripple logic 8:1 MUX. In this architecture, no load signal is needed. Both $Clock_1$ and $Clock_2$ are eight times the input data rate. There is a delay between $Clock_1$ and $Clock_2$. A T flip-flop binary tree divides $Clock_1$ into eight clock signals equal to the input data rate, but with their phases evenly spaced. One phase interval equals one $Clock_1$ period. So the 8-bit input data are clocked at the input rate but with eight evenly spaced phases. When they ripple through and are combined by the CB networks, the parallel input data are con-

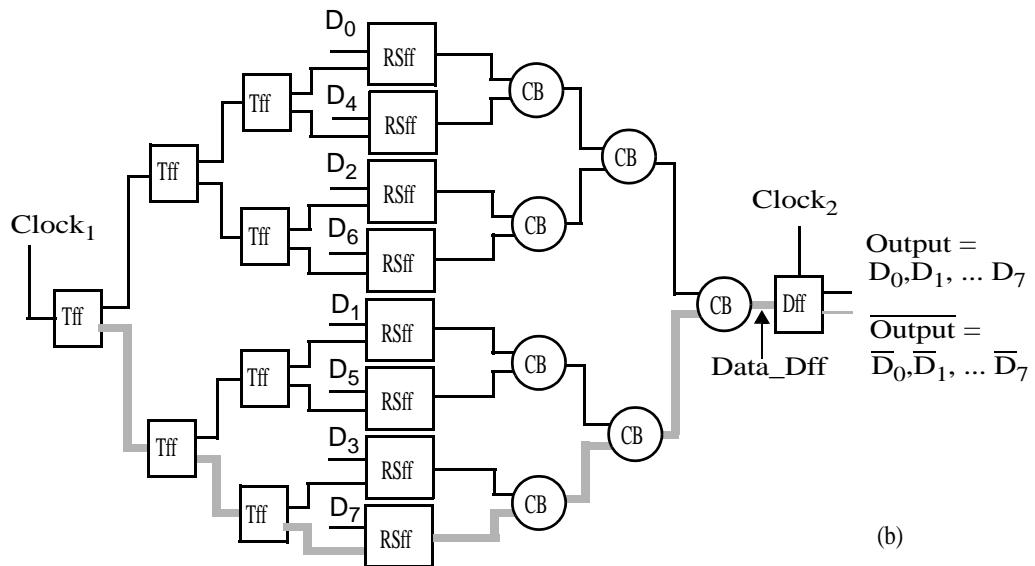
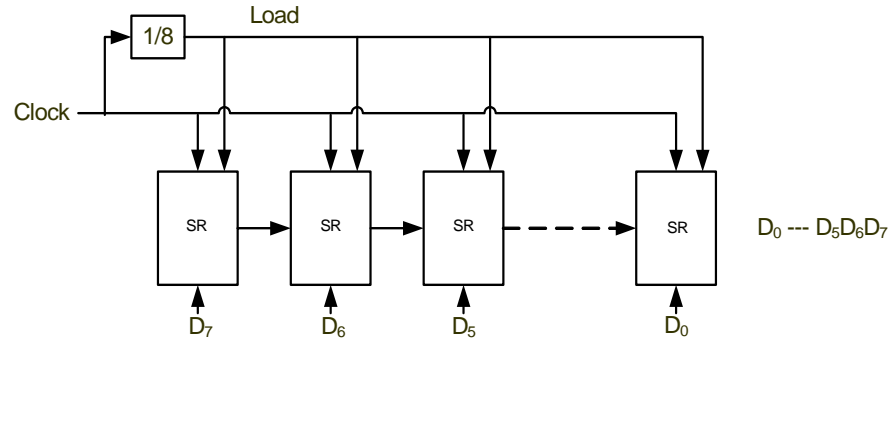


Figure 3.3 Block diagrams of two 8:1 MUX architectures. (a) Load-and-shift architecture. (b) Ripple logic architecture.

verted to the serial data with eight times higher data rate. The D flip-flop placed after the CB is to recover dual-rail outputs if the application requires it. Otherwise it can be removed. The main advantage of this architecture is that only one TFF at the top of the tree, one CB before the D flip-

flop and the D flip-flop need to operate at the highest data rate. The key of this design is to balance the delays of the eight clock-data paths tracing from Clock_1 to the clock inputs of the eight RS flip-flops, then from the outputs of the eight RS flip-flops to the output of the last CB. The drawback is that only 2^n bit MUX circuits can be constructed this way. We choose to build an 8:1 MUX based on the ripple logic architecture because the timing requirement is more relaxed and the components are simpler than for the other architectures.

3.3 Circuit Factors of Merit

The factors of merit in the MUX and DEMUX design includes: speed, yield, dc bias margin, parameter margins, power, and area.

Correct functioning at the targeted operation speed is the first thing we need to achieve in the design. Circuits are verified and optimized at the operation speed. As discussed in Chap. 2, the maximum speed of RSFQ circuits is proportional to the junction I_cR value, which in turn is determined by the junction critical current density. We chose to design a 20 GHz 1:8 DEMUX and a 20 GHz 8:1 MUX for HYPRES 1 kA/cm² niobium process and ported them to UCB 1 kA/cm² niobium process with layout modification. A 50 GHz 1:8 DEMUX and a 50 GHz 8:1 MUX are also designed for the UCB 6.5 kA/cm² niobium process. At such high operation speed, timing is especially important.

Yield is another important factor. Due to the process variations, the fabricated circuit parameters are not the same as the designed values. Yield is defined as the success rate of a large amount of fabricated parts. Circuits must be designed to be robust enough to achieve good yield in spite of the randomly spread parameters. Monte Carlo analysis can be used to calculate a theoretical circuit yield based on the process variations.

Dc bias margin is defined as the operational dc bias voltage range assuming all the circuit parameters are at their nominal values. The nominal dc bias voltage of the 20 GHz, 1 kA/cm² design is 2.5 mV. The one for the 50 GHz, 6.5 kA/cm² design is scaled to 5.75 mV. In a large system, each component is designed to have a large dc bias margin. So when the components are put together, the circuits can still work with a common dc bias voltage with a certain margin. A large dc bias margin can also help to overcome non-idealities such as thermal noise, ground bounce. Dc bias margin can be evaluated from simulation and verified in testing.

Parameter margins are the operational ranges of the parameters assuming one parameter is varying while the other parameters are kept at the nominal values. The purpose to design with large parameter margins is to allow for the process variations.

The power consumption in RSFQ circuits include two parts, the static power and the dynamic power. As stated in Section 2.1.3, the powers can be estimated as $P_{static} = I_b V_b = (I_b/I_c) I_c V_b$ and $P_{dynamic} = I_c \Phi_0 f$. While the dynamic power scales with the circuit speed, the static power does not. In the 1 kA/cm² design, for a junction with $I_c = 250 \mu\text{A}$, $I_b/I_c = 0.7$, $V_b = 2.5 \text{ mV}$, and $f = 20 \text{ GHz}$, we get $P_{static} = 0.44 \mu\text{W}$ and $P_{dynamic} = 10 \text{ nW}$. In the corresponding 6.5 kA/cm² design, $f = 50 \text{ GHz}$, $V_b = 5.75 \text{ mV}$, we get $P_{static} = 1 \mu\text{W}$ and $P_{dynamic} = 26 \text{ nW}$. In both cases, the static power dominates. This dominance can extend to a few hundred gigahertz. In contrast, the power consumption scales up with the increasing circuit operation speed in CMOS circuits. Heat dissipation is a bottleneck issue in CMOS technology scaling. Low power consumption extending to a very high operation speed is one of the main advantages of the superconductor RSFQ circuits. To reduce the power consumption, both I_c and the dc bias voltage can be reduced. The minimum I_c value in our design is around 100 μA . The corresponding junction size is around 3 $\mu\text{m} \times 3 \mu\text{m}$ in 1 kA/cm² process, which is a relatively comfortable target. The corresponding junction size is 1.3

$\mu\text{m} \times 1.3 \mu\text{m}$ in 6.5 kA/cm^2 process (6.5 kA/cm^2 was chosen because good spreads were already demonstrated for $1.3 \mu\text{m} \times 1.3 \mu\text{m}$ junctions in the UCB process). The commonly used dc bias voltage is 2.5 mV for the 1 kA/cm^2 design in the field. We used 5.75 mV in the 6.5 kA/cm^2 design for the layout convenience to port the 1 kA/cm^2 design. The shunt resistance for the same junction in the 6.5 kA/cm^2 process is increased to 2.3 times the original value in the 1 kA/cm^2 process to keep $\beta_c = 1$. Instead of changing resistor layout, the sheet resistance in the 6.5 kA/cm^2 process is adjusted to 2.3 times of that in the 1 kA/cm^2 process. So to keep the correct dc bias current values, the dc bias voltage is increased to 5.75 mV , 2.3 times 2.5 mV . The dc bias voltage is not chosen to minimize the power consumption in the current 6.5 kA/cm^2 design; instead it is chosen for the convenience to port old designs.

Area is another figure of merit of the circuit. In our design and layout, we focused on getting a robust working circuit. Circuit area is not a focus for the time being.

3.4 The Design Procedure

A typical design procedure is illustrated in the flow chart in Fig. Fig. 3.4. The main tasks include schematic capture, pre-layout simulation and optimization, layout, inductance extraction, post-layout simulation and optimization. First a circuit schematic is created and captured. Then a pre-layout simulation is done to verify the circuit function. It may take iterations to achieve the correct function. Then the optimization is performed to increase the circuit parameter margins and to improve the circuit yield. Several CAD tools can be employed to assist the optimization. Margin analysis and Monte Carlo analysis are used to evaluate the circuit performance. The optimization stops when the circuit performance is satisfying. Layout is done based on the optimized circuit parameters. During the transformation from the schematic to the layout, circuit parameters are

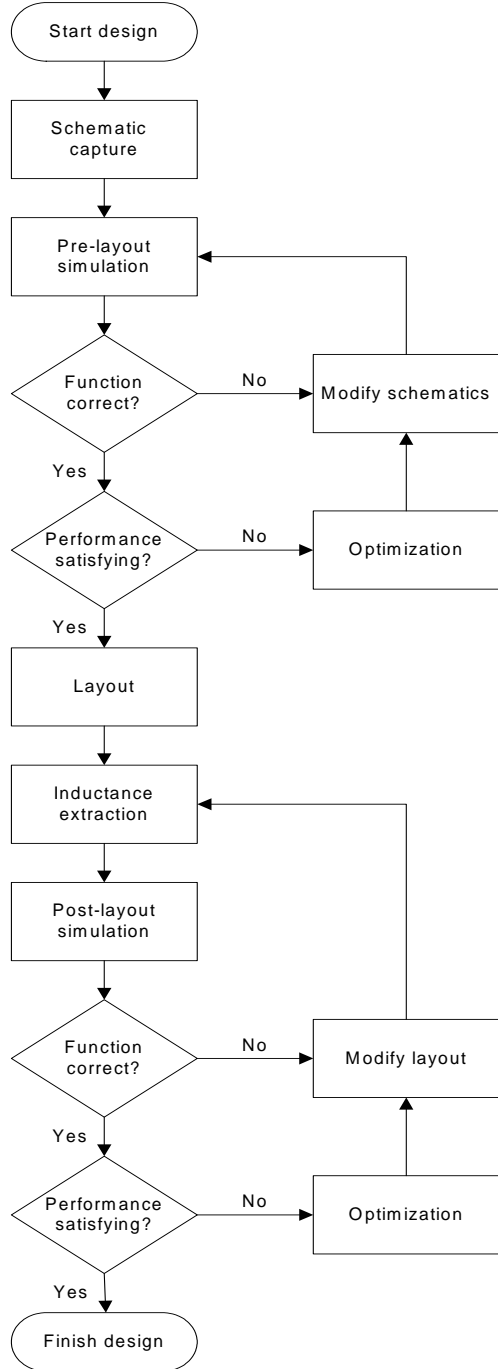


Figure 3.4 Design flow chart.

altered. The junction sizes change to the closest values from the pre-drawn junction library. The actual inductance values and the parasitic inductance values are extracted. With the new circuit parameters, post-layout simulations and analyses are done to check the circuit function and performance again. In most cases, the circuit function is still correct but the circuit performance deteriorates with the addition of parasitic inductances. If the function also fails, circuit parameters and the layout need to be modified until the post-layout simulation shows the function is correct. Then post-layout optimization is performed to improve the circuit performance until satisfying results are achieved. In the post-layout optimization, parasitic inductances are included and constraints imposed by the practical layout are considered.

The CAD tools investigated and employed in our design include: Xic[41] for schematic capture and layout; WRspice [41], JSIM [42], JSPICE3 [41] for circuit simulation and analysis; WinS [43], MALT [44], MJSIM [45] for optimization; Cadence Virtuoso layout tool for layout; INDUCT [42] and LMETER [46] for inductance calculation or extraction.

Details of some tasks, analysis methods and the use of related CAD tools are introduced in the following sections.

3.4.1 Schematic Capture

A schematic is a way to visually describe and record the circuit configuration and parameters. Both Xic and WinS can be used for schematic capture in RSFQ circuit design. But WinS is mainly an RSFQ circuit optimization tool. The schematics captured in WinS can only be simulated in WinS, and only resistively shunted junctions (RSJs) and RSFQ circuits can be captured and simulated in WinS. So schematics are captured in Wins as part of the optimization. Compared with Wins, Xic is a more versatile tool for IC design. Besides Josephson junctions, inductors, resistors, other devices such as transmission lines, mutual inductors and MOSFETs are also supported. Vari-

ous current sources and voltage sources can also be captured to set up simulations. Both tunnel junctions and resistively shunted junctions can be used in the circuits. The captured schematics can be simulated within the tools by calling WRspice. The junction models can be modified by the users to facilitate both pre-layout and post-layout simulation. Furthermore, a SPICE netlist including both the circuit configuration and the simulation setup can then be exported from Xic.

3.4.2 Circuit Simulation

The state-of-art superconductor circuit simulator is WRspice. It is SPICE based, fully incorporating Josephson junction devices. It has many features needed in the modern superconductor integrated circuit design. It is the main simulation tools used in our design work. Two other simulation tools JSPICE3, JSIM are used as the simulation engines in the optimization tools.

3.4.2.1 Functional Check

The circuit function is checked in the simulations. For RSFQ circuits, usually the node voltages, the phases of the junctions, and the current flowing through the inductances are monitored. The circuit function can be checked visually from the plotted signal waveforms. A measurement statement can be used to extract various information such as timing, power, voltage, current, junction phase etc. The information can then be analyzed for further design improvement. A control block can be added in the circuit input file to set the pass/fail criteria including the information obtained from the measurement. So the program can report pass/fail automatically after a simulation run.

3.4.2.2 Margin Analysis

There is a built-in function in WRspice to check two-dimensional operating range. This can be used to check a parameter margin handily. Compared to the margin analysis in other optimization

tools, the pass/fail criteria can be more complicated and more flexible, so the circuit function check is more complete.

3.4.2.3 Monte Carlo Analysis

Monte Carlo analysis is a statistical method to simulate the effect of process variations on the circuit function and performance. There are global process variations and local process variations. The global process variations reflect run-to-run, wafer-to-wafer, chip-to-chip process variations, while the local process variations are the process variations within the same chip. Usually the global variations are much larger than the local variations. For a specific process, measurement data of a large number of samples are gathered to get the standard deviation of a parameter, $\sigma = \sqrt{\frac{1}{N} \sum_{k=1}^N (x_k - \bar{x})^2}$. x_k is the k th measured parameter value. $\bar{x} = \frac{1}{N} \sum_{k=1}^N x_k$ is the average value and N is the total sample number and should be large. For global variations, x_k s are gathered from different runs, different wafers, and different chips. For local variations, x_k s are from the same chip. In a simulation, a circuit parameter is generated equal to $(\text{nominal value} * p_{\text{global}} * \text{guass}(\sigma_{\text{local}}, 1))$ and $p_{\text{global}} = \text{guass}(\sigma_{\text{global}}, 1)$. $\text{guass}(\sigma, 1)$ is a pseudo-random number generated by the simulator based on its Gaussian probability distribution centered at 1.0 and with standard deviation σ . In one simulation run, each time $\text{guass}(\sigma, 1)$ is called, a different random number is generated. So in each simulation, $\text{guass}(\sigma_{\text{global}}, 1)$ is called only once and assigned to p_{global} to reflect the global variation for one parameter category. However, $\text{guass}(\sigma_{\text{local}}, 1)$ is called for each parameter to reflect the local variation. So the circuit parameter values are randomly generated in a simulation to mimic a real process run. Over a large number of simulation runs, we can evaluate the circuit behavior statistically.

Listed in Table 3-1 is the process variations of HYPRES 1 kA/cm² niobium process used in our calculations. The numbers are summarized from measurements of a large number of samples.

Since HYPRES guarantees the critical current density within 15% deviation and sheet resistance value within 20% deviation, we constrain $abs(p_{global_Ic}-1)$ within 15%, and $abs(p_{global_R}-1)$ within 20% during the random parameter generation.

TABLE 3-1 Process variations of HYPRES 1 kA/cm² niobium process.

	3σ global variation	3σ local variation
Resistance	23%	2.5%
Critical Current	37%	11%
Inductance	15%	5%

Listed in Table 3-2 are the process variations of the UCB 6.5 kA/cm² niobium process used in our calculations. The numbers are from limited number of successful runs. They should be treated as reachable goals instead of statistical summaries.

TABLE 3-2 Process variations of UCB 6.5 kA/cm² niobium process

	3σ global variation	3σ local variation
Resistance	7.5%	2.8%
Critical Current	10%	3%
Inductance	15%	5%

Monte Carlo analysis is applied to predict the circuit yield in our designs. The yield is defined as the ratio of the number of passing runs over the total number of runs. By the statistical nature of the Monte Carlo analysis, the yield has a Gaussian distribution. The calculated yield Y is the mean value. And the variance of yield $\sigma^2 = Y(1-Y)/N$, where N is the total number of runs. For a 95% confidence level, the confidence interval $L = 2\sigma = 2 \cdot \sqrt{Y(1-Y)/N}$. I.e., the predicted yield lies in the range of $Y \pm L$ with a 95% probability [47]. The total number of runs is usually above 100. And the circuit is normally optimized with a calculated yield above 99%. With 100 runs, and a cal-

culated yield of 99%, the yield lies in the range of 97% -100% with a 95% probability. Monte Carlo analysis is also used to estimate the timing variation along the data path due to process variations in the MUX design.

In WRspice, the yield calculation can be done easily using the built-in Monte Carlo analysis function. While for the timing variation, a separate script is written to run the simulations repetitively and extract the timing information.

3.4.3 Comparison of Optimization CAD tools

The purpose of optimization is to build a robust circuit in spite of the process variations. So the optimization should be a process to improve the circuit yield.

Several optimization CAD tools and the methods they are based on are compared. Listed in Table 3-3 are three RSFQ circuit optimization tools and their main features, advantages and disadvantages. The three tools are WinS, MALT and MJSIM.

TABLE 3-3 Comparison of three RSFQ circuit optimization CAD tools: WinS, MALT and MJSIM

CAD tool	WinS	MALT	MJSIM
Figure of merit	• Critical margin	• Margin along critical direction	• Yield
Simulation engine	• WinS	• JSPICE3	• JSIM
Advantages	• Many parameters	• Process variations considered	• Process variations considered
Disadvantages	• Process variations not considered	• 8 parameters • Convex operation region required	• Computation costing

WinS is a Windows program which can do RSFQ circuit simulation, margin analysis and optimization. The figure of merit in Wins optimization is the critical margin. The critical margin is

defined as the smallest among all the circuit parameter margins. Each circuit parameter margin is found with all other parameters kept at their nominal values. WinS tries to improve the circuit yield through maximizing the critical margin. This is an indirect but often effective way to improve the circuit yield. The algorithm implementation is straightforward. Large numbers of parameters can be included in one optimization. However, the result does not guarantee optimal circuit yield. First, process variations are not taken into consideration. Different circuit parameters such as junction critical currents and inductances can have different process variations. The global process variation of a parameter is also different from the local process variation. But in the WinS optimization, all the parameters or parameter combinations are treated equally. Second, WinS optimizes the critical margins along the parameter axes with only one parameter varying. In reality, all the parameters can deviate from their nominal values simultaneously. The smallest margin in the operation space may not lie on the direction of the parameter axes.

To address the above two issues, MALT optimizes the margin along the critical direction. It uses an inscribed-sphere algorithm. A convex hull approximating the circuit operating region is expanded and refined iteratively. A sphere (the largest that will fit) is inscribed in the hull and the largest tangent plane is found. The perpendicular passing through the center of this plane defines the direction of the next binary search. The new boundary point is found and the hull and inscribed sphere are redrawn. When the optimization is done, the optimum parameter values lie in the center of the sphere, the radius of the sphere is a measure of the allowed variation. The directions of the radius vectors to the tangent planes are the critical directions along which the parameter variations are most restricted. The process variations are taken into consideration when the convex hull is formed. The operating region is scaled along each parameter axis to make the axis with larger process variation more critical. Theoretically, this algorithm should achieve better circuit yield since both multi-dimensional circuit operating range and the process variations are evaluated during the

optimization. But there are some practical limitations in applications. First, the recommended number of parameters in each optimization is no larger than eight. Even in a simplest RSFQ circuit, eight dimensions are not enough. The practical strategy is to include the most critical parameter such as global inductance variation, global bias current variation in all optimizations. Other parameters are separated into several optimizations. The iterations are gone through manually until a satisfying result is achieved. Second, the operating region of the optimized parameters has to be a convex region. In RSFQ circuits, the operating region of the global inductance and the global junction critical current is concave. To solve this problem, we use a derived parameter, the inverse of the critical current, in the optimization to change the operating region to a convex contour. But not every case with concave region can be visualized and solved this way. So we might get a local optimal parameter set depending on the initial values.

MJSIM uses yield as its figure of merit directly. The simulation engine underneath is JSIM, another Josephson junction simulator. This program was still under development. The main drawback is the computation cost. For each parameter set, hundreds of runs of simulation runs are needed to evaluate the corresponding circuit yield.

In our design work, both Wins and MALT are used to help automate the optimization. But margin analysis and yield calculation are performed in WRspice to check and confirm the circuit performance. The pass/fail criteria in Wins and MALT are restricted.

3.4.4 Layout and Inductance Extraction

Layout is done in either the Cadence Virtuoso layout tool or with the Xic physical mode. The basic flow is: floor planning; physical implementation; reviewing and design rule check (DRC). DRC rules for the specific process need to be compiled by the designer. LVS check is not set up in

either tool. So whether the layout matches the circuit schematic relies on the designer's labor intensive reviewing. This is where the design flow can be improved.

3.4.4.1 Junction Layout

A library of junctions, unshunted or shunted, with two kinds of shunt resistor placement are pre-drawn. During circuit layout implementation, the junction size is always rounded to the closest junction size in the junction library. Fig. 3.5 shows a junction layout example in the 6.5 kA/cm^2 library. $I_c = 251 \mu\text{A}$, $R_s = 2.36 \Omega$. Notice the junction shape is similar to an octagon. But the slope

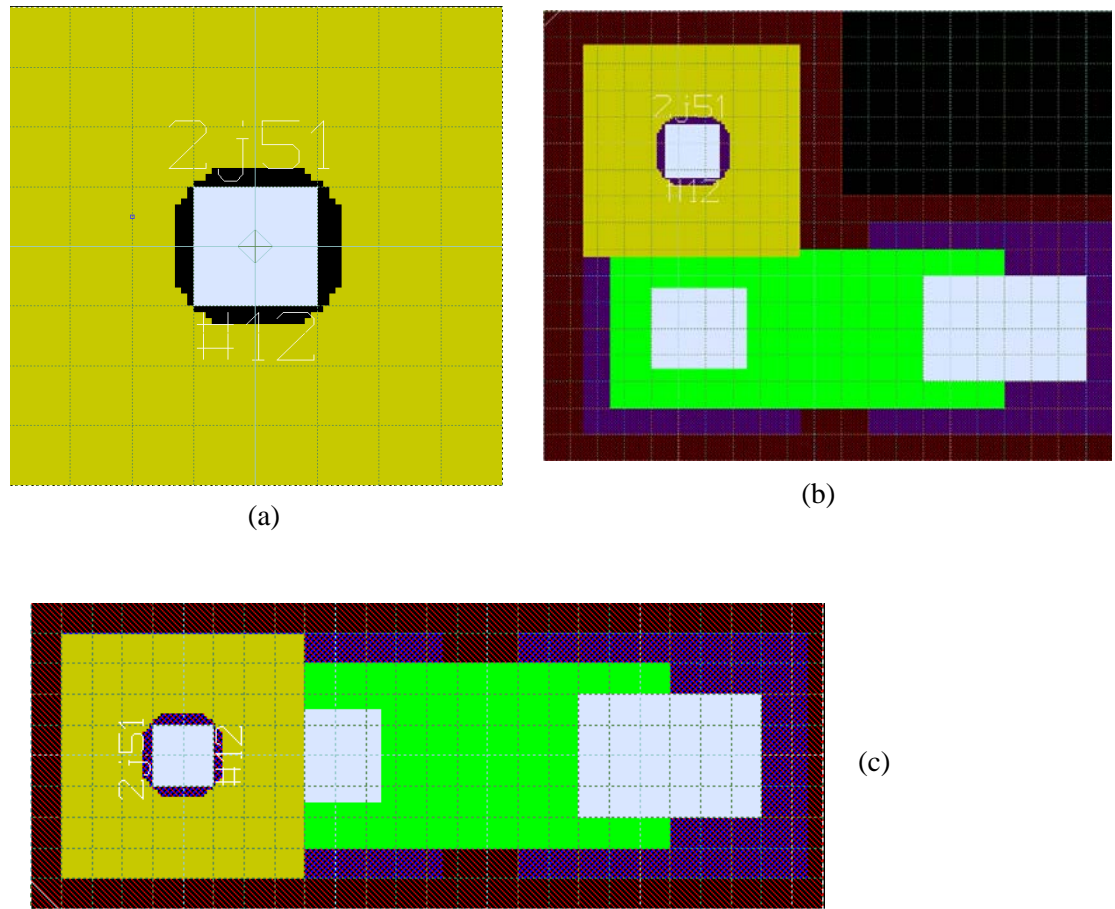


Figure 3.5 Junction library layout. (a) Junction definition layer with M_2 contact to CE. (b) and (c) Junction with shunted resistor.

is implemented by stairs so all lines are on the resolution grid. The junction drawn size is larger than the target size to compensate the $0.5 \mu\text{m}$ width bias due to over etching and anodization.

Table 3-4 lists the junction sizes in our 6.5 kA/cm^2 process. The actual drawn size should be the listed value minus the removed corner areas (which is too much detail to be listed here). Ideally, the critical current value of each junction should be verified in testing. We use them in the layout before they get verified. The critical current values are same as in the 1 kA/cm^2 library for the convenience of design porting.

TABLE 3-4 6.5 kA/cm^2 junction layout library cell parameters

$I_c (\mu\text{A})$	$R_s (\Omega)$	Drawn size ($\mu\text{m} \times \mu\text{m}$)	Target area (μm^2)
120	4.93	2.0 x 2.1	1.85
130	4.55	2.1 x 2.1	2.00
140	4.23	2.1 x 2.2	2.15
151	3.92	2.2 x 2.2	2.32
163	3.63	2.2 x 2.3	2.51
174	3.40	2.3 x 2.3	2.68
186	3.18	2.3 x 2.4	2.86
198	2.99	2.4 x 2.4	3.05
211	2.81	2.5 x 2.5	3.25
224	2.64	2.5 x 2.6	3.45
238	2.49	2.6 x 2.6	3.66
251	2.36	2.6 x 2.7	3.86
264	2.24	2.7 x 2.7	4.06
279	2.12	2.7 x 2.8	4.29
294	2.01	2.8 x 2.8	4.52
309	1.92	2.8 x 2.9	4.75
325	1.82	2.9 x 2.9	5.00
339	1.75	2.9 x 3.0	5.22
356	1.66	3.0 x 3.0	5.48
373	1.59	3.0 x 3.1	5.74
390	1.52	3.1 x 3.2	6.00

3.4.4.2 Inductance Estimation and Extraction

In our layout, double ground layers are used for all the RSFQ circuit inductances. This is to reduce the undesired parasitic inductance. We used INDUCT calculations to make a convenience sheet for layout reference. And we use LMETER for inductance extraction after the layout is done. The concept of superconductor metal line inductance and INDUCT can be referred to Section 3.09 in [1]. LMETER can be referred to in the SUNY RSFQ laboratory web site [46]. LMETER can take layout database, and process information, to calculate the superconductor wire inductance even with odd shapes. This is most useful where a few lines meet together at a junction. LMETER refers to Chang's work [48]. It shows close match in the strip line test case. For cases with complicated shapes where it is most useful, it is believed in the field to have accuracy within $\pm 10\%$. Process information such as layer stack-up, thickness of insulation layers, superconductor penetration depth, and line width bias for each metal layer are all included in a technology file as one of the input files for LMETER. For the HYPRES and UCB processes, the technology files need to be compiled accordingly.

3.5 1:8 DEMUX Design and Optimization

The main design effort is focused on designing and optimizing the 1:2 DEMUX module. A 1:4 DEMUX and a 1:8 DEMUX can then be easily built from the optimized 2-bit module.

3.5.1 20 GHz DEMUX Design, Layout and Optimization

A 20 GHz 1:2 DEMUX is designed and optimized for the 1 kA/cm^2 process. Fig. 3.6 shows an asynchronous 1:2 DEMUX, its Moore diagram, and the connection JTL. The circuit structure was suggested by A. F. Kirichenko [49]. But the circuit parameters are developed independently. Other related references for developing this circuit are [50][51][17]. The clock information is embedded in the incoming data. Reading from the Moore diagram, this circuit has two internal states, state

“0” and state “1”. During power up, the circuit is biased to its quiescent state, which is state “0”. J_2 and J_{21} are biased close to their I_c s. J_4 and J_{41} are biased away from their I_c s. The current flowing in L_{store} from left to right is small. This is equivalent to a more balanced biasing between J_2/J_{21} and J_4/J_{41} superimposed on the circulating currents in the loops as marked in Fig. 3.6. With an SFQ pulse arriving at Input/ \overline{Input} , the circuit is switched to state “1”, an output pulse is generated at Output₀/ \overline{Output}_0 accordingly. In state “1”, J_2/J_{21} are biased away from their I_c s and J_4/J_{41} are biased close to their I_c s, the circulating currents are flowing in the direction opposite to the ones in state “0”. The current flowing in L_{store} from left to right is larger. During the state transition from “0” to “1”, if the input pulse comes into Input, junctions J_2, J_3 and J_{61} switch and the output pulse is generated at Output₀. If the input pulse comes into \overline{Input} , junctions J_{21}, J_{31} and J_6 switch and the output pulse is generated at \overline{Output}_0 . On the other hand, the transition from state “1” to state “0” is also triggered by an SFQ pulse at Input/ \overline{Input} , an output pulse is generated at Output₁/ \overline{Output}_1 cor-

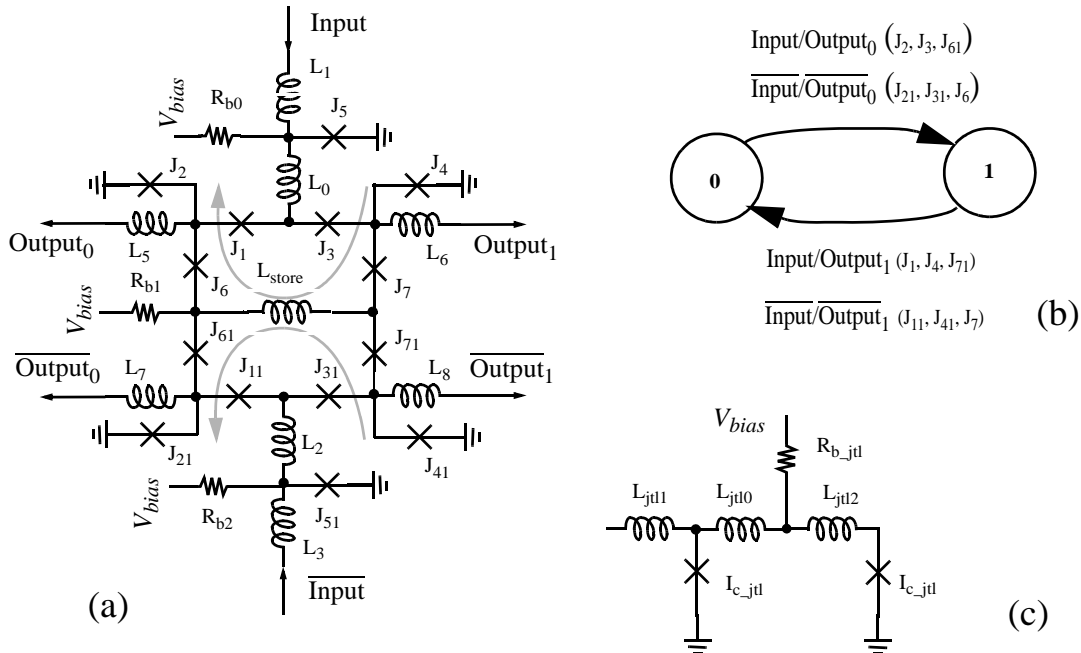


Figure 3.6 An asynchronous 1:2 DEMUX circuit. (a) Core circuit schematic. (b) Moore diagram. (c) Connection JTL schematic.

respondingly. During this transition, if the input pulse is at Input, junctions J_1 , J_4 and J_{71} switch and the output pulse goes to $Output_1$. If the input pulse is at \overline{Input} , junctions J_{11} , J_{41} and J_7 switch and the output pulse goes to \overline{Output}_1 . So this new 1:2 DEMUX circuit behaves like a dual-rail T flip-flop. The input pulses from Input/ \overline{Input} are diverted to $Output_0/\overline{Output}_0$ and $Output_1/\overline{Output}_1$ alternatively. The output data rate is reduced to one half of the input data rate.

Comparing the circuit schematic of the 1:2 DEMUX with that of the T flip-flop in Fig. 1.11, the 2-bit DEMUX is similar to two T flip-flops combined except that junctions J_6 , J_{61} , J_7 , J_{71} are added to prevent the Input pulses from entering $\overline{Output}_0/\overline{Output}_1$ and to prevent the \overline{Input} pulses from entering $Output_0/Output_1$. The resistor R in the T flip-flop is also removed from the 1:2 DEMUX due to the difficulty to place it in the layout. A set of working parameters of the T flip-flop are referred as the starting point to design the 2-bit DEMUX. The dynamics described in the Moore diagram are referred to for the parameter adjustment. Fig. 3.7a shows the input/output voltage waveforms of a correct functioning of the 2-bit DEMUX. Fig. 3.7b shows the corresponding phase waveforms of the junctions in the JTLs connected to the inputs/outputs of the 2-bit DEMUX. Each 2π phase transition in the junctions produces an SFQ voltage pulse at the corresponding input/output.

After the correct functioning is achieved, a pre-layout optimization is done in MALT. Details of the optimization procedure are explained below. The pass/fail criterion is automatically generated based on the waveforms of the circuit with the initial parameters. Input/output pulse positions are extracted as the time points when the junction phases are equal to $(2k + 3/2)\pi$, k is an integer. During the optimization, the phase of each output junction is checked at the nominal pulse positions $+$ / $-$ a delay variation. The delay variation is set to be 20 ps in the optimization and can be varied according to the designs. If the difference between the simulated phase and the expected phase

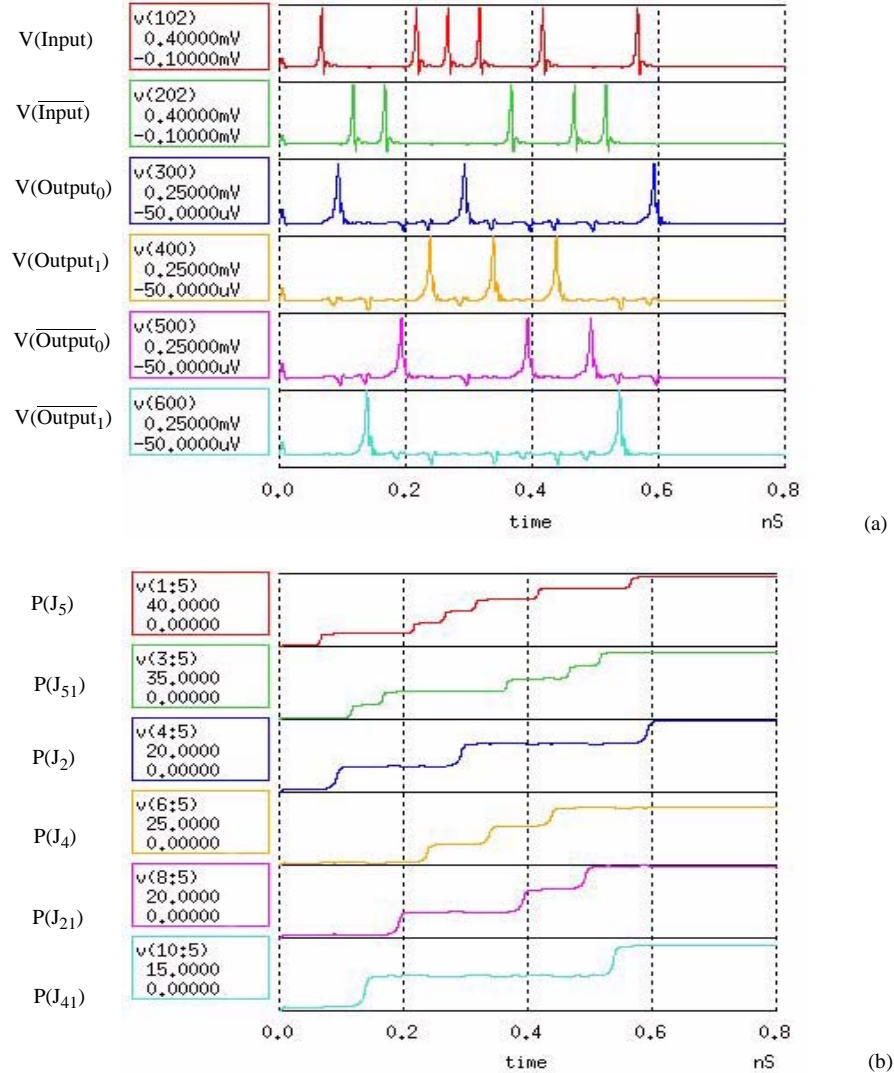


Figure 3.7 Simulation waveforms of a correct function of the 2-bit DEMUX. (a) Input/output voltages. (b) Input/output JTL junction phases.

is larger than the fail threshold, it is considered a fail. The fail threshold of phase is set to be 2.0 in the optimization. The input junction phases are checked at the last check point. The data sequences in Fig. 3.7 are used. Two stages of JTLs are connected to each of the inputs/outputs and are included to be optimized. Due to the symmetry of the circuit, the symmetric parameter pairs are set to vary together, such as J_1-J_{11} , J_2-J_{21} and L_0-L_2 . The most critical parameters, the global inductance variation XL and the inverse global critical current density DI_{cb} are included in all the itera-

tions. DI_{cb} is set to be static. Other parameters, the individual inductances and individual junction critical current values are grouped and optimized in different runs. The dc bias voltage V_{bias} is also allowed to vary in some runs. The parameter values after the pre-layout optimization and related margins are reported in the left columns in Table 3-5. The margin of $XL(-27.0\%, +54.0\%)$ is large

TABLE 3-5 pre-layout and post-layout margin calculation.

	(a) Pre-layout simulation (after optimization)		(b) Post-layout simulation (before re-optimization)		(c) Post-layout simulation (after re-optimization)	
Parameter	value	Margin	value	Margin	value	Margin
XL	1	(-27.0, +54.0)	1	(-19.4, +35.2)	1	(-30.6, +50.8)
DI_{cb}	1	(-21.0, +17.0)	1	(-18.1, +53.9)	1	(-26.9, +50.8)
XI_{cb}	1	(-14.5, +26.6)	1	(-35.0, +22.1)	1	(-33.7, +36.8)
V_{bias}	3.264 V	(-18.8, +20.3)	2.5V	(-9.4, +22.7)	2.5V	(-14.4, +11.7)
$R_{b0}-R_{b2}$	13.61 Ω	(-42.6,+100*)	13.6 Ω	(-55.6, +58.6)	12.7 Ω	(-48.1, +100*)
R_{b1}	5.75 Ω	(-26.1, 29.6)	5.8 Ω	(-36.9, +18.0)	5.5 Ω	(-33.1, +30.5)
R_{b-jtl}	9.325 Ω	(-25.0,+100*)	7.61 Ω	(-30.6, +38.3)	7.12 Ω	(-21.9, +77.3)
$I_{c1}-I_{c11}$	279 μA	(-28.7, 39.4)	279 μA	(-11.9, +30.5)	264 μA	(-20.6, +30.5)
$I_{c2}-I_{c21}$	224 μA	(-53.6, 40.2)	224 μA	(-53.1, +18.0)	211 μA	(-50.6, +30.5)
$I_{c3}-I_{c31}$	174 μA	(-51.7, +51.7)	174 μA	(-46.9, +41.1)	174 μA	(-56.9, +33.6)
$I_{c4}-I_{c41}$	151 μA	(-80*,+100*)	151 μA	(-71.9, +66.4)	151 μA	(-55.6, +82.0)
$I_{c5}-I_{c51}$	264 μA	(-80*,+83.3)	264 μA	(-71.9, +32.0)	251 μA	(-76.9, +49.2)
$I_{c6}-I_{c61}$	294 μA	(-34.0, +47.6)	294 μA	(-55.6, +36.7)	279 μA	(-50.6, +39.8)
$I_{c7}-I_{c71}$	294 μA	(-18.4, +23.8)	294 μA	(-31.9, +27.3)	294 μA	(-30.6, +21.1)
I_{c-jtl}	250 μA	(-21.0, +44.0)	251 μA	(-26.9, +19.5)	251 μA	(-15.8, +38.5)
L_1-L_3	3.20 pH	(-80*,+100*)	4.2 pH	(-80.0*, +38.3)	4.3 pH	(-80*, +72.7)
L_0-L_2	0.89 pH	(-80*, +100*)	1.1 pH	(-75.6, +68.0)	1.1 pH	(-80*, +88)
L_{store}	2.77 pH	(-27.9, +100*)	3.0 pH	(-51.9, +77.3)	2.9 pH	(-66.9, +100*)
$L5-L7$	3.6 pH	(-80*,+100*)	3.3pH	(-43.1, +100*)	3.4pH	(-80*, +100*)
$L6-L8$	3.6 pH	(-80*,+100*)	3.3pH	(-80*, +100*)	3.3pH	(-80*, +100*)
$L_{jtl0}-L_{jtl2}$	1.8 pH	(-80*,+100*)	1.45 pH	(-80*, +100*)	1.45 pH	(-80*, +100*)
L_{jtl1}	3.6 pH	(-80*,+100*)	2.8 pH	(-80*, +100*)	2.8 pH	(-80*, +100*)
Parasitic Ls	N/A	N/A	Stated separately	(-80*, +100*)	Stated separately	(-80*, +100*)

*(-80, +100) is the maximum parameter variation range in the margin calculation. The actual circuit parameter margin may be larger.

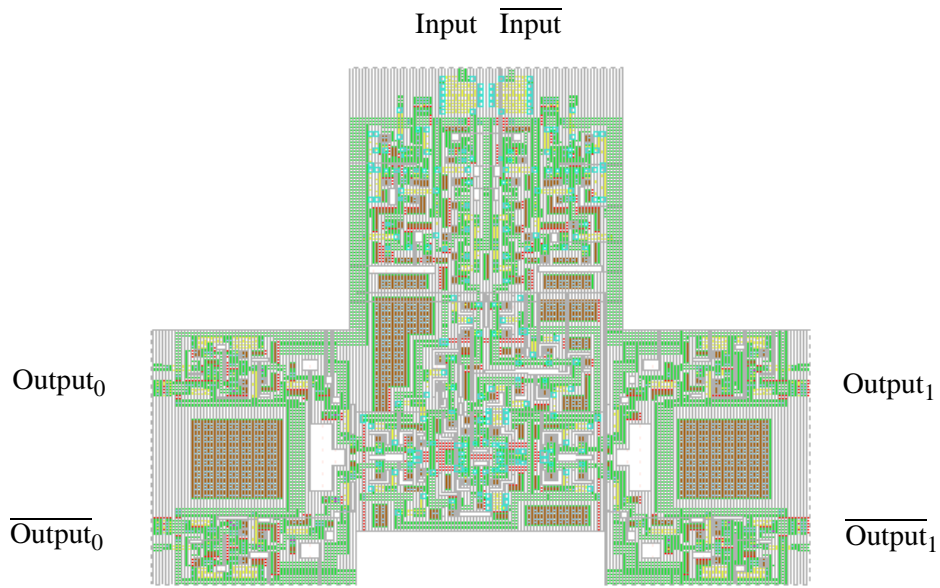


Figure 3.8 Layout of the 2-bit DEMUX.

considering the 3σ global L variation is 15%. And that of XI_{cb} (-14.5%, +26.6%) is fair since the global I_c variation is guaranteed to be within 15% by the foundry. The dc bias voltage margin is (-18.8%, +20.3%). I.e., the operational dc bias voltage range is (2.65 mV, 3.93 mV) with the center voltage at 3.264 mV. The critical parameter margins is the lower margin of $I_{c7}-I_{c71}$ (-18.4%). The pre-layout dc bias margin of a 1:8 DEMUX based on the above 2-bit DEMUX is (-18%, +18%). Not being able to handle more than eight parameters in the same optimization setting made it difficult to achieve good results without carefully grouping the parameters and many iterations. The results achieved above can be further improved.

Fig. 3.8 shows the layout based on the above parameters. To facilitate the cascading, \overline{Input} was wrapped around to be with Input. Moats were added near the junctions and wherever space allowed. Moats are the area in the layout with the ground planes removed to avoid flux trapping in the circuits. Without paying special attention to the fact that connection JTLs can affect the circuit performance, standard JTLs from the library were used instead of the ones as the results of the

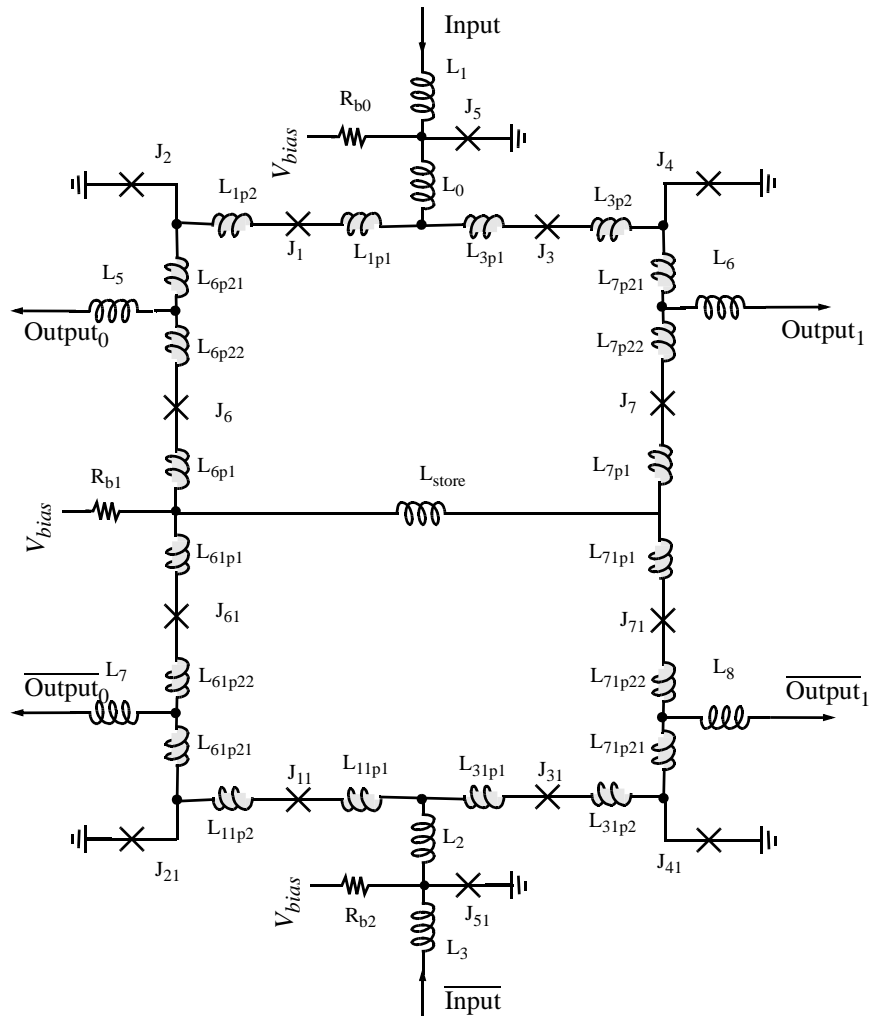


Figure 3.9 2-bit DEMUX schematic with parasitic inductances.

optimization. Bias resistance values were not scaled to center the dc bias voltage range to 2.5 V in this layout but will be corrected in the post-layout optimization. Testing results based on this layout implementation without further optimization will be reported in Section 5.2.2.1 and Section 5.2.2.2.

Fig. 3.9 shows the post-layout schematics with the parasitic inductances. The updated parameter values and margins analyzed in MALT are listed in the middle columns in Table 3-5. The para-

sitic inductance values in Fig. 3.9 are: $L_{1p1} = 0.04 \text{ pH}$, $L_{11p1} = 0.06 \text{ pH}$, $L_{1p2} = 0.57 \text{ pH}$, $L_{11p2} = 0.57 \text{ pH}$, $L_{3p1} = 0.05 \text{ pH}$, $L_{31p1} = 0.06 \text{ pH}$, $L_{3p2} = 0.62 \text{ pH}$, $L_{31p2} = 0.63 \text{ pH}$, $L_{6p1} = 0.02 \text{ pH}$, $L_{61p1} = 0.02 \text{ pH}$, $L_{6p21} = 0.32 \text{ pH}$, $L_{61p21} = 0.22 \text{ pH}$, $L_{6p22} = 0.32 \text{ pH}$, $L_{61p22} = 0.31 \text{ pH}$, $L_{7p1} = 0.02 \text{ pH}$, $L_{71p1} = 0.02 \text{ pH}$, $L_{7p21} = 0.25 \text{ pH}$, $L_{71p21} = 0.24 \text{ pH}$, $L_{7p22} = 0.32 \text{ pH}$, $L_{71p22} = 0.31 \text{ pH}$. The margins of the parasitic inductances are all very large, beyond $(-80\%, +100\%)$. But the parasitic inductances change the circuit bias condition and reduce other parameter margins. The global inductance XL margin reduces to $(-19.4\%, +35.2\%)$. The margins of the global critical current XI_{cb} are changed to $(-35.0\%, +22.1\%)$. The dc bias voltage margins drop to $(-9.4\%, +22.7\%)$. The operational dc bias voltage range is $(-2.27 \text{ mV} \text{ to } 3.07 \text{ mV})$ with the center voltage at 2.5 mV . The critical parameter margin is that of I_{c1} and I_{c11} (-11.9%) . The pass/fail criteria used in MALT require that the output pulses arrive within 20 ps from the nominal positions, which is not a necessary requirement for asynchronous circuits if the latency is not in the specification.

With the same pass/fail criteria as the one used by MALT, the dc bias margin calculated in WRspice is $(-9.3\%, +22.5\%)$ which agrees with the MALT report. In WRspice, more flexible pass/fail criteria can be scripted. Two other criteria have been tried. In one criterion, the sequence of the output pulses are checked for every pulse, but not at the fixed time points. The pulse interval has to be within $50 \text{ ps} \pm \text{tvar}$. Parameter tvar is the allowed interval variation. We set $\text{tvar} = 20 \text{ ps}$ in our calculation. Using the other criterion, a fixed number of input pulses are fed into the circuit. The final junction phases are checked after the last junction transition. With this approach, as long as the waiting period after the last junction transition is long enough, sufficient latency variation is allowed for the circuit. This criterion is less strict than the previous one since the details of the pulse sequence and pulse interval are ignored. But since the sequence check uses the measurement results from the simulation, it takes 3 to 4 times longer calculation time in the margin and yield calculation. The dc bias margin value with sequence check is $(-8.6\%, 34.9\%)$. The one with final

phase check is (-9.3%, 34.9%). The two results are close enough. In comparison, the MALT result shows a big reduction on the upper end dc bias margin, showing the effect of the latency variation. The circuit yields calculated in WRspice are (70% +/- 3%) using the MALT criterion., (71% +/- 3%) using the sequence check, (77% +/- 3%) using the final phase check with a 95% confidence level. In all three calculations, the same data patterns are applied. The total number of Monte Carlo runs is the same, 798 runs. Listed in Table 3-6 is a summary of the dc bias margin and yield calculation results using different criteria. Sequence check is a good choice for the asynchronous DEMUX circuit compared to the more pessimistic MALT criterion and the more optimistic final phase check criterion. The low yield requires a post-layout circuit re-optimization.

TABLE 3-6 Post-layout dc bias margin and yield calculation results before circuit re-optimization, using different pass/fail criteria in WRspice.

	dc bias margin	Yield range w/ 95% confidence level
MALT criterion (fixed time point check)	(-9.3%, +22.5%)	(67% – 73%)
Sequence check	(-8.6%, +34.9%)	(68% – 74%)
Final phase check	(-9.3%, +34.9%)	(74% – 80%)

The inductance values are kept unchanged in the post-layout reoptimization. The MALT results are reported in the right columns in Table 3-5. The margin of XL recovers to (-30.6%, +50.8%). The margin of XIcb recovers to (-33.7%, +36.8%). Dc bias voltage margin is more centered (-14.4%, +11.7%). The critical parameter margin improves to -15.8%, the lower margin of I_{c_jtl} . The reason why the parameter margin of I_{c_jtl} is getting worse after the reoptimization is that it is not included in the parameters to be optimized due to the program limitation on the total number of parameters to be optimized. The circuit dc bias margin is verified in WRspice. Further yield calculation in WRspice proves that the reoptimization improves the circuit yield. The total number of Monte Carlo runs for the yield calculation is 798. Table 3-7 summarizes the dc bias margin and

yield results in WRspice after post-layout re-optimization using different criteria. When the circuit is optimized, the yield values using different criteria get close enough.

TABLE 3-7 Post-layout dc bias margin and yield calculation results after circuit re-optimization, using different pass/fail criteria in WRspice.

	dc bias margin	Yield range w/ 95% confidence level
MALT criterion (fixed time point check)	(-14.5%, +12.9%)	(85% – 89%)
Sequence check	(-14.5%, +25.2%)	(87% – 91%)
Final phase check	(-14.7%, +25.2%)	(89% – 93%)

MALT optimization did help to improve the circuit yield to some extent. The main limitation is that a maximum of eight parameters can be optimized together. Optimization based on one group of parameters could hurt parameter margins of others which are not included, and therefore, not necessarily improve the yield overall. Margins and yield verification in WRspice is necessary since the yield reported by MALT only takes into account variations of some of the parameters and the pass/fail criteria in MALT is not the most proper one.

Shown in Fig. 3.10 is the 2-bit DEMUX dc bias margin for operation frequency above 20 GHz. The dc bias margin of the 2-bit DEMUX varies little at frequency below 20 GHz. But when the frequency is beyond 20 GHz, the lower end dc bias margin starts to shrink and crosses zero at around 35 GHz while the upper end dc bias margin remains above 20% up to 50 GHz. So for operation above 20 GHz, this circuit needs to be re-optimized for the specific frequency. And furthermore, a process with higher current density may be preferred to solve the speed limitation.

The layout of a 1:4 DEMUX and a 1:8 DEMUX are implemented based on the above reoptimization results. Fig. 3.11 shows the micrograph of a 1:4 DEMUX. The test results of this layout will be reported in Section 5.2.2.3 and Section 5.2.2.4. Fig. 3.12 is the micrograph of a 1:8

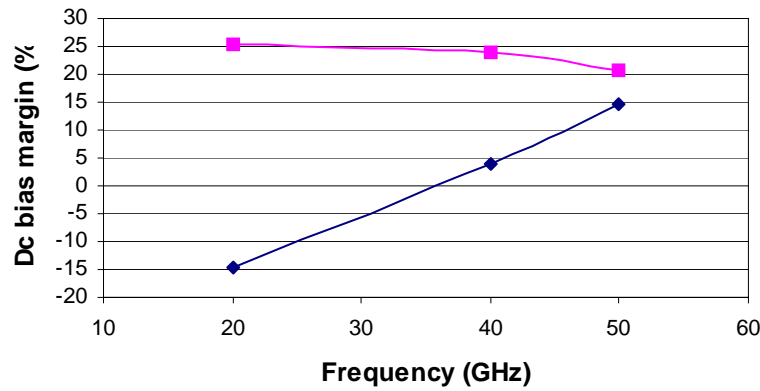


Figure 3.10 2-bit DEMUX dc bias margins vs. frequency. The data are from post-layout simulation after reoptimization including the parasitic inductances. The marked data points are for the frequencies simulated.

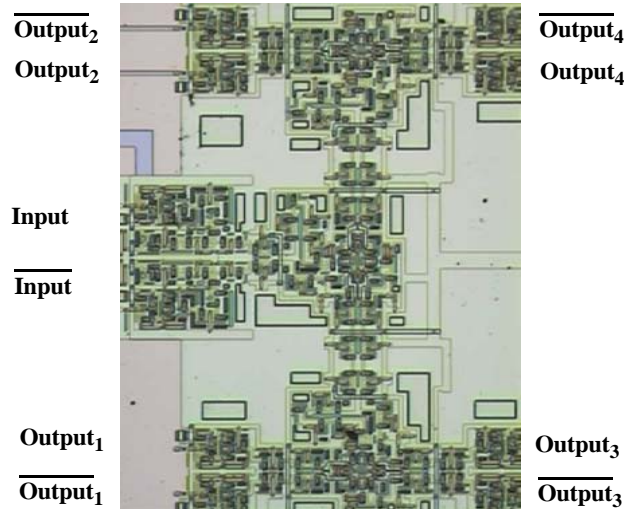


Figure 3.11 Micrograph of a 1:4 DEMUX.

DEMUX with a DDST on-chip high-speed test system. The concept of the on-chip high-speed test system will be discussed in Chap. 4. The configuration above is actually used to verify the 1:4 DEMUX by on-chip high-speed testing and to verify 1:8 DEMUX operation directly. To verify the 8-bit DEMUX on-chip, it requires an 8-bit shift register and an 8-bit clock generator. We only had

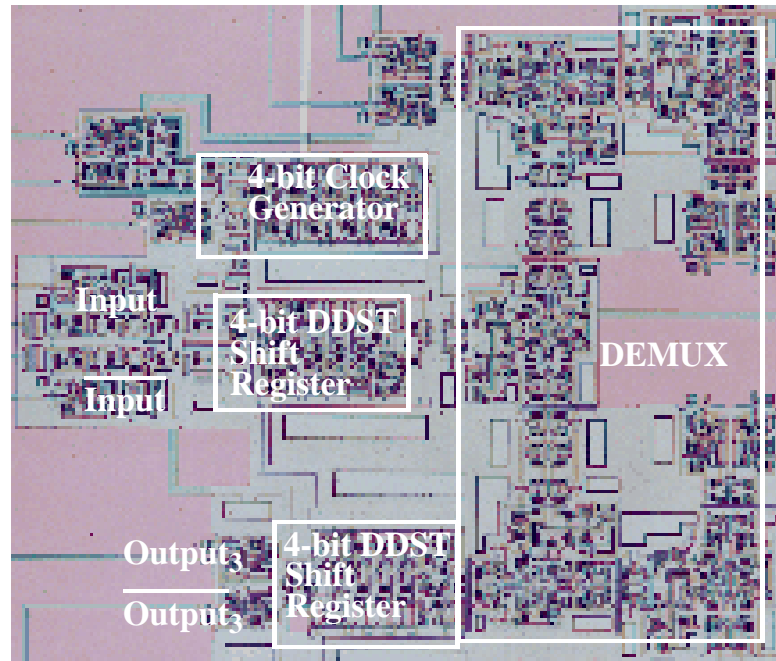


Figure 3.12 Micrograph of a 1:8 DEMUX with DDST on-chip high-speed test system.

a verified 4-bit shift register and an 4-bit clock generator. This chip was not able to be demonstrated due to a layout mistake.

3.5.2 50 GHz DEMUX Design, Layout, and Optimization

A 50 GHz 1:8 DEMUX is designed in the 6.5 kA/cm^2 process based on the 20 GHz design in 1 kA/cm^2 process. Again the optimization of the 2-bit DEMUX is the design focus. To overcome the limitation of MALT, a different optimization tool, WinS, is used in the 50 GHz design. The performance of the 1:8 DEMUX based on the optimized 2-bit module is verified in WRspice.

The performance of the 20 GHz design gets boosted simply by replacing the 1 kA/cm^2 junction model with the 6.5 kA/cm^2 junction model. Fig. 3.13 shows the 1:2 DEMUX simulation waveform at 50 GHz. A comparison of dc bias margins as the function of the operational fre-

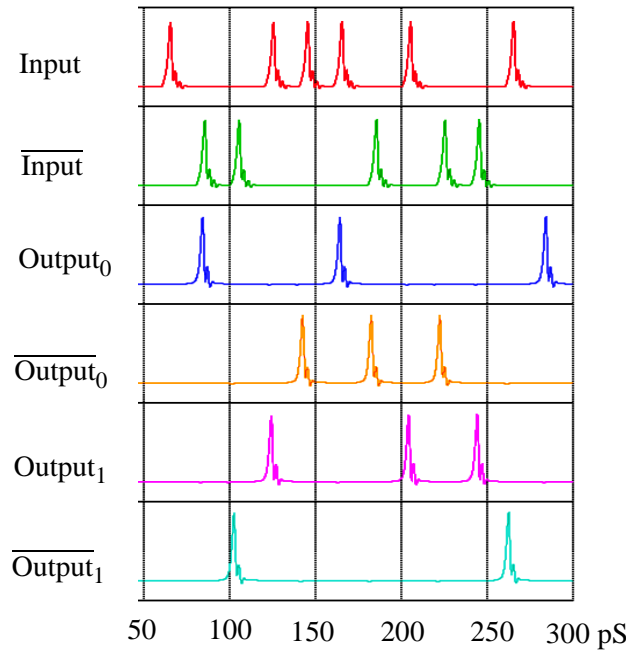


Figure 3.13 1:2 DEMUX simulation waveforms at 50 GHz.

quency is illustrated in Fig. 3.14. Parasitic inductances are included in the simulation. Below 50 GHz, the circuit dc bias margins in 6.5 kA/cm^2 are recovered to the same level as the ones at 20 GHz in 1 kA/cm^2 , which are about (-12%, +24%). Above 50 GHz, the dc bias margin starts to shrink. At 80 GHz, the lower-end dc bias margin is reduced to zero. So the 20 GHz design is already a good starting point for further optimization. The goal of the optimization is to center the dc bias margin and expand the operational frequency range with good yield.

The 20 GHz design parameters are used as the initial values for the 50 GHz design optimization. First, the circuit optimization is done in WinS without any parasitic inductances included. The WinS reported dc bias margins are (-27.4%, +29.5%), the critical parameter margin is that of I_{c7} and I_{c71} (-27.1%) after the optimization. WRspice verified that the dc bias margins are (-25.6%, +32%).

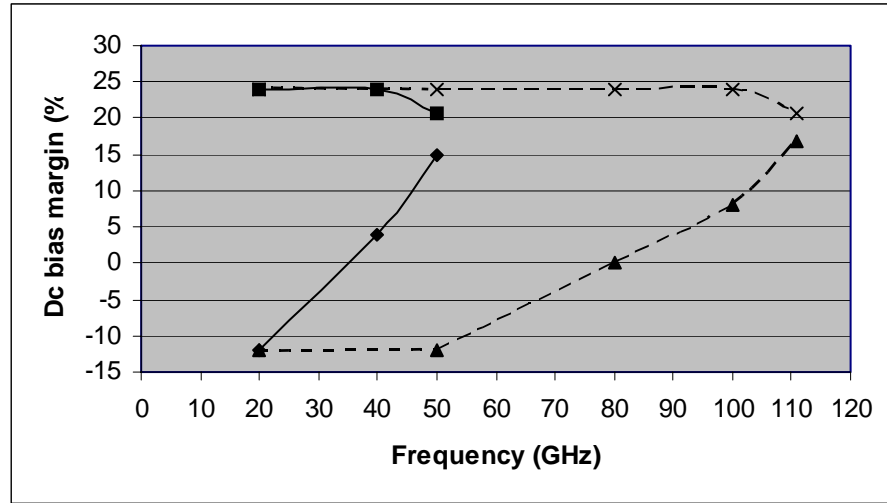


Figure 3.14 Dc bias margin comparison of the 20 GHz 2-bit DEMUX design using the 1 kA/cm^2 process (solid lines) and the 6.5 kA/cm^2 process (dashed lines). The latter is not optimized. Input data pattern is the same as that in Fig. 3.13.

Fig. 3.15 shows the layout of the 1:2 DEMUX in the 6.5 kA/cm^2 process. Moats are systematically added surrounding the superconductor devices, junctions, and inductors.

When the layout parasitic inductances are included, the circuit performance degrades. The WinS checked dc bias margins are $(-29.2\%, +17.2\%)$ and the critical parameter margin is that of I_{c1} and I_{c11} $(+13.4\%)$. In WinS, no parasitic inductances can be added to the built-in RSJ junction model. Only parasitic inductances between the junctions are included in the WinS optimization and parameter margin evaluation. WRspice showed that the dc bias margins are $(-21.7\%, +13\%)$, which include junction parasitic inductances.

Post-layout reoptimization is done to recover circuit margins. The WinS reported that dc bias margins are $(-28.8\%, +30.6\%)$ and the critical parameter margin is that of I_{c1} and I_{c11} $(+27.8\%)$. WRspice verified that dc bias margins are $(-26.1\%, +29.9\%)$, the critical parameter margin is that of I_{c1} and I_{c11} $(+25\%)$ with extra junction parasitic inductances. Since RSFQ circuit components

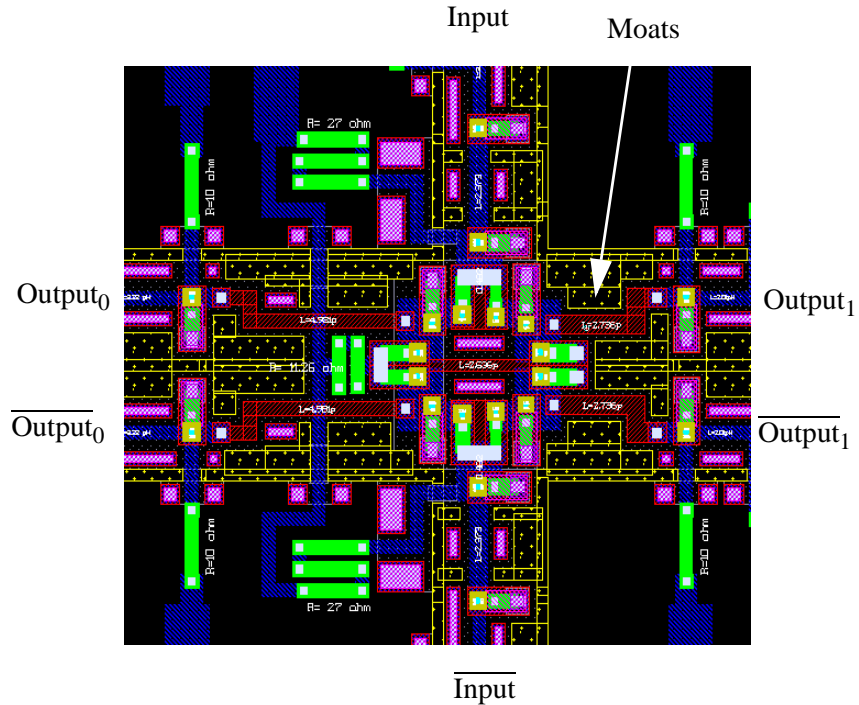


Figure 3.15 1:2 DEMUX layout in the 6.5 kA/cm^2 process.

are connected by inductances and interfere with the neighboring cell's dc bias current distribution, we connect the DEMUX core cell with a few stages of standard JTLs during optimization. And when this optimized cell is used in the future, standard JTLs should be used to connect this cell with other circuits.

Fig. 3.16 shows the 50 GHz 1:2 DEMUX circuit schematic with key circuit parameters. For simplicity, the junction parasitic inductances are not shown here. Fig. 3.17 shows the WinS margin calculation results after the post-layout reoptimization.

We further investigated the 1:2 DEMUX dc bias margins when the operation frequency is varied. Fig. 3.18 shows the variation of the dc bias margins of the 1:2 DEMUX with frequency for different conditions. The input data pattern is the same as that in Fig. 3.13 if not specially noted.

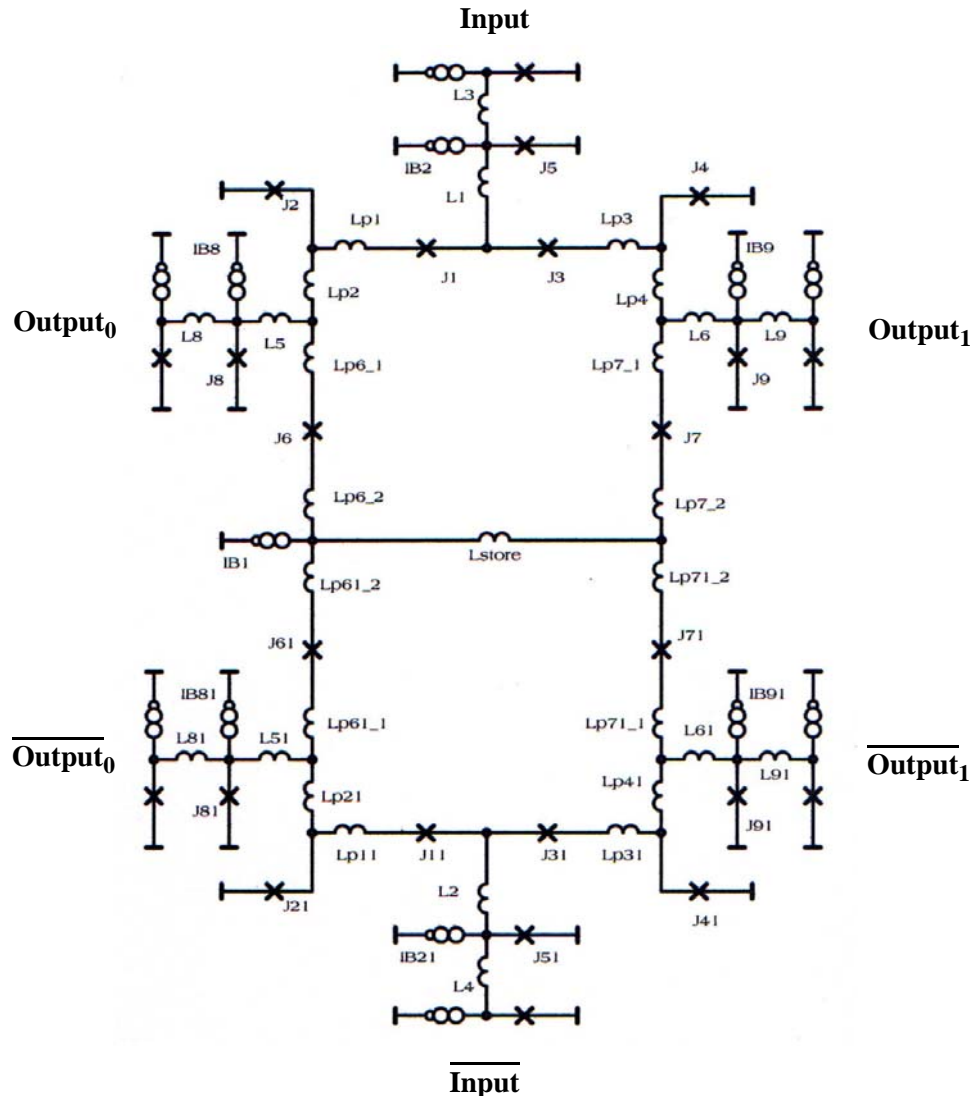


Figure 3.16 50 GHz 1:2 DEMUX schematic with parasitic inductances. The key circuit parameters after the re-optimization are: $I_{c1} = I_{c11} = 264 \mu\text{A}$, $I_{c2} = I_{c21} = 224 \mu\text{A}$, $I_{c3} = I_{c31} = 186 \mu\text{A}$, $I_{c4} = I_{c41} = 264 \mu\text{A}$, $I_{c5} = I_{c51} = 264 \mu\text{A}$, $I_{c6} = I_{c61} = 264 \mu\text{A}$, $I_{c7} = I_{c71} = 264 \mu\text{A}$, $I_{c8} = I_{c81} = 251 \mu\text{A}$, $I_{c9} = I_{c91} = 251 \mu\text{A}$; $L_1 = L_2 = 0.482 \text{ pH}$, $L_3 = L_4 = 2.373 \text{ pH}$, $L_5 = L_{51} = 4.981 \text{ pH}$, $L_6 = L_{61} = 2.736 \text{ pH}$, $L_8 = L_{81} = 5.183 \text{ pH}$, $L_9 = L_{91} = 3.74 \text{ pH}$, $L_{\text{store}} = 2.636 \text{ pH}$; $I_{B1} = 511 \mu\text{A}$, $I_{B2} = I_{B21} = 213 \mu\text{A}$, $I_{B8} = I_{B81} = 117 \mu\text{A}$, $I_{B9} = I_{B91} = 108 \mu\text{A}$.

Comparing curve 1 in Fig. 3.18 with the 6.5 kA/cm^2 margins in Fig. 3.14, we can see that the pre-layout optimization improves the circuit dc bias margins dramatically. Comparing curve 3 with curve 1 and curve 2 in Fig. 3.18, we can tell that the post-layout reoptimization recovers the dc

```

Lstore Inductor 2.6525p .....59.8 | 90.0
IB1 dc Current 0.5106m .....37.3 | 37.3
combias(IB1,IB2,IB21,jtis(4stages each branch)) Collection 1. 28.8 | 30.6
J1,J11 Collection 1. .....30.2 | 27.8
J2,J21 Collection 1. .....38.3 | 39.4
J3,J31 Collection 1. .....39.0 | 40.8
J4,J41 Collection 1. .....90.0 | 62.9
J5,J51 Collection 1. .....90.0 | 79.1
IB2,IB21 Collection 1. .....89.6 | 90.0
L1,L2 Collection 1. .....90.0 | 90.0
L3,L4 Collection 1. .....90.0 | 90.0
IN-jtibias(4-stages) Collection 1. 66.4 | 45.0
J8,J81 Collection 1. .....86.5 | 43.9
J9,J91 Collection 1. .....71.0 | 77.7
L8,L81 Collection 1. .....90.0 | 90.0
L9,L91 Collection 1. .....90.0 | 90.0
IB8,IB81 Collection 1. .....90.0 | 90.0
IB9,IB91 Collection 1. .....90.0 | 90.0
Out1jtis combias (3 stages) Collection 1. 74.2 | 49.6
Out2jtis combias (3 stages) Collection 1. 90.0 | 66.1
L5,L51 Collection 1. .....75.6 | 78.4
L6,L61 Collection 1. .....71.4 | 90.0
J6,J61 Collection 1. .....35.5 | 59.1
J7,J71 Collection 1. .....28.8 | 34.1
Lp1,11 Collection 1. .....90.0 | 90.0
Lp2,21 Collection 1. .....90.0 | 90.0
Lp3,31 Collection 1. .....90.0 | 90.0
Lp4,41 Collection 1. .....90.0 | 90.0
Lp6,1,61_1 Collection 1. ....90.0 | 90.0
Lp6,2,61_2 Collection 1. ....90.0 | 90.0
Lp7,1,71_1 Collection 1. ....90.0 | 90.0
Lp7,2,71_2 Collection 1. ....90.0 | 90.0

```

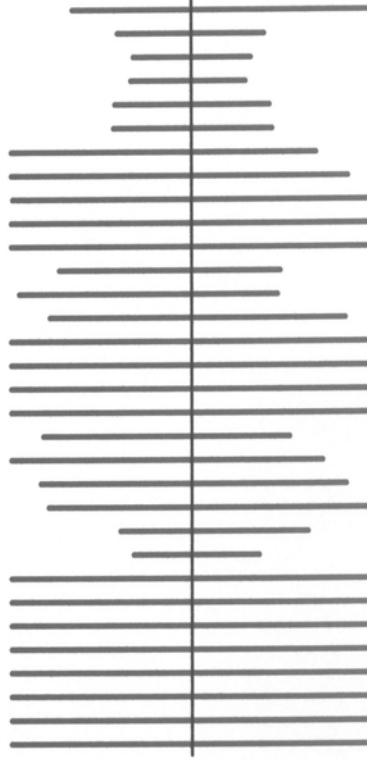


Figure 3.17 WinS margin report of the 50 GHz 1:2 DEMUX after post-layout re-optimization.

bias margins almost to the pre-layout level with slight loss. When the frequency is above 50 GHz, the circuit lower dc bias margin is continuously decreasing. It shrinks to zero at around 100 GHz. So for this circuit to operate at frequency above 50 GHz, it should be re-optimized for that frequency for better circuit parameter margins. This re-optimized 1:2 DEMUX can operate up to 125 GHz with reduced dc bias margin (16.5%, 29.9%).

We also investigated the dc bias margin of 1:2 DEMUX when a simplified input pattern, all 1s, is fed to one input. This corresponds to our test plan where no DC/SFQ converter is used to convert the external pattern generator signals. All 1s data pattern is generated at one input by over biasing the input Josephson junction above its critical current value up to very high frequency (a few hundred gigahertz). Curve 4 in Fig. 3.18 shows the result including parasitic inductances.

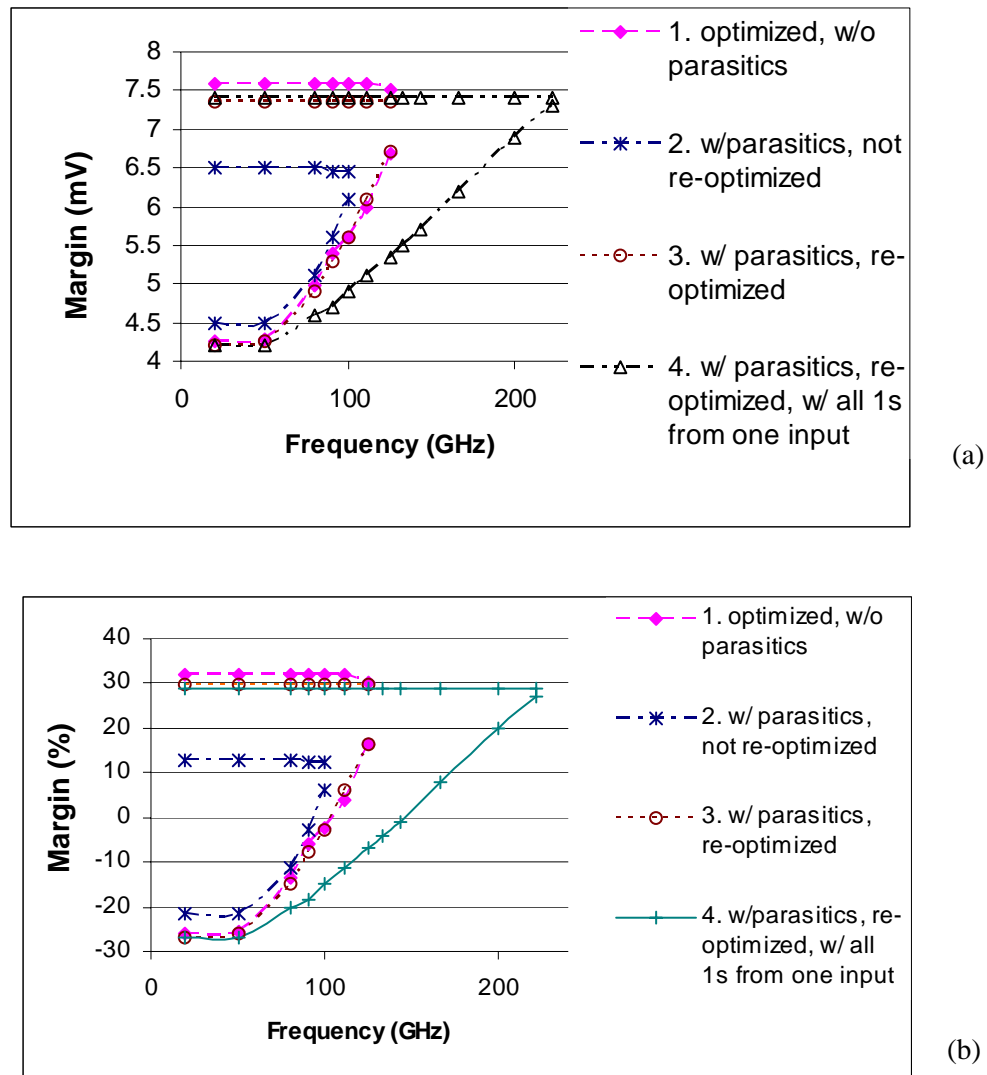


Figure 3.18 1:2 DEMUX dc bias margins vs. frequency (a) in millivolts (b) in percentage.

With the simplified input data pattern, the dc bias margin is widened compared to the case with more complicated complementary input data pattern. It can operate up to 222 GHz as simulated in WRspice.

When the 1:8 DEMUX is built from the 1:2 DEMUX cells according to the binary tree structures as we presented earlier in Fig. 3.2, standard JTLs are used for connections. The dc bias margins simulated in the WRspice are very close to the 2-bit DEMUX result. It demonstrates that our strategy to include standard JTLs in optimization works.

3.6 MUX Simulation and Optimization Result

3.6.1 20 GHz Ripple Logic MUX Design, Layout and Optimization

The architecture of the MUX was discussed in Section 3.2.2. The building blocks include confluence buffers, RS flip-flops, D flip-flops, and T flip-flops. All the basic cells were built and verified in the 1 kA/cm^2 HYPRES process in the previous projects by other members of the UCB cryogroup.

We built a 2:1 MUX based on the old cells. The block diagram of the 2:1 MUX is shown in Fig. 3.19. It was fabricated in the HYPRES 1 kA/cm^2 process and was shown to have $(-7\%, +7\%)$ dc bias margins and to work up to 4 GHz. The detailed testing results are in Section 5.2.1. Compared with the block diagram in Fig. 3.3b, Dffs are used to latch the parallel input data instead of Tffs. The advantage of using Dffs is that there is no need to take care of the timing between Clock₁ and Clock₂ within the MUX. But when a 2-bit MUX is expanded to an 8-bit MUX, the layout of

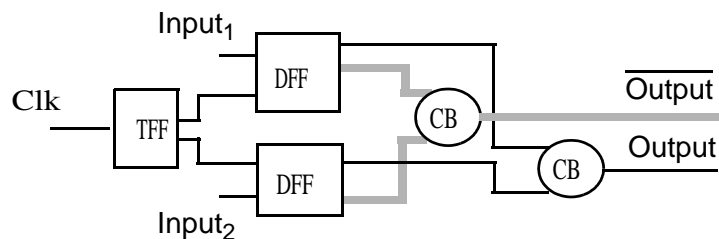


Figure 3.19 A 2:1 MUX block diagram

the CB network for the complementary outputs of the Dffs becomes very difficult since the connection is done by JTLs instead of metal wires in RSFQ circuits. So we decided to use RSffs to latch the input data to reduce the CB network complexity to half in the further design. It is also advantageous to reduce the number of the Dffs used in the circuit since this is the cell with smallest dc bias margin among all the basic blocks used in the MUX.

We optimized all the basic blocks for better dc bias margin and yield. The optimizations are mainly done in wither MALT or WinS. Key parasitic inductances are included in the simulation and the optimization. Fig. 1.11 shows the Tff circuit diagram with the circuit parameters. Fig. 3.20 shows the CB circuit diagram with circuit parameters. Fig. 3.21 shows the RSff circuit diagram with the circuit parameters. Fig. 3.22 shows the Dff circuit diagram with the circuit parameters. The parasitic inductances in the storage loop are carefully extracted and included in the optimization.

Monte Carlo analysis is also used to estimate the clock/data path delay variations caused by the process variations. Shown in Fig. 3.3b is the block diagram of the 8:1 MUX. The Dff has a setup/hold time requirement. So the delay between Clock₁ and Clock₂ has to be designed to com-

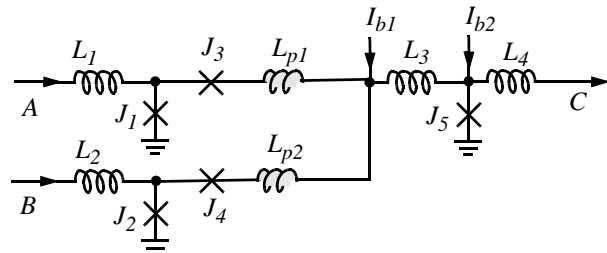


Figure 3.20 A circuit diagram of confluence buffer with optimized parameters in 1 kA/cm² Nb process. $I_{c1} = I_{c2} = 294 \mu\text{A}$, $I_{c3} = I_{c4} = 279 \mu\text{A}$, $I_{c5} = 238 \mu\text{A}$; $L_1 = L_2 = 2.91 \text{ pH}$, $L_3 = 3.67 \text{ pH}$, $L_4 = 3.6 \text{ pH}$, $L_{p1} = L_{p2} = 0.39 \text{ pH}$; $I_{b1} = 407 \mu\text{A}$, $I_{b2} = 123 \mu\text{A}$.

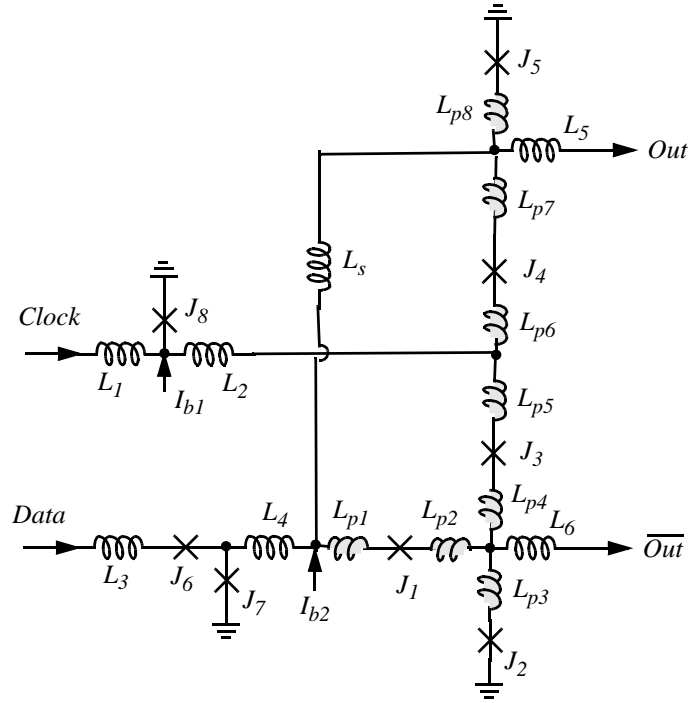


Figure 3.22 A circuit diagram of Dff with optimized parameters in 1 kA/cm^2 Nb process. $I_{c1} = 151 \mu\text{A}$, $I_{c2} = 186 \mu\text{A}$, $I_{c3} = 309 \mu\text{A}$, $I_{c4} = 224 \mu\text{A}$, $I_{c5} = 339 \mu\text{A}$, $I_{c6} = 279 \mu\text{A}$, $I_{c7} = 198 \mu\text{A}$, $I_{c8} = 373 \mu\text{A}$; $L_1 = 2.54 \text{ pH}$, $L_2 = 0.98 \text{ pH}$, $L_3 = 2.54 \text{ pH}$, $L_4 = 3.22 \text{ pH}$, $L_s = 3.51 \text{ pH}$, $L_5 = 3.71 \text{ pH}$, $L_6 = 3.71 \text{ pH}$, $L_{p1} = 0.29 \text{ pH}$, $L_{p2} = L_{p3} = L_{p5} = L_{p6} = 0.20 \text{ pH}$, $L_{p4} = L_{p7} = 0.39 \text{ pH}$, $L_{p8} = 0.59 \text{ pH}$; $I_{b1} = 307 \mu\text{A}$, $I_{b2} = 284 \mu\text{A}$.

pensate the long delay from Clock_1 to the Data input of the Dff, which is around 110 ps, much larger than one 20 GHz clock cycle. There are eight Clock_1 to Data_Dff signal paths in a 8:1 MUX. One of the eight clock/data paths is highlighted in Fig. 3.3(b) for illustration. It consists of

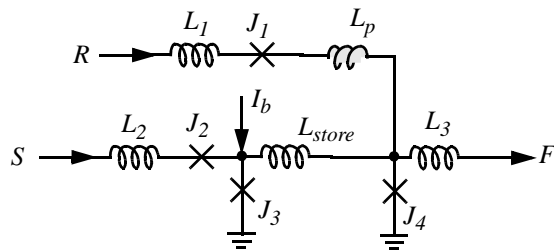


Figure 3.21 A circuit diagram of RSff with optimized parameters in 1 kA/cm^2 Nb process. $I_{c1} = 224 \mu\text{A}$, $I_{c2} = 325 \mu\text{A}$, $I_{c3} = 325 \mu\text{A}$, $I_{c4} = 294 \mu\text{A}$; $L_1 = 2.14 \text{ pH}$, $L_2 = 2.99 \text{ pH}$, $L_3 = 3.60 \text{ pH}$, $L_{\text{store}} = 4.13 \text{ pH}$, $L_p = 0.4 \text{ pH}$; $I_b = 240 \mu\text{A}$.

three Tffs, one RSff, and three CBs. Due to process variations, the delay along the eight paths could be different from each other. Fig. 3.23 shows waveforms in the simulation to characterize the delay. Data_Dff has eight consecutive pulses, each goes through one of the eight clock/data signal paths. In Monte Carlo analysis, in each simulation run, each Tff of the total seven, each RSff of the total eight, and each CB of the total seven have different circuit parameters, which are pseudo-randomly generated based on the local process variations in Table 3-1. The histogram of the delay variations with the Gaussian fitting curve is plotted in Fig. 3.24. The total counts is 102. The standard deviation is 1.38 ps. So the 6σ delay variation is 8.3 ps. With a 50 ps clock period at 20 GHz, we still have enough timing margin reserved for the Dff setup/hold time requirement.

Fig. 3.25 shows the waveforms of a correctly functioning 20 GHz 8:1 MUX. Clock₁ is at 20 GHz. Inputs D₀, D₁, D₅, D₆, D₇ are 2.5 GHz pulses, D₂, D₃, D₄ are all 0s. So Output is 20 GHz

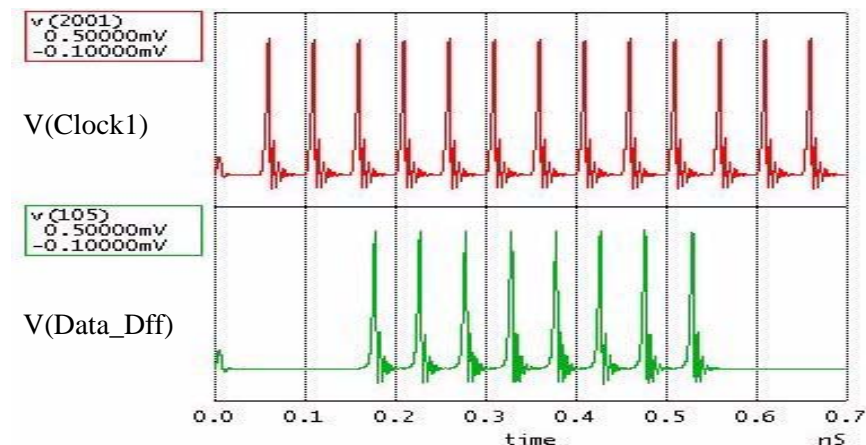


Figure 3.23 Waveforms of the 20 GHz 8:1 MUX data path delay simulation.

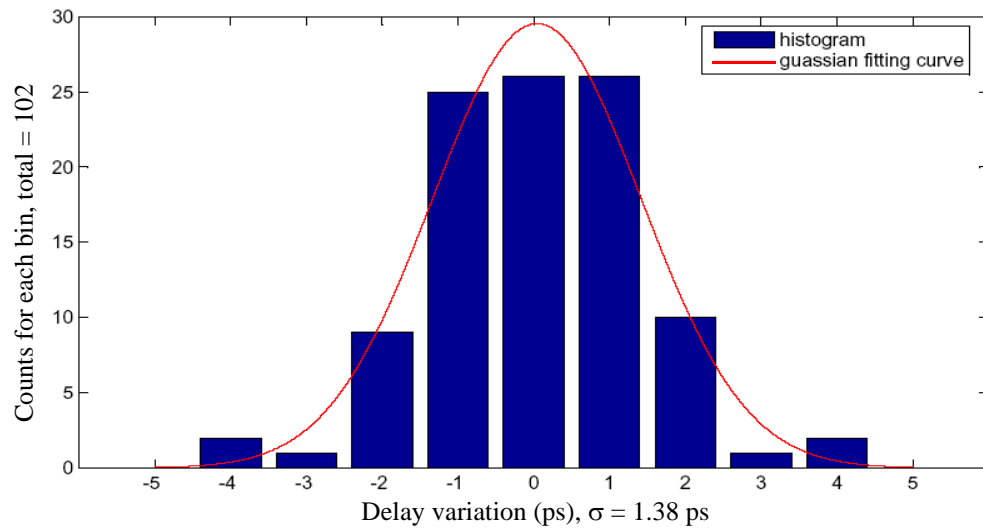


Figure 3.24 Histogram of the delay variation for one data path in the 20 GHz 8:1 MUX. $\sigma = 1.38 \text{ ps}$

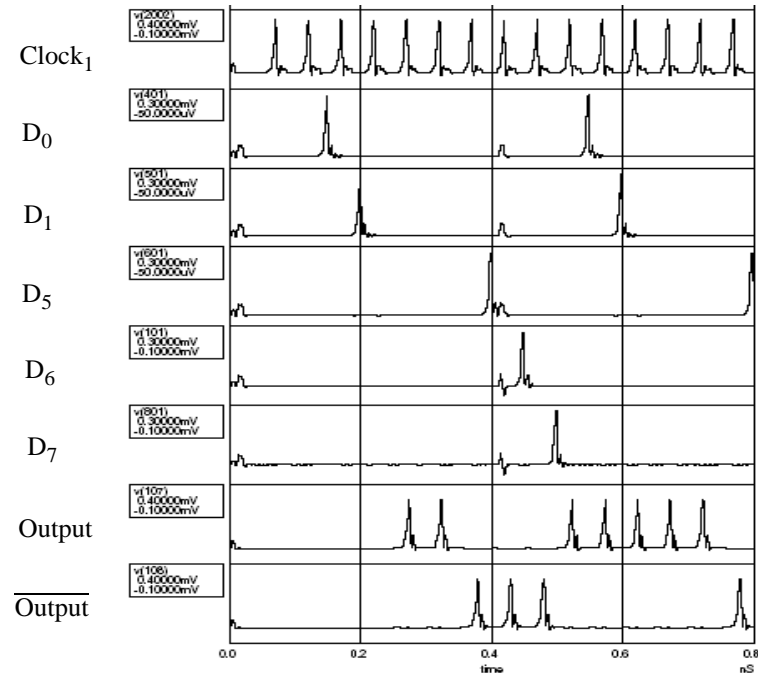


Figure 3.25 Waveforms of the 20 GHz 8:1 MUX simulation. D₂, D₃, D₄ are all 0s.

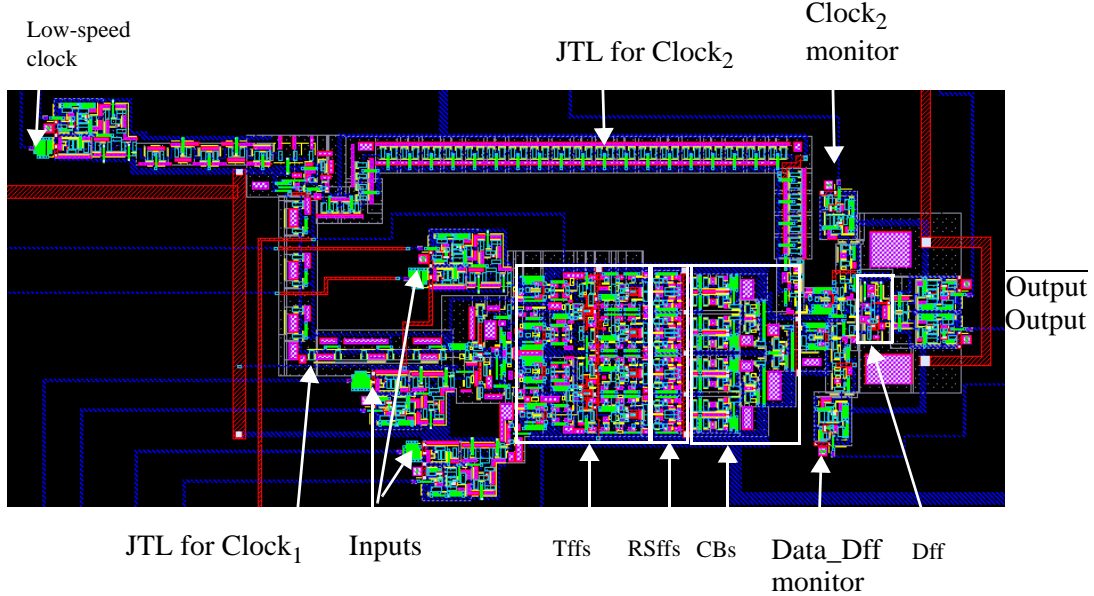


Figure 3.26 Layout of a 20 GHz 8:1 MUX in 1 kA/cm² UCB Nb process.

“11000111” pattern. The complementary $\overline{\text{Output}}$ is a 20 GHz “00111000” pattern. The dc bias margin of the 8:1 MUX is limited by the Dff and is the same as that of the Dff.

Fig. 3.26 shows the layout of a 20 GHz 8:1 MUX in 1 kA/cm² UCB Nb process. Clock₁ and Clock₂ are from the same external clock source, but with different JTL stages. The skew between the two clocks was chosen according to the Dff setup/hold time and previous calculated Clock₁-to-Data_Dff delay. We also made a 4:1 MUX layout, a 4:1 MUX with on-chip high-speed test system and an 8:1 MUX with an on-chip high-speed test system layout for verifications, which will be discussed in Section 5.3.

3.6.2 50 GHz MUX Design, Layout and Optimization

The basic cells using the 1 kA/cm² design parameters are verified in 6.5 kA/cm² process. As before, some connection parasitic inductances are included in the simulations already. The dc bias

margins of the cells in 6.5 kA/cm^2 are listed in Table 3-8. The dc bias margin of the 8:1 MUX is (-26%, +28%). Again the large dc bias margins achieved are partly due to not including all the junction parasitic inductances.

TABLE 3-8 Dc bias margins of the basic cells used in 50 GHz 6.5 kA/cm^2 MUX.

Cell name	Dc bias margins
CB	(-40%, +46%)
Tff	(-28%, +32%)
RSff	(-46%, +36%)
Dff	(-26%, +28%)

Monte Carlo analysis is performed to evaluate the Clock₁-to-Data_Dff delay variation. The 6.5 kA/cm^2 process variations in Table 3-2 are used. The histogram of the delay variations and its Gaussian fitting curve are plotted in Fig. 3.27. The total counts is 138. The standard deviation is 0.46 ps. The 6σ delay variation is 2.8 ps, which is still a small portion of 20 ps clock period at 50

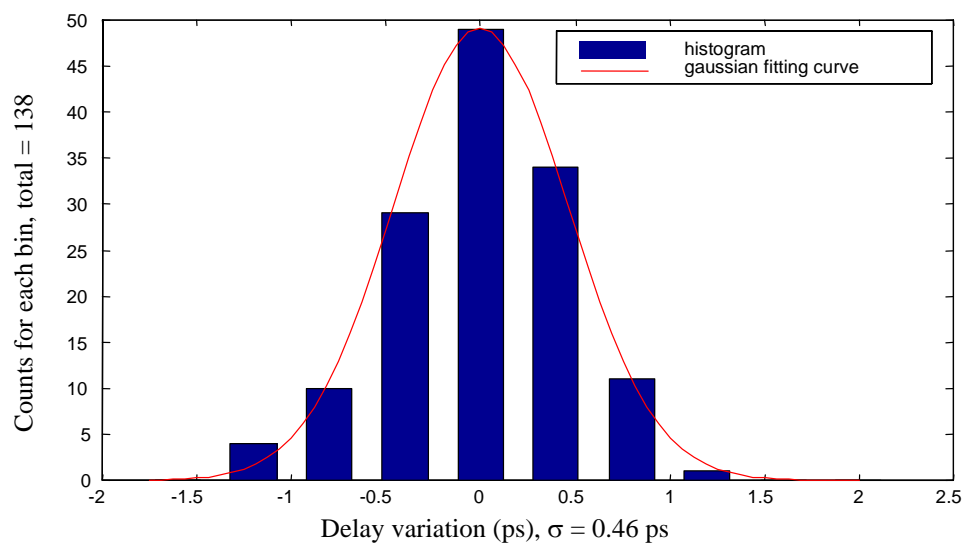


Figure 3.27 Histogram of the 50 GHz 8:1 MUX data path delay variation in the 6.5 kA/cm^2 process.

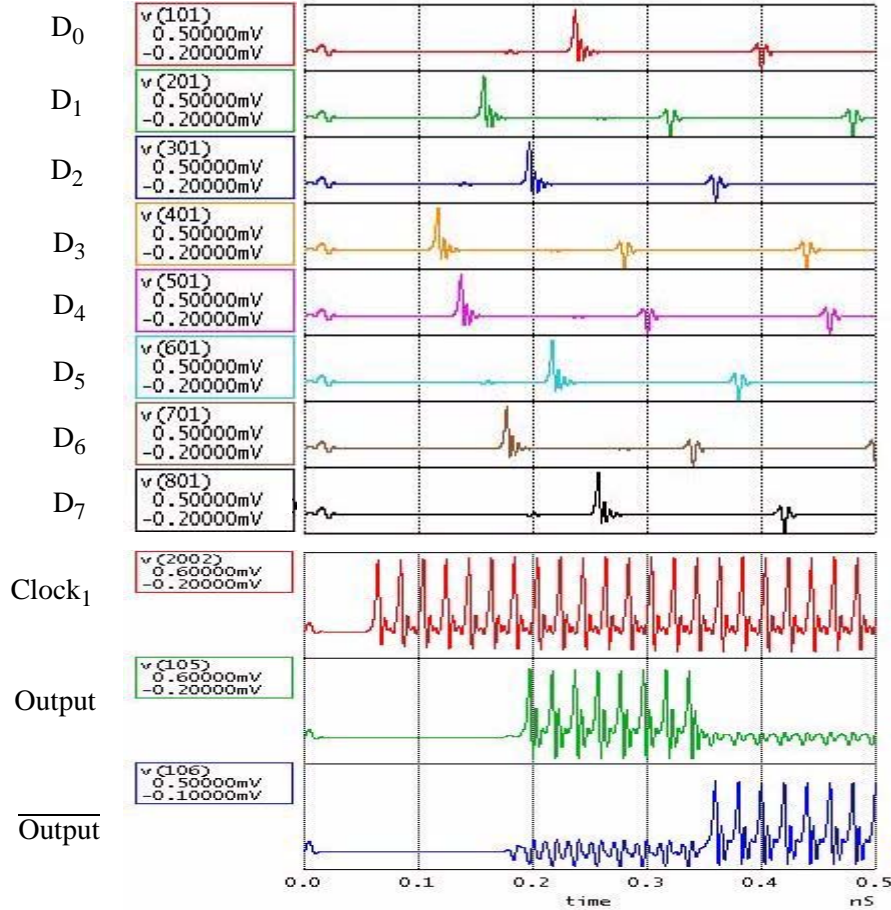


Figure 3.28 50 GHz 8:1 MUX simulation waveforms.

GHz. The small delay variation is due to the assumed small process variations in UCB high- J_c Nb process. Fig. 3.28 shows the 50 GHz waveforms of the 8:1 MUX.

The Tff, CB, Dff are then laid out and post-layout optimizations are done. Since in WinS, the junction model has to be an RSJ model without parasitic inductances, further circuit performance enhancement was done by manually adjusting the circuit parameters.

Fig. 3.29 shows the layout of the Tff in 6.5 kA/cm² process and its corresponding block diagram. Systematic moats are applied in the circuit layout. I_{c3} is changed to 325 μ A from 356 μ A for

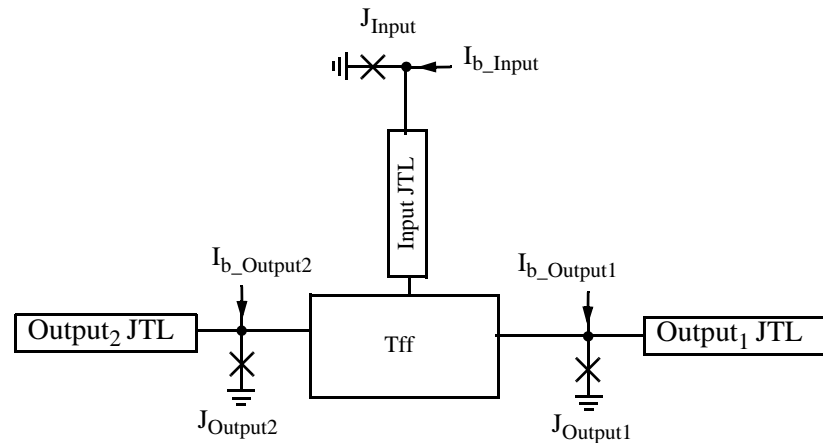
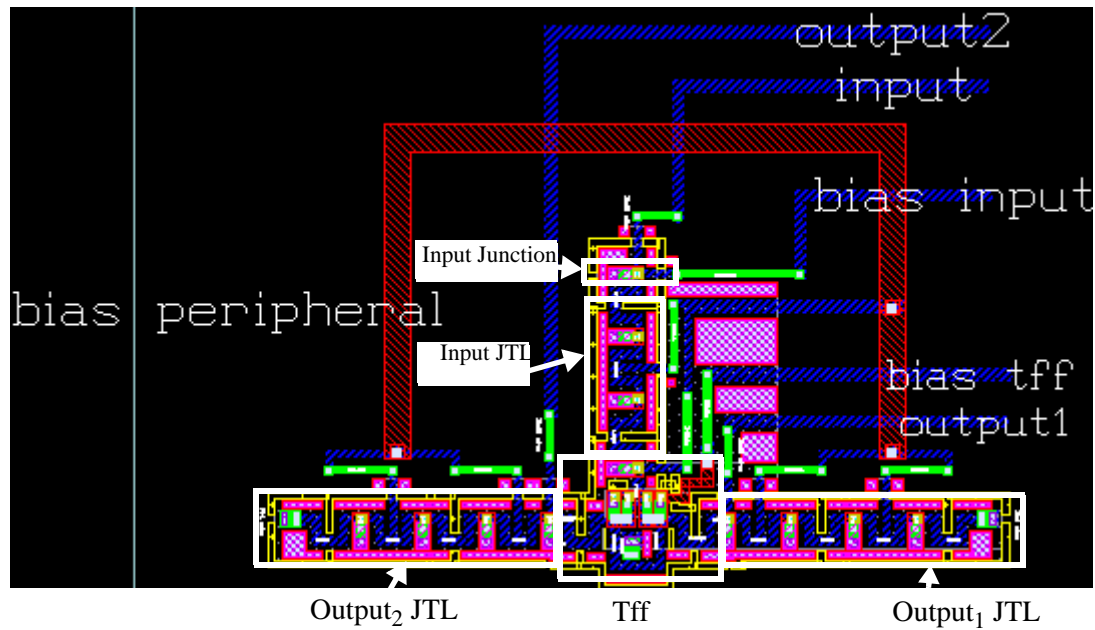


Figure 3.29 The 6.5 kA/cm^2 Tff layout and its corresponding block diagram.

better parameter margins. This block is put on the first 6.5 kA/cm^2 test chip to be verified. The verification of this cell was designed to be very simple, without DC/SFQ and SFQ/DC cells. The input SFQ pulses are generated by over-biasing the input junction J_{Input} . $I_{\text{c_Input}} = 251 \mu\text{A}$. When

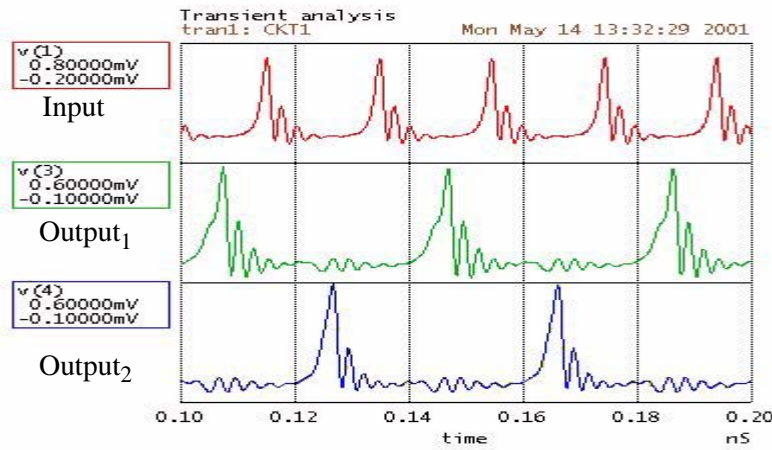


Figure 3.30 Simulation waveforms of the 6.5 kA/cm^2 Tff.

$I_{b_Input} = 323 \mu\text{A}$ in simulation, the input pulse frequency is about 50 GHz. $I_{c_Output1} = I_{c_Output2} = 251 \mu\text{A}$, and they are biased at $175 \mu\text{A}$. The voltage waveforms in Fig. 3.30 shows that the output pulse frequency is half of the input frequency. With such simple arrangement, this Tff has dc bias margins of (-30%, +38%) and can work up to 220 GHz.

Shown in Fig. 3.31 is the layout of the Dff in 6.5 kA/cm^2 process. Post-layout simulation shows substantial margin loss if all the junction parasitic inductances are included in the simulations. The manual re-optimization could only recover the circuit dc bias margins to (-21.7%, +15.7%). The new circuit parameters are implemented in this layout and put on the first 6.5 kA/cm^2 test chip. The circuit parameters are recorded in Section 4.3.3, since the 50 GHz high-speed test system also used this Dff too.

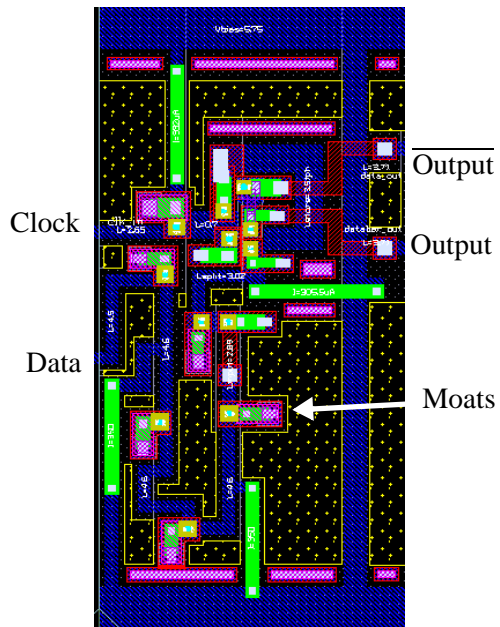


Figure 3.31 Layout of the 6.5 kA/cm^2 Dff.

Post-layout optimization was also done for the CB, which is also discussed in detail in Section 4.3.1 as part of the high-speed test system design. The achieved post-layout dc bias margins are (-28.7%, +29.6%). The post-layout dc bias margins of the re-optimized cells are listed in Table 3-9.

TABLE 3-9 Post-layout dc bias margins of the basic cells to be used in 50 GHz 6.5 kA/cm^2 MUX.

Cell name	Dc bias margins
CB	(-28.7%, +29.6%)
Tff (w/ all 1s as Input)	(-30%, +38%)
Dff	(-21.7%, +15.7%)

CHAPTER 4

50 GHz On-Chip Testing System

4.1 Introduction

Direct high-speed testing of RSFQ circuits is expensive, and it is limited by the signal loss along the cables to around 20 GHz with the current commercially available testing equipment. The difficulty arises from very high circuit operation speed and small amplitude of signals. SFQ/DC converters are placed at the RSFQ circuit outputs to convert SFQ pulses to voltage waveforms. So the signals coming out of SFQ/DC converters are a few hundred microvolts. Without the SFQ/DC conversion, the picosecond SFQ pulses would be even less likely to survive the dispersion and loss along the cables. RSFQ circuits can operate at a few tens of gigahertz, with potential to go up to above 100 GHz. For RSFQ circuit function verification at speeds above 20 GHz, an on-chip high-speed testing system is necessary [52].

The idea of on-chip high-speed testing is that input data are loaded to input shift registers at low speed and stored there until an on-chip high-speed clock is turned on to push these data through the circuit under test (CUT). After the high-speed operations of the CUT are finished, the on-chip high-speed clock is turned off. The results of the circuit's high-speed operation are stored in output shift-registers and can be read out at low speed later on to verify the circuit operation.

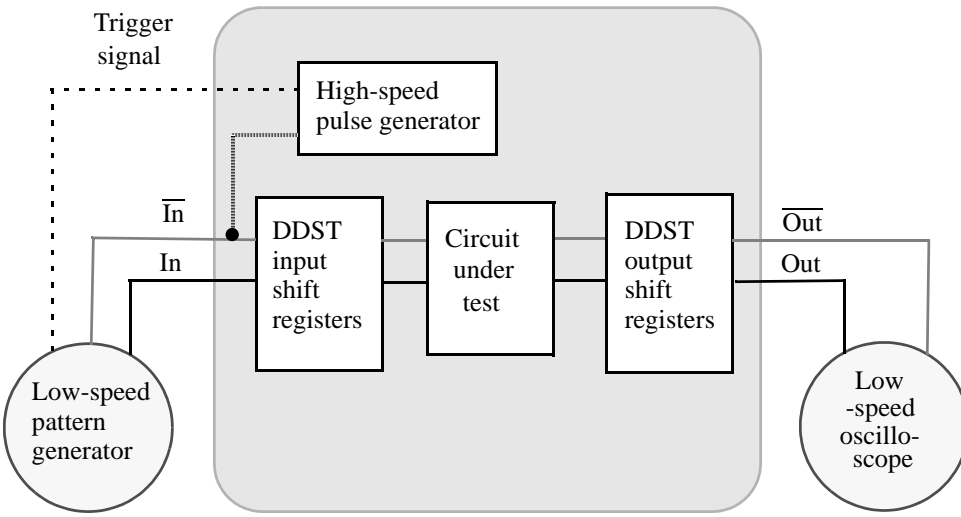


Figure 4.1 Block diagram of a DDST on-chip high-speed testing system. High-speed operations of the circuit under test are controlled by the on-chip high-speed clock pulses and recorded by the output shift registers. Input and output data are fed into and read out by low-speed instruments.

Various configurations have been developed [53][54]. Shown in Fig. 4.1 is a block diagram of the Data-Driven Self-Timed (DDST) on-chip high-speed testing system [39][55]. Unlike other designs, an on-chip pulse generator is used to produce a fixed number of high-speed clock pulses initialized by a trigger signal. Such a pulse generator avoids the difficulty of accurate timing control in gating a continuous clock generator. DDST shift registers are based on the application of dual-rail data. Timing information is embedded in the data. Therefore, no external low-speed clock is required to load and read out data so the effort on timing control between a high-speed clock and a low-speed clock is saved. Previously, 20 GHz operations of such a testing system in the 1 kA/cm² niobium process were demonstrated successfully [56][57]. In this chapter the design and optimization of such a test system for 50 GHz operation in the 6.5 kA/cm² niobium process will be described. A pulse generator is designed and optimized to produce SFQ clock pulses at a fre-

quency between 11.4 GHz and 88.2 GHz. The DDST shift register is modified from the 20 GHz design parameters and optimized to recover the dc bias margins from $\pm 5\%$ to (-18.3%, 15.7%) at 50 GHz. The whole testing system's dc bias margins recover from zero to (-25.2%, 15.7%) upon reoptimization.

4.2 50 GHz Pulse Generator

As discussed above, high-speed operations of the CUT are governed by an on-chip high-speed clock. The clock pulse generator to be introduced has the merits of simple configuration and controllable start and stop. Shown in Fig. 4.2a is a block diagram of a 4-bit ladder pulse generator. Each stage consists of an SFQ pulse splitter (PS), a confluence buffer (CB), and JTLs inserted along the signal paths represented by the arrows. The PS is a fork and the CB is a merger for signals. The first clock pulse is generated after the trigger pulse travels through the first PS, the first rung of the ladder and the first CB. The second clock pulse comes out through the first two PSs,

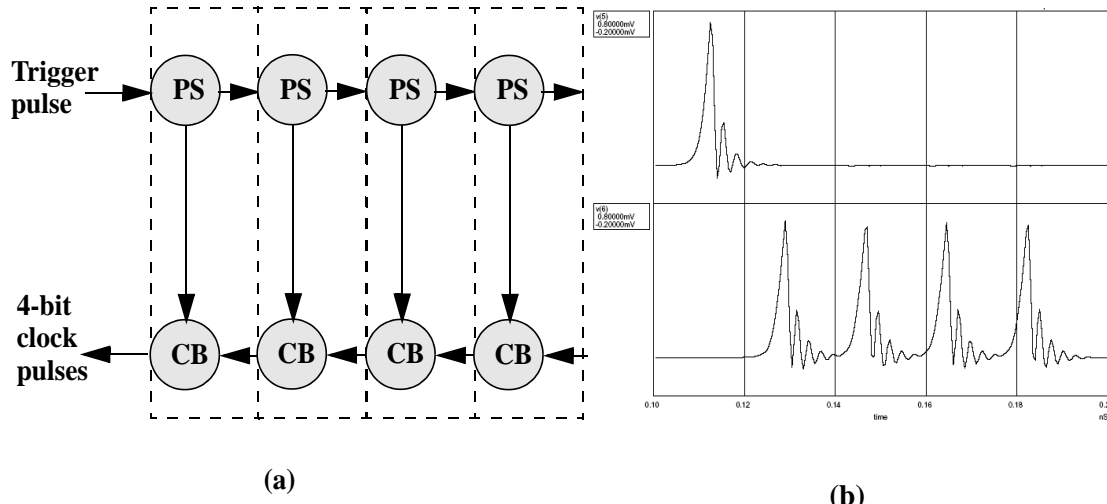


Figure 4.2 A 4-bit ladder pulse generator. (a) block diagram, (b) WRspice simulation result.

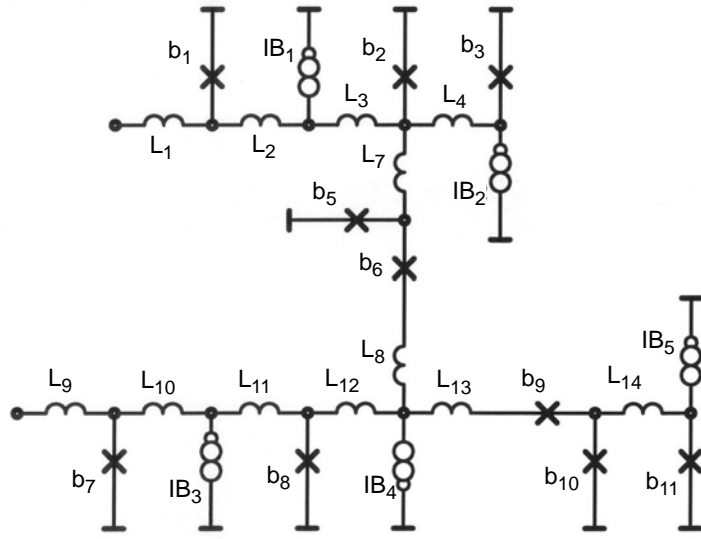


Figure 4.3 The circuit schematic of one stage PS–CB combination in the 50 GHz pulse generator. The optimized device parameter values are shown as below. Junction critical current values are: $I_{c1} = 262.5 \mu\text{A}$, $I_{c2} = 320 \mu\text{A}$, $I_{c3} = 250 \mu\text{A}$, $I_{c5} = I_{c10} = 312.6 \mu\text{A}$, $I_{c6} = I_{c9} = 269.1 \mu\text{A}$, $I_{c7} = 250 \mu\text{A}$, $I_{c8} = 250 \mu\text{A}$, $I_{c11} = 250 \mu\text{A}$. Inductance values are: $L_1 = 4.0 \text{ pH}$, $L_2 = 1.848 \text{ pH}$, $L_3 = 1.391 \text{ pH}$, $L_4 = 4.6 \text{ pH}$, $L_7 = 4.232 \text{ pH}$, $L_8 = L_{13} = 0.7 \text{ pH}$, $L_9 = 4.0 \text{ pH}$, $L_{10} = 1.2 \text{ pH}$, $L_{11} = 2.8 \text{ pH}$, $L_{12} = 3.0668 \text{ pH}$. Bias current values: $IB_1 = 439.6 \mu\text{A}$, $IB_2 = 192.8 \mu\text{A}$, $IB_3 = 253.4 \mu\text{A}$, $IB_4 = 507.7 \mu\text{A}$, $IB_5 = 192.8 \mu\text{A}$.

the second rung of the ladder and the first two CBs. The total number of clock pulses generated from a single trigger pulse is controlled by the number of stages in the pulse generator. The pulse interval is roughly the delay of one stage which can be adjusted by the number of JTLs inserted, and also depends on the dc bias. In the last stage, the unconnected PS output and CB input are each terminated by a 3.6 pH inductor and a 1Ω resistor to ground. Fig. 4.2b shows a simulation result of a 50 GHz 4-bit pulse generator.

Fig. 4.3 shows the circuit schematic of one stage PS–CB combination in the pulse generator. The junctions shown in the schematic are resistor-shunted junctions (RSJs). They are made with $I_cR = 0.592 \text{ mV}$, $\beta_c = 1$. The parameter values listed are the result of WinS optimization. The initial parameter values put into the optimization are obtained from modifying the earlier 20 GHz pulse

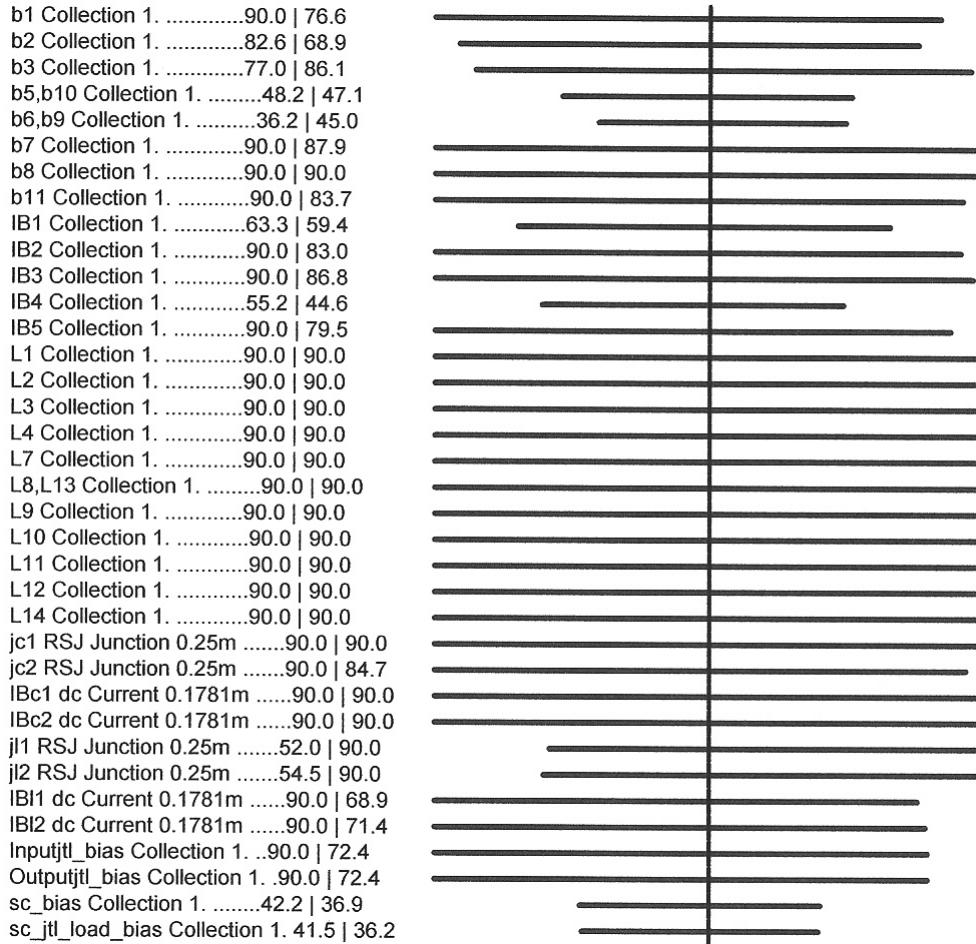


Figure 4.4 WinS margin report on the pulse generator with parameters shown in Fig. 4.3.

generator. The 6.5 kA/cm^2 junction model replaces the 1 kA/cm^2 model, and some JTLs are taken out of the original circuit to shorten the clock period to about 20 ps corresponding to 50 GHz. Parasitic inductances are not yet included in the optimization.

In WinS, optimization is set up to maximize the critical margin among the junction critical current values, inductance values, individual bias current values and the global bias current value. Seen from the WinS report in Fig. 4.4, the critical parameter margins are those of b6,b9 collection

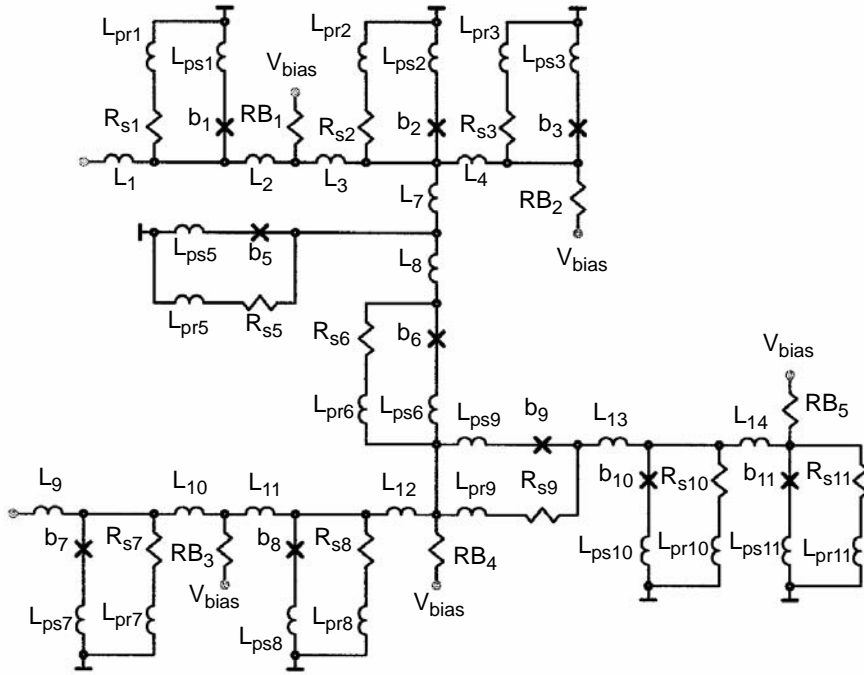


Figure 4.5 Post-layout circuit schematic of one stage PS-CB combination in the 50 GHz pulse generator. The device parameter values are shown as below. Junction critical current values: $I_{c1} = 264 \mu\text{A}$, $I_{c2} = 325 \mu\text{A}$, $I_{c3} = 251 \mu\text{A}$, $I_{c5} = I_{c10} = 309 \mu\text{A}$, $I_{c6} = I_{c9} = 264 \mu\text{A}$, $I_{c7} = I_{c8} = I_{c11} = 251 \mu\text{A}$. Shunt resistor values: $R_{s1} = 2.24 \Omega$, $R_{s2} = 1.82 \Omega$, $R_{s3} = 2.36 \Omega$, $R_{s5} = R_{s10} = 1.92 \Omega$, $R_{s6} = R_{s9} = 2.24 \Omega$, $R_{s7} = R_{s8} = R_{s11} = 2.36 \Omega$. Parasitic inductance values: $L_{ps6} = L_{ps9} = 0.5 \text{ pH}$, $L_{pr6} = L_{pr9} = 1 \text{ pH}$, all other $L_{ps} = 0.1 \text{ pH}$, $L_{pr7} = 0.7 \text{ pH}$. Inductance values: $L_1 = 4.0 \text{ pH}$, $L_2 = 1.85 \text{ pH}$, $L_3 = 1.39 \text{ pH}$, $L_4 = 4.6 \text{ pH}$, $L_7 = 4.23 \text{ pH}$, $L_8 = L_{13} = 1 \text{ pH}$, $L_9 = 4.0 \text{ pH}$, $L_{10} = 1.2 \text{ pH}$, $L_{11} = 2.8 \text{ pH}$, $L_{12} = 3.07 \text{ pH}$. Bias resistor values: $RB_1 = 13.1 \Omega$, $RB_2 = 29.8 \Omega$, $RB_3 = 22.7 \Omega$, $RB_4 = 11.3 \Omega$, $RB_5 = 29.8 \Omega$.

(-36.2%) and that of the global bias collection (+36.2%). The margin result is confirmed by the WRspice simulation.

Fig. 4.5 shows the post-layout circuit schematics of the one stage PS-CB combination. The bias current sources are implemented by bias resistors connected to a common bias voltage source V_{bias} . For connection convenience in layout, the order of L_8 and b_6 , L_{13} and b_9 are switched compared to the pre-layout schematics. Junction critical current values are rounded to the closest values available from our shunted junction library. Inductance extraction is done using the program

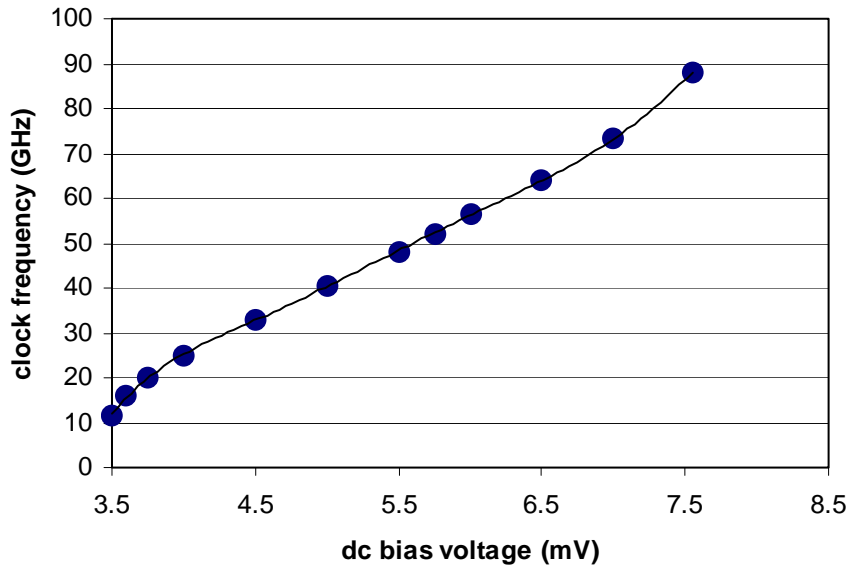


Figure 4.6 Pulse frequency vs. dc bias voltage, V_{bias} in Fig. 4.5.

LMETER. The updated device parameter values including parasitic inductances are listed with the post-layout schematics. Post-layout simulation in WRspice shows that the circuit performance with the parasitic inductance is sufficient. The critical parameter margin is that of b_6 (+36%). The dc bias margin is (-42.4%, 36%). Or equivalently, the viable dc bias voltage range is (3.5 mV to 7.55 mV) with the nominal value at 5.75 mV. No further design modification is needed. Fig. 4.6 shows the frequency-bias voltage relationship from the post-optimization. The 4-bit pulse generator produces pulses in the frequency range (11.4 GHz to 88.2 GHz) by varying its dc bias voltage in the range (3.5 mV to 7.55 mV). The center frequency is 52.2 GHz at the nominal bias voltage 5.75 mV.

Further simulation shows that longer pulse generators can be built without sacrificing margins. Fig. 4.7 shows a micrograph of a 16-bit pulse generator put on the test chip for verification. A T

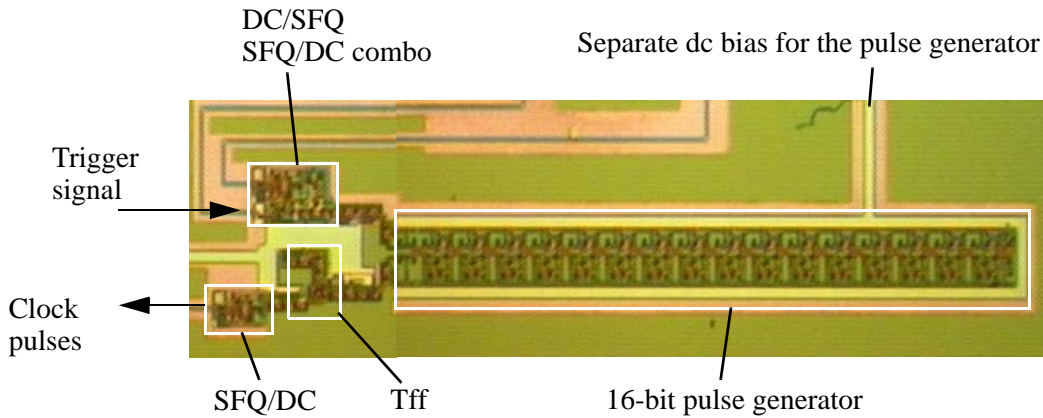


Figure 4.7 Micrograph of a 16-bit pulse generator with peripheral circuits on test chip.

flip-flop is connected to the output of the pulse generator to reduce the output frequency to one half. There is an additional built-in T flip-flop in the SFQ/DC converter following the Tff. So, with a spectrum analyzer with an upper frequency limit of 20 GHz, the pulse generator can be verified up to 80 GHz. As marked in the micrograph, the pulse generator's dc bias voltage can be adjusted independently. So its dc bias full operating range and corresponding clock frequency can be tested without being limited by the peripheral circuits' dc bias margins.

4.3 Data-Driven Self-Timed (DDST) Shift Registers

The DDST shift registers are used to store the input data used by the CUT in the high-speed operations and to record the high-speed operation result which we can read off-chip at low-speed. Fig. 4.8 shows the block diagram of a 4-bit DDST shift register. It consists of a front stage to recover timing information, three stages of single-rail shift registers (SR) and a D flip-flop at the end to regenerate dual-rail outputs. The SR and D flip-flop are clocked gates. The front stage combines the dual-rail input data to generate a local clock for the SR and the D flip-flop. Meanwhile,

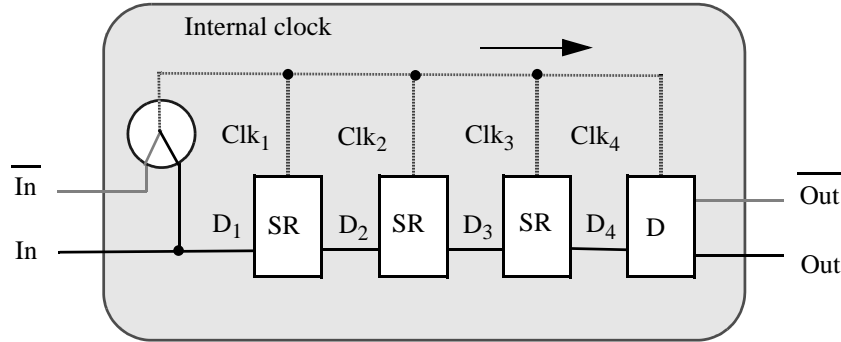


Figure 4.8 Block diagram of a 4-bit DDST shift register. Solid dots are pulse splitters (PS).

the positive input data propagate to the first SR. In each clock cycle, the data are shifted right one bit. The last stage is a D flip-flop instead of a single-rail SR, where the dual-rail outputs are recovered. With the data-driven self-timing strategy, the difficulty of generating and distributing a very high-speed global clock is avoided. But within the DDST system careful timing is still very important for the circuit to achieve good dc bias margin at 50 GHz. We will introduce each building block and its timing concern in the following sections. Since the D flip-Flop and the SR both are synchronous circuits, the data signal has to arrive a t_{setup} before the clock signal and a t_{hold} after the clock signal as illustrated in Fig. 1.16(b). The required setup and hold time of the D flip-flop and the SR are carefully characterized within the entire dc bias range. The previous stage clock-to-data delay is calculated to compare with the setup/hold time requirement to make sure enough timing margins are guaranteed. The simulation results on a 4-bit shift register and a two-stage cascaded 4-bit shift register will also be reported at the end. One limitation of the DDST shift register is that it requires dual-rail data.

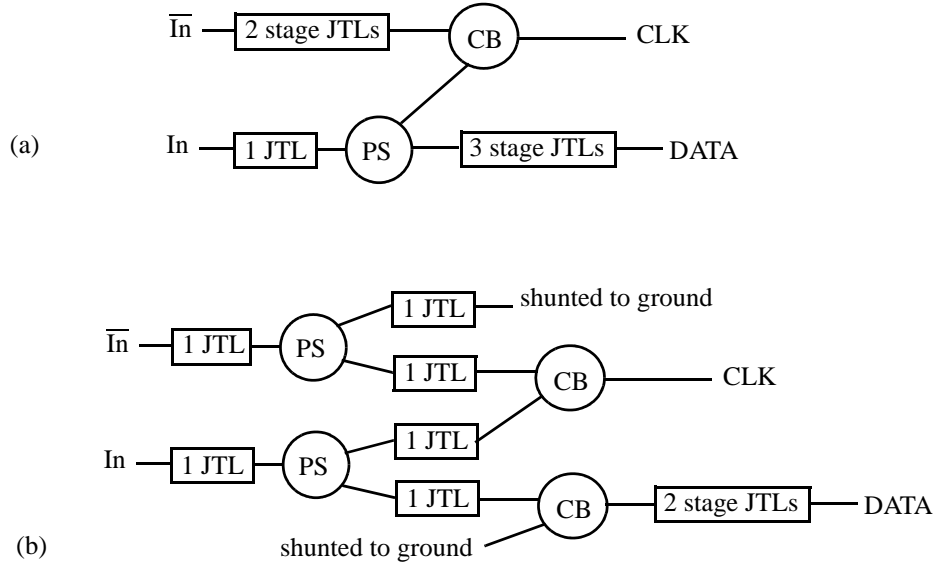


Figure 4.9 Block diagrams of the front stage in the DDST shift register. (a) Current implementation. (b) Possible improvement.

4.3.1 Front Stage

Shown in Fig. 4.9a is the circuit block diagram of the currently implemented front stage in the DDST shift register. The complementary inputs In and \bar{In} are combined by a confluence buffer (CB) to generate the local clock signal CLK. One extra JTL stage is inserted between \bar{In} and CB to match the delay of the PS. Three-stage JTLs are used before DATA to achieve proper timing between CLK and DATA. Fig. 4.10 shows the post-layout circuit schematics of the components in the front stage. The inductance values are extracted from the layout. Parasitic inductance values are also included. The dc bias current values in parentheses are at $V_{bias} = 5.75$ mV. The CB is the critical block in the front stage, and it has dc bias margins of (4.25 mV, 7.65 mV), (-26.1%, 33.0%). The dc bias margins of the front stage from the post-layout simulation are (4.6 mV, 7.6 mV), (-20%, 32.2%). The lower-end dc bias margin of the front stage is worse than that of the CB. One possible reason is that the delay difference between the data In path and \bar{In} path gets larger at

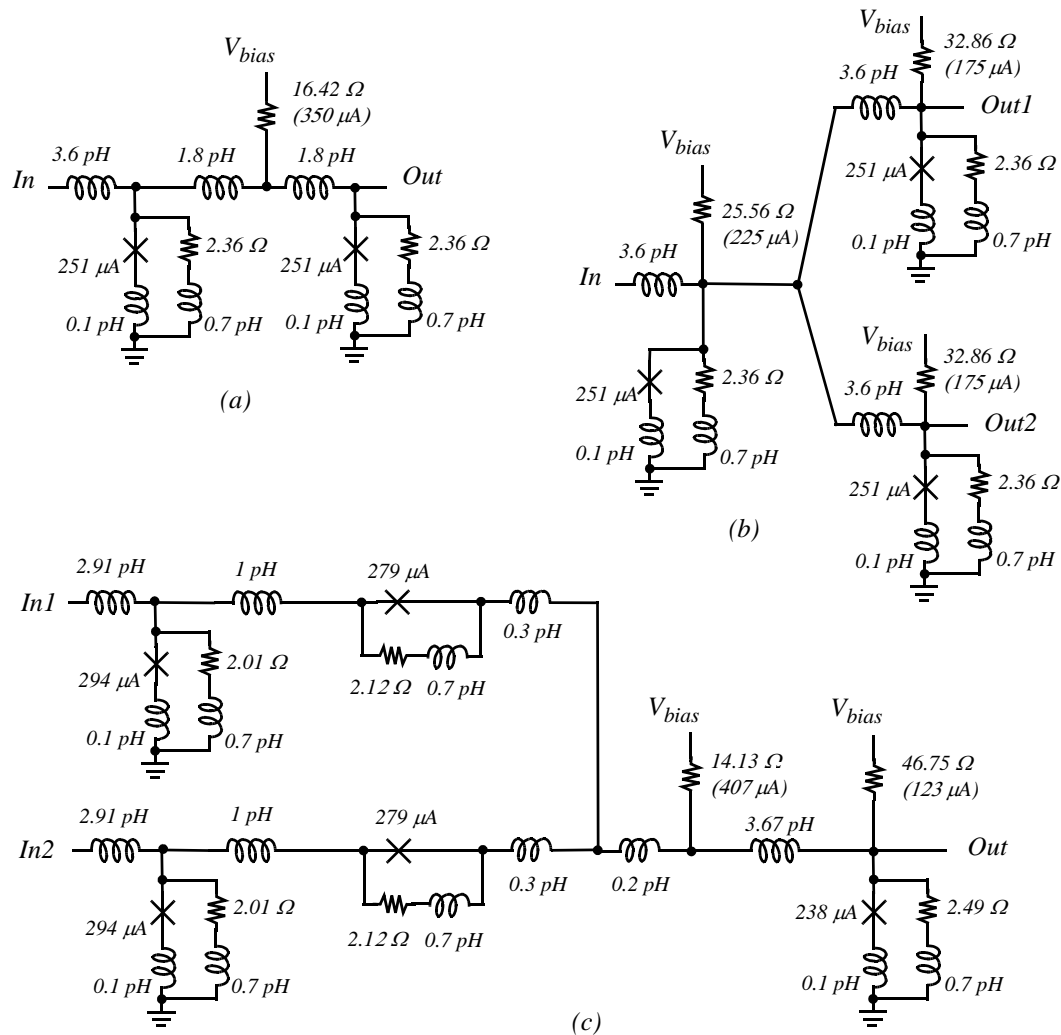


Figure 4.10 Post-layout circuit schematics of the components in the front stage.

(a) JTL (b) PS (c) CB.

lower dc bias voltage, which causes CB to fail at 4.6 mV instead of 4.25 mV. The delay from CLK to DATA is a function of the dc bias voltage. Table 4-1 shows the CLK to DATA delay from the post-layout simulation.

TABLE 4-1 CLK to DATA delay of the front stage as a function of the dc bias voltage.

CLK to DATA delay (ps)	dc bias voltage (mV)
4.5	7.6
4.1	5.75
1.2	4.6

Shown in Fig. 4.9b is a block diagram of the input stage with some timing improvement. Instead of using one stage of JTL to match the PS delay, the same PS is inserted in the \bar{I}_{in} path for perfect delay matching. This approach can help increase the lower-end dc bias margin of the CB at 50 GHz, which is the bottleneck of the whole front stage. A CB is inserted in the DATA output path to match the CB delay in the CLK path. As a result, when dc bias voltage is decreased, the delay from CLK to DATA is increased, which is the timing condition preferred by the next stage. One JTL is inserted between PS and CB to improve slightly the circuit dc bias margins. Besides the timing adjustment, the dc bias level of CB is scaled to center its dc bias margins. The two bias resistors are changed from $14.13\ \Omega$ and $46.75\ \Omega$ as in Fig. 4.10 to $13.66\ \Omega$ and $45.19\ \Omega$. The new dc bias margins of the CB are (4.1 mV, 7.45 mV), (-28.7%, 29.6%) at 50 GHz, exactly the same as that of new improved whole front stage at 50 GHz. So we know the timing matching here helped to increase the circuit dc bias margin. The new delay from CLK to DATA from post-layout simulation is listed in Table 4-2.

TABLE 4-2 CLK to DATA delay of the improved front stage as a function of the dc bias voltage.

CLK to DATA delay (ps)	dc bias voltage (mV)
5.2	7.45
7.1	5.75
10.5	4.1

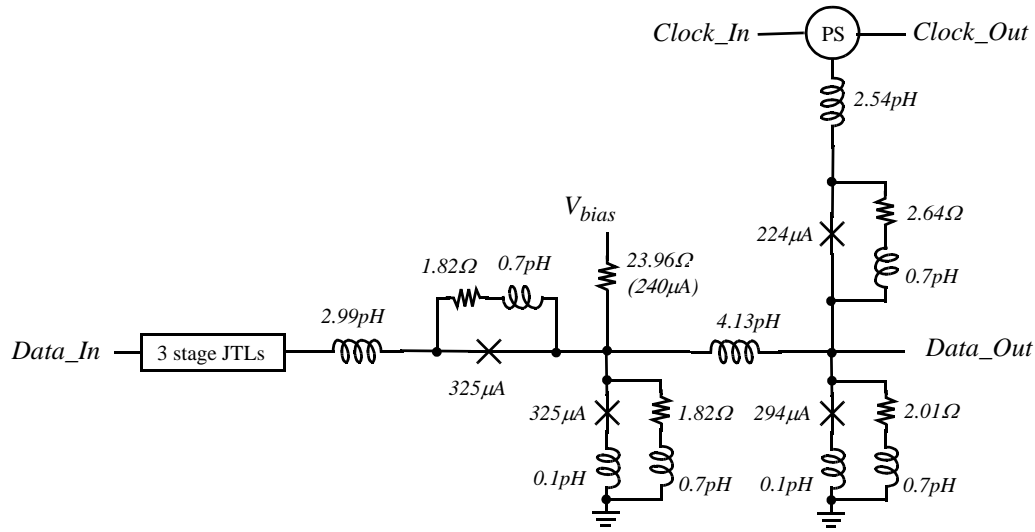


Figure 4.11 Post-layout circuit schematics of one stage SR.

The timing improvement is at the cost of more devices, area and power. As we will see later, the bottleneck of the whole DDST shift register is not the front stage, even without the timing improvement. So we did not implement the timing-improved version.

4.3.2 SR Stage

Fig. 4.11 shows one stage of the single-rail shift register (SR). The core of the SR is an RS flip-flop with the detailed post-layout parameters marked. The JTL and SP have the same circuit parameters as in Fig. 4.10. Between the clock pulses, incoming data set the state of the RS flip-flop. With the arrival of clock pulses, the RS flip-flop resets its state and generates output pulses accordingly. The JTLs are inserted to adjust timing. The PS is for clock propagation. The timing of the SR is designed to have one clock cycle latency.

Fig. 4.12 shows the two-dimensional operation range simulation result of one stage SR at 50 GHz. The horizontal axis is the dc bias voltage. The vertical axis is the delay from clock_in to data_in. At the nominal dc bias voltage 5.75 mV, the viable delay range is (-4.5 ps to 14 ps). For larger dc bias voltage up to 7.45 mV, the viable delay range is kept almost the same. But when the dc bias voltage is below 4.5 mV, the viable delay range starts to shrink. At 4.2 mV, the viable delay range is (0 ps to 17 ps). The minimum operable dc bias voltage is 3.9 mV, where the viable delay range is (4.5 ps to 12.5 ps). So we know the maximum achievable dc bias margins are (3.9 mV, 7.4 mV), (-32.2%, 28.7%) if we control the input delay within (4.5 ps to 12.5 ps). For delay less than 4.5 ps, the dc bias margin starts to shrink. When the delay is 0 ps, the dc bias margins shrinks to (4.2 mV, 7.4 mV), (-27.0%, 28.7%).

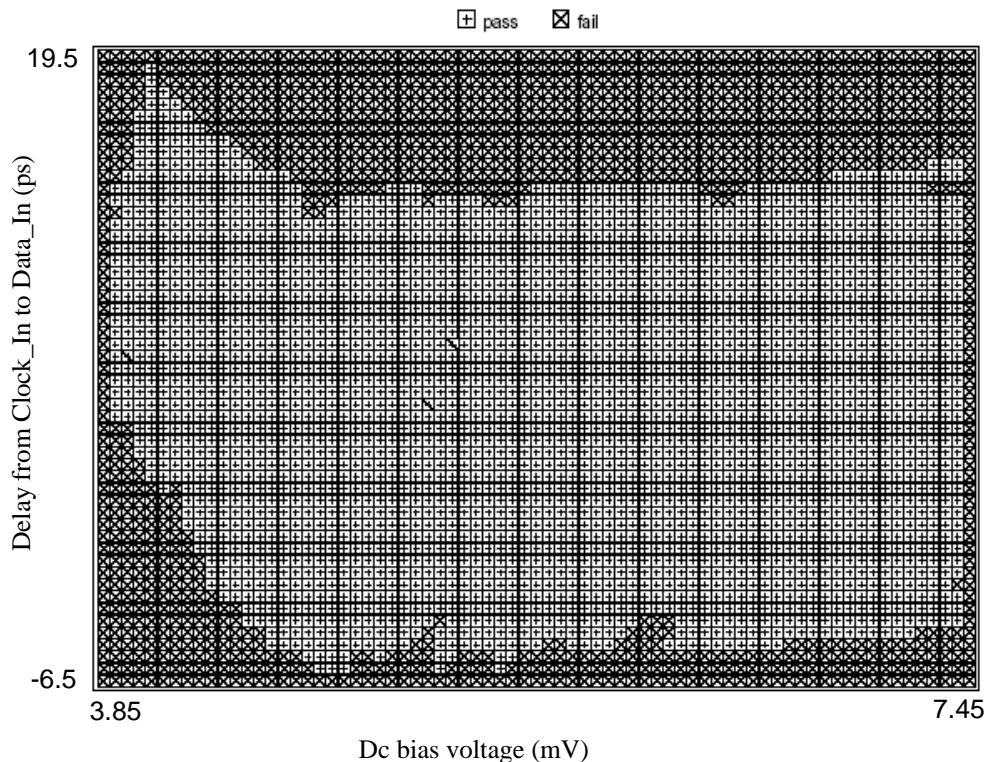


Figure 4.12 Two-dimensional operation range of a one-stage SR at 50 GHz.

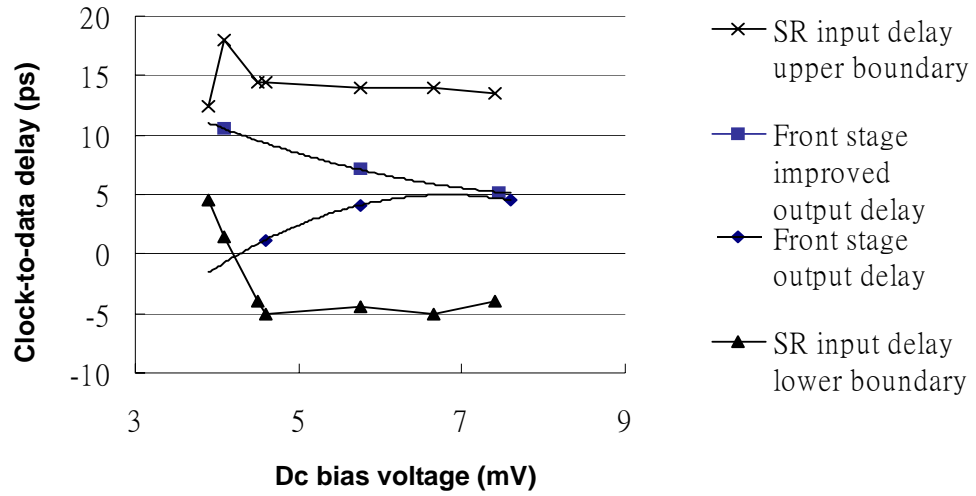


Figure 4.13 Timing at the input of the first SR in the DDST shift register at 50 GHz.

In Fig. 4.13, the output clock-to-data delays of the front stage in Table 4-1 and Table 4-2 are plotted and compared with the timing requirement at the input of the first SR. We can see that both the current design and timing-improved front stage satisfy the SR timing requirement within their own operable dc bias voltage range. However, the timing-improved version can extend its dc bias margin down to 3.9 mV, while the current version works only down to 4.6 mV. On the other hand, the smaller delay of the current version is actually preferred when we are trying to push the circuit to operate at speeds higher than 50 GHz. As long as 4.6 mV is not the bottleneck of the whole block, the current version has a satisfactory timing design.

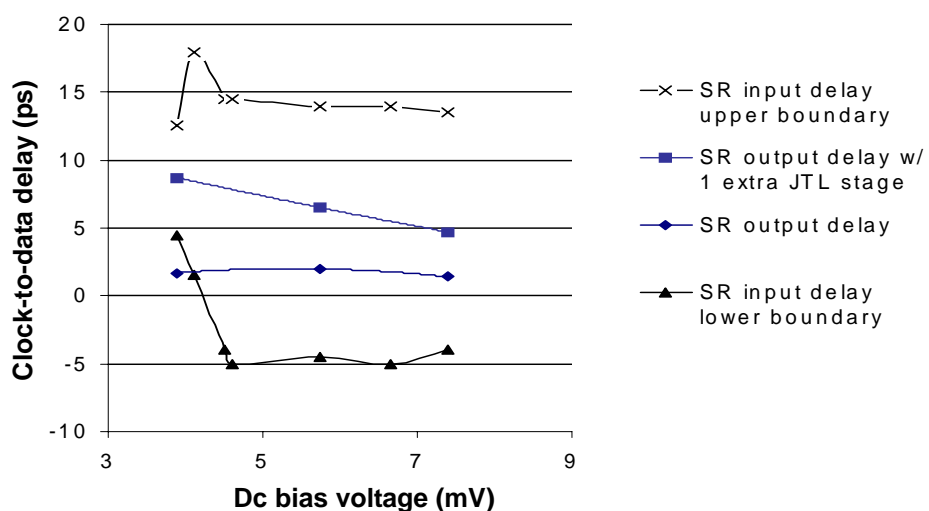
The timing when two SRs are cascaded is also checked. Table 4-3 lists the Clock_Out to Data_Out delay of one stage SR when its setup/hold time is well satisfied. The delay with one extra JTL inserted at the output is also listed for discussion. In Fig. 4.14, the delay from Table 4-3 is plotted in comparison with the timing requirement at the input of the SR. The current implemen-

TABLE 4-3 Clock_Out to Data_Out delay vs. dc bias voltage of one stage of SR.

Clock_Out to Data_Out delay (ps)		dc bias voltage (mV)
current implementation	w/ 1 extra JTL at the output	
1.4	4.7	7.4
2.0	6.5	5.75
1.7	8.7	3.9

tation satisfies the timing for dc bias voltage above 4.1 mV. With one extra JTL inserted at the output, the timing requirement is satisfied for the entire dc bias range.

Fig. 4.15 shows the two-dimensional operation range simulation results of three stages of cascaded SRs at 50 GHz. The maximum achievable dc bias margins are (4.55 mV, 7.3 mV), (-20.9%, 27.0%), which is much smaller than that of one stage SR (3.9 mV, 7.4 mV), (-32.2%, 28.7%). It does not improve with one stage JTL inserted at SR output. It means timing violation is not the reason for the circuit failure at 50 GHz at the low dc bias voltage. The interaction and interference among the clock pulses and data pulses could be the main reason for the failure. At the low dc bias

**Figure 4.14** Timing at the input of the 2nd and 3rd SR in the DDST shift register at 50 GHz.

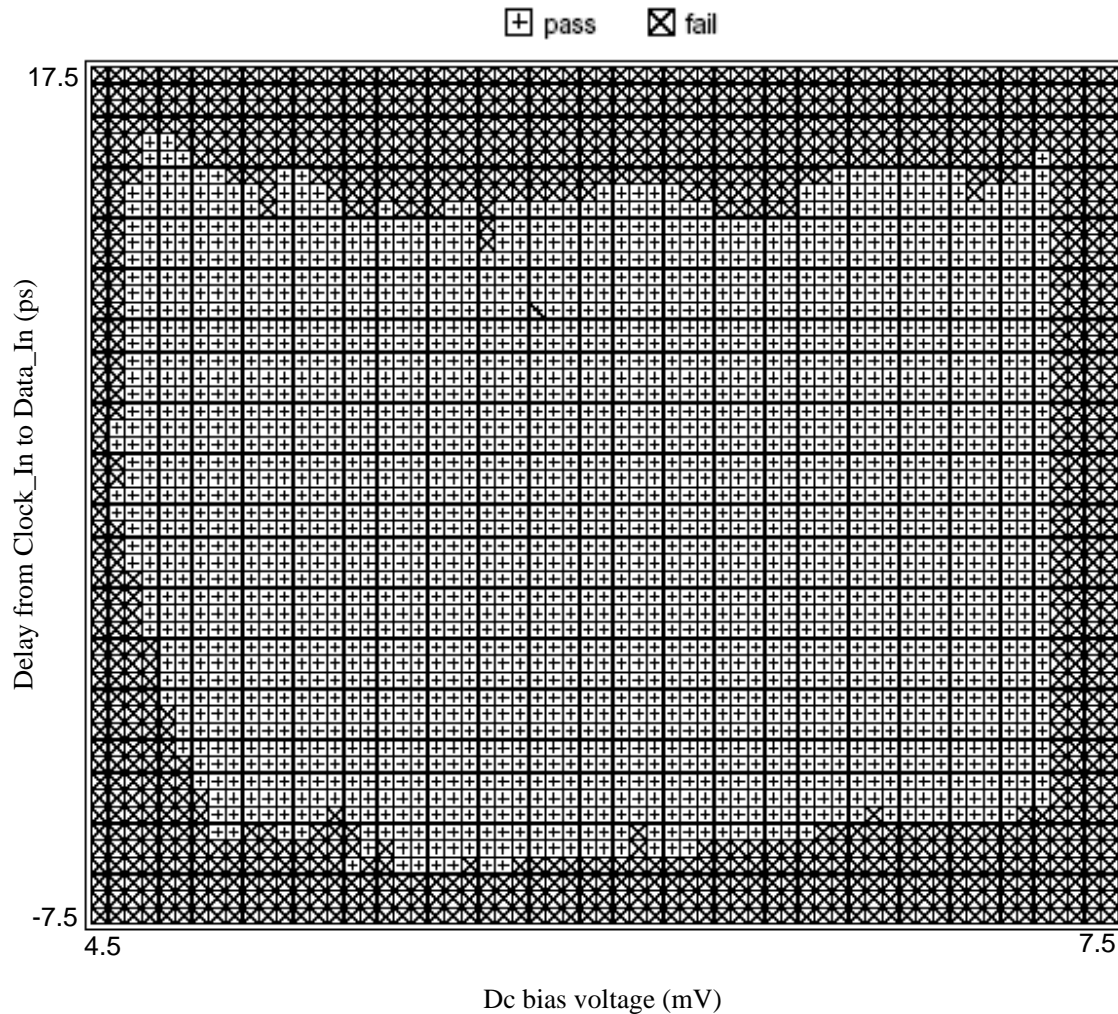


Figure 4.15 Two-dimensional operation range of 3-stage cascaded SRs at 50 GHz.

voltage, the junctions switch slower and the SFQ pulses start to smear out and interact with each other. An RSFQ digital gate such as an SR shows some analog nature. Its inputs and outputs do not have strict isolation. When multiple gates are put together, the dc bias margins are further reduced due to the interference among the signal pulses at 50 GHz. This is the bottleneck for the lower end dc bias margin for the entire DDST shift register. So the timing improvement of the front stage and SR is not necessary.

Some previous shift register design works were studied as references. [58][59][60][61].

4.3.3 D Flip-Flop

Fig. 4.16 shows the post-layout circuit schematics of the D flip-flop. This is the most difficult circuit block in the shift register due to the multiple junction-inductance loops involved to recover the dual outputs. The detailed operation of this circuit was discussed already in Section 1.3.2. Each incoming data pulse sets the internal state of the D flip-flop. The clock pulse resets the flip-flop and generates a pair of complimentary outputs. The pre-layout simulation with optimized circuit parameters, not including the parasitic inductances can achieve (-29%, 29%) dc bias margins. However, due to the complicated loops, with the parasitic inductances, the dc bias margin based on the original circuit parameters drops dramatically. Reoptimization is necessary. Since Wins can not model such complicated parasitic effects, the re-optimization was done manually. The parameters shown in Fig. 4.16 are the results of the reoptimization.

Fig. 4.17 shows the two-dimensional operation range of the D flip-flop at 50 GHz. The maximum achievable dc bias margins are (4.5 mV, 6.65 mV), (-21.7%, 15.7%), a substantial decrease from the pre-layout simulation results.

Fig. 4.18 compares the output clock-to-data delay of the SR with the timing requirement at the input of the D flip-flop. The current SR implementation satisfies the input timing requirement in the D flip-flop's entire operable dc bias range. Removing a half stage of JTL from the data input of the D flip-flop may improve the timing margin further.

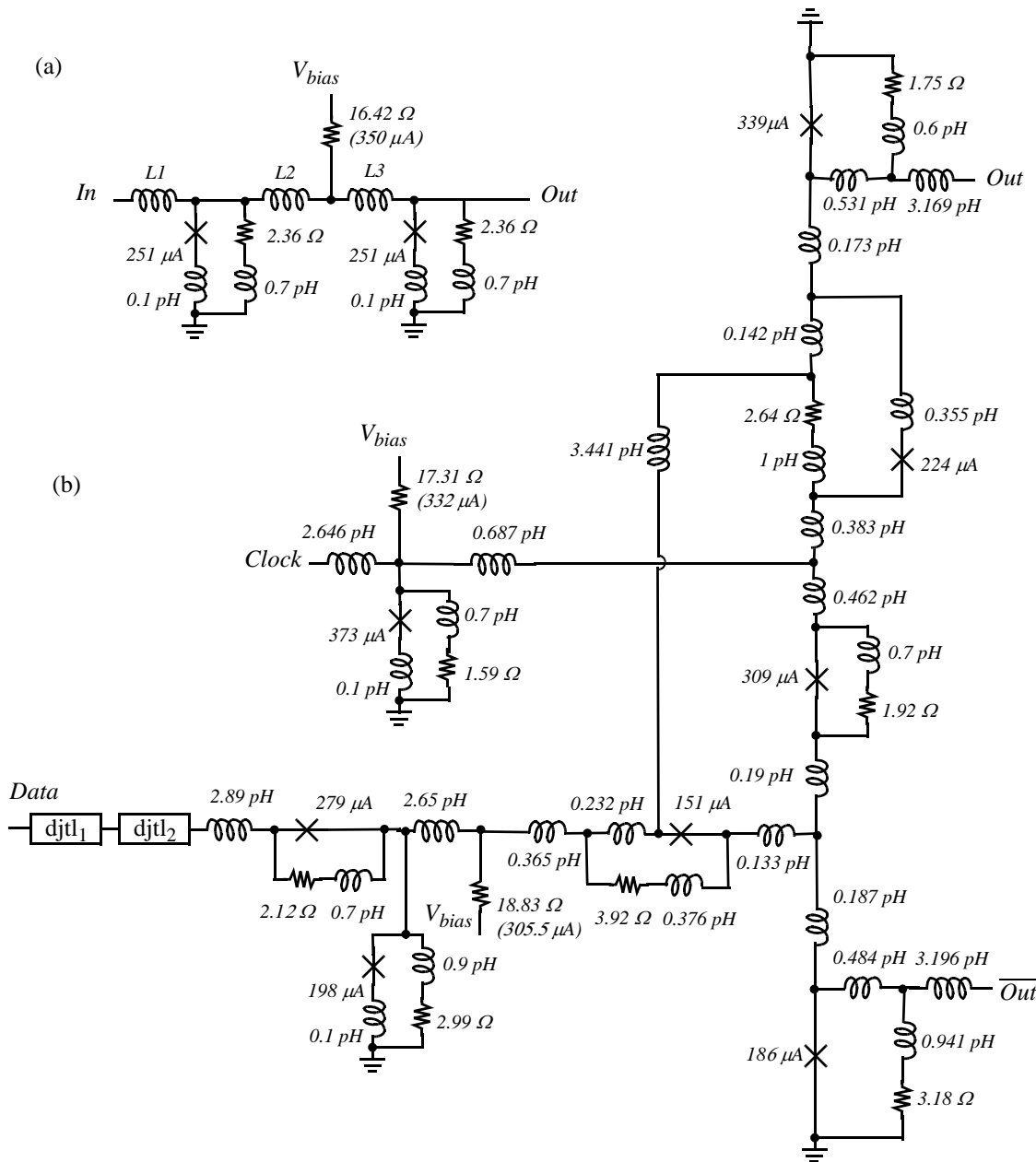


Figure 4.16 Post-layout schematics of (a) djtl and (b) the D flip-flop in the DDST shift register.
 $L_1 = 4.5 \text{ pH}$, $L_2 = L_3 = 2.3 \text{ pH}$ in djtl₁. $L_1 = 4.635 \text{ pH}$, $L_2 = L_3 = 2.33 \text{ pH}$ in djtl₂.

4.3.4 4-bit DDST Shift Register

A 4-bit DDST shift register can be built from the blocks discussed above. The block diagram was shown in Fig. 4.8. The operation was explained at the beginning of Section 4.3. It is a self-

timed circuit with internal synchronous blocks. For the clock distribution inside the shift register, the concurrent timing strategy is used, i.e., data and clock flow in the same direction. Compared to the counter-current timing, where data and clock flow at opposite direction, concurrent timing is more favorable for high-speed operation since the delay along the data path is partially matched with the delay along the clock path. With this strategy and careful timing control of each stage, the correct functioning of the 4-bit DDST shift register at 50 GHz is achieved. Fig. 4.19 shows the simulation waveforms of the 50 GHz operation of the 4-bit DDST shift register. $\text{In}/\overline{\text{In}}$ and $\text{Out}/\overline{\text{Out}}$ are the complementary inputs and outputs of the DDST shift register. D_1 and Clk_1 are the data and clock inputs to the 1st SR. D_4 and Clk_4 are the data and clock inputs to the D flip-flop. The CLK_4

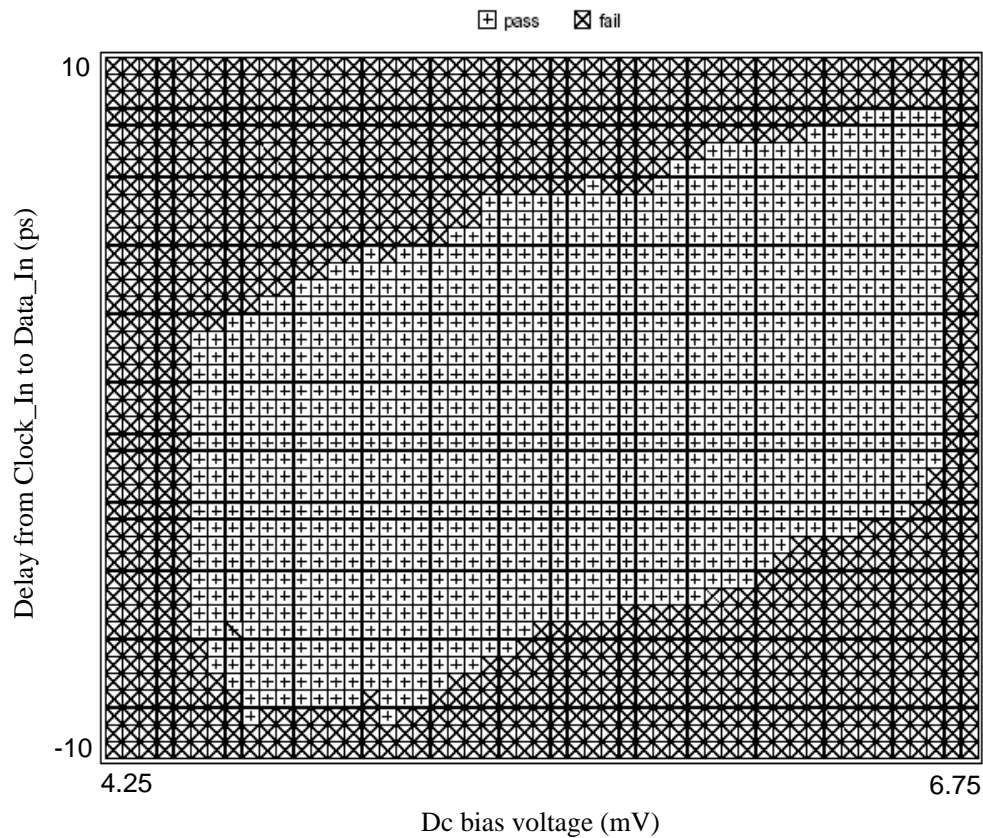


Figure 4.17 Two-dimensional operation range of the D flip-flop at 50 GHz.

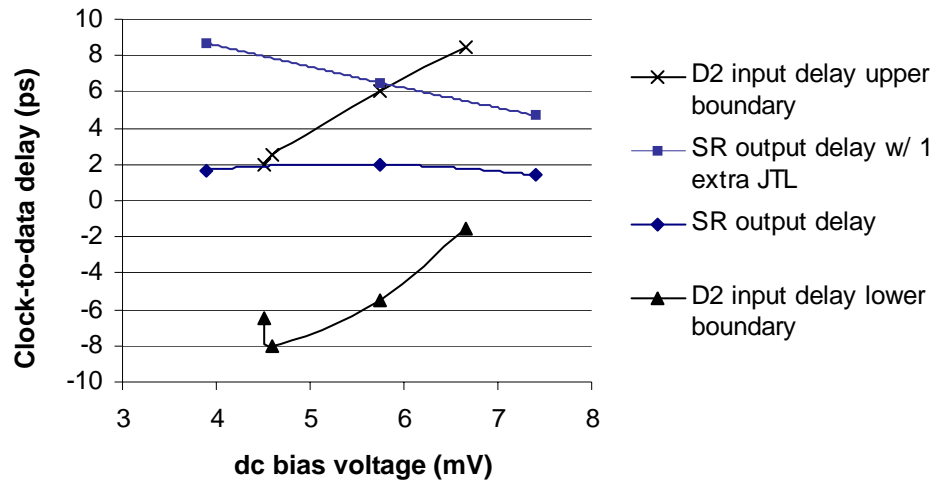


Figure 4.18 Timing at the input of the D flip-flop in the DDST shift register at 50 GHz.

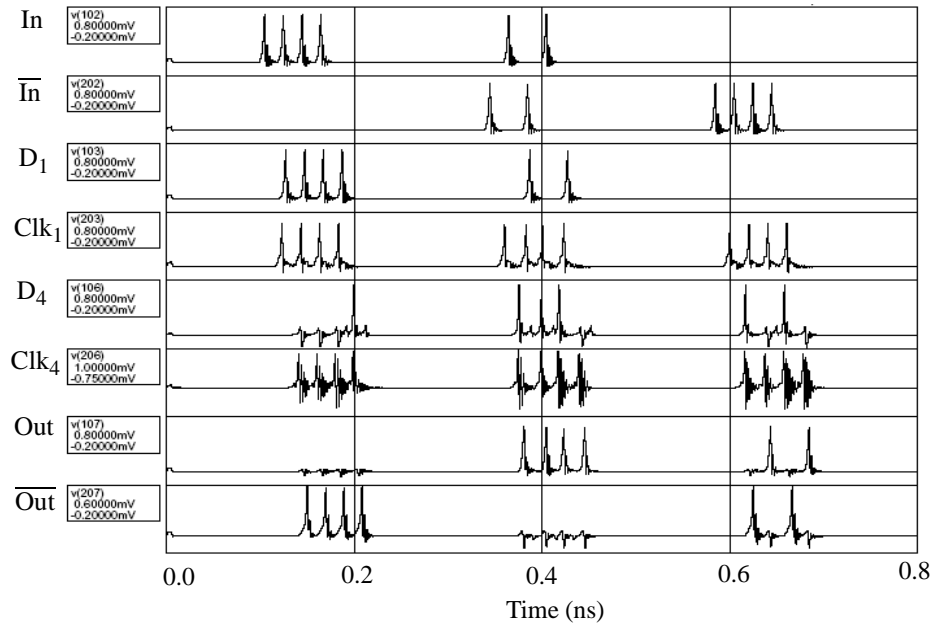


Figure 4.19 Simulation waveforms of the 4-bit DDST shift register with 50 GHz operations at nominal dc bias voltage 5.75 mV.

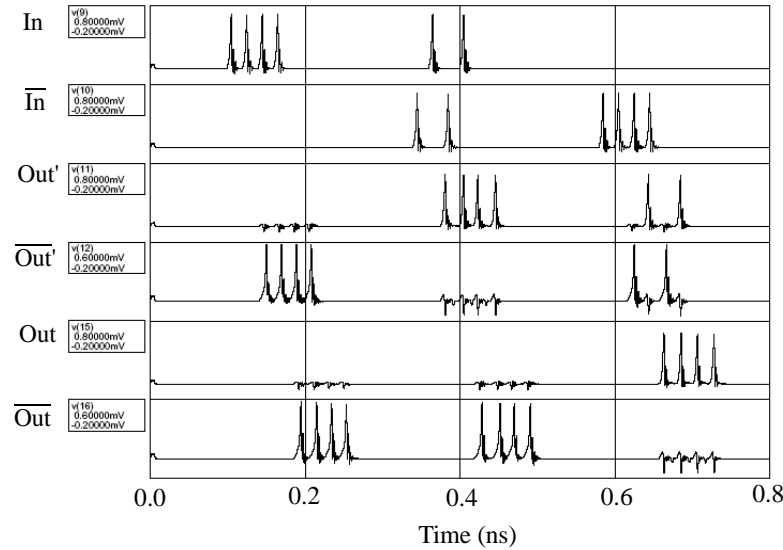


Figure 4.20 Simulation waveforms of two cascaded 4-bit shift registers with 50 GHz operations at nominal dc bias voltage 5.75 mV.

pulse ringing is the effect which limits the lower-end dc bias margin of the 4-bit DDST shift register. $\text{Out}/\overline{\text{Out}}$ are the delayed versions of $\text{In}/\overline{\text{In}}$ with a 4-clock-cycle latency. One virtue of the circuit is that the data-clock relative delay variation will not accumulate over stages since each stage is clocked, which is useful to combat process variations. The dc bias margins of the 4-bit DDST shift register are (4.7 mV, 6.65 mV), (-18.3%, 15.7%).

An 8-bit DDST shift register can be easily constructed from two cascaded 4-bit DDST shift registers. Fig. 4.20 shows the simulation waveforms of two cascaded 4-bit DDST shift registers with 50 GHz operation. $\text{In}/\overline{\text{In}}$ are the complementary inputs. $\text{Out}'/\overline{\text{Out}'}$ are the outputs of the 1st DDST shift register. $\text{Out}/\overline{\text{Out}}$ are the outputs of the 2nd DDST shift register. $\text{Out}'/\overline{\text{Out}'}$ are the delayed version of $\text{In}/\overline{\text{In}}$ with a 8-clock-cycle latency. The dc bias margins are (4.75 mV, 6.65 mV), (-17.4%, 15.7%).

Table 4-4 lists the dc bias margin of the individual blocks, the 4-bit shift register, 2-stage cascaded 4-bit shift registers and the whole testing system which will be discussed in the next section.

TABLE 4-4 Summary of the dc bias margin of the 4-bit DDST shift register and its components at 50 GHz.

Circuit	dc bias margin	
front stage	(4.6 mV, 7.6 mV)	(-20%, 32.2%)
1SR	(4.2 mV, 7.4 mV)	(-27.0%, 28.7%)
3SRs	(4.7 mV, 7.3 mV)	(-18.3%, 27.0%)
D flip-flop	(4.5 mV, 6.65 mV)	(-21.7%, 15.7%)
4-bit DDST shift register	(4.7 mV, 6.65 mV)	(-18.3%, 15.7%)
Two 4-bit DDST shift registers	(4.75 mV, 6.65 mV)	(-17.4%, 15.7%)
whole testing system w/o DUT	(4.3 mV, 6.65 mV)	(-25.2%, 15.7%)

Comparing the dc bias margin of the 4-bit DDST shift register with that of the individual blocks, we can see the upper margin is limited by the D flip-flop and the lower margin is limited by SFQ pulse interaction in the 3-stage cascaded SRs. It would be hard to build an 8-bit DDST shift register from 7 SRs and 1 D flip-flop while maintaining the dc bias lower-end margin since the interaction would be worse. However, if the 8-bit DDST shift register is built from two cascaded 4-bit DDST shift registers, the dc bias margin remains almost the same as for the single 4-bit DDST shift register.

4.4 Whole System

Shown in Fig. 4.21 is the block diagram of the whole testing system without the DUT. It mainly consists of a 4-bit pulse generator, two 4-bit DDST shift registers, a CB and JTLs between the blocks. The CB combines the on-chip high-speed clock Clk_hs and $\overline{\text{In}}$ data to feed the input $\overline{\text{In}'}$ of the following DDST shift register, while data In propagates through a series of JTLs to the input In' of the DDST shift register. The delay of the In path and that of $\overline{\text{In}}$ path are balanced.

The testing system can be verified in different ways. The low-speed function of the two DDST shift registers can be verified by muting the pulse generator. Fed with complementary data at $\text{In}/\overline{\text{In}}$ from a pattern generator, the DDST shift registers can be tested from 1 kHz to a few gigahertz. For testing above 20 GHz, the pattern generator is programmed to assert the trigger signal in between low-speed $\text{In}/\overline{\text{In}}$ data sets. So four consecutive high-speed pulses are generated and merged to $\overline{\text{In'}}$. Those push the 4-bit data stored in the input DDST shift register to transfer to the output DDST shift register at high-speed. The results in the output DDST shift register can be read out at low-speed by feeding the next input data pattern. That simultaneously resets the output DDST shift register to all “0”s.

Fig. 4.22 shows the simulation waveforms of the testing system with the mixed 50 GHz and 20 GHz operation. 20 GHz is chosen instead of a very low speed such as 1 kHz, which is often used in the lab testing, to save simulation time. Three sets of 20 GHz complementary data "1 1 1 1", "0 1 0 1", "0 0 0 0" are fed through In/ \overline{In} . Two trigger pulses are programmed between the three data sets. Each trigger pulse produces four 50 GHz clock pulses at Clk_hs. As the signals propagate, In' is simply a delayed version of In. \overline{In}' is the merge of \overline{In} and Clk_hs. The first set of data '1 1 1 1' is loaded into the input shift register at 20 GHz. When the four 50 GHz clock pulses arrive at \overline{In}' , the

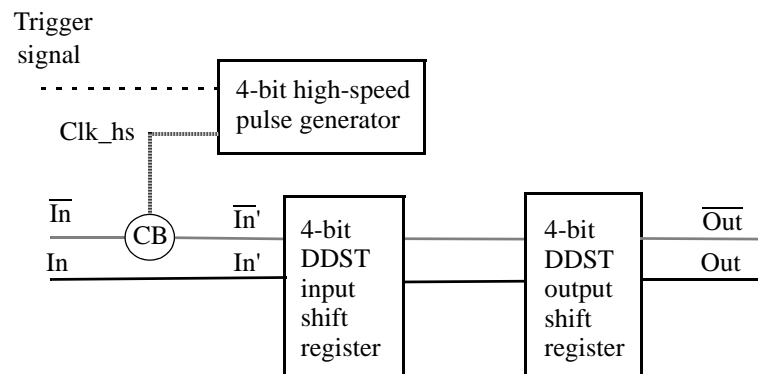


Figure 4.21 A block diagram of the DDST on-chip high-speed testing system w/o DUT.

dataset “1 1 1 1” is pushed to the output shift register at 50 GHz. When the second set of data “0 1 0 1” is loaded into the input shift register, the first set of data is shifted out at $\text{Out}/\overline{\text{Out}}$ at 20 GHz. There is an eight-clock-cycle latency from $\text{In}'/\overline{\text{In}'}$ to $\text{Out}/\overline{\text{Out}}$ independent of the clock rate. In turn, the second burst of high-speed clock pulses pushes the second set of data to the output shift register at 50 GHz. The third set of low-speed data pushes the second set of data to the $\text{Out}/\overline{\text{Out}}$ at 20 GHz. Overall, $\text{Out}/\overline{\text{Out}}$ is the delayed version of $\text{In}'/\overline{\text{In}'}$ with an 8-clock-cycle latency. In laboratory testing, 1 kHz data instead of 20 GHz data are usually programmed in a pattern generator. The 50 GHz burst at $\overline{\text{Out}}$ can't get off chip due to the limited bandwidth. So only the 1 kHz transitions can be observed on the oscilloscope. By verifying the correct 1 kHz output, we can infer the high-speed operation in between is correct. The simulated dc bias margins of the whole testing system are (4.3 mV, 6.65 mV), (-25.2%, 15.7%). The reason why the whole testing system has an wider

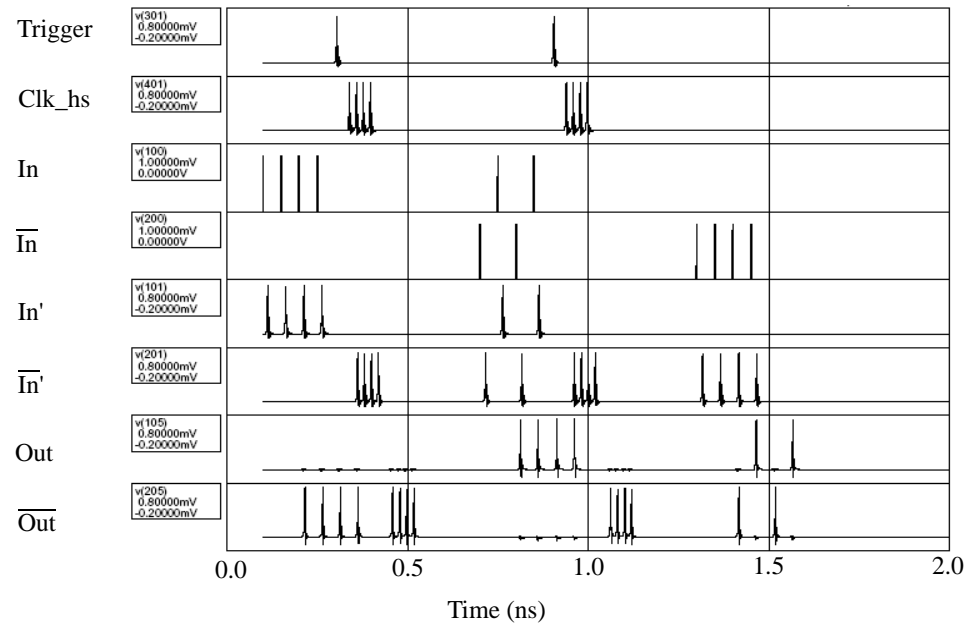


Figure 4.22 Simulation waveforms of the high-speed testing system with mixed 50 GHz and 20 GHz operation at the nominal dc bias voltage 5.75 mV.

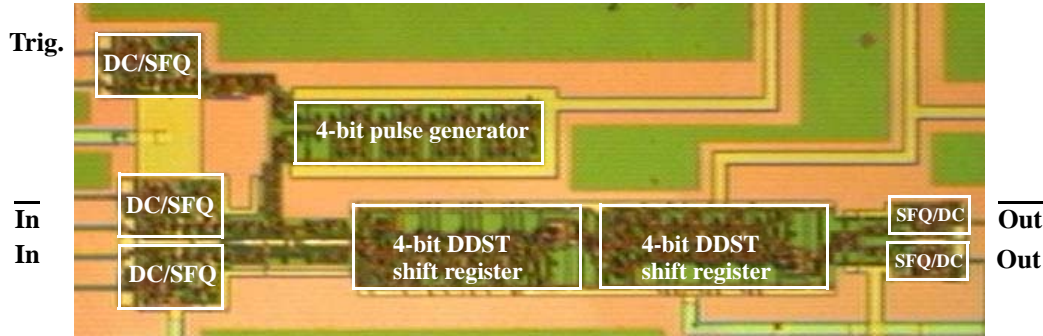


Figure 4.23 A micrograph of a 50 GHz testing system in 6.5 kA/cm^2 process.

lower-end dc bias margin than that of the 4-bit DDST shift register is that only 4 cycles of consecutive 50 GHz operations are required in between the 20 GHz operations, which relaxes the interference between the high-speed SFQ pulses.

Fig. 4.23 shows a micrograph of the test system for 6.5 kA/cm^2 process. DC/SFQ and SFQ/DC converters are added as the interface circuits. A separate dc bias is applied on the pulse generator to be able to control the speed of the clock pulses independently. This test chip was not tested due to the failure of the fabrication process.

But recently, a similar test system was implemented by others using the NEC Nb process and was verified successfully up to 50 GHz [62].

CHAPTER 5

Test Results

5.1 Testing Setup

5.1.1 Special Considerations

Testing superconductor circuits has some special considerations. First, it requires cooling. Chips are mounted inside a probe head and immersed in the liquid helium to be cooled to 4.2 K. The cables inside the probe body connect the signal pads inside the probe head to the BNC or SMA connectors on the other end of the probe for testing.

Second, superconductor circuits are very sensitive to flux trapping. The trapped flux is accompanied by a circulating current in the superconductor loop. Existence of stray magnetic field during the circuit cooling to the superconductor state or applying large transient current can cause flux trapping. There are several ways to combat this issue. A double layer magnetic shield is applied enclosing the probe head to prevent the earth magnetic field entering the chip. Another layer magnetic shield is built-in with the liquid helium dewar used for this work. All the shields need to be degassed to remove the residual magnetic field from the shields themselves. The degaussing of the cylinder shield for the probe head can be done using an external degasser. With the degasser

turned on, drag the cylinder shield through the center of the deguasser coils and slowly move away from the deguasser until the field is weak enough. For the inner layer of the double layer shield, the degaussing is done in-situ with the existence of the outer shield. Coils are wrapped around the inner shield. Exponentially decaying ac current is supplied to coils to generate a decaying magnetic field for degaussing. With proper degaussing, the magnetic field can be reduced to about 1 mG level inside the double shield. Degaussing needs to be done before the chip is cooled. External cable connections should be done before cooling to avoid unnecessary current spikes. There is a big blue dewar in our laboratory. The magnetic shield is wrapped with coils. With proper degaussing, the magnetic field can be reduced to about 1 μ G in the sweet spot. The sweet spot range is about 10 inch along the vertical axis. That small range and the fast evaporation of the liquid helium in this dewar make it not very useful practically. The magnetic shield in other dewars used for this project can not be degaussed in-situ. The testing doesn't show better results or less flux trapping with the big blue dewar. With all the effort, flux trapping is still unavoidable from time to time. Once it is trapped, the only way to remove it is to heat the chip or lift the probe out of helium for the chip to warm up by itself to return to normal conducting state. Adding moats (slots cut from ground planes) surrounding circuits on-die proved an effective approach [63]. For a 5 mm x 5mm chip, 1 mG magnetic field, $BA/\Phi_0 = 1 \text{ mG} \times 5 \text{ mm} \times 5 \text{ mm} / (20.7 \text{ G } \mu\text{m}^2) = 1208$. That is one flux quantum for every $20,695 \mu\text{m}^2$, or $144 \mu\text{m} \times 144 \mu\text{m}$. The area enclosed and protected by each moat should be smaller than this value.

Third, electrical shielding and impedance matching are very important to measure the high-frequency low-voltage signals. Two kinds of probes are used in our testing, low-speed probe and high-speed probe. The low-speed probe has 40 signal pads and four ground pads. The 40 signal pads are connected to the centers of the 40 BNC connectors. The four ground pads are connected to the BNC connector grounds and also connected to the metal shield covering the signal wires

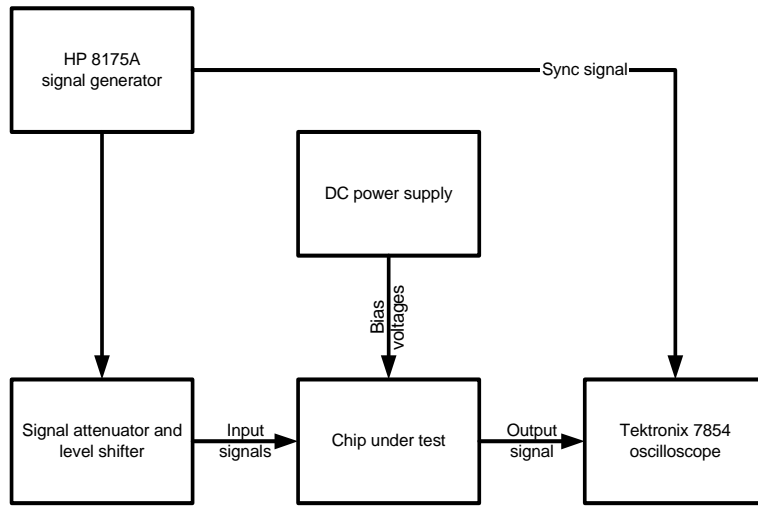


Figure 5.1 The equipment setup for the low-speed testing experiment.

inside the probe body. The high-speed probe has 24 signal pads. The 24 signal pads are connected to the centers of the 24 SMA connectors on the other end. For each signal line, it has its own ground shielding to form 50Ω impedance transmission line. On the probe head, co-planar wave guide layout is done to keep 50Ω impedance matching.

5.1.2 Low-Speed Testing Setup

Fig. 5.1 shows a typical low-speed testing setup. The input data patterns are programmed and generated by HP 8175A digital signal generator. The signal amplitude and offset can be further adjusted by the attenuator and level shifter to meet the requirement of the DC/SFQ circuit on-die. The dc power supply sets the test chip bias voltages. Output waveforms typically of $100 \mu\text{V}$ amplitude are observed by a Tektronix 7854 oscilloscope. A sync signal is sent from the signal generator to the oscilloscope as the trigger signal. The low-speed signal data rate is in the range of 1 kHz to a few hundred kilohertz, and its amplitude is about 100 mV with some negative offset voltage. The low-speed testing is used to confirm the circuit functionality.

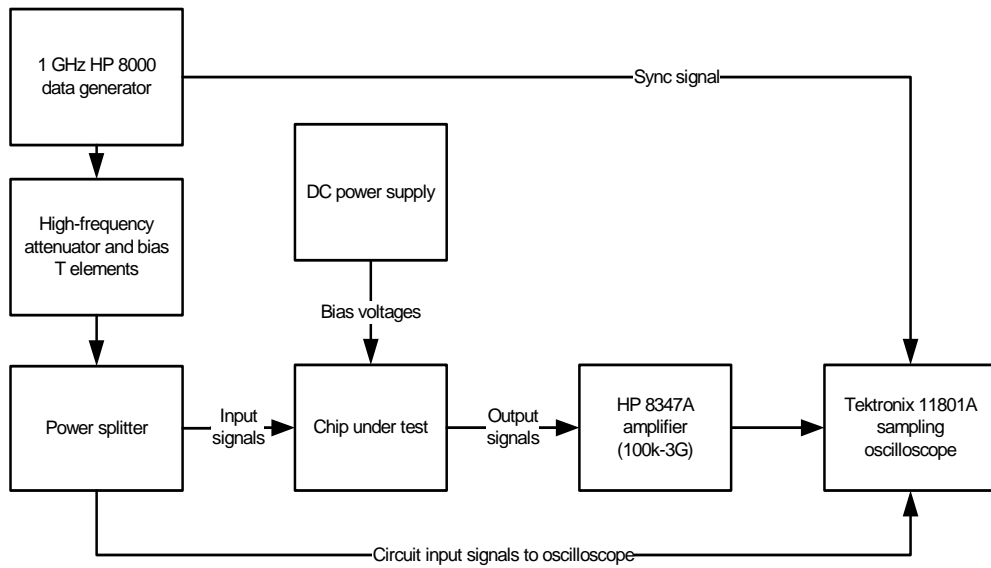


Figure 5.2 The equipment setup for medium-speed testing.

5.1.3 Medium-Speed and High-Speed Testing Setup

Fig. 5.2 shows a typical medium-speed testing setup. Data patterns with frequency up to one gigahertz can be programmed and generated by the HP 8000 data generator. The high-speed attenuator and bias T elements can be used to further adjust the input signals amplitude and offset. The input signal requirement is the same as in the low-speed test. The high-speed output signals are pre-amplified from 100 μ V level to a few mV level and then observed at the Tektronix 11801A sampling oscilloscope which has bandwidth of 20 GHz. The noise level of the sampling oscilloscope is about 2 mV. So the pre-amplification of the output signals is required. Another technique to observe the small signal on the sampling oscilloscope is by averaging. This way the noise from the amplifier is averaged out while the signal remains. Signal-to-noise-ratio (SNR) is improved by the square root of the number of averaging. The power splitters can be used to probe input signals and observe them on the oscilloscope. This setup can be used to test circuits from tens of megahertz up to one gigahertz.

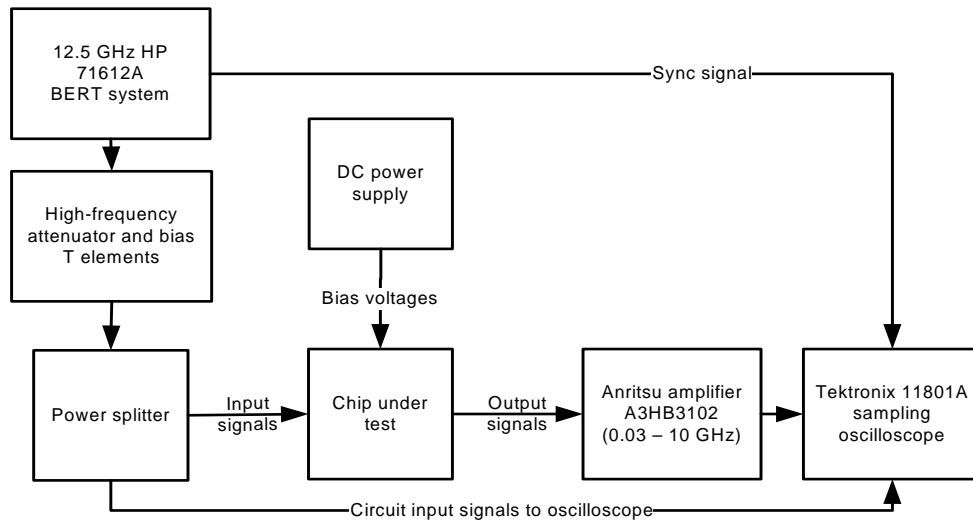


Figure 5.3 The equipment setup for high-speed testing.

Fig. 5.3 shows a high-speed setup. The HP 71612A BERT system can generate up to 12.5 GHz NRZ random data pattern and 12.5 GHz clock outputs. The high-speed output signals are amplified by a wide-band Anritsu amplifier (gain 28 dB, BW 0.03 - 10 GHz) to a few mV and observed at the Tektronix 11801A sampling oscilloscope. This setup can verify circuit up to 10 GHz.

5.2 Testing Results

5.2.1 MUX Testing Results

5.2.1.1 Low-Speed Testing Results of a 2:1 MUX

Shown in Fig. 5.4a is the micrograph of a 2:1 MUX fabricated in HYPRES 1 kA/cm² Nb process. The size of circuit is approximately 700 μ m x 700 μ m.

Shown in Fig. 5.4b are the measured output waveforms at 250 kHz. The input patterns are not shown here. Input₁ is “0 0 0 0” at 125 kHz; Input₂ is “1 0 1 0” at 125 kHz. So the output signals should be, Output “0 1 0 0 0 1 0 0” at 250 kHz and $\overline{\text{Output}}$ “1 0 1 1 0 1 1” at 250 kHz. As

explained in Section 1.3.4, in each clock cycle, a transition in the output waveform means “1”; no transition means “0”. Voltage levels do not represent “0” and “1”. Other input patterns not shown here were also tested with success.

The measured dc bias margins are (-7%, 7%).

5.2.1.2 Medium-Speed and High-Speed Testing Results of a 2:1 MUX

Shown in Fig. 5.5 are 5 MHz testing results for the MUX using setup in Fig. 5.2. The input signals Clk, Input₁, Input₂ are normal RZ patterns, observed on the oscilloscope before entering the test chip. Clk is at 5 MHz rate. Input₁ is a “1 1 1 1 1” pattern at 2.5 MHz. Input₂ is an all-zeros pattern, not shown in the figure. So the output is a “1010101010” pattern. $\overline{\text{Output}}$ is a complementary “0101010101” pattern. Again, transitions in the output waveforms mean “1”.

Shown in Fig 5.6 are testing results of the same test chip at 3.5 GHz using setup as in Fig. 5.3. We observed correct functions with two different input patterns. Fig. 5.6a has the same input pat-

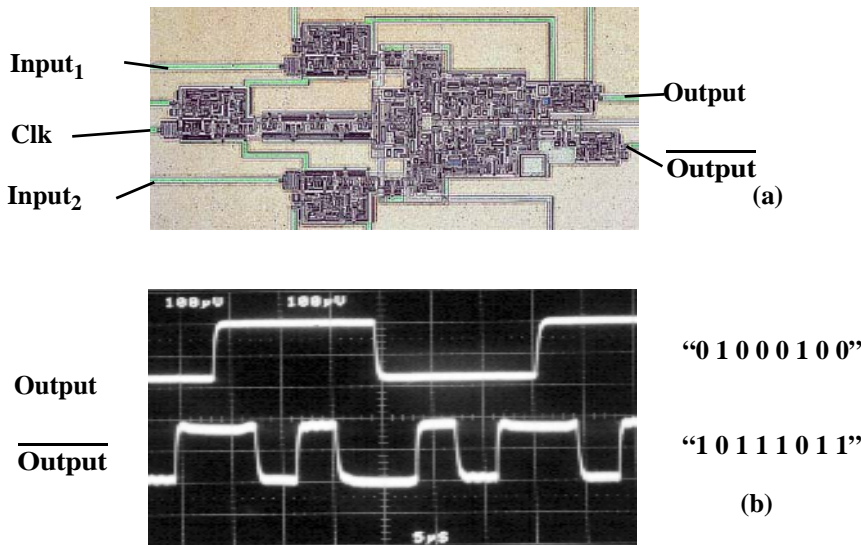


Figure 5.4 Testing results of a 2:1 MUX at 250 kHz. (a) Micrograph of a 2:1 RSFQ MUX. (b) Output waveforms. 100 μ V/div on y-axis, 5 μ s/div on x-axis.

terns as in Fig. 5.5 at 3.5 GHz clock rate. Fig. 5.6b has Input₁ “1 1 1 1 1” at 1.75 GHz and Input₂ “1 1 1 1 1” at 1.75 GHz. The output data patterns are Output “1111111111” at 3.5 GHz, $\overline{\text{Output}}$ “0000000000” at 3.5 GHz.

The DC bias margins in these measurements are very small, probably due to flux trapping. These measurements were performed about two years after the low-speed testing was done. Material degradation could be one reason causing the chips to be prone to flux trapping.

5.2.2 DEMUX Testing Results

5.2.2.1 Low-Speed Testing Results of a 1:2 DEMUX

Shown in Fig. 5.7 is the testing waveform of the 1:2 DEMUX shown in Fig. 3.8. It's a 20 GHz design fabricated in the HYPRES 1 kA/cm² Nb process.

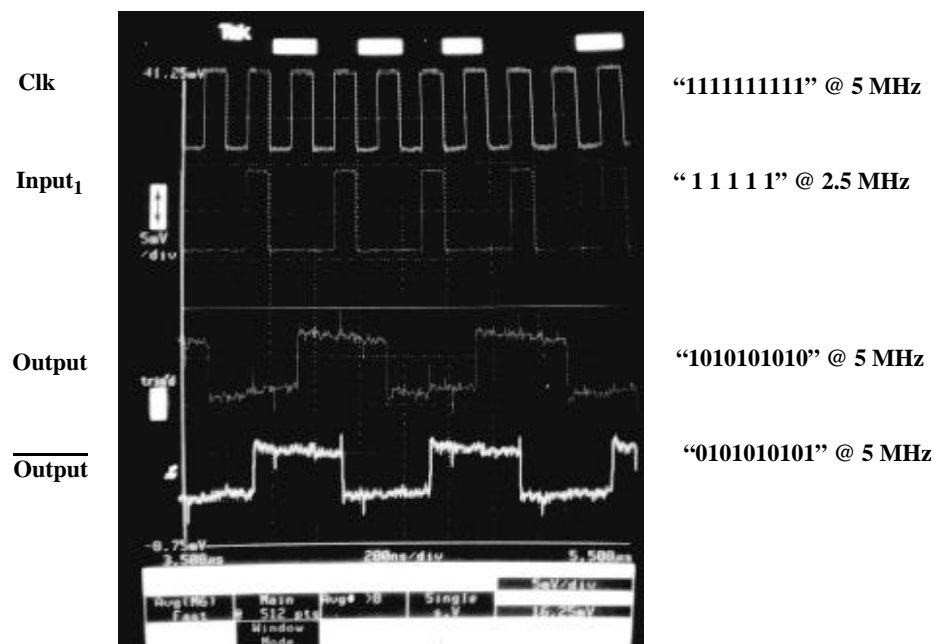


Figure 5.5 Testing results of a 2:1 MUX at 5 MHz. 50 mV/div on y-axis for Clk and Input₁. 5 mV/div on y-axis for Output and $\overline{\text{Output}}$. 200 ns/div on x-axis for all signals.

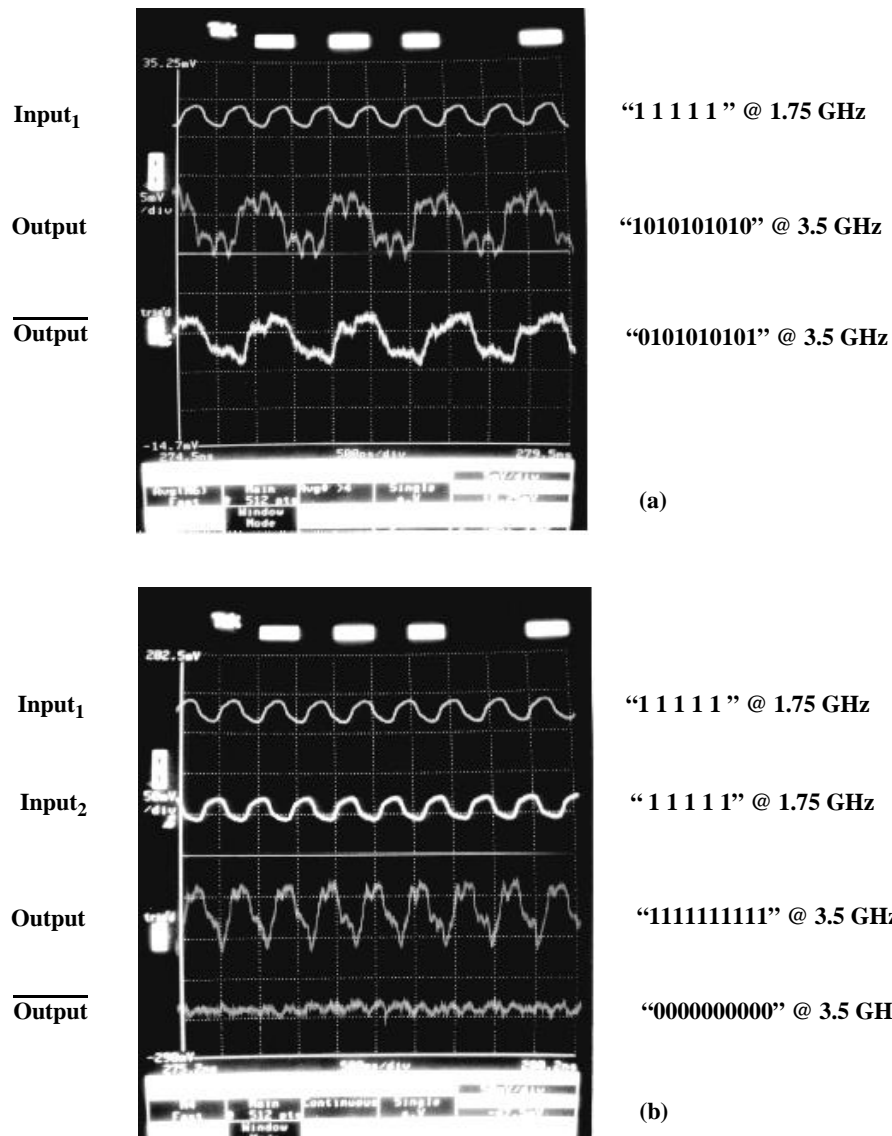


Figure 5.6 Testing results of a 2:1 MUX at 3.5 GHz for two different input patterns, (a) Input₁ “1 1 1 1 1”, Input₂ “0 0 0 0 0” (b) Input₁ “1 1 1 1 1”, Input₂ “1 1 1 1 1”. 50 mV/div on y-axis for Input₁ and Input₂. 5 mV/div on y-axis for Output and Output_{bar}. 500ps/div on the x-axis for all signals.

Input waveforms shown here are the outputs of SFQ/DC converters which are monitoring the on-die input SFQ signals, so each transition represents a “1”. The complementary inputs are Input

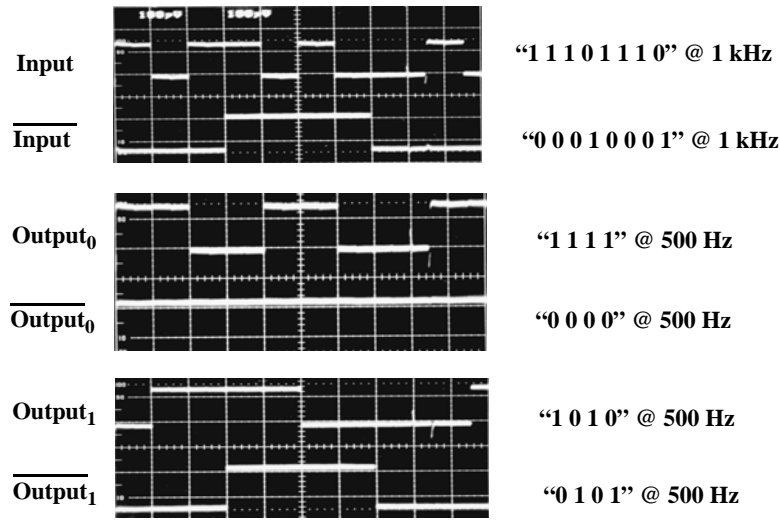


Figure 5.7 Testing results of a 1:2 DEMUX at 1 kHz. The scales of the above waveforms are 100 μ V/div for the y-axis and 1ms/div for the x-axis.

“11101110”, $\overline{\text{Input}}$ “00010001” at 1 kHz. The two pairs of complementary outputs are Output_0 “1111”, $\overline{\text{Output}}_0$ “0000” and Output_1 “1010”, $\overline{\text{Output}}_1$ “0101” at 500 Hz.

The experimental dc bias margin is (-15%, 15%).

5.2.2.2 Medium-Speed Testing Results of a 1:2 DEMUX

Fig. 5.8 and Fig. 5.9 are the testing results of the same 1:2 DEMUX test chip as above with the same input data patterns as above at 10 MHz and 1 GHz. The Input and $\overline{\text{Input}}$ are the input waveforms before they enter the test chip. Output_0 , $\overline{\text{Output}}_0$, Output_1 are correct results except $\overline{\text{Output}}_1$. The dc bias margin for all the three outputs to work remains (-15%, +15%) up to 100 MHz. And it is (-13%, +13%) at one gigahertz. Outputs were not terminated on this test chip, so the refection distorted the Output_1 waveform at 1 GHz. It is believed that cause of the failure at $\overline{\text{Output}}_1$ is flux trapping in spite of repeated efforts. This was an old chip. Medium-speed and high-speed testing were performed about two years after it was fabricated. If the circuit function is verified at 1 kHz,

it should work easily at one megahertz, which is a very low speed for RSFQ circuits, but it did not.

Defluxing in the usual way was not successful, probably a result of degradation of the niobium.

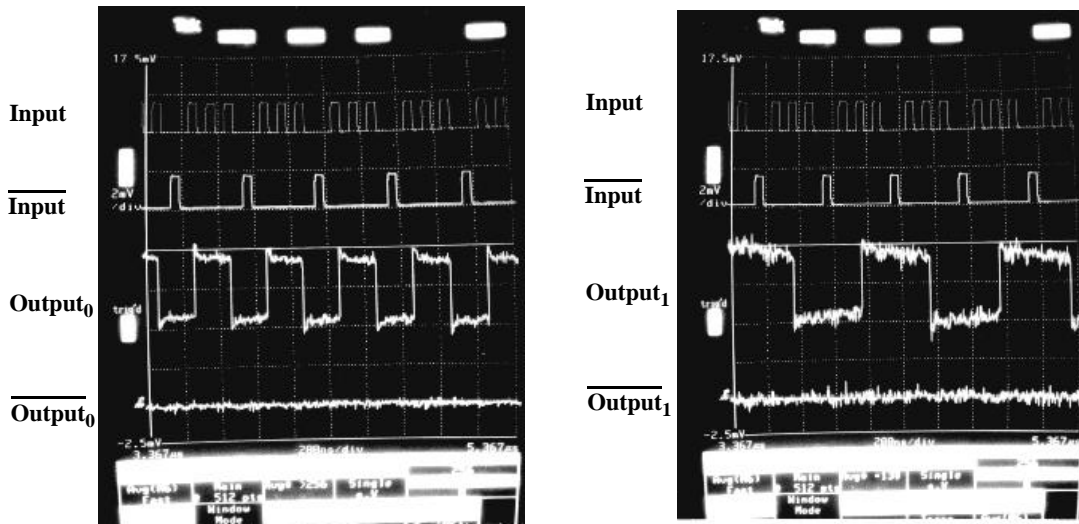


Figure 5.8 Testing results of a 1:2 DEMUX at 10 MHz. 50 mV/div on y-axis for Input, Input. 2 mV/div on y-axis for Output₀, Output₀, Output₁, Output₁. 200 ns/div on x-axis for all signals.

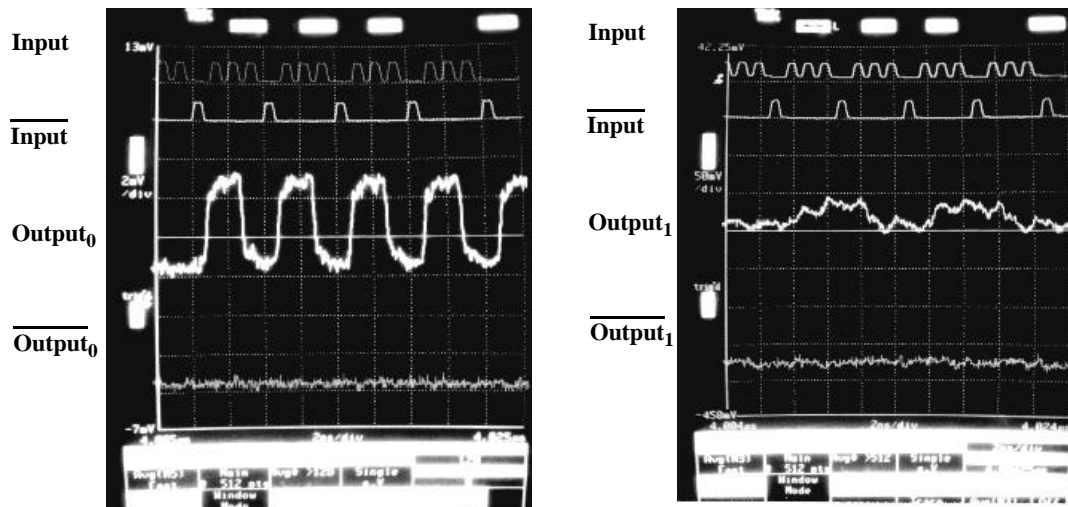


Figure 5.9 Testing results of a 1:2 DEMUX at 1 GHz. 50 mV/div on y-axis for Input, Input. 2 mV/div on y-axis for Output₀, Output₀, Output₁, Output₁. 2 ns/div on x-axis for all signals.

5.2.2.3 Medium-Speed Testing Results of a 1:4 DEMUX

Shown in Fig. 5.10a is the micrograph of a 1:4 DEMUX fabricated in the HYPRES 1 kA/cm² Nb process. Fig. 5.10b shows a testing result at 10 MHz. Input is “111111111111” at 100 MHz, $\overline{\text{Input}}$ is all zeros, not shown in the figure. Correct functioning of Output₄ “1 1 1” at 25 MHz, $\overline{\text{Output}}_4$ all zeros were observed.

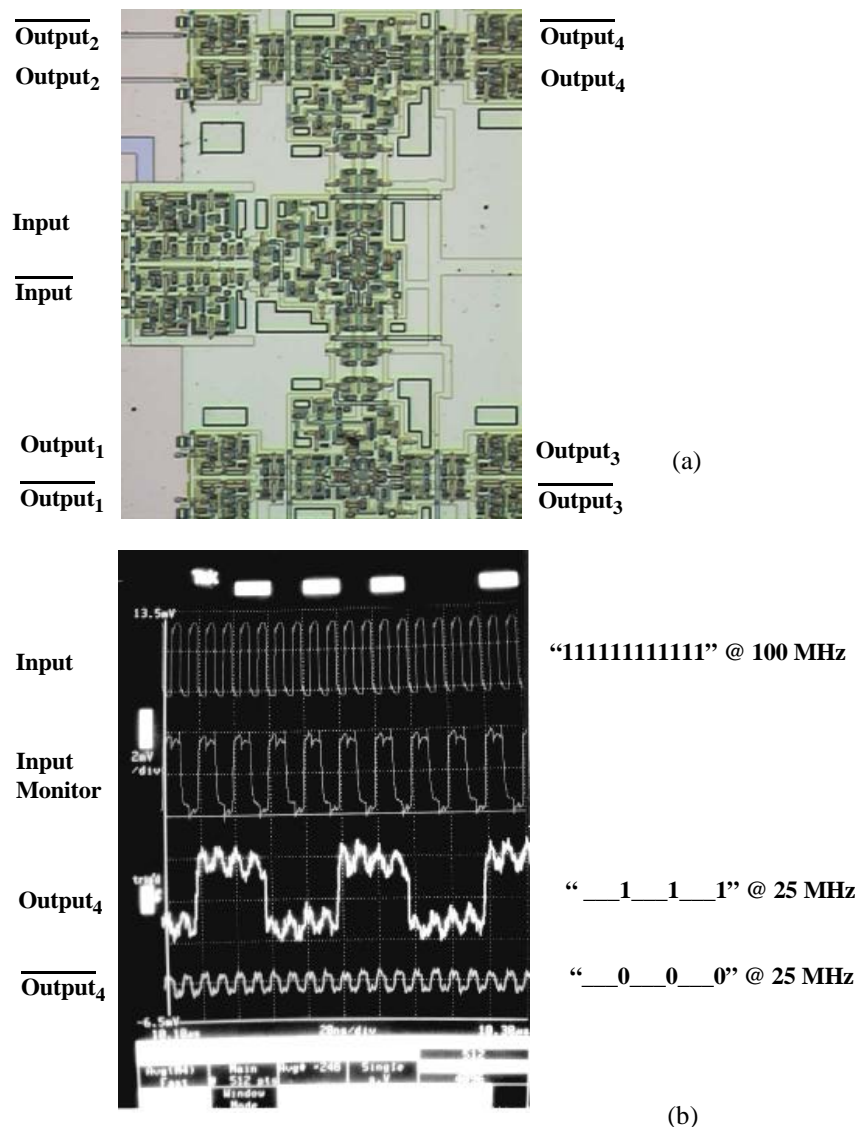


Figure 5.10 Testing results of a 1:4 DEMUX at 100 MHz. (a) micrograph (b) waveforms. 50 mV/div on y-axis for Input. 2 mV/div on y-axis for Input Monitor, Output₄, $\overline{\text{Output}}_4$. 20 ns/div on x-axis for all signals.

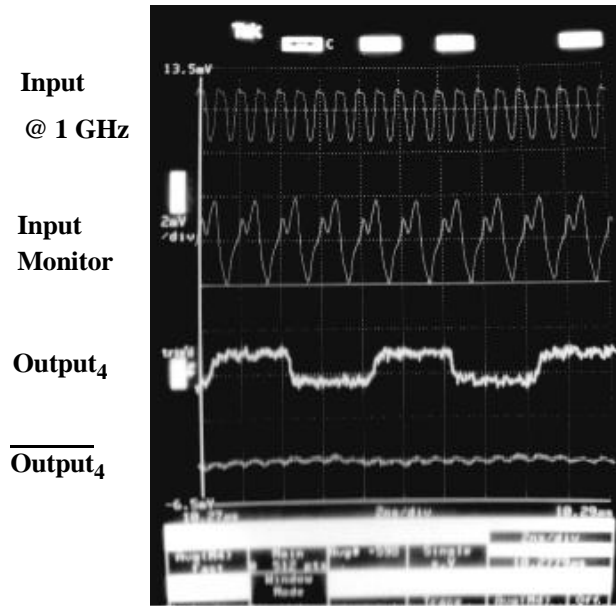


Figure 5.11 Testing results of a 1:4 DEMUX at 1 GHz. 50 mV/div on y-axis for Input. 2 mV/div on y-axis for Input Monitor, Output₄, Output₄. 2 ns/div on x-axis for all signals.

Fig.5.11 shows the correct testing results of the same 1:4 DEMUX with the same input pattern at 1 GHz. Proper termination resistors were added in this test chip. So the waveform is not distorted as in Fig. 5.9.

No dc bias margins were recorded at 100 MHz and at 1 GHz. However, at 1 kHz, the dc bias margins (-6.5%, +6.5%) were observed.

5.2.2.4 High-Speed Testing Results of a 1:4 DEMUX

Fig. 5.12 shows the direct high-speed testing results of the same 1:4 DEMUX with the same input pattern at 9.2 GHz as in Fig. 5.10 and 5.11. The outputs are at 2.3 GHz. The bandwidth of the amplifier used to enlarge the output signals in this experiment is 3 GHz. So the observed Output₄ waveform became a more sinewave like signal instead of square wave. If the amplifier bandwidth

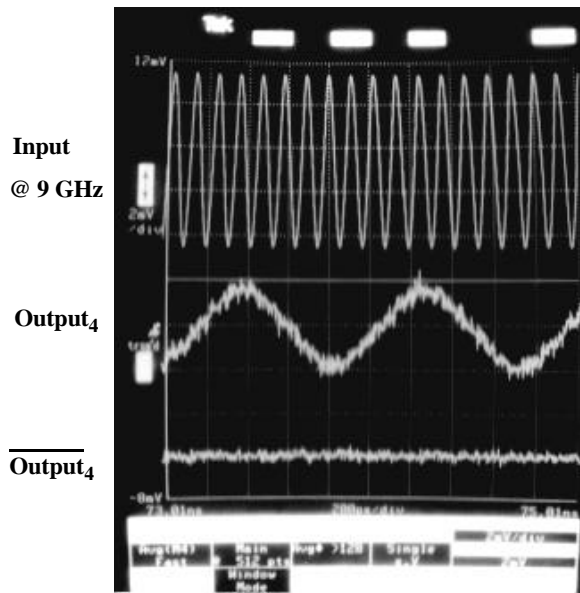


Figure 5.12 Testing results of a 1:4 DEMUX at 9.2 GHz. 20 mV/div on y-axis for Input. 2 mV/div on y-axis for Output₄, Output₄. 200 ps/div on x-axis for all signals.

is improved, higher-speed operation can be observed since no dc bias margin degradation is observed when the frequency was increased from 1 GHz to 9.2 GHz although the margin is small. Flux trapping is again the main difficulty in measurement.

5.3 Unmeasured Test Chips

Three sets of masks were made for circuits to be fabricated in the 1 kA/cm^2 UCB Nb process. And one set was made for the 6.5 kA/cm^2 UCB Nb process. Lack of funding prevented completion of the processing of these chips in our Microfabrication Laboratory. A future prosecution of this project could use the designs presented here. The masks for the critical layers including junction definition layer AN, metal layers M1 and M2 are made by high-resolution e-beam writing at Dupont. So the junction areas and the inductances in the circuits have good mask control. We made masks of all other layers in the Berkeley Microfabrication Laboratory.

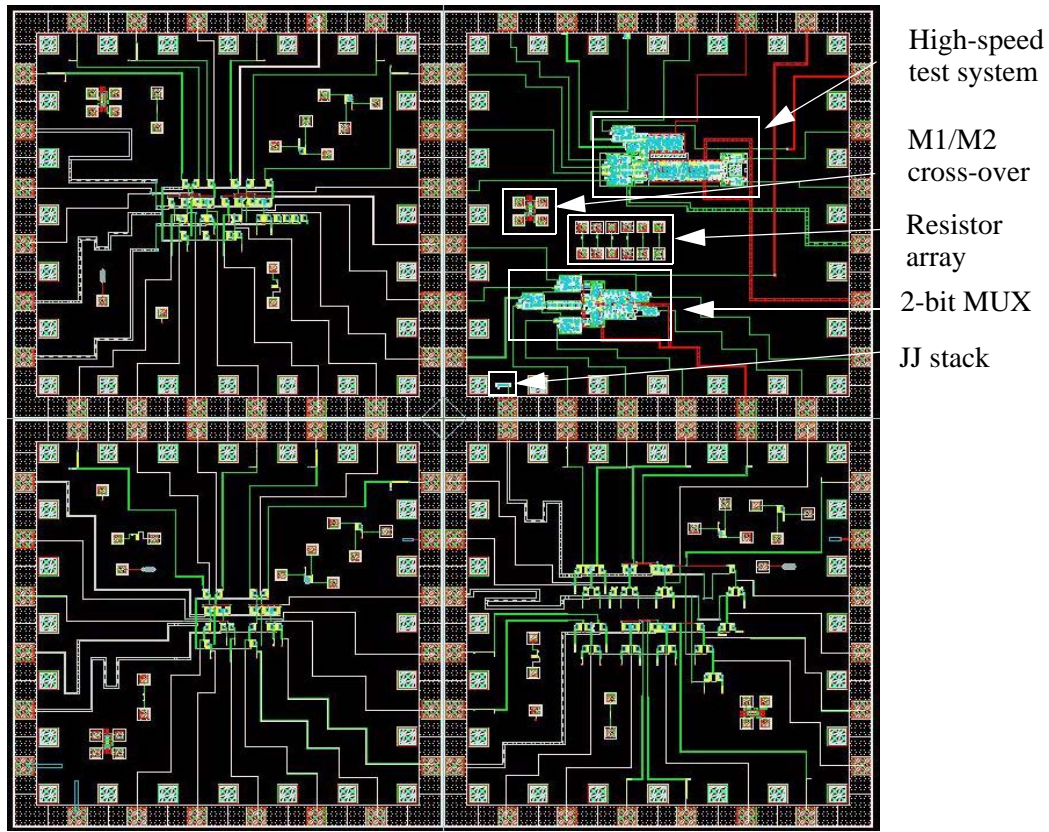


Figure 5.13 Mask set No. 1 for UCB 1 kA/cm^2 Nb process.

Shown in Fig. 5.13 is the mask set No. 1 for the UCB 1 kA/cm^2 Nb process. Each mask set can host four 5000 μm x 5000 μm chips. On the upper-right chip, we placed two circuits laid out for the HYPRES 1 kA/cm^2 Nb process that were previously verified. One circuit is the high-speed test system [55]. The other circuit is the 2-bit MUX, as in Fig. 5.4(a). They are good candidates to compare UCB 1 kA/cm^2 process with HYPRES 1 kA/cm^2 process. Other diagnostic structures such as 50-Josephson junction (JJ) series array, resistor array and M1/M2 cross-over are put on chips for the process verification. These structures are placed on every chip whenever the space and the pin assignments allow. The other three chips belong to other projects. These chips are

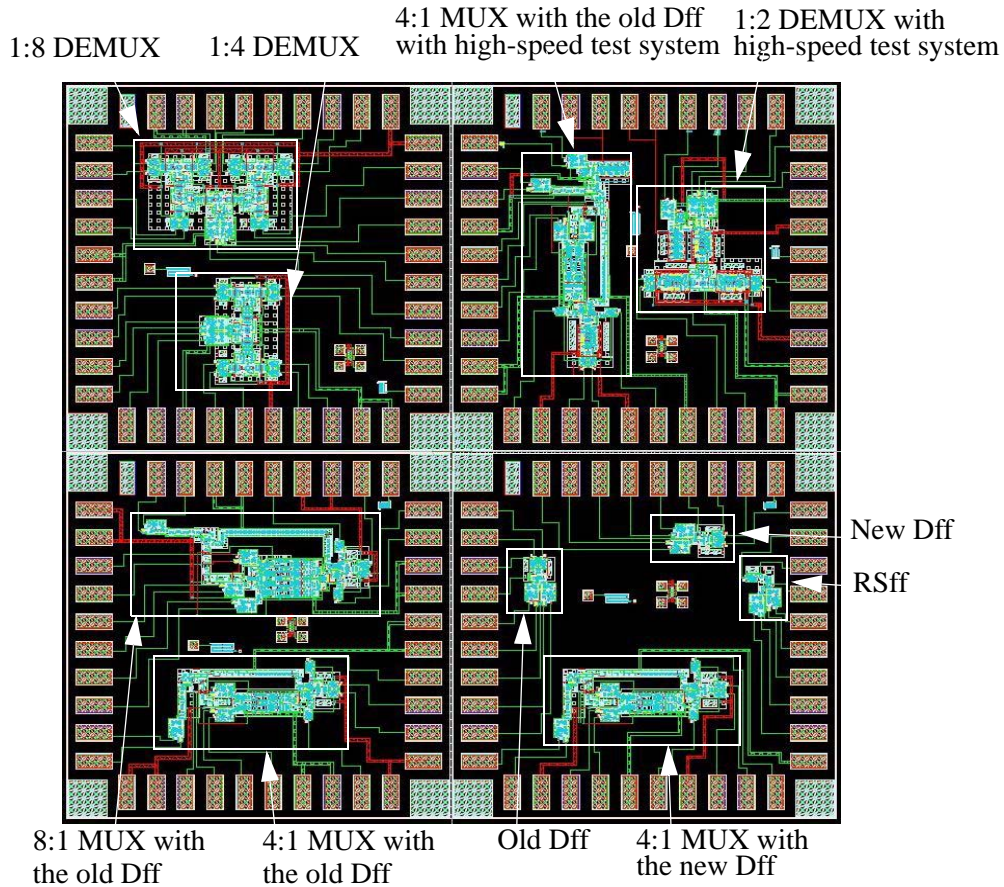


Figure 5.14 Mask set No. 2 for UCB 1 kA/cm² Nb process.

made to be tested in the 24-pad high-speed probe. High-speed probe is preferred due to better shielding and higher testing speed it supports.

Shown in Fig. 5.14 is mask set No. 2 for UCB 1 kA/cm² Nb process. These four chips are all made for the 40-pad low-speed probe. We chose the low-speed probe layout for the larger number of available pads so that we are able to include more basic blocks for verification.

The RSff and Dffs used in the MUX are included in the test chip for verification. Layout of Dff was previously verified in HYPRES process, but the simulation and testing dc bias margin is not

good. So a new improved version is made. 4:1 MUXs with both the old Dff and the new one are included in the test chip. Furthermore, a 8:1 MUX with the old Dff and a 4:1 MUX with the old Dff and with high-speed test system are included on the test chip. The Dff used in the DDST shift register is also the old verified version.

A 1:4 DEMUX, a 1:8 DEMUX and a 1:2 DEMUX with the high-speed test system are included in the test chip.

With this test chip set, we are able to perform low-speed function verification from the basic blocks to the more complicated 8:1 MUX and 1:8 DEMUX circuits. We are also able to perform on-chip high-speed testing of a 4:1 MUX and a 1:2 DEMUX.

Shown in Fig. 5.15 is the mask set No. 3 for UCB 1 kA/cm² Nb process. The new improved 4-bit and 8-bit MUX and DEMUX with high-speed test systems are included. These circuits are difficult to fabricate in the Microlab environment due to the circuit complexity. But if fabricated successfully, the high-speed verification of 8:1 MUX and 1:8 DEMUX can be performed.

Compared to the HYPRES 1 kA/cm² Nb process layout, we added layer AN for both junction CE definition and anodization ring definition. The 24-pad and 40-pad frame layouts are modified to avoid non-orthogonal geometries to for the masks made in the microlab.

Fig. 5.16 shows the first mask set made for the UCB 6.5 kA/cm² Nb process. Even though we did not get successful experimental results from the 1 kA/cm² UCB process, we proceeded to work on 6.5 kA/cm² designs based on some promising high J_c junction and circuit results from our group. We put the key, yet simple, blocks on the first run. If these blocks are verified successfully, we can build more complicated MUX and DEMUX circuits from these blocks in the next test chip.

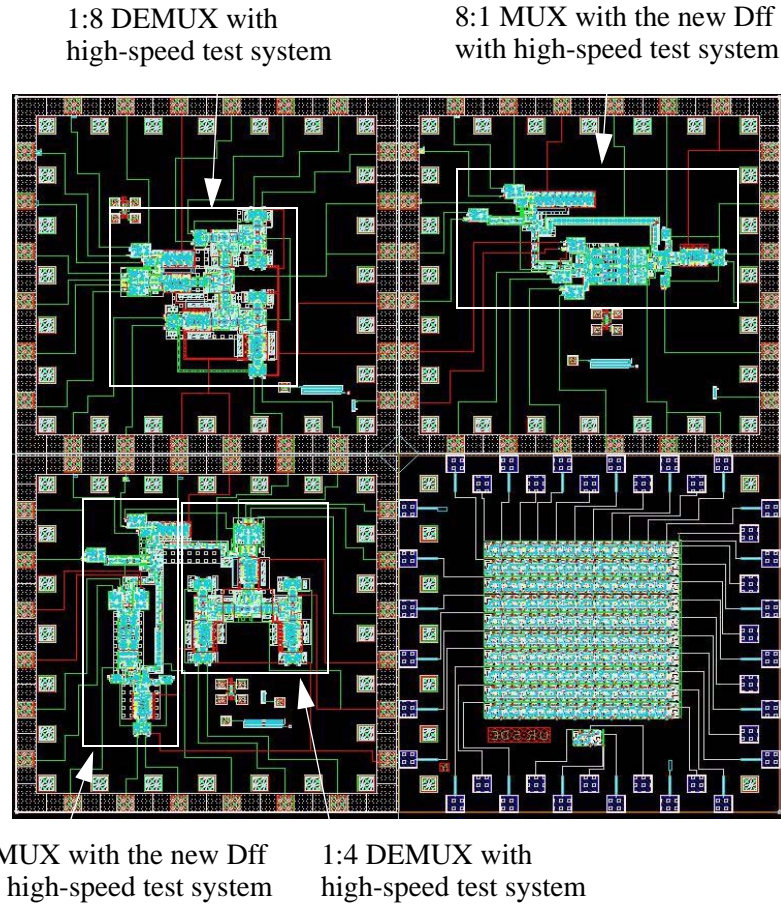


Figure 5.15 Mask set No. 3 for UCB 1 kA/cm² Nb process.

In our plan, the first circuit to be tested is the Tff without DC/SFQ and SFQ/DC converters. It has only 11 junctions. It can be verified by dc voltage measurement. Shown in Fig. 5.17 is a micrograph of the fabricated 6.5 kA/cm² Tff. When V_{bias_Input} is increased such that the bias current for the input junction is larger than its critical current, SFQ pulses are generated across the input junction and propagated through the JTLs to the input of the Tff. The frequency of the output SFQ pulses are half of that of the input. The DC voltage measured at the input junction $V_{Input} = f_{in} \Phi_0$. The dc voltages measured at the output junctions are $V_{Output1} = f_{out} \Phi_0$ and $V_{Output2} = f_{out} \Phi_0$. Since $f_{in} = 2f_{out}$, $V_{Output1} = V_{Output2} = 2V_{Input}$.

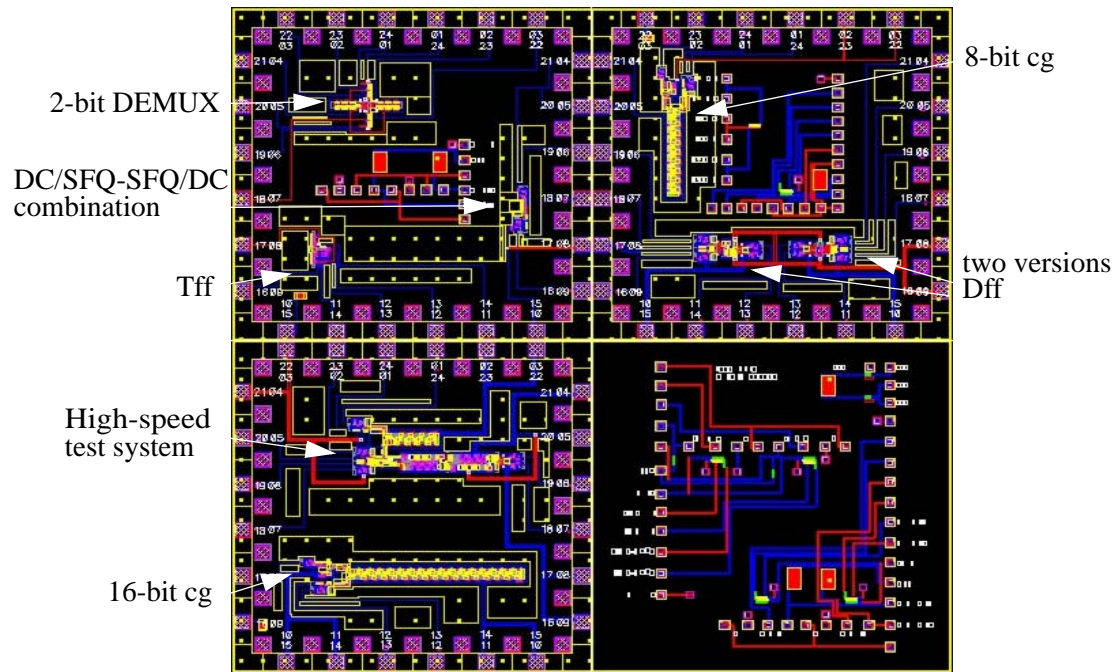


Figure 5.16 Mask set No. 1 for UCB 6.5 kA/cm² Nb process.

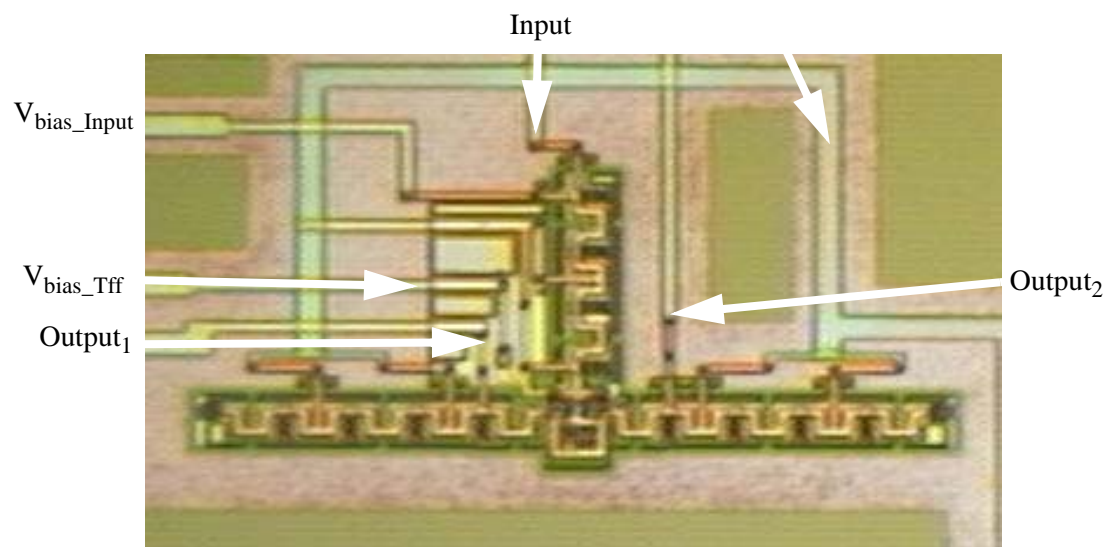


Figure 5.17 A 6.5 kA/cm^2 Tff micrograph.

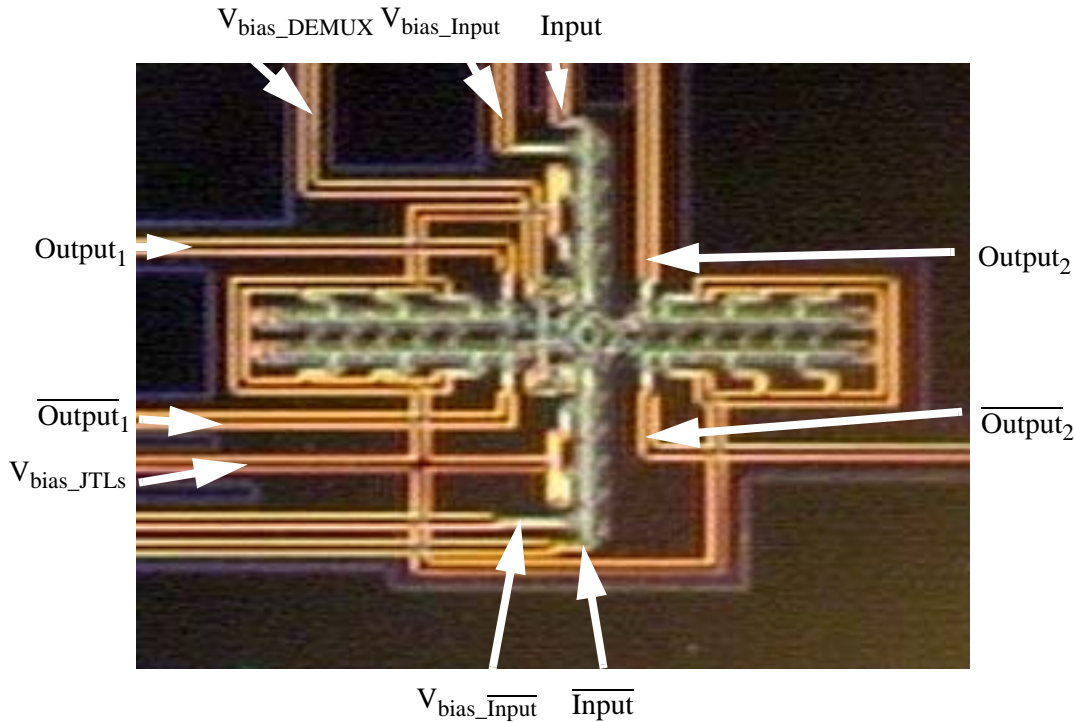


Figure 5.18 A 6.5 kA/cm^2 1:2 DEMUX micrograph.

Similarly, a 1:2 DEMUX is also planned to be verified through the input/output dc voltage comparison. Fig. 5.18 shows a micrograph of the 1:2 DEMUX. In this layout, it has total 48 Josephson junctions. When Input is over-biased, we check $V_{\text{Output1}} = V_{\text{Output2}} = 2V_{\text{Input}}$. When $\overline{\text{Input}}$ is over-biased, we check $V_{\overline{\text{Output1}}} = V_{\overline{\text{Output2}}} = 2V_{\overline{\text{Input}}}$. This is not a complete test with random input patterns, but good enough to get the DEMUX verified at one simple pattern up to very high-speed without involving complicated test circuits which reduce the chance of success in the new technology.

We chose to verify the DC/SFQ converter and the SFQ/DC converter since they are the necessary interface circuits for any RSFQ circuits to be tested with external pattern generator data. They

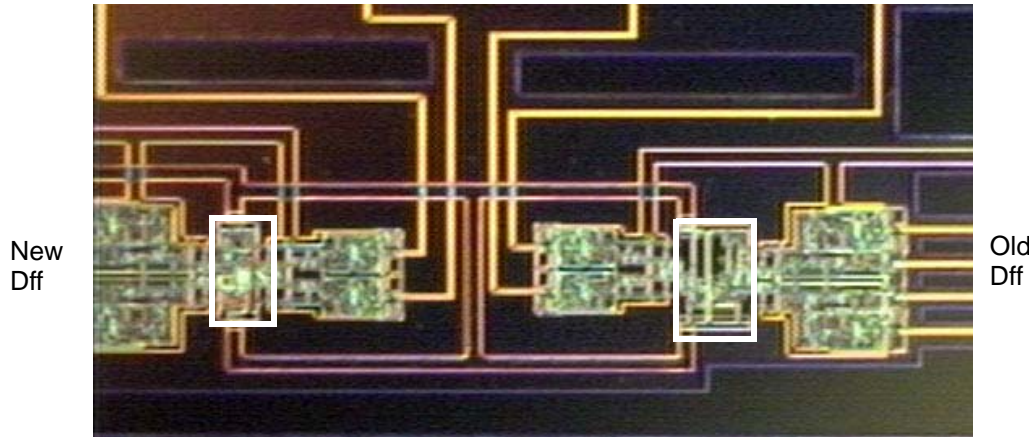


Figure 5.19 Micrograph of two versions of 6.5 kA/cm^2 Dffs.

are wide-margin circuits. But the smallest junction ($I_c = 120 \mu\text{A}$) in our junction library is used in these two circuits, which made them fabrication challenging.

We also put two versions of Dffs on the first run since Dff is a critical blocks used in our test system design and MUX design. One is the a ported version from a previous verified Dff in 1 kA/cm^2 process by only modifying junction areas in the layout. The other one is our optimization result and is used in the 6.5 kA/cm^2 DDST SR layout.

The cgs and the high-speed test system are also put on the first run. If they are verified successfully, they can be applied for on-chip high-speed testing of the MUX and the DEMUX.

In the 6.5 kA/cm^2 chips, moats are more systematically added. The principle is that the magnetic flux inside a complete moat enclosure should be less than one magnetic flux quantum. For a square moat enclosure, that is, the area $A < \Phi_0/B$; the length of one side $L < \sqrt{(\Phi_0/B)}$. For 1 mG magnetic field, the moat size should be smaller than $144 \mu\text{m} \times 144 \mu\text{m}$. In our design, we chose size for 3 mG residual magnetic field. The moat sizes are smaller than $83 \mu\text{m} \times 83 \mu\text{m}$.

5.4 Conclusion

Some successful testing results [64] are achieved in both low-speed testing and direct high-speed testing for the early stage designs where post layout optimization was not implemented. The achieved dc bias margins are smaller than simulated. Flux trapping is a major obstacle in measurement in spite of all the effort made improving degaussing procedure.

The newer designs have improvements in the following ways. 1. The circuits are optimized with extracted parasitic inductances. 2. More systematic moats are added in the layout surrounding the junction-inductor loops in the entire circuit area to combat the flux trapping. 3. All the input signals have impedance matching resistors and all the output signals have termination resistors added in the layout. So we expect better testing results when they are fabricated successfully.

APPENDIX

High- T_c Superconductor RSFQ Circuits; Monte-Carlo Analysis

A.1 Introduction

The main motivation of making high- T_c superconductor (HTS) digital circuits is the relative ease of refrigeration compared to the one used for low- T_c superconductor (LTS) circuits. But due to the fabrication and design difficulty, only small HTS digital circuits composed of 10-20 Josephson junctions have been demonstrated. To investigate how large, how fast and at how high temperature the circuit can operate, a joint study was performed involving collaborations between UC Berkeley and three companies: TRW, Conductus, and Northrop Grumman. (TRW later became a part of Northrop Grumman.) Process and device information were supplied by the three companies. Some representative circuit designs under development were also provided by the three companies. UC Berkeley was responsible for carrying out the theoretical calculations to predict yield and bit-error-rate (BER) including thermal noise. An operating temperature of 40 K was chosen because of interest in refrigerators at that temperature.

Large process variations and thermal noise related to higher operating temperature are the two main factors impeding implementation of larger HTS digital circuits. In this section, we will elaborate these two challenges and other trade-offs in HTS RSFQ circuit design. Methodologies used

to analyze these issues will be presented, with the focus on Monte Carlo calculations. In Section A.2, details of Monte Carlo calculations for two versions of HTS T flip-flops are presented and the effect of parasitic inductance is demonstrated. In Section A.3, the theoretical yield of a counter circuit consisting of three stages of T flip-flops is calculated. In Section A.4, a conclusion will be drawn and direction will be given based on the above calculation results.

In the well developed LTS tunnel junction technology, we have to shunt the Josephson junction with an external resistor to achieve the proper nonhysteretic I-V characteristics used by RSFQ circuits. HTS junctions made from the $\text{YBa}_2\text{Cu}_3\text{O}_{7-x}$ material have an intrinsic nonhysteretic I-V characteristic, which makes the RSFQ logic family a natural choice for HTS digital circuits.

HTS circuit design is challenging due to the undesirable material and process limitations. Due to the larger penetration depth in HTS materials, the minimum realizable inductance per square is about 1 pH. In layout, it is hard to make a loop with less than 4 squares ($L_{\min} \sim 4 \text{ pH}$). In an RSFQ circuit, the typical loop $I_c L = \Phi_0/2$. So that L_{\min} of 4 pH determines $I_{c\max} \sim 250 \mu\text{A}$. However in HTS, larger I_c is desired to combat the more significant thermal noise. So L_{\min} imposes an undesirable design constraint. And even more, the parasitic inductance between the junctions and the ground plane is about $1 \sim 3 \text{ pH}$, which is harmful to circuit margin. The series linear inductance weakens the effectiveness of the nonlinearity of the switching junction. Larger $I_c R_n$ is desired so the circuit can run faster. With I_c limited, we would like to increase R_n . But for HTS junctions, I_c and R_n are correlated. When the process is adjusted to achieve higher R_n , I_c may be reduced, so $I_c R_n$ is limited by the process.

With the circuit design requirements in mind, we have studied the collected state-of-the-art HTS junction information [65][66][67] and written a junction model required for the WRspice simulation program.

```
.model ybco jj(rtype=1, cct=1, icon=10m, vg=2.8m delv=0.08m
+ icrit=0.5m, r0=1, rn=1, cap=0.0025p)
```

In this model, $I_c R_n = 500 \mu\text{V}$, $\beta_c = (2\pi/\Phi_0)^*(I_c R_n)^*(CR_n) = 3.8 \times 10^{-3}$. This is based on the measurement of I_c and R_n . But the determination of the junction capacitance is more ambiguous. Fortunately, with $\beta_c \ll 1$ in HTS junctions, the accuracy of the capacitance value is not important. In other words, a change of one or two orders of capacitance value in the model will not much affect the circuit performance. This is verified by JTL pulse width simulation by increasing the capacitance value 100 times. The $I_c R_n$ value of $500 \mu\text{V}$ is close to the one of $592 \mu\text{V}$ in LTS 6.5 kA/cm^2 Nb process. This enables a circuit such as a T flip-flop to run at above 100 GHz. As a matter of fact, J_c , I_c and $I_c R_n$ are functions of temperature. J_c , I_c and $I_c R_n$ decrease with increasing temperature. For junctions operated at a temperature different from 40 K, the above junction model should be modified.

Severe process variations prevent implementation of large HTS circuits. At the time of this study, the standard deviation of the HTS junction critical current was about 10%, which is several times larger than that in LTS. The process variation of inductance is also larger in HTS. The circuit yield is foreseeably low. But how low is it? And how does the yield decrease with the increasing circuit size? Monte Carlo analysis is done here to explore these issues and provide a theoretical answer. The process variations can be divided into two categories: global variations and local variations. The global variations reflect the parameter spreads from lot to lot, from wafer to wafer and from chip to chip. The local variations are the parameter spreads on the same chip. In our Monte Carlo analysis, circuit yield is defined as the success rate among the total runs (usually >100 runs). In each run, the circuit parameters are pseudo-randomly generated by the simulator based on the

global and local variations. The circuit parameters are assumed to have a gaussian distribution with the mean values as designed.

The process variations used in our calculation are listed in the table below.

TABLE A-1 HTS global process variations (1 σ value)

J_c	I_cR_n	L	R
0%	0%	15%	12%

The global variations of J_c and I_cR_n are not investigated here. It was agreed to screen the samples under study to have the target J_c and I_cR_n values.

TABLE A-2 HTS local process variations (1 σ value)

	I_c	I_cR_n	L	R
ideal spreads	5%	2.5%	5%	4%
state-of-the-art spreads	10%	5%	15%	4%
medium spreads	15%	10%	10%	4%
large spreads	25%	15%	20%	4%

For local process variations, the state-of-the-art process variations are collected from the three major companies. And a set of ideal process variations equivalent to the state-of-the-art in LTS are set to see how much the circuit yield can be improved with better process control. Simulation with the set of more realistic and the set of sloppy process variations reveals how the yield deteriorates when the process control is worse than the state-of-the-art.

By the statistical nature of the Monte Carlo analysis, the yield is not a certain value. It has a Gaussian distribution. The calculated yield Y is the mean value. And the variance of yield $\sigma^2 = Y(1-Y)/N$, where N is the total number of runs, equal to 100 in our calculations. For a 95% confi-

dence level, the confidence interval $L = 2\sigma = 2 \cdot \sqrt{Y(1 - Y)/N}$. The predicted yields lie in the range of $Y \pm L$ with a 95% probability.

Another issue in HTS circuit design is thermal noise related to the higher operation temperature (40-70 K vs. 4.2 K in LTS). The thermal noise can be modeled by a random current source in parallel with each resistor or junction in the circuit. The rms value of the current fluctuations is given by the Nyquist formula

$$i_{rms} = \sqrt{\frac{4kTf_c}{R}}$$

where k is Boltzman's constant, T is temperature, R is resistance or R_n of the junction, and f_c is the cutoff frequency of the noise frequency band. In WRspice, a random Gaussian noise is generated in time domain, defined by

```
@ define noise(R,T,Δ,n) guass(sqrt(4*boltz*T/(R*2*Δ)),0,Δ,n)
```

where $\Delta = 1/(2f_c)$, is the time spacing between two random numbers. n is an integer which defines the interpolation type, either first-order interpolated or piecewise linear steps. The simulation time step should be much smaller than Δ to ensure interpolation algorithm stability. And Δ should be small compared to the time constant of the circuit.

A simulation including the above defined thermal noise with and without process variation were used to predict BER [69][70][71]. And a combination of Monte Carlo analysis and thermal noise in transient simulation can predict both the yield and the BER more accurately. The Monte Carlo analysis reported in the following sections only considers process variations in order to keep the computation time within reasonable bounds.

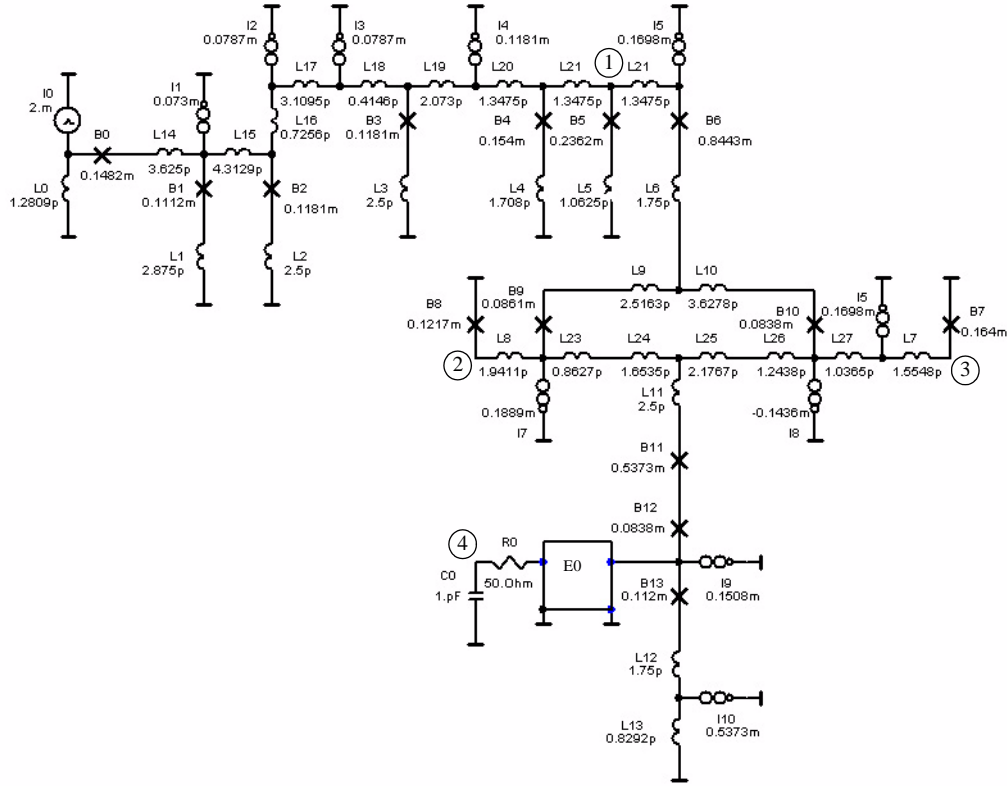


Figure A.1 TRW T flip-flop schematic.

A.2 Monte-Carlo Calculation on T Flip-Flops

A.2.1 TRW T Flip-Flop

The first circuit we studied is a toggle, or “T”, flip-flop shown in Fig. A.1. A.G. Sun in TRW provided us the original design which was optimized in MALT with the extracted parasitic inductance. (They later on reported this T flip-flop with some parameter changes working at 65K [68].)

The Sun design has a total of 14 junctions and includes parasitic inductances. We can see that the parasitic inductance is in the order of $1 \sim 3$ pH. On the left, $B_0, L_0, B_1, L_1, L_{14}$ form a dc-to-sfq converter. On the right, $B_6, B_7, B_8, B_9, B_{10}$ and the related inductors and bias current sources form

the Tff core. In between are some connection JTLs. Junctions B_{11} , B_{12} , and inductors L_{11} , L_{12} , L_{13} form a monitor to detect the state of the Tff. A voltage-controlled voltage source E_0 and the RC network are added here purely for our simulations. It is used to test the average voltage at the node that E_0 is monitoring. A triangle waveform fed through I_0 is converted to SFQ pulse trains across B_1 . The pulses travel down the JTLs, and switch B_8 and B_7 in turn. The voltage at the output of E_0 will switch between two values.

We took the circuit parameters and did simulation with the original Sun junction model *ybcotrw* and the new model *ybc0* to confirm its operation defined below. Fig. A.2 shows example

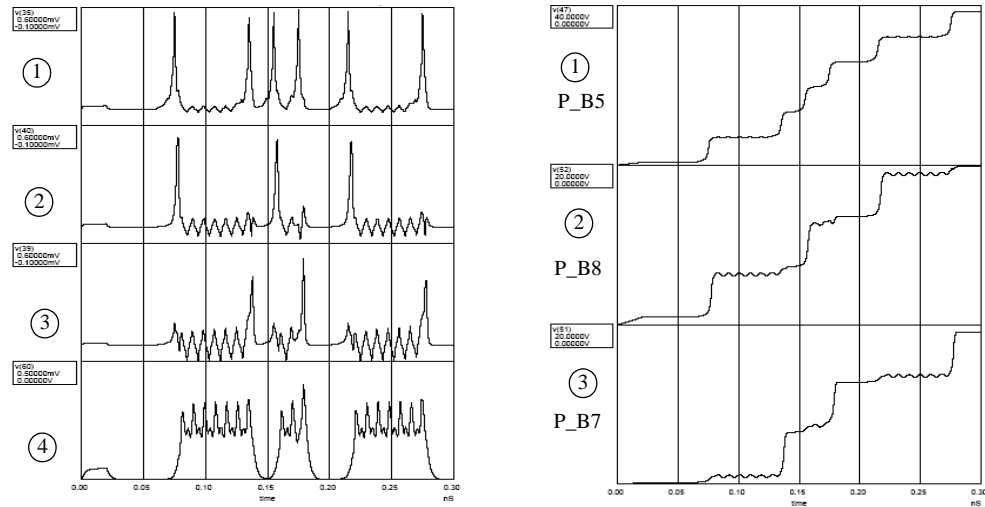


Figure A.2 Simulation waveform of TRW Tff at 50 GHz. (a) Voltage waveforms. (b) Phase waveforms.

simulation waveforms at 50 GHz using the new model *ybc0*. Fig. A.2a shows the node voltages at B_5 , B_8 , B_7 and after the output monitoring RC filter. The first three nodes represent the input and the two outputs of the T flip-flop. The input pulses are diverted to the two outputs alternately. The filter output switched between 0 and an average voltage of about 0.25 mV corresponding to each

output switching at B8 and B7. Fig. A.2b shows the phase waveforms of B5, B8, B7. These phase values and the filter output voltages are monitored in simulation to judge circuit pass/failure.

For reference, the Sun junction model is listed below.

```
.model ybcotrw jj(rtype=1, cct=1, icon=10m, vg=2.8m delv=0.08m
+ icrit=0.16m, r0=0.469, rn=0.469, cap=0.05p)
```

It has an I_cR_n value of 75 μ V. $\beta_c = 5.3 \times 10^{-3}$. The new model *ybc*o has an improved I_cR_n value of 500 μ V. It reflects the progress on HTS junction process. So the circuit can be operated at a higher speed. But we did not re-optimize the circuit for the new junction model because we reasoned that the I_cR_n value should not change circuit optimization results at low speed where the pulse interference doesn't impact circuit operation.

Table A-3 lists the calculated yield based on the Sun model. Some other results were previously reported by P. Xie [69]. The improvement is that the circuit pass/failure criteria is examined and modified, so the yield values are better in this report.

TABLE A-3 TRW HTS Tff theoretical yield with $I_cR_n = 75 \mu$ V

Process variation	Yield (95% confidence level)	
	5 GHz	10 GHz
State-of-art spreads	52.9% ($\pm 9.1\%$)	50.4% ($\pm 9.1\%$)
Ideal spreads	94.2% ($\pm 4.3\%$)	84.3% ($\pm 6.6\%$)

With $I_cR_n = 75 \mu$ V, the yield of the Tff is not very good for the state-of-art spreads. The yield at 5 GHz is about 52.9% ($\pm 9.1\%$). Better process control with the ideal spreads can improve the yield at 5 GHz to 94.2% ($\pm 4.3\%$). The severe reduction of yield from the ideal spreads to the state-of-the-art spreads for $I_cR_n = 75 \mu$ V implies that the parameter margins of the optimized cir-

cuit are still not large enough to fight the process variations. Improving I_cR_n is necessary to improve the circuit yield at 5 GHz and higher speeds.

The yield calculation based on the new model with the improved I_cR_n (500 μ V) are summarized in Table A-4.

TABLE A-4 TRW HTS Tff theoretical yield with $I_cR_n = 500 \mu$ V

Process variation	Yield (95% confidence level)			
	5 GHz	10 GHz	20 GHz	50 GHz
State-of-art spreads	80.2% ($\pm 7.3\%$)	79.3% ($\pm 7.4\%$)	77.7% ($\pm 7.6\%$)	71.1% ($\pm 8.2\%$)
Ideal spreads	93.4% ($\pm 4.5\%$)	96.7% ($\pm 3.3\%$)	96.7% ($\pm 3.3\%$)	95.0% ($\pm 4.0\%$)

With the ideal spreads, the yield with the new I_cR_n value remains good ($> 90\%$) up to 50 GHz while with the old I_cR_n value, the yield can drop below 80% at 10 GHz. At 5 GHz, the new yield is similar with the one with lower I_cR_n . This proves our previous point that increasing I_cR_n value from 75 μ V to 500 μ V doesn't require circuit re-optimization at low speed where the pulse interference effect is negligible.

With the state-of-the-art spreads, the improved I_cR_n value improves the circuit yield a great amount. At 5 GHz, the yield increases from 52.9% ($\pm 9.1\%$) to 80.2% ($\pm 7.3\%$). At 50 GHz, it still has a yield of 71.1% ($\pm 8.2\%$). Fig. A.3 illustrates the data in Table A-4.

A.2.2 Conductus T Flip-Flop

We also studied another T flip-flop shown in Fig. A.4 from V. K. Kaplunenko in Conductus. It does not contain any parasitic inductance associated with the junctions. The junction model used for this circuit is

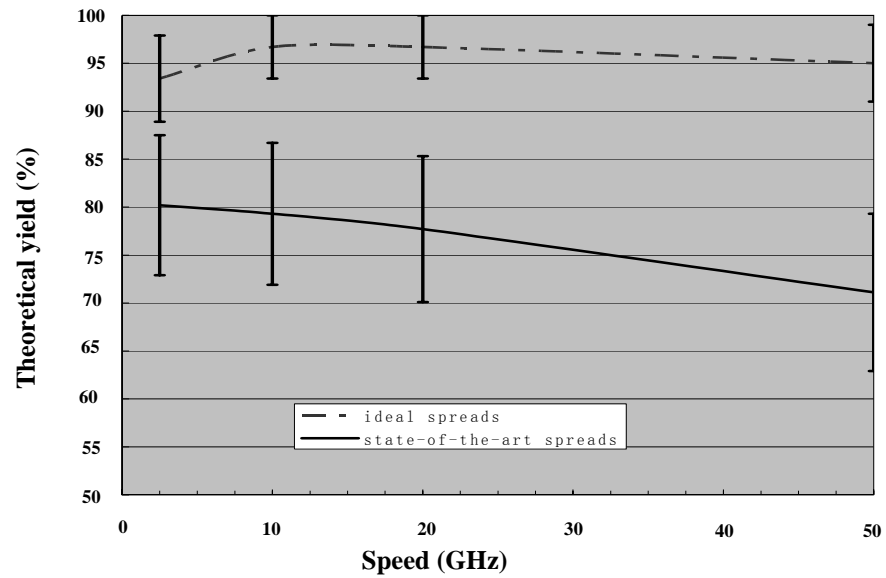


Figure A.3 TRW Tff theoretical yield with $I_c R_n = 500 \mu\text{V}$.

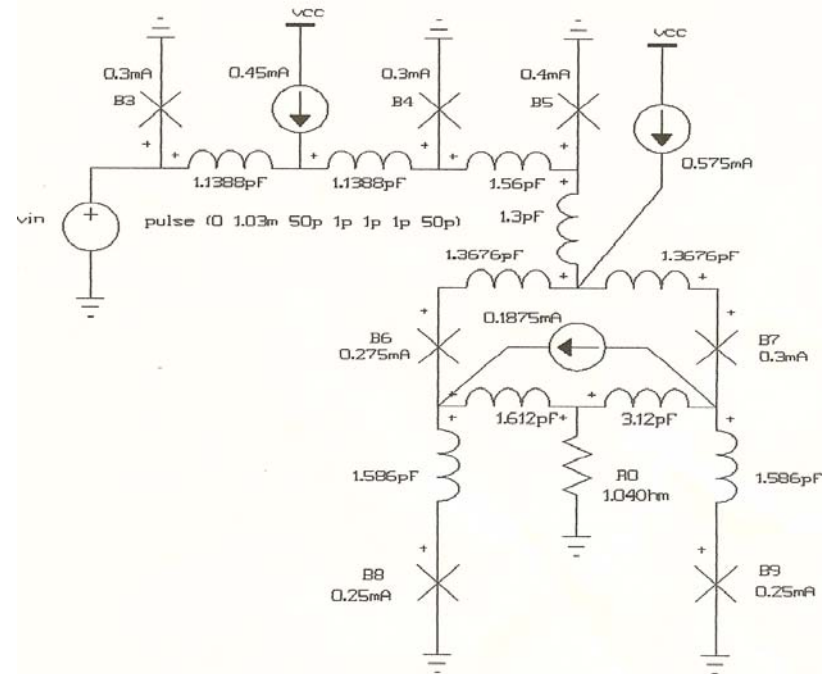


Figure A.4 Conductus T flip-flop.

```
.model ybcocond jj(rtype=1, cct=1, icon=10m, vg=2.8m delv=0.08m
+ icrit=0.25m, r0=2, rn=2, cap=0.26p)
```

It has an $I_c R_n$ value of 500 μ V and $\beta_c = 0.79$. The calculated yields for this idealized T flip-flop were published in [69] and copied here to be compared with the results of the TRW T flip-flop. Fig. A.5 illustrates the data in Table A-5.

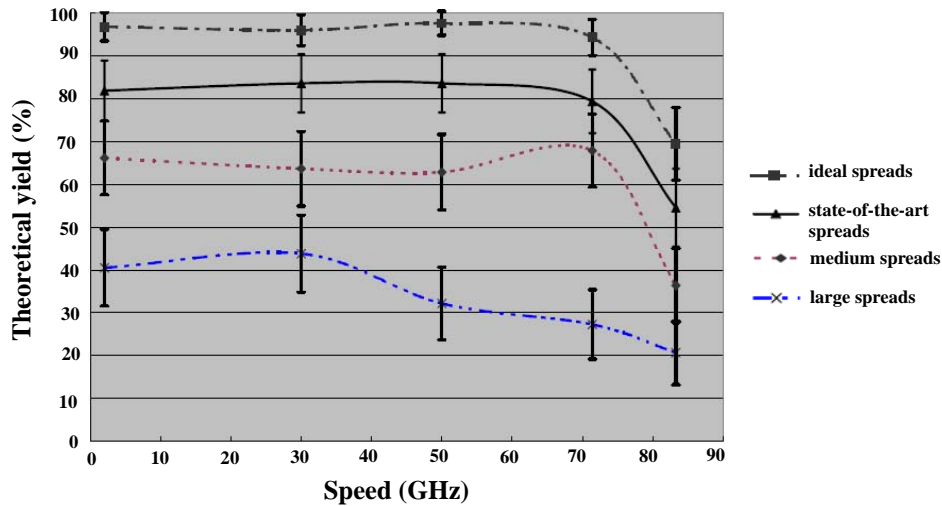


Figure A.5 Conductus idealized Tff theoretical yield with $I_c R_n = 500 \mu$ V.

TABLE A-5 Conductus HTS Tff theoretical yield with $I_c R_n = 500 \mu$ V

Process variation	Yield (95% confidence level)				
	2 GHz	30 GHz	50 GHz	71.4 GHz	83.3 GHz
State-of-art spreads	81.8% ($\pm 7.0\%$)	83.5% ($\pm 6.8\%$)	83.5% ($\pm 6.8\%$)	79.3% ($\pm 7.4\%$)	54.5% ($\pm 9.1\%$)
Ideal spreads	96.7% ($\pm 3.3\%$)	95.9% ($\pm 3.6\%$)	97.5% ($\pm 2.8\%$)	94.2% ($\pm 4.2\%$)	69.4% ($\pm 8.4\%$)
Medium spreads	66.1% ($\pm 8.6\%$)	63.6% ($\pm 8.7\%$)	62.8% ($\pm 8.8\%$)	67.8% ($\pm 8.5\%$)	36.4% ($\pm 8.7\%$)
Large spreads	40.5% ($\pm 8.9\%$)	43.8% ($\pm 9.0\%$)	32.2% ($\pm 8.5\%$)	27.3% ($\pm 8.1\%$)	20.7% ($\pm 7.4\%$)

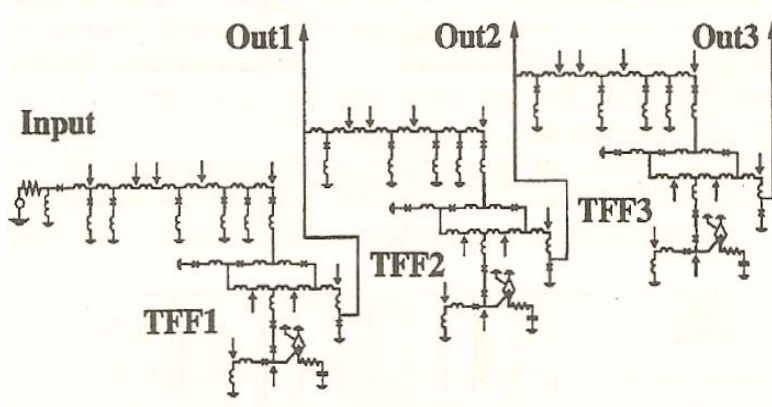


Figure A.6 TRW 3b-counter.

With the state-of-the-art spreads, at a few gigahertz, the Conductus T flip-flop yield is slightly larger than for the TRW T flip-flop. Both are around 80%. But the Conductus T flip-flop yield remains this value up to about 70 GHz. The yield of the TRW tff drops to about 70% at 50 GHz. With the ideal spreads, both T flip-flops have similar good yield up to 50 GHz.

Eliminating the junction parasitic inductance as much as possible is another way to improve circuit parameter margins and yield. This requires developing a new junction-formation process. With the state-of-the-art process at the time of the study, the parasitic inductance was as high as 1-3 pH.

A.3 3-Stage Counter

We further investigated the yield of a counter consisting of a three-stage cascaded TRW T flip-flops which we studied in Section A.2.1. The counter circuit schematic is shown in Fig. A.6. It contains 38 junctions. In Monte Carlo analysis, the output junction phases and the voltage after the

RC filter of all three stages were monitored to judge the success of the circuit operation. The calculated yield results are listed in Table A-6. Fig. A.7 illustrates the data in Table A-6.

TABLE A-6 TRW HTS 3-stage counter theoretical yield with $I_c R_n = 500 \mu\text{V}$

Process variation	Yield (95% confidence level)		
	10 GHz	20 GHz	50 GHz
State-of-art spreads	45.5% ($\pm 9.1\%$)	42.1% ($\pm 9.0\%$)	33.9% ($\pm 8.6\%$)
Ideal spreads	76.9% ($\pm 7.7\%$)	71.9% ($\pm 8.2\%$)	64.5% ($\pm 8.7\%$)

The 3b-counter yield values are much smaller than the ones of the one stage T flip-flop. With the state-of-the-art spreads, at 10 GHz, the yield drops from 79.3% ($\pm 7.4\%$) to 45.5% ($\pm 9.1\%$). At 50 GHz, it drops from 71.1% ($\pm 8.2\%$) to 33.9% ($\pm 8.6\%$). And even with the ideal spreads, at 10 GHz, the yield drops from 96.7% ($\pm 3.3\%$) to 76.9% ($\pm 7.7\%$). At 50 GHz, it drops from 95.0% ($\pm 4.0\%$) to 64.5% ($\pm 8.7\%$).

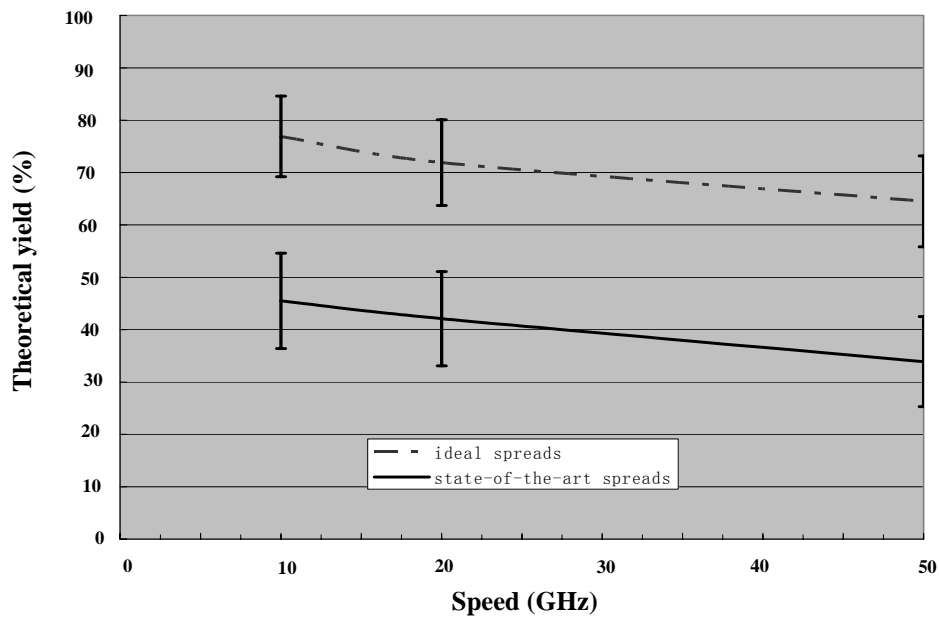


Figure A.7 TRW 3b-counter theoretical yield with $I_c R_n = 500 \mu\text{V}$.

A.4 Conclusion and Future Work

A few conclusions can be drawn based on the simulations in this chapter.

1. Without considering the thermal noise, with the state-of-the-art process variations and $I_cR_n = 500 \mu V$, the yield of a basic cell T flip-flop (14 junctions) is 77.7% ($\pm 7.6\%$) at 20 GHz; 71.1% ($\pm 8.2\%$) at 50 GHz. The yield of a medium circuit 3b-counter (38 junctions) is 42.1% ($\pm 9.0\%$) at 20 GHz; 33.9% ($\pm 8.6\%$) at 50 GHz. These yield values are too low to make any useful large HTS circuit as we can see the yield degrades rapidly as the number of devices in the circuit increases.

Improvement on several aspects can help increase the yield value.

2. The most important factor affecting the yield is the process variation. The LTS state-of-the-art equivalent process spreads can improve the yield of the HTS T flip-flop to 96.7% ($\pm 3.3\%$) at 20 GHz; 95.0% ($\pm 4.0\%$) at 50 GHz. The yield of the 3b-counter is improved to 71.9% ($\pm 8.2\%$) at 20 GHz; 64.5% ($\pm 8.7\%$) at 50 GHz.

3. Increasing junction I_cR_n value can increase circuit maximum operation speed and increase circuit yield at high speed. With the state-of-the-art process variation, the yield of the TRW flip-flop is 50.4% ($\pm 9.1\%$) at 10 GHz for $I_cR_n = 75 \mu V$ compared to 71.1% ($\pm 8.2\%$) at 50 GHz for $I_cR_n = 500 \mu V$.

4. Reducing parasitic inductances is favorable. The idealized Conductus T flip-flop without parasitic inductance has a better yield at 50 GHz and above with the same process variations.

BER calculations incorporating thermal noise in the WRspice transient analysis was performed by M. Jefferey in this study. With $I_cR_n = 250 \mu V$, and in the absence of parasitics, it appears that $BER < 10^{-6}$ with $T = 40$ K is achievable even with the clock frequency as high as 100 GHz. However, the BER is worsened by at least one order of magnitude when taking account of

the parasitics. A combination of Monte Carlo analysis and noise calculation shows the average BER of the ideal T flip-flop without parasitics at 50 GHz is approximately doubled when the state-of-the-art spreads are taken into account. With these spreads, it is estimated the temperature needs to be lowered to 20-30 K to get $\text{BER} < 10^{-6}$ [72]. Further study is needed to confirm it.

The BER results show the importance of reducing parasitics. The yield results show the importance of controlling process variation. $I_c R_n$ increases the circuit maximum operation speed and is favorable for both the BER and the yield at high speed. Improvement on all the above three aspects are needed to obtain more robust HTS digital circuits.

References

- [1] T. Van Duzer and C. W. Turner, *Principles of Superconductive Devices and Circuits*, New York, Elsevier, 1999.
- [2] T. Van Duzer, "Superconductor Electronics, 1986 - 1996," *IEEE Trans. Applied Superconductivity*, Vol. 7, pp. 98-111, June 1997.
- [3] K. Likharev and V. Semenov, "RSFQ logic/memory family: a new Josephson-junction technology for sub-terahertz-clock-frequency digital systems," *IEEE Trans. Applied Superconductivity*, Vol. 1, pp. 3-28, March 1991.
- [4] D. K. Brock, E. K. Track, and J. M. Rowell, "Superconductor ICs: The 100-GHz second generation," *IEEE spectrum*, vol. 37, Dec. 2000, pp. 40-46.
- [5] P. Bunyk, M. Leung, J. Spargo, and M. Dorojevets, "FLUX-1 RSFQ microprocessor: physical design and test results," *IEEE Trans. Applied Superconductivity*, Vol. 13, pp. 433-436, June 2003.
- [6] N. B. Dubash, V. V. Borzenets, Y. M. Zhang, V. Kaplunenko, J. W. Spargo, A. D. Smith and T. Van Duzer, "System demonstration of a multigigabit network switch," *IEEE Trans. Applied Superconductivity*, Vol. 48, pp. 1209-1215, July 2000.
- [7] Y. Kameda, S. Yorozu, Y. Hashimoto, H. Terai, A. Fujimaki and N. Yoshikawa, "40-GHz operation of a single-flux-quantum (SFQ) 4x4 switch scheduler," *Physica C*, Vol. 445-448 , pp. 1008-1013, 2006.
- [8] R. W. Simon, R. B. Hammond, S. J. Berkowitz, and B. A. Willemsen, "Superconducting microwave filter systems for cellular telephone base stations," *Proceedings of the IEEE*, Vol. 92, No. 10., pp. 1585-1596, October 2004.
- [9] O. A. Mukhanov, D. Gupta, A. M. Kadin and V. K. Semenov, "Superconductor analog-to-digital converters," *Proceedings of the IEEE*, Vol. 92, No. 10., pp. 1564-1584, October 2004.
- [10] D. K. Brock, O. A. Mukhanov, and J. Rosa, "Superconductor digital RF development for software radio," *IEEE communication magazine*, pp. 174-179, 2001.

- [11] B. D. Josephson, "Possible new effects in superconductive tunneling," *Phys. Lett.*, Vol. 1, pp. 251–253, July 1962. P. W. Anderson, "How Josephson discovered his effect," *Phys. Today*, Vol. 23, pp. 23–29, November 1970.
- [12] P. W. Anderson and J. M. Rowell, "Probable observation of the Josephson superconducting tunneling effect," *Phys. Rev. Lett.*, Vol. 10, pp. 230–232, March 1963.
- [13] R. P. Feynman, R. B. Leighton, and M. Sands, *The Feynman Lectures on Physics*, Vol. III, Reading, Massachusetts: Addison-Wesley, 1965, pp. 21–14. A more detailed treatment is given by B. D. Josephson, "Weakly coupled superconductors," in *Superconductivity*, Vol. I (R. D. Parks, Ed.). New York: Marcel Dekker, 1969.
- [14] M. Maezawa, M. Aoyagi, H. Nakagawa, I. Kurosawa, and S. Takada, "Specific capacitance of Nb/AlO_x/Nb Josephson junctions with current densities in the range of 0.1–18 kA/cm²," *Appl. Phys. Lett.*, Vol. 66, pp. 2134–2136, April 1995.
- [15] S. V. Polonsky, V. K. Semenov and D. F. Schneider, "Transmission of single-flux-quantum pulses along superconducting microstrip lines," *IEEE Trans. Appl. Superconduct.*, Vol.3, pp. 2598-2600, March 1993.
- [16] Q. P. Herr, A. D. Smith and M. S. Wire, "High speed data link between digital superconductor chips," *Appl. Phys. Lett.*, Vol. 80, pp. 3210–3212, April 2002.
- [17] S. V. Polonsky, V. K. Semenov, P. I. Bunyk, A. F. Kirichenko, A. Y. Kidiyarov-Shevchenko, O. A. Mukhanov, P. N. Shevchenko, D. F. Schneider, D. Y. Zinoviev, and K. K. Likharev, "New RSFQ circuits," *IEEE Trans. Appl. Superconduct.*, Vol.3, pp. 2566-77, March 1993.
- [18] V. K. Kaplunenko, M. I. Khabipov, V. P. Koshelets, K. K. Likharev, O. A., Mukhanov, V. K. Semenov, I. L. Serpuchenko and A. N. Vystavkin, "Experimental study of the RSFQ logic elements," *IEEE Trans. Magnetics*, Vol. 25, pp. 861-864, March 1989.
- [19] A. M. Kadin, C. A. Mancini, M. J. Feldman, and D. K. Brock, "Can RSFQ logic circuits be scaled to deep submicron junctions?" *IEEE Trans. Appl. Superconduct.*, Vol. 11, pp.1050-1055, March 2001.
- [20] D. K. Brock, A. M. Kadin, A. F. Kirichenko, O. A. Mukhanov, S. Sarwana, J. A. Vivalda, W. Chen, and J. E. Lukens, "Retargeting RSFQ cells to a submicron fabrication process," *IEEE Trans. Appl. Superconduct.*, Vol. 11, pp. 369-372, March 2001.
- [21] W. Chen, A. V. Rylyakov, V. Patel, J. E. Lukens, and K. K. Likharev, "Rapid single flux quantum T-flip flop operating up to 770 GHz," *IEEE Trans. Appl. Superconduct.*, Vol 9, pp.3212-3215, June 1999.
- [22] X. Meng, L. Zheng, A. Wong, and T. Van Duzer, "Micron and submicron Nb/Al-AlOx/Nb tunnel junctions with high critical current densities," *IEEE Trans. Appl. Superconduct.*, Vol. 11, pp. 365-368, March 2001.
- [23] G. L. Kerber, L. A. Abelson, M. L. Leung, Q. P. Herr, and M. W. Johnson, "A high density 4 kA/cm² Nb integrated circuit process," *IEEE Trans. Appl. Superconduct.*, Vol. 11, pp.1061-1065, March 2001.
- [24] A. B. Kaul, S. R. Whiteley, T. Van Duzer, L. Yu, N. Newman and J. M. Rowell, "Internally shunted sputtered NbN Josephson junctions with a TaNx barrier for nonlatching logic applications," *Appl. Phys. Lett.*, Vol. 78, pp. 99-101, 1 Jan. 1995.

[25] L. Yu, N. Newman, and J. M. Rowell, "Measurement of the coherence length of sputtered $\text{Nb}_{0.62}\text{Ti}_{0.38}\text{N}$ thin films," *IEEE Trans. Appl. Superconduct.*, Vol. 12, pp.1795-1798, June 2002.

[26] X. Meng, A. Bhat and T. Van Duzer, "Very small critical current spreads in Nb/AlOx/Nb integrated circuits using low temperature and low stress ECR PECVD silicon oxide films," *IEEE Trans. Appl. Superconduct.*, Vol. 9, pp. 3208-3211, June 1999.

[27] X. Meng, H. Jiang, A. Bhat, and T. Van Duzer, "Precise control of critical current and resistance in a Nb/AlOx/Nb integrated circuit process," *Extended Abstracts of the 6th International Superconductive Electronics Conference, ISEC'97*, Vol. 2, pp. 164-166, Berlin, Germany, June 1997.

[28] Toppan Photomasks, Inc. <http://www.photomask.com>.

[29] V. K. Kaplunenko, "Fluxon interaction in an overdamped Josephson transmission line," *Appl. Phys. Lett.*, Vol. 66, pp. 3365-3367, 12 June 1995.

[30] K. K. Likharev, "Superconductor devices for ultrafast computing," *Applications of Superconductivity*, H. Weinstock, ed. Dordrecht, Netherlands: Kluwer Acad. Pub., 2000.

[31] J. X. Przybysz, D. L. Miller, S. S. Martinet, J. Kang, A. H. Worsham, and M. L. Farich, "Interface circuits for chip-to-chip data transfer at GHz rate," *IEEE Trans. Appl. Superconduct.*, Vol. 7, pp. 2657-2660, June 1997.

[32] M. Maezawa, H. Yamamori, and A. Shoji, "Demonstration of chip-to-chip propagation of single flux quantum pulses," *IEEE Trans. Appl. Superconduct.*, Vol. 11, pp. 337-340, March 2001.

[33] T. L. Sterling, P. M. Kogge, G. Gao, K. K. Likharev and M. J. MacDonald, "Steps to petaflops computing", *First Workshop on Hybrid Technology Multithreaded Architecture For Very High Performance Computing*, Pasadena, USA, Feb. 25-26, 1997

[34] Z. J. Deng, A. Flores, L. Zheng, M. Jeffery, U. Ghoshal, E. Fang, X. Meng, S. R. Whiteley and T. Van Duzer, "Hybrid CMOS-RSFQ wideband memory system for multithreaded parallel vector processors", *First Workshop on Hybrid Technology Multithreaded Architecture For Very High Performance Computing*, Pasadena, USA, Feb. 25-26, 1997

[35] T. Van Duzer, L. Zheng, X. Meng, C. Loyo, S. R. Whiteley, L. Yu, N. Newman, J. M. Rowell, and N. Yoshikawa, "Engineering issues in high-frequency RSFQ circuits," *Physica C*, Vol.372-376, pt.1, pp. 1-6, 1 Aug. 2002.

[36] Q. Liu, T. Van Duzer, X. Meng, S. R. Whiteley, K. Fujiwara, T. Tomida, K. Tokuda, and N. Yoshikawa, "Simulation and measurements on a 64-kbit hybrid Josephson-CMOS memory," *IEEE Trans. Appl. Superconduct.*, Vol. 15, pp. 415-418, June 2005.

[37] S. B. Kaplan and O. A. Mukhanov, "Operation of a superconductive demultiplexer using rapid single flux quantum (RSFQ) technology," *IEEE Trans. Appl. Superconduct.*, Vol. 5, pp. 2853-2856, June 1995.

[38] D. L. Miller, J. X. Przybysz, A. H. Worsham, and J. Kang, "A single-flux-quantum demultiplexer," *IEEE Trans. Appl. Superconduct.*, Vol. 7, pp. 2690-2693, June 1997.

[39] N. Yoshikawa, Z. J. Deng, S. R. Whiteley, and T. Van Duzer, "Simulation and 18 Gb/s testing of a data-driven self-timed RSFQ demultiplexer," *IEEE Trans. Appl. Superconduct.*, Vol. 9,

pp. 4349-4352, June 1999.

[40] L. Zheng, N. Yoshikawa, J. Deng, X. Meng, S. R. Whiteley, and T. Van Duzer, "RSFQ multiplexer and demultiplexer," *IEEE Trans. Appl. Superconduct.*, Vol. 9, pp. 3310-3313, June 1999.

[41] Xic and WRspice by Whiteley Research, <http://wrcad.com/>.

[42] <http://www-cryo.eecs.berkeley.edu/CADtools.html>

[43] <http://www.kapl.tv/>

[44] <http://www.ece.rochester.edu/~sde/research/software/malt/index.html>

[45] N. Yoshikawa and K. Yoneyama, "Parameter Optimization of Single Flux Quantum Digital Circuits Based on Monte Carlo Yield Analysis," *IEICE TRANS. ELECTRON.*, Vol. E83-C No. 1 pp.75-80, January 2000.

[46] <http://pavel.physics.sunysb.edu/RSFQ/>

[47] R. Spence and R. S. SOIN, *Tolerance design of electronic circuits*, 1988.

[48] W. H. Chang, "The inductance of a superconductor strip transmission line," *J. Appl. Phys.*, Vol. 50, pp. 8129-8134, December 1979.

[49] A. F. Kirichenko, "High-speed asynchronous data multiplexing/demultiplexing," *IEEE Trans. Appl. Superconduct.*, Vol. 9, pp. 4046-4048, June 1999.

[50] S. V. Polonsky, V. K. Semenov, and A. F. Kirichenko, "Single flux, quantum B flip-flop and its possible applications," *IEEE Trans. Appl. Superconduct.*, Vol. 4, pp. 9-18, March 1994.

[51] A. F. Kirichenko, V. K. Semenov, Y. K. Kwong, V. Nandakumar, "4-bit rapid single-flux-quantum decoder," *IEEE Trans. Appl. Superconduct.*, Vol. 5, pp. 2857-2860, June 1995.

[52] L. Zheng, X. Meng, S. R. Whiteley, and T. Van Duzer, "50 GHz Multiplexer and Demultiplexer Designs with On-Chip Testing," *IEICE TRANS. ELECTRON.* Vol. E85-C, No. 3, pp.621-624, March 2002.

[53] A. F. Kirichenko, O. A. Mukhanov, and A. I. Ryzhikh, "Advanced on-chip test technology for RSFQ circuits," *IEEE Trans. Appl. Superconductivity*, Vol. 7, pp. 3438-3441, June 1997.

[54] Q. P. Herr, K. Gaj, A. M. Herr, N. Vukovic, C. A. Mancini, M. F. Bocko, and M. J. Feldman, "High speed testing of a four-bit RSFQ decimation digital filter," *IEEE Trans. Appl. Superconduct.*, Vol. 9, pp. 2975 - 2978, June 1997.

[55] Z. J. Deng, N. Yoshikawa, S. R. Whiteley and T. Van Duzer, "Data-driven self-timed RSFQ high speed test system," *IEEE Trans. Appl. Superconductivity*, Vol. 7, pp. 3634-3637, June 1997.

[56] Z. J. Deng, N. Yoshikawa, S. R. Whiteley and T. Van Duzer, "Data-driven self-timed RSFQ digital integrated circuit and system," *IEEE Trans. Appl. Superconductivity*, Vol. 7, pp. 3634-3637, June 1997.

[57] N. Yoshikawa, Z. J. Deng, S. R. Whiteley and T. Van Duzer, "Design and testing of data-driven self-timed RSFQ shift register," Extended Abstract of *6th International Superconductive Electronics Conference (ISEC'97)*, Berlin, Germany, July 25-28. 1997.

[58] O. A. Mukhanov, S. V. Polonsky, and V. K. Semenov, "New elements of the RSFQ logic

family," *IEEE Trans. Magnetics*, Vol. 27, pp. 2435-2438, March 1991.

[59] O. A. Mukhanov, "Rapid single flux quantum (RSFQ) shift register family," *IEEE Trans. Appl. Superconduct.*, Vol. 3, pp. 2578-2581, March 2003.

[60] C. A. Mancini, N. Vukovic, A. M. Herr, K. Gaj, M. F. Bocko, and M. J. Feldman, "RSFQ circular shift registers," *IEEE Trans. Appl. Superconduct.*, Vol. 7, pp. 2832-2835, June, 1997.

[61] A. M. Herr, C. A. Mancini, N. Vukovic, M. F. Bocko, and M. J. Feldman, "High-speed operation of a 64-bit circular shift register," *IEEE Trans. Appl. Superconduct.*, Vol. 8, pp. 120-123, September, 1998.

[62] Y. Kameda, S. Yorozu, Y. Hashimoto, H. Terai, A. Fujimaki, and N. Yoshikawa, "High-speed demonstration of single-flux-quantum cross-bar switch up to 50 GHz," *IEEE Trans. Appl. Superconduct.*, Vol. 15, pp. 6-9, March 2005.

[63] M. Jefferey, T. Van Duzer, J. R. Kirtley, and M. B. Ketchen, "Magnetic imaging of moat-guarded superconducting electronic circuits," *Appl. Phys. Lett.*, Vol. 67, pp. 1769-1771, September 1995.

[64] L. Zheng, S. R. Whiteley, X. Meng, and T. Van Duzer, "High-speed and Medium-speed Testing of the RSFQ Multiplexer and Demultiplexer," Presented at *the International Superconductor Electronics Conference, (ISEC'99)*, June 21-25, 1999, Berkeley, CA.

[65] W. H. Mallison, S. J. Berkowitz, A. S. Hirahara, M. J. Neal, and K. Char, "A multilayer $\text{YBa}_2\text{Cu}_3\text{O}_x$ Josephson junction process for digital circuit applications," *Appl. Phys. Lett.*, Vol. 68, pp. 3808-3810, June 1996.

[66] B. D. Hunt, M. G. Forrester, J. Talvacchio, J. D. McCambridge, and R. M. Young, "High- T_c superconductor/normal-metal/superconductor edge junctions and SQUIDs with integrated groundplanes," *Appl. Phys. Lett.*, Vol. 68, pp. 3805-3807, June 1996.

[67] B. H. Moeckly and K. Char, "Properties of interface-engineered high T_c Josephson junctions," *Appl. Phys. Lett.*, Vol. 71, pp. 2526-2528, June 1996.

[68] A. G. Sun, D.J. Durand, J.M. Murduck, S.V. Rylov, M.G. Forrester, and B.D. Hunt, "HTS SFQ T-flip flop with directly coupled readout," *IEEE Trans. Appl. Superconduct.*, Vol 9, pp. 3825-3828 June 1999.

[69] M. Jeffery, P. Y. Xie, S. R. Whiteley, and T. Van Duzer, "Monte Carlo and thermal noise analysis of ultra-high-speed high temperature superconductor digital circuits," *IEEE Trans. Appl. Superconduct.*, Vol. 9, pp. 4095-4098, June 1999.

[70] M. Jeffery, L. Zheng, S. R. Whiteley, and T. Van Duzer, "Simulations of ultra-high-speed high temperature superconductor digital circuits combining process variations and thermal noise," Presented at *the International Super-conductor Electronics Conference, (ISEC'99)*, June 21-25, 1999, Berkeley, CA.

[71] M. Jeffery, L. Zheng, S. R. Whiteley, and T. Van Duzer, "Simulations of HTS digital circuits with process spreads and thermal noise," Presented at *the International Workshop on Superconductivity*, June 27-30, 1999, Kauai, Hawaii.

[72] T. Van Duzer, "Analysis of ultra-high-speed, high-temperature super-conductor (HTS) digital circuits," *ONR N00014-98-0084* 10/01/1997 -09/30/1999 final report.